Engineering quantum coherence in the integer quantum Hall effect regime

Phuong-Anh Huynh Hyunh

Université Paris-Sud 11

École Doctorale "Physique de la Région Parisienne"

Spécialité: Physique Quantique

Thèse de Doctorat

présentée par Phuong-Anh HUYNH

préparée au sein du Service de Physique de l'État Condensé,
CEA-Saclay 91191 Gif-sur-Yvette

Amélioration de la cohérence quantique dans le régime d'effet Hall quantique entier

Thèse soutenue le Jeudi 09 Février 2012, devant le jury composé de:

Christophe CHAUBET (Rapporteur)
Thierry JOLICOEUR (Examinateur)
Bernard PLACAIS (Examinateur)
Patrice ROCHE (Directeur de Thèse)
Marc SANQUER (Rapporteur)

Remerciements

Je remercie Patrice Roche, Fabien Portier et Christian Glattli de m'avoir accueillie pendant les trois ans (et plus...) qu'on duré ma thèse dans le groupe Nanoélectronique au Service de Physique de l'Etat Condensé du CEA-Saclay, et pour m'avoir fait découvrir la physique mésoscopique.

Je remercie en particulier Patrice Roche et Fabien Portier pour l'attention qu'ils ont portée aux corrections de ce manuscrit.

Je remercie également les thésards, stagiaires, post-docs passés et présents du groupe: Preden Roulleau, qui m'a laissée travailler avec lui sur l'expérience constituant le sujet de sa thèse, Eva Zakka-Bajjani, pour sa gentillesse. Merci aussi à Brice Dubost qui a poursuivi le travail réalisé pendant mon stage. Merci aux nouveaux, de m'avoir tenu compagnie le temps que j'achève ma thèse: Ivana, Julie, Thibaud et Andrey. Merci à Patrice Jacques pour son admirable (!) expertise technique Je remercie également Pepe, Philipe, Matthieu, Geneviève, Keyan, Jérémie, Simone, Valentin, Kyril, Joseph pour les repas et les cafés que nous avons partagé tous ensemble dans la bonne humeur. Merci aussi aux ami(es) de jogging et de pauses café: Gwen, Dorothée, Areta, Coralie, Andreas... Merci à tous les autres et à mon vélo en particulier.

Get a bicycle. You will not regret it. If you live. - Mark Twain

Amélioration de la cohérence quantique dans le régime d'effet Hall quantique entier

Cette thèse est consacrée à l'amélioration de la cohérence dans le régime d'effet Hall quantique entier (EHQE) à facteur de remplissage $\nu = 2$, obtenu en appliquant un fort champ magnétique perpendiculairement au plan d'un gaz bidimensionnel d'électrons formé à l'interface d'une hétérostructure semiconductrice d'AlGaAs/GaAs. On obtient alors des conducteurs unidimensionnels chiraux (états de bord) permettant de réaliser l'équivalent électronique de l'interféromètre de Mach-Zehnder (IMZ), pour étudier la cohérence dans ce régime. L'observation inattendue d'une structure périodique en forme de lobes dans la visibilité des interférences en fonction de la tension appliquée en entrée suggère un rôle non négligeable des interactions.

Dans un première partie nous expliquons l'émergence des états de bord dans le régime d'EHQE. Nous faisons ensuite l'état de l'art des connaissances concernant leur cohérence, puis nous présentons l'IMZ électronique du point de vue expérimental.

Ensuite, nous détaillons les résultats expérimentaux, d'abord concernant la visibilité à tension finie: nos mesures confirment une prédiction théorique concernant un transition de phase quantique en fonction de la dilution de l'état de bord qui interfère ; nous ne voyons pas d'effet flagrant de la relaxation en énergie. Enfin, de précédents travaux [1] ayant identifié clairement l'état de bord voisin de celui qui interfère comme l'environnement limitant la cohérence du système, nous avons réalisé un nouveau type d'échantillon afin de diminuer le couplage à cet environnement de manière contrôlée. Nous avons ainsi doublé la cohérence en accord quantitatif avec la théorie issue de précédents travaux [1].

Mot-clefs: effet Hall quantique entier ; cohérence quantique ; états de bord ; interactions.

Engineering quantum coherence in the integer quantum Hall effect regime

This PhD thesis is devoted to the engineering of quantum coherence in the integer quantum Hall effect regime (IQHE) at filling factor $\nu = 2$, obtained by applying a strong perpendicular magnetic field to a bidimensional electron gas formed at the interface of a GaAlAs/GaAs semiconducting heterostructure. Then unidimensional chiral conductors called edge states appear which can be used as electron beams to build the equivalent in

condensed matter of a Mach-Zehnder interferometer (MZI) so as to study coherence in this regime. The unexpected periodic lobe structure of the visibility as function of the bias voltage suggests that interactions play an important role.

In the first part, we explain how edge states emerge in the IQHE regime. We picture the state of the art on the edge states coherence. Then we present the MZI from the experimental point of view.

Next we show our results, first concerning the visibility at finite bias: our measurements confirm a prediction about a quantum phase transition as function of the interfering edge state dilution. We don't see any significant manifestation of energy relaxation in the visibility. Finally, having identified the adjacent edge state as the noisy environment limitating coherence thanks to previous works, we have designed a new kind of sample to decrease the coupling of the system to this environment in a controlled manner. We thus decreased dephasing by half, in quantitative agreement with the theory developped previously in our group.

Keywords: integer quantum Hall effect ; quantum coherence ; edge states ; interactions.

Contents

1. Résumé de la thèse

Contents

1.1. Introduction

L'objectif principal de cette thèse est l'amélioration de la cohérence quantique dans les systèmes de gaz bidimensionnels d'électrons (GE2D) formés à l'interface d'une hétérostructure semiconductrice de GaAs/AlGaAs, dans le régime d'effet Hall quantique entier (EHQE) à facteur de remplissage $\nu = 2$, obtenu lorsqu'on applique un fort champ magnétique perpendiculairement au plan du gaz.

Dans le régime d'EHQE, la conduction des électrons se fait par l'intermédiaire de canaux unidimensionnels chiraux appelés états de bord, qui assurent un transport ballistique – avec un transmission parfaitement contrôlée – le long des bords du GE2D.

Ces 'rayons électroniques' sont l'équivalent, en matière condensée, des rayons optiques. On peut en effet les manipuler facilement en taillant l'échantillon de façon appropriée (puisque ces rayons suivent les bords du GE2D). Il existe de plus un dispositif faisant office de lame séparatrice, appelé contact ponctuel quantique (CPQ), consistant en une grille métallique déposée à la surface de l'échantillon qui, grâce à la tension de polarisation qui lui est appliquée, contrôle la largeur du GE2D se trouvant juste en dessous et par là-même,

la transmission des rayons électroniques. On dispose ainsi de tous les éléments pour bâtir l'analogue, en matière condensée, des expériences d'optique quantique.

Afin d'en savoir plus sur la cohérence des électrons dans le régime d'EQHE, on peut ainsi construire un interféromètre, ici un interféromètre de Mach-Zehnder.

1.2. État de l'art

Que savait-on sur la cohérence des électrons dans le régime d'EHQE, au moment où j'ai commencé mon travail de thèse? Mon prédecesseur, Preden Roulleau, a mis en évidence un longueur de cohérence l_φ de 20 μm à 20 mK, étonnamment courte (l'on espérait une longueur de cohérence plus importante), variant comme l'inverse de la température [2] (Fig. 1.1 (gauche)). Il a également identifié une source probable de limitation de cette longueur de cohérence: à $\nu = 2$, il y a deux états de bords qui se propagent le long des bords du GE2D. L'état de bord interne – le plus éloigné du bord – voisin de celui qui interfère (l'état de bord externe), brouille la phase des électrons qui voyagent dans les bras de l'interféromètre, par l'intermédiaire d'un bruit de charge thermique qui fait fluctuer le potentiel interne vu par les électrons [1] (Fig. 1.1 (droite)).

Auparavant, Neder *et al.* [4] ont mesuré un comportement curieux de la visibilité en fonction de la tension appliquée en entrée de l'interféromètre V_1: la visibilité décroît à mesure que la tension augmente en oscillant avec de multiples extinctions tandis que la phase des interférences est rigide le long d'un 'lobe' de visibilité et effectue un saut de π à chaque extinction (Fig. 1.2). Il semble que l'on distingue des structure à lobes multiples (deux lobes au moins de chaque côté du lobe central) mesurées à $\nu = 2$ uniquement, et des structures à un seul lobe de chaque côté du lobe central, observées à $\nu = 2$ et $\nu = 1$.

Ce comportement non attendu dans le cadre d'une théorie de champ moyen à motivé de nombreux travaux théoriques s'intéressant au rôle des interactions entre et à l'intérieur des états de bord [5–11]. Pour l'instant, il n'y a pas de consensus pour expliquer cette structure.

Comment fitter ces structures de lobes et quels sont les paramètres pertinents, comment varient-ils avec les paramètres de l'expérience ? Les fonctions que nous avons utilisé pour fitter ces différentes structures présentent un seul paramètre ajustable pour les structures simples et deux paramètres pour les structure multiples.

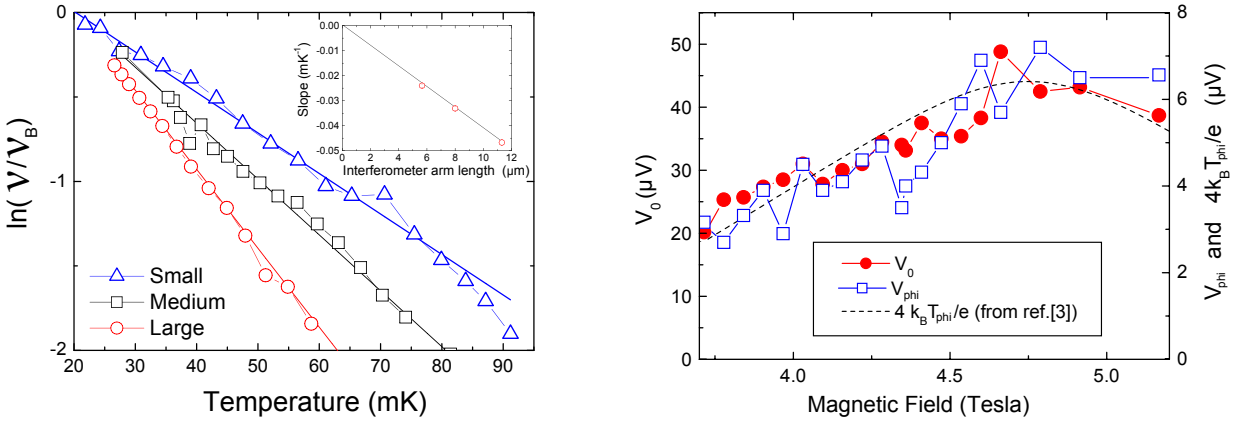

Figure 1.1.: *(gauche) Visibilité en échelle logarithmique en fonction de la température pour trois échantillons de longueur de bras $L = 5.6,\ 8$ et $11.3\ \mu m$. La visibilité décroît exponentiellement avec la température avec un taux T_φ^{-1} qui croît linéairement avec L (insert) [2]. (droite) Échelle gauche: V_0 en fonction du champ magnétique (cercles rouges pleins). Échelle droite: V_φ (carrés bleus vides) et $4k_BT_\varphi/e$ (pointillés) en fonction du champ magnétique. Les variations de V_0 sont proportionnelles à celles de V_φ (qui caractérise un bruit de partition additionnel dans l'état de bord interne) et de $4k_BT_\varphi/e$. V_φ et $4k_BT_\varphi/e$ tombent l'un sur l'autre, validant notre approche rendant le bruit de charge dans l'état de bord interne responsable de la perte de cohérence [1, 3].*

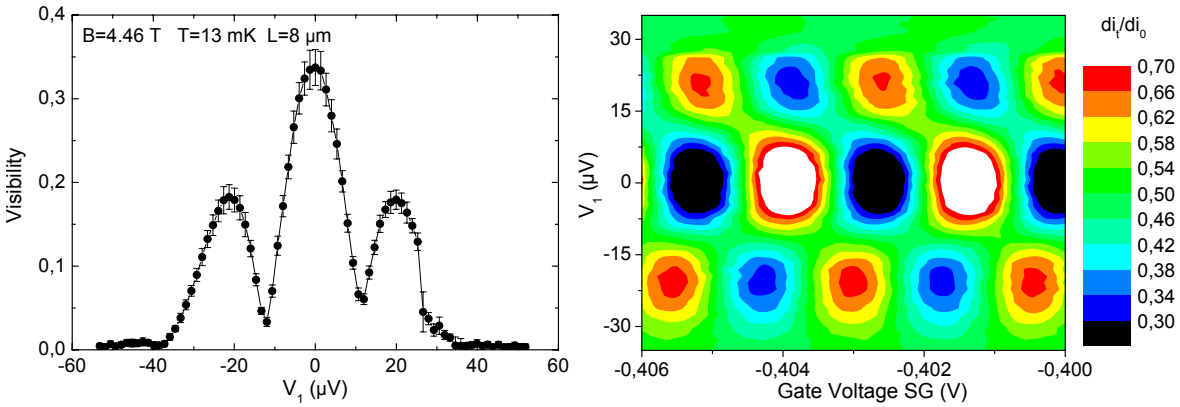

Figure 1.2.: *(gauche) Visibilité décroissant avec la tension appliquée en entrée $|V_1|$ montrant des oscillations avec de multiples extinctions pour un échantillon de longueur de bras $L = 8\ \mu m$, à $B = 4.46\ T$ et $T = 13\ mK$. Il y a deux lobes de chaque côté du lobe central. (droite) Transmission différentielle de l'état de bord externe en code couleur, en fonction de la tension de polarisation de la grille SG selon l'axe des abscisses, et en fonction de la tension V_1 sur l'axe des ordonnées. À l'intérieur d'un lobe la phase des interférences est rigide, et subit un saut de π aux extinctions.*

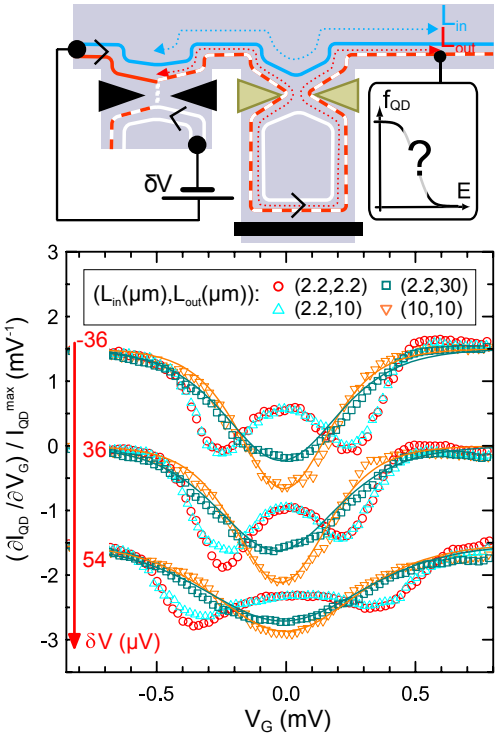

Figure 1.3: *(dessus) Une distribution hors équilibre se propage dans l'état de bord externe sur une distance L_{out} et l'état bord interne voisin se propage sur une longueur L_{in}. L_{out} peut être rallongée par rapport à L_{in} en forçant l'état de bord externe à passer dans une boucle. (dessous) La conductance à travers la boîte quantique qui sert de filtre à énergie montre deux 'puits' pour les courtes distances $(L_{in}, L_{out}) = (2.2, 2.2)$ et relaxe en un simple 'puits' pour les distances plus longues $(10, 10)$. Cette relaxation en énergie est gelée lorsque l'état de bord externe parcourt une boucle assez petite ($\sim$ 8 μm): $(2.2, 10)$ où l'état de bord interne est localisé [15].*

D'autres expériences par Altimiras *et al.* [12] ont mis en évidence le rôle joué par l'interaction entre les deux états de bord à $\nu = 2$ dans la relaxation d'une distribution hors équilibre lors de sa propagation dans un état de bord. Celle-ci se fait par échange d'énergie avec l'autre état de bord [13, 14]. Par ailleurs, en confinant l'état de bord interne dans une boucle fermée de longueur 8 μm, les auteurs ont gelé la relaxation en énergie dans l'état de bord externe (Fig. 1.3), en ouvrant un gap de taille suffisante dans le spectre des excitations de basse énergie de l'état de bord interne.

1.3. Interféromètre de Mach-Zehnder électronique

Nous avons étudié deux types d'échantillons toujours à $\nu = 2$, alors que deux états de bord (en rouge et bleu sur la Fig. 1.4) étaient présents. L'état représenté en bleu qui correspond à l'état de bord externe, est celui qui interfère.

Les premiers échantillons étudiés correspondent à la configuration de base de l'interféromètre (Fig. 1.4 (dessus)). L'état de bord interne (en rouge) est réfléchi à tous les CPQs, l'état

de bord externe (en bleu) est transmis vers l'interferomètre par le CPQ d'injection, $G0$. Il est séparé en deux chemins par le premier CPQ de l'interféromètre, $G1$, chemins qui sont recombinés au niveau du second CPQ de l'interféromètre, $G2$. Les deux trajets interfèrent dans le courant transmis vers le contact de mesure (contact n°3) alors que le courant réfléchi est collecté à la masse de l'échantillon (contact n°4).

On révèle les interférences dans le courant transmis en faisant varier la phase Aharonov-Bohm des électrons, soit en faisant varier lentement le champ magnétique, soit en changeant la surface entre les deux bras de l'interféromètre, par l'intermédaire de la grille SG qui change la longueur du bras inférieur (noté D sur la Fig. 1.4), avec sa polarisation. Il est aussi possible d'utiliser l'état de bord interne comme une grille pour changer la longueur du bras supérieur (noté U sur la Fig. 1.4), en faisant varier la tension V_2 appliquée au contact n°2. La période V_0 des interférences ainsi révélées diminue quand le couplage entre les deux états de bord augmente. On montre dans une approche de champ moyen que cette période est proportionnelle à la somme des inverses de la capacité géométrique entre les deux états de bord et de la capacité quantique.

Dans les nouveaux échantillons (Fig. 1.4 (dessous)), des grilles supplémentaires G_U et G_D permettent, quand on les pince, de confiner l'état de bord interne en petites boucles fermées. On espère ainsi modifier le couplage entre les deux états de bord, et peut-être aussi, ainsi que les travaux de Altimiras *et al.* le suggèrent [15], geler les fluctuations de charges dans l'état de bord interne qui sont responsables de la longueur de cohérence finie selon les travaux de Roulleau *et al.* [1]

1.4. Visibilité à tension finie

Dans un premier temps nous avons poursuivi l'étude commencée par P. Roulleau sur la structure de lobes [3], pour déterminer de quels paramètres physiques dépendent les deux échelles d'énergie mises en évidence par nos fits (celle caractérisant les lobes simples, et celle caractérisant les lobes multiples).

Dans cette perspective, nous avons regardé comment la structure de lobes multiple était modifiée par la transmission $\mathcal{T}_0$ de l'état de bord externe par le CPQ d'injection, $G0$ (dilution). Nous avons comparé nos résultats à une théorie développée par Levkiviskyi *et al.* [16] qui prévoit une transition de phase quantique dans la structure de lobes, provoquée par le bruit de partition du CPQ $G0$, lorsque $\mathcal{T}_0 = 0.5$ (Fig. 1.5 (gauche)). Données et

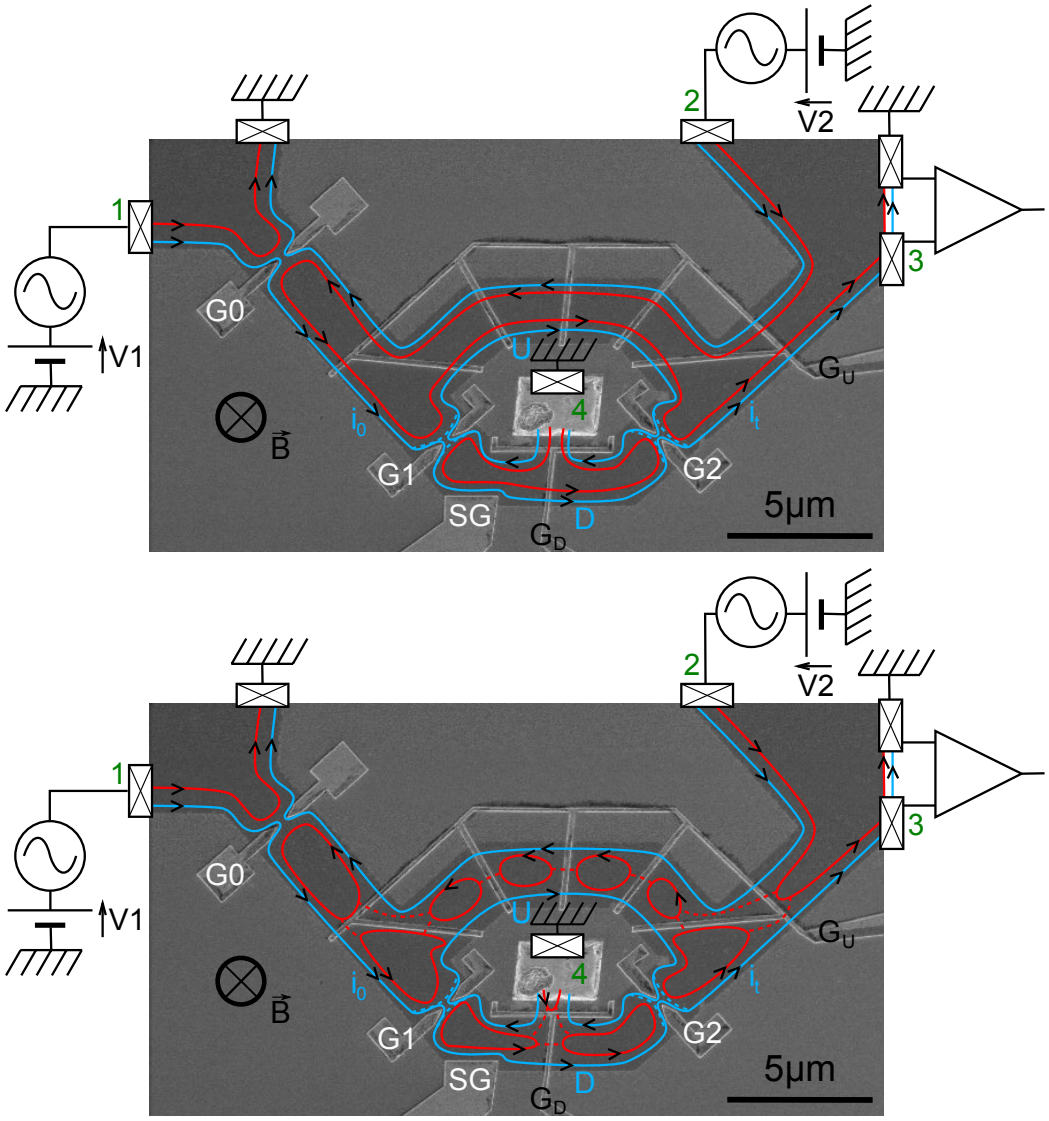

Figure 1.4.: *Image de l'échantillon au microscope électronique à balayage. Le courant est injecté au contact n°*1*, le contact n°*2 *sert à polariser l'état de bord interne (en rouge), que l'on peut utiliser pour mesurer le couplage* V_0^{-1} *avec l'état de bord externe (en bleu) dans le bras supérieur, en faisant une expérience de type 'which path'. Le courant transmis est mesuré en* 3*, grâce à une conversion tension-courant due aux propriétés de l'EHQE. Le contact n°*4 *ramène à la masse le courant du bras inférieur qui a été réfléchi à la deuxième séparatrice. (dessus)* G_U *et* G_D *sont ouvertes. Nous sommes dans la configuration de base des premiers échantillons. (dessous)* G_U *et* G_D *transmettent partiellement l'état de bord interne déformé en boucles qui se ferment lorsque* G_U *et* G_D *sont pincées davantage. Les fluctuations de charge dans l'état de bord interne sont gelées si l'on ouvre un gap assez grand dans le spectre des excitations de l'état de bord interne, les seules fluctuations de charge de l'environnement doivent alors venir de l'état de bord externe contrapropageant sur le bord opposé qui se couple à l'état de bord externe du bras supérieur à travers les bloucles fermées de l'état de bord interne. Le couplage à l'environnement est alors diminué.*

théorie semblent en accord, dans la limite des (grandes) incertitudes expérimentales, qui viennent principalement de la dépendance de la transmission $\mathcal{T}_0$ avec la tension V_1 appliquée à l'entrée de l'interféromètre (Fig. 1.5 (droite)). On observe à $\mathcal{T}_0 = 0.5$ la transition d'une structure multiple pour $\mathcal{T}_0 > 0.5$ avec rigidité de la position des zéros de visibilité, vers une structure simple pour $\mathcal{T}_0 < 0.5$ avec un lobe central dont la taille diverge quand $\mathcal{T}_0$ tend vers 0.

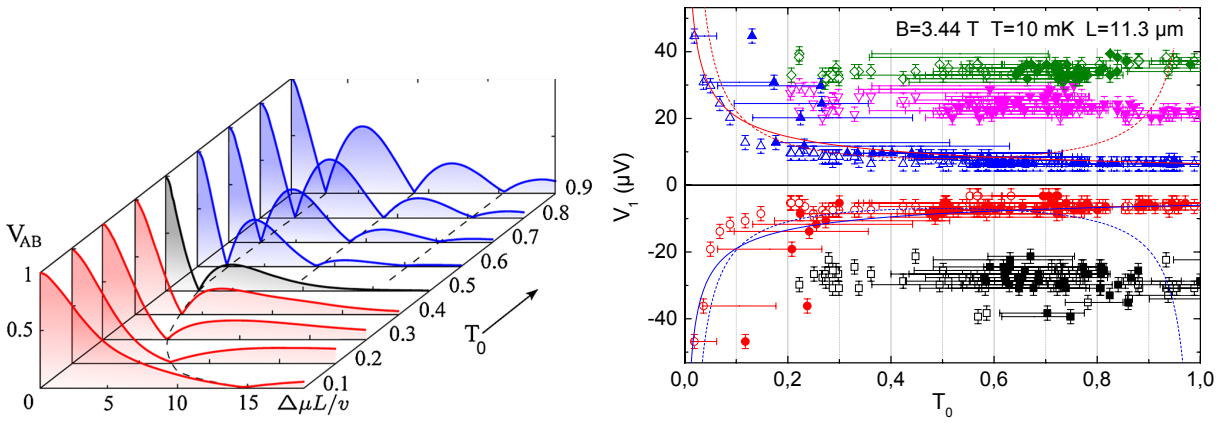

Figure 1.5.: *(gauche) Prédiction concernant un transition de phase quantique à transmission $\mathcal{T}_0 = 0.5$ de l'état de bord externe, d'une structure multiple à une structure simple, induite par le bruit de partition du CPQ d'injection, G0 [16]. (droite) Mesures expérimentales. Position des zéros de visibilité, en fonction de $\mathcal{T}_0$ à tension nulle (symboles vides), et à tension V_1 (symboles pleins). La largeur du lobe central diverge conformément à la prédiction de Levkiviskyi* et al. *(ligne en pointillés) si l'on considère $\mathcal{T}_0$ à tension nulle (symboles vides).*

Nous avons également mesuré la visibilité lorsqu'une distribution en double marche est injectée à l'entrée de l'interféromètre par l'intermédiaire de $G0$, dans le cas d'une structure de lobes simple: nous avons regardé comment la visibilité varie en fonction de la hauteur des marches (paramétrée par les tensions V_1 et V_2), à largeur de marches fixée (paramétrée par $\mathcal{T}_0$). Nous obtenons une figure en 'papillon' (Fig. 1.6), que nous parvenons à reproduire en utilisant un fit qui semble indiquer que le mécanisme provoquant la structure de lobe simple a lieu avant le CPQ $G0$...

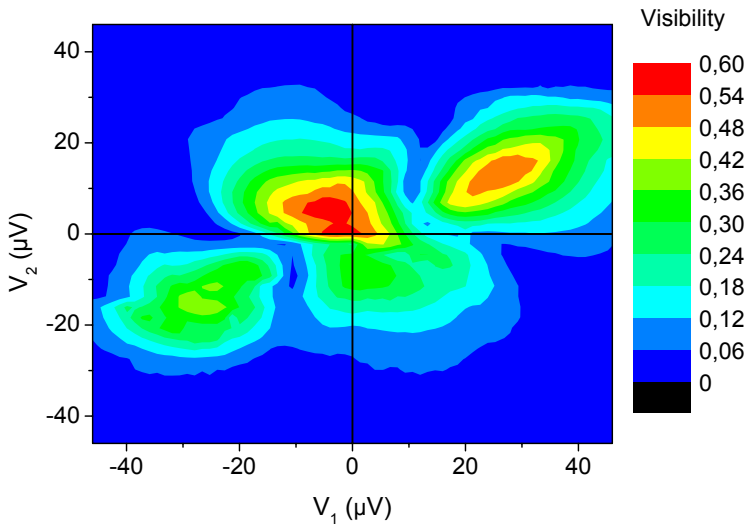

Figure 1.6.: *Visibilité en code couleur en fonction des tensions à l'entrée de l'interféromètre V_1 et V_2 pour une transmission $\mathcal{T}_0 = 0.2$ de l'état de bord externe à tensions V_1 et V_2 nulles. V_1 et V_2 paramètrent la hauteurs des marches de la distribution en double marche qui est injectée dans l'état de bord externe à l'entrée de l'interféromètre. $\mathcal{T}_0$ paramètre leur largeur.*

1.5. Amélioration de la cohérence quantique dans le régime d'effet Hall quantique entier

Dans cette partie, nous avons mis en oeuvre la grille G_U afin de diminuer le couplage entre états de bord dans le bras supérieur du IMZ, et de geler les fluctuations de charge dans l'état de bord interne en le localisant en boucles fermées de taille 8 μm.

A tension V_1 nulle, la cohérence augmente de façon spectaculaire: la visibilité passe de 20 à 50 %, et la contribution du bras supérieur à la dépendance de la visibilité avec la température, $T_{\varphi,U}^{-1}$, est divisée par 2, proportionnellement au couplage entre états de bords dans le bras supérieur, mesuré par V_0^{-1} (Fig. 1.7). Cependant, alors que comme attendu, lorsqu'on ferme l'état de bord interne sur lui même, la période des interférences révélées en variant V_2 est multipliée par 2, on n'observe pas d'effet sur la cohérence, suggérant que les fluctuations de charge dans l'état de bord interne demeurent ou n'influent pas sur la cohérence.

Parallèlement, on constate un élargissement des lobes latéraux de la structure de lobes lorsque le couplage V_0^{-1} diminue. Cependant le lobe central n'est que très légèrement affecté (Fig. 1.8). On mesure que l'échelle d'énergie caractérisant les lobes multiples est

proportionnelle à V_0, conformément à la théorie de Levkiviskyi *et al.* [6], avec le bon ordre de grandeur, et que l'échelle d'énergie caractérisant l'enveloppe gaussienne reste relativement constante (Fig. 1.9).

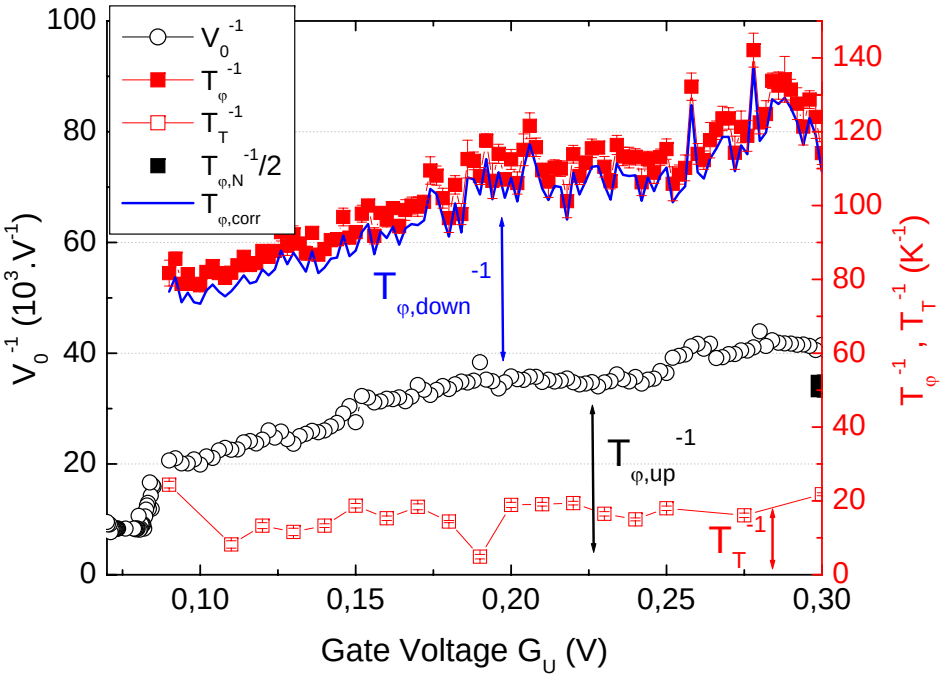

Figure 1.7.: *Échelle gauche: couplage V_0^{-1} entre états de bord dans le bras supérieur en fonction de la tension de polarisation appliquée à G_U (cercles noirs vides). V_0^{-1} diminue à mesure que G_U est fermée. Vers $V_{G_U} \approx 0.08$ V, il chute brutalement alors que l'état de bord interne est déconnecté du contact n°2. Échelle droite: T_φ^{-1} en fonction de V_{G_U} (carrés pleins rouges). L'échelle est telle que les variations de T_φ^{-1} et de V_0^{-1} apparaîssent identiques. La diminution de T_φ^{-1} est à peu près proportionnelle à V_0^{-1}. La ligne bleue pleine correspond au taux T_φ^{-1} moins la contribution effective due à l'asymétrie entre les deux bras $T_{T,eff}^{-1} \approx 5\ K^{-1}$, négligeable par rapport aux autres contributions: on considère que celle du bras supérieur $T_{\varphi,U}^{-1}$ est proportionnelle à V_0^{-1}, alors celle du bras inférieur est constante de l'ordre de $52\ K^{-1}$; celle du bras supérieur, lorsque G_U est ouverte, mesurée indépendemment donne $51\ K^{-1}$, une valeur comparable (carré noir plein).*

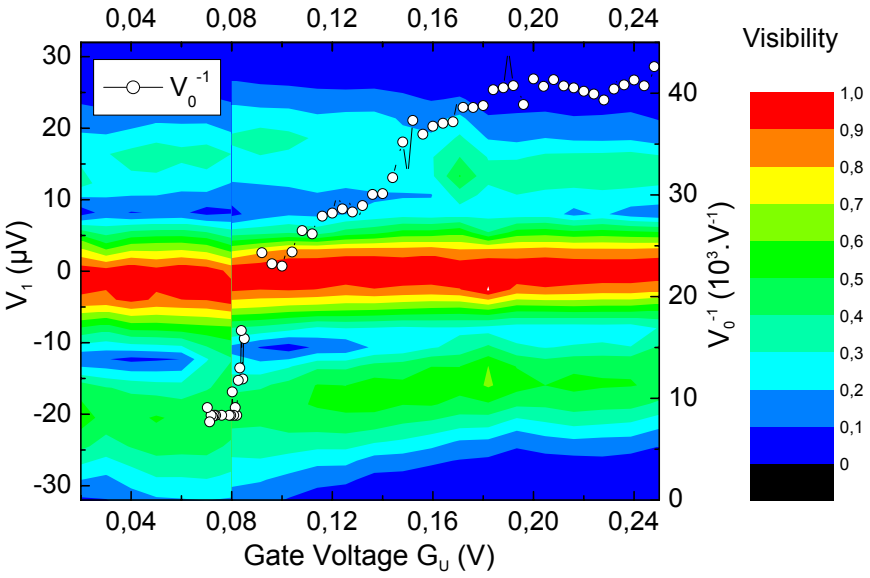

Figure 1.8.: *Échelle gauche: plot couleur de la visibilité normalisée en fonction de la tension de grille V_{G_U} sur l'axe des x, et de la tension de bias V_1 sur l'axe des y. Échelle droite: V_0^{-1} en fonction de V_{G_U}.*

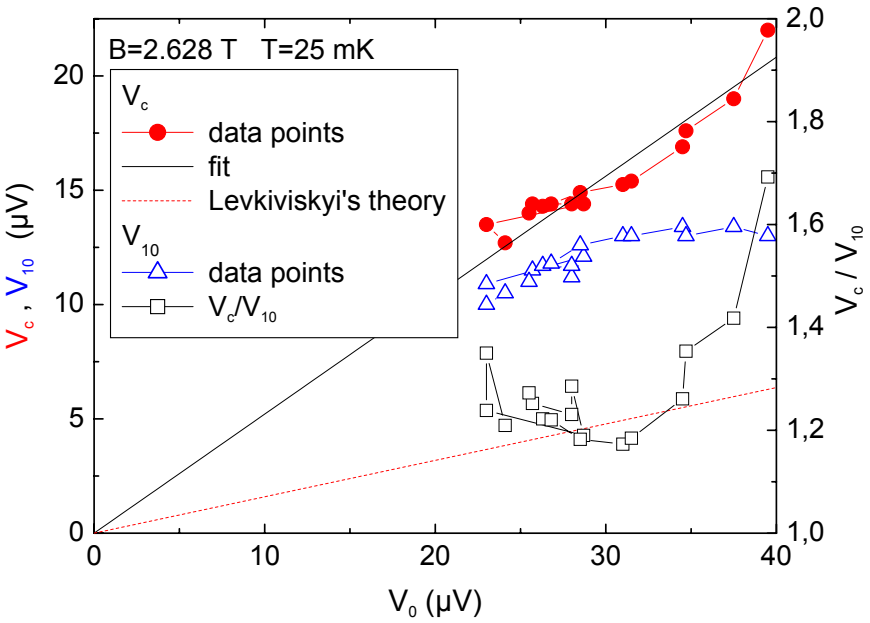

Figure 1.9.: *Échelle gauche: V_c et V_{10} en fonction de V_0. Échelle droite: V_c/V_{10} en fonction de V_0. À mesure que G_U se ferme, la largeur du lobe central paramétrisée par V_{10} augmente assez peu, alors que la largeur du premier lobe latéral mesurée par V_c croît linéairement avec V_0 (du moins jusqu'au pinch-off).*

2. Introduction

The interest in the edge states on the integer quantum Hall effect comes from the fact that they constitute pure one dimensional systems in which one can tune the interaction with an additional knob: the magnetic field. Thus, they are an ideal test bed for one dimensional physics. They also were good candidates for flying Q-Bits: it is possible (in principle) to entangle edge state electrons from opposite edges *via* tunneling, and coherence in these systems was believed to be strong because of the great value of the Landau gap compared to the available energies at low temperature. However, so far actual knowledge on quantum coherence and energy relaxation in these systems is scarce, and to achieve the ultimate goal of verifying the violation of Bell inequalities as suggested by Samuelsson *et al.* [17], we need to find a way to circumvent the rather low coherence length [2]. Another question which hasn't been treated in this PhD thesis is the one of fractional quantum Hall effect. Fractional charges were demonstrated to exist by noise measurements, but what about their coherence? and what are the 'good quasiparticles' in this regime, in the sense of quasipaticles whose lifetime is larger than the inverse of the energy?

There is two main aspects to my work. First, on coherence: knowing that dephasing from a well identified environment explain a large part of the results at $\nu = 2$, can we find a way to freeze this environment so as to enhance the coherence? If so, this would confirm our theory on the main cause for dephasing.

Second, we want to see if the recent findings of the LPN group on relaxation can explain the observed features on the visibility of the edge states interferences at finite bias. To do so, we inject an out-of-equilibrium distribution and study the resulting interferences.

3. Electron beams in condensed matter

Contents

3.1. Introduction

How can one obtain electron beams? An electron beam is a one dimensional object. It can be constructed from a two dimensional electrons system by freezing one degree of freedom. This is done by applying a high magnetic field. Following this procedure, we build pure one dimensional chiral electron systems which mimick photon beams.

In this chapter, I will first describe the two dimensional electron system that is used and how it is obtained. Then I will introduce the quantum Hall effect and finally the object of my study: the edge states.

3.2. The bidimensional electron gas

The recipe for a high mobility bidimensional electron gas (2DEG) e.g. the two dimensional electron system, is to localize electrons into a trap formed at the interface of two semiconductors with different gaps. I will first detail how electrons are trapped in a two dimensional layer, and then I will give the typical values for the relevant quantities which characterize this conductor.

3.2.1. Formation

The base material of our sample is a bidimensional electron gas (2DEG) which forms at the interface of a GaAs/$Al_xGa_{(1-x)}$As semiconductor heterostructure (for our samples, $x \approx 0.3$). The heterostructures were grown at LPN Marcoussis by U. Gennser and ETH Zurich by W. Wegscheider using molecular beam epitaxy. The 2DEG is trapped in a quantum well at the interface GaAs/AlGaAs, $\sim$ 100 nm below the surface (Fig. 3.1 (left)). To understand how this quantum well appears, one must observe how valence and conduction bands align in the z direction when both semiconductors are put together.

The Fermi energy E_F of the semiconductor with the greater gap, AlGaAs is higher then the one which has a smaller gap, GaAs. As a consequence, electrons depart from the n-doped semiconductor GaAlAs, leaving behind positively charged donnors. This space charge creates an electrostatic potential $V(z)$ which curves the bands as represented on Fig. 3.1 (right): a quantum well forms near the GaAs/AlGaAs interface. At equilibrium the Fermi energy is constant everywhere. All parameters are chosen so that the Fermi energy lies within the quantum well effectively trapping the electrons coming from the

AlGaAs side. Because of the low temperatures at which we usually work (a few tenths of millikelvins) only the first energy level of the quantum well is populated, forming a bidimensional conductive layer in the $x - y$ plane that is usually called a bidimensional electron gas.

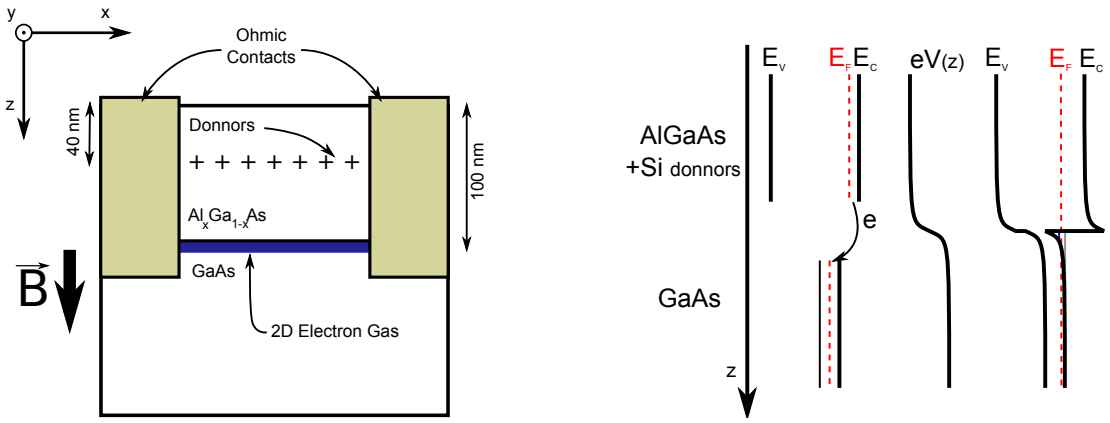

Figure 3.1.: *(left) Schematic cross-section of the GaAs/AlGaAs heterostructure. (right) From left to right: electrons migrate to the GaAs layer where the Fermi energy is lower, leaving positively charged donnors in the AlGaAs layer. Consequently an electrostatic potential $V(z)$ appears, which curves the energy bands of the heterostructure so that a potential well is created at the interface trapping the electrons in a x-y plane.*

3.2.2. Typical values

The typical values of the relevant quantities for the GaAs/AlGaAs 2DEGs that we used in our experiments are given in the table of Fig. 3.2 [18]. Some are a given, the other are chosen specifically to fullfill necessary conditions so as to observe the quantum Hall effect.

The electron effective mass in GaAs is $m_e{}^* = 0.068\ m_e$ where m_e is the bare electron mass. It is determined by the temperature dependence of the amplitude of the Shubnikov-de-Haas oscillations and is characteristic of the GaAs/$Al_{0.3}Ga_{0.7}As$ heterostructure [18].

The 2DEG electron surface density n_s has to be low enough so that one is able to reach the integer quantum Hall regime at low filling factors $\nu = n_s h/eB$ (see later § 3.4). We are using a magnet with a maximum field of 12 Tesla at 4 K, therefore we need electron densities lower than 6×10^{11} cm^{-2} to reach $\nu = 2$.

From 2D conductance measurements at 4.2 K one gets the mobility $\mu_0 = \sigma_0/n_s e$ where σ_0 is the conductance at zero magnetic field. The mobility is linked to the average time

between elastic collisions of electrons at zero magnetic field, τ_0, through $\mu_0 = e\tau_0/{m_e}^*$. For the IQHE to emerge, τ_0 must be large compared to the inverse of the cyclotron frequency: $\omega_c\tau_0 \gg 1$, which leads to $\mu_0 B \gg 1$. Samples with mobilities of the order of 10^5 cm^2.V^{-1}. s^{-1} make possible the observation of the QHE at 1 Tesla.

Finally, another relevant quantity is the two dimensional Fermi energy $E_F = \pi\hbar^2 n_s/{m_e}^*$, the associated Fermi wavelength $\lambda_F = \sqrt{2\pi/n_s}$ and the Fermi velocity [1] $v_F = \sqrt{2E_F/{m_e}^*}$.

It is noteworthy that during this PhD, many samples were tested at low temperature (4.2 K and sometimes 20 mK), just to check the quality of the ohmic contacts and the gates. Having changed of 2DEG provider during my PhD, several months were needed to ajust the fabrication procedure. Finally, the results presented here have been obtained on two different samples for the energy exchange experiment and on one sample for the modified MZI (although with different cooling cycles and magnetic fields).

I will now introduce the integer quantum Hall effect starting from the classical Hall effect in order to show how edge states (one dimensional chiral electron beams) emerge from a 2DEG in the IQHE regime.

${m_e}^*$	n_s	μ_0	τ_0	g^*	E_F	λ_F	v_F
(m_e)	(10^{11} cm^{-2})	(10^6 cm^{2}V^{-1}.s^{-1})	(10^{-10} s)		(meV)	(nm)	(10^5 m.s^{-1})
0.068	2	2.5	0.97	-0.44	7	56	2.1

Figure 3.2.: *Typical values of the quantities characterizing the GaAs/$Al_{0.3}Ga_{0.7}$As 2DEGs that we will use. The effective mass of the electron ${m_e}^*$ in units of the bare electron mass (m_e) is listed along the 2DEG electron density (n_s), its zero magnetic field mobility (μ_0), the electron effective Landé factor (g^*) [19–21], the average scattering time in zero field (τ_0), the Fermi energy (E_F), wavelength (λ_F) and velocity (v_F).*

[1] We will see that in the QHE regime, the Fermi velocity is no longer relevant. Instead, one must consider the electron drift velocity $\mathbf{v_d} = \mathbf{E} \times \mathbf{B}/B^2$.

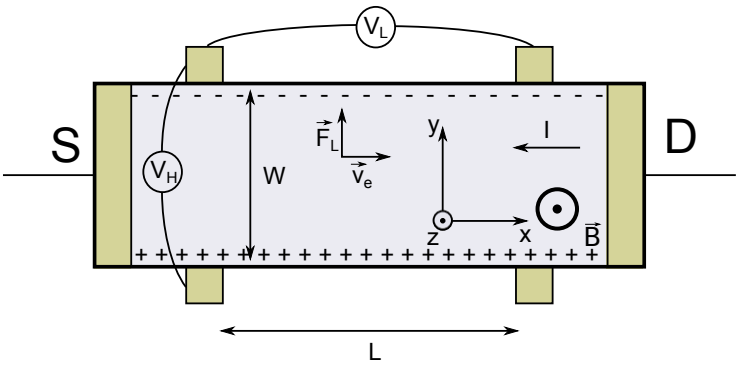

Figure 3.3: *Schematic of a Hall bar. In the $x-y$ planar conductor, current I flows from D to S driven by the electric field $E_x\,\mathbf{e_x}$. Under magnetic field $B\,\mathbf{e_z}$, electrons accumulate on the upper side because of the Lorentz force $\mathbf{F_L}$. In the steady state a force $-eE_y\,\mathbf{e_y}$ exactly compensates $\mathbf{F_L}$.*

3.3. The Hall effect

3.3.1. Prehistory

When an electrical current flows through a metallic strip under a magnetic field perpendicular to the plane of the strip, it is known since E. H. Hall (1879), that a transverse voltage appears across the strip because of the accumulation of charge on the sides due to the Lorentz force (see Fig. 3.3). This transverse voltage (V_H) is proportional to the current I *via* the Hall resistance R_H, which in turn is proportional to the magnetic field:

$$R_H = \frac{B}{n_s e}$$

where n_s is the electron surface density. This is the Hall effect. The longitudinal resistance is equal to the zero magnetic field resistance $R_L = L/\sigma_0 W$, where L is the length of the strip, W its width and σ_0 its zero magnetic field conductivity.

However, as Klaus von Klitzing found later [22], in two dimensional electron systems like 2DEGs (if the sample is clean enough and if the temperature is low enough), at high magnetic field, the Hall resistance as function of the magnetic field exhibits steps at quantized values as seen on Fig. 3.4 (left) [2]. This quantum Hall effect (QHE) owed Klitzing the Nobel Prize in Physics in 1985. For curiosity's sake, we reported on Fig. 3.4 (right) [23–25], the progress that was made on the mobility of the samples as years passed by. Since 1980, the low temperature mobilities have improved by two to three order of magnitude. It was only in the 80's that appropriate values for the mobility were reached in order to be able to see the QHE (for magnets with maximum field of a few Teslas).

[2] As said before, the criterion for observation of quantum Hall effect is $\omega_c \tau_0 \gg 1$

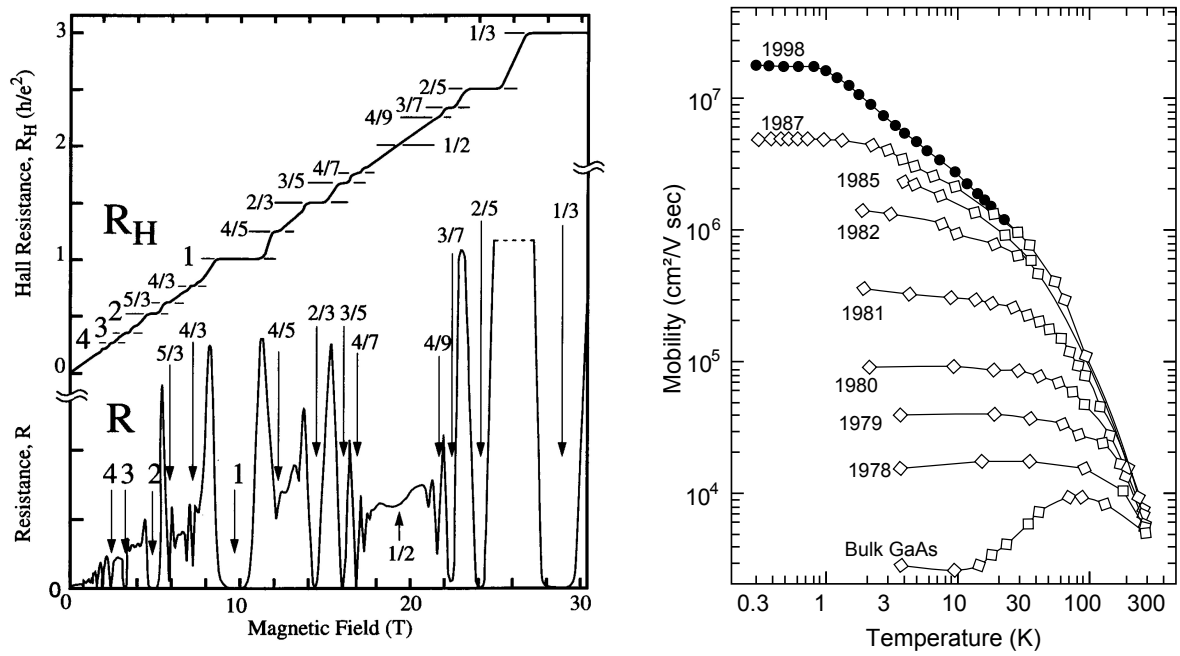

Figure 3.4.: *(left) Hall (R_H) and longitudinal (R_L) resistance as function of the magnetic field in an ultrahigh mobility GaAs/AlGaAs 2DEG. R_H shows plateaus of quantized values $h/(\nu e^2)$ with ν an integer (integer quantum Hall effect) or a rational (fractional quantum Hall effect). A plateau in R_H corresponds to a zero in R_L. The periodicity of these Shubnikov-de-Hass oscillations in R_L scales as B^{-1} [26]. (right) Evolution of GaAlAs 2DEGs mobilities since 1978 as function of the temperature. It is only since the end of the 80's that high enough mobilities allow the observation of the QHE effect at reasonable magnetic fields [23–25].*

3.3.2. Conductivity tensor

If we consider a perfect 2DEG under a magnetic field perpendicular to the plane of the gas, in the classical limit, the electrons trajectories are circular orbits gyrated at the cyclotron pulsation $\omega_c = eB/{m_e}^*$, where ${m_e}^*$ is the effective mass of an electron of the conduction band, which takes into account the effect of the lattice. For $B \sim 3$ T, the cyclotron period is about $T_c \sim 8 \times 10^{-13}$ s.

In the classical Hall regime, the conductivity tensor $\hat{\sigma}$ defined by $\mathbf{j} = \hat{\sigma}\mathbf{E}$ is [27]:

$$\hat{\sigma} = \frac{\sigma_0}{1 + \omega_c^2 \tau_0^2} \begin{pmatrix} 1 & -\omega_c\tau_0 \\ \omega_c\tau_0 & 1 \end{pmatrix} \tag{3.1}$$

where $\sigma_0 = n_s e^2 \tau_0 / {m_e}^*$ is the conductivity in zero magnetic field. The resistivity tensor is then:

$$\hat{\rho} = \rho_0 \begin{pmatrix} 1 & \omega_c\tau_0 \\ -\omega_c\tau_0 & 1 \end{pmatrix} \tag{3.2}$$

where $\rho_0 = 1/\sigma_0$ is the 2DEG resistivity in zero magnetic field. Diagonal terms correspond to the longitudinal resistivity and do not depend on the magnetic field while off-diagonal terms give the transverse resistivity (equal to the Hall resistance in 2D [3]) which is linear in the magnetic field: $\rho_{xy} = R_H = \rho_0 \omega_c \tau_0 = B/n_s e$.

This classical description of transport in a magnetic field holds as long as the average time between collisions at zero field is small compared to the inverse of the cyclotron frequency [4] $\omega_c\tau_0 \ll 1$.

In the limit where samples are clean enough so that an electron excitation of the Fermi sea with velocity v_F undergoes many cyclotron orbits before any collision occurs, one must consider quantum effects.

[3] In two dimensions resistivity and resistance are homogeneous: I being the current, V_L the longitudinal voltage difference, V_H the transverse voltage difference or Hall voltage, L the ribbon length and W its width, the current density is $j = I/W$ and the longitudinal electrical field $E_L = V_L/L$ so that the longitudinal resistivity is $\rho_{xx} = R_L(W/L)$, where R_L is the longitudinal resistance.

[4] We see that for $B \sim 3$ T since $T_c \sim 8 \times 10^{-13}$ s, we are in the opposite limit $T_c \ll \tau_0$ (see tabular 3.2).

3.4. The quantum Hall effect

When one goes at a temperature low enough (there are hints at 4.2 K but features are more marked at 20 mK) one can observe quantization of the transverse resistance of the 2DEG in well defined plateaus with respect to the magnetic field (see Fig. 3.4 (left)). This is the quantum Hall effect.

The origin of the quantum Hall effect lies in the quantization of the electron cyclotron motion, hence the need for clean samples and high magnetic fields: indeed, for the cyclotron motion to be quantized, it must be well defined. An electron must me able to undergo a whole cyclotron orbit before any collision, and for it to be so, collisions must be scarce (high mobility samples) and/or the magnetic field high ($\omega_c \tau_0 \gg 1$).

Let us do a full quantum treatment of the problem [28].

3.4.1. Landau quantization

Lets consider electrons without spin and without interactions, bound to a surface of finite size $L_x \times L_y$ in the horizontal plane, in the presence of a magnetic field perpendicular to this plane. The hamiltonian of the system can be written as $H = (\mathbf{p} + e\mathbf{A})^2 / 2m_e{}^*$.

Energy spectrum

To derive the energy spectrum let us choose a particular gauge (the result doesn't depend on this choice). The Landau gauge defined by $\mathbf{A} = (-By, 0)$, is more convenient for geometries invariant in the x direction. The hamiltonian becomes $H = (p_x^2 + (p_y - eBy)^2) / 2m_e{}^*$. Since operators H and p_x commute, we can seek solutions in the form $\Psi_k(x, y) = e^{ikx} f_k(y)$, so that the hamiltonian becomes: $H_k = p_y^2/2m_e{}^* + m_e{}^* \omega_c^2 (y - k l_m^2)^2/2$, where $l_m = \sqrt{\hbar/eB}$ is the magnetic length. We recognize the hamiltonian of a one dimensional harmonic oscillator centered in $Y_k = k l_m^2$. Then, the energy spectrum is independent of the wavevector k, and quantized in Landau levels (LLs) in the following manner:

$$E_n = \left(n + \frac{1}{2}\right) \hbar \omega_c \quad \text{with } n \in \mathbb{N} \tag{3.3}$$

Eigenfunctions

Still in the Landau gauge, the eigenfunctions are, for the ground state [5]:

$$\Psi_{0,k}(x,y) = \frac{1}{\sqrt{L_x}}\, e^{ikx} e^{-(y-kl_m^2)^2/(2l_m^2)} \tag{3.4}$$

and for an electron form the n^{th} Landau level, $\mathcal{H}_n$ being the n^{th} Hermite polynom, the eigenfunction becomes: $\Psi_{n,k}(x,y) \propto e^{ikx} e^{-(y-kl_m^2)^2/2l_m^2}\, \mathcal{H}_n\left(\left(y-kl_m^2\right)/l_m\right)$. In the Landau gauge, the eigenfunction are strips in the x direction, centered on the positions Y_k with the width l_m. In the ground state, l_m is the variance of the zero point spatial fluctuations in the y direction. We will derive the following results within the Landau gauge but one must keep in mind that they are independent of the gauge [6].

Degeneracy

We have seen that the LLs are highly degenerate (for one energy level, many k vectors are possible), let us derive their degeneracy. Considering that all eigenfunctions are products of a plane wave in the x direction an a function of $y-kl_m$, if one imposes periodic boundary conditions in the x direction, then k takes the values $k_q = 2\pi q/L_x$, with $q \in \mathbb{N}$. Thus, electrons are centered in $Y_q = 2\pi q l_m^2/L_x$, and the degeneracy of the energy levels with respect to k is:

$$\xi = \frac{L_x L_y}{2\pi l_m^2} = \frac{\Phi_B}{\Phi_0} \tag{3.5}$$

where $\Phi_B = BS$ is the magnetic flux threading through the sample, with S the surface of the sample, and where $\Phi_0 = h/e$ is the quantum flux i.e. the smallest amount of magnetic flux which can be enclosed by an electron cyclotron orbit. This means that the number of electrons that one Landau level can accept (its degeneracy) is equal to the number of flux quanta that go through the sample.

[5] The eigenfunctions within the cylindrical gauge are, for the ground state:

$$\Psi_{0,m} = \left(1/\sqrt{2\pi l_m^2 2^m m!}\right)\, z^m e^{|z|^2/4l_m^2} \quad \text{with} \quad m \in \mathbb{N}^* \quad \text{and} \quad z = x+iy$$

[6] Actually in the cylindrical gauge the coordinates X and Y of the center of the cyclotron motion are conjugate variables, with commutator $[X,Y] = il_m^2$, which shows in a straightforward manner that an electron occupies at least the minimum area h/eB. It also shows that since X and Y are conjugate, the 2D system turns into a pure 1D system.

Modulation of the Electronic Properties

The high degeneracy of the LLs we just mentionned is one key ingredient to the peculiar modulation of the electronic properties of the system. Indeed, the electronic properties are determined by the low energy excitations of the Fermi sea. Therefore they depend on the density of states at the Fermi energy. The latter being peaked periodically at the quantized energy levels [7], the electronic properties (the Hall resistance, for example) are modulated by the passing of the Fermi energy through these energy levels. At constant electronic density n_s, when ramping up the magnetic field, the degeneracy of the energy levels increases linearly. The separation in energy between levels increases as well since the total number of electrons is constant, therefore, the energy levels cross the Fermi level periodically with a periodicity which scales as B^{-1}.

Filling factor

According to the previous remark, we understand that to describe the physics of the system, we need an index in order to locate the Fermi level with respect to the quantized energy levels of the 2DEG. The filling factor ν which is defined as the number of electrons per flux quantum, serves this purpose:

$$\nu \equiv \frac{n_s S}{\Phi_B/\Phi_0} = \frac{n_s h}{eB} \tag{3.6}$$

when the Fermi energy lies within the last energy level partially filled, ν is not an integer ($[\nu] < \nu < [\nu] + 1$), when the Fermi energy lies between a full energy level and empty energy levels of superior indexes, ν is an integer.

Until now, we considered an ideal 2DEG under a vertical magnetic field, with no spin, translational invariant, with no particular confinement. In real samples however, electrons have a spin, there is always some disorder, and samples have a finite size. Let us refine our description in the system, we will see that some of these elements are actually not refinements but rather essential ingredients to explain the observed properties of the quantum Hall effect.

[7] Those 'energy levels' can either be spin-split branches of LLs or LLs of a 2DEG with no spin, in both cases with the degeneracy ξ and a gap which depends linearly of the magnetic field.

3.4.2. Realistic hamiltonian

A realistic hamiltonian for the system should take into account disorder, spin and confinement:

$$H_{\text{realistic}} = H + H_{\text{disorder}} + H_{\text{spin}} + H_{\text{confinement}}$$

Disorder

Disorder can be present, but it must not be too strong so that the cyclotron orbits are quantized ($\omega_c \tau_0 \gg 1$). As we mentionned earlier, it implies high mobility samples and/or high magnetic fields ($\mu_0 B \gg 1$): for $B \sim 1$ T, we need $\mu_0 \gtrsim 10^5$ cm^2.V^{-1}.s^{-1}. Nevertheless, we will see later (¶ 3.4.3) that disorder is actually *essential* for the observation of the Hall plateaus [18, 29].

Spin 1/2

If the electrons have a spin, because of the Zeeman gap each LL splits into two energy levels with spin up (↑) and spin down (↓):

$$E_{n,\uparrow\downarrow} = \left(n + \frac{1}{2}\right) \hbar\omega_c \pm \frac{1}{2}\, g^* \mu_B B \tag{3.7}$$

where $\mu_B = e\hbar/2m_e$ is the Bohr magneton and g^* the electron effective Landé factor. Each of these levels has the same degeneracy ξ as before and is spin polarized. The Zeeman splitting $\Delta_z = g^* \mu_B B$ depends linearly of the magnetic field as does the Landau gap.

At $B \sim 3$ T, the Zeeman gap is of the order of $\Delta_z \equiv 1$ K, which is smaller that the Landau gap ($\hbar\omega_c \equiv 70$ K) by one order of magnitude. Then for temperatures above 1 K, plateaus corresponding to odd filling factors $\nu = 2n + 1$ should not be visible because of thermal excitations which are enough to populate both spin split energy levels coming from the last LL. This is not the case: at 4.2 K, both plateaus corresponding to $\nu = 1$ and $\nu = 2$ are visible on Fig. 3.5.

The reason for this is that situations corresponding to odd filling factors are further protected by the exchange interaction. Indeed the energy gain per particle can be evaluated [18] to be of the order of

$$\sqrt{\frac{\pi}{8}}\, \frac{e^2}{\epsilon_0 \epsilon_r l_m} \equiv 200 \text{ K} \quad \text{at} \quad B \sim 3 \text{ T}$$

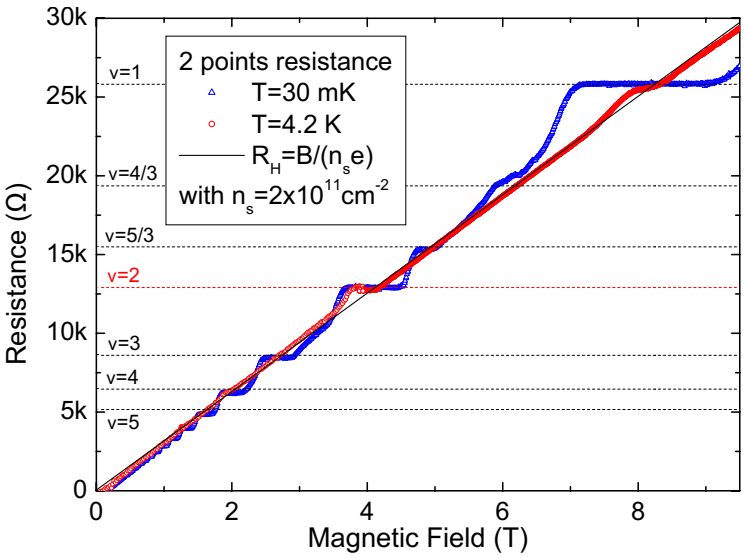

Figure 3.5: *Two points resistance of a high mobility 2DEG as function of the magnetic field showing Hall plateaus at 4.2 K (red) and 30 mK (blue). Contribution of the ohmic contacts ($\sim 300\ \Omega$) has been substracted. The classical relationship $R_H = B/(n_s e)$ yields the electronic density of the 2DEG: $n_s = 2 \times 10^{11}\ cm^{-2}$.*

where $\epsilon_r = 12.9$ for GaAs. This is two orders of magnitude higher than the Zeeman gap $\Delta_z \equiv 1$ K. The polarized states are therefore protected by the exchange energy for higher energies than those dictated the Zeeman gap only. Depending on the parity of the filling factor, the excitation gap is determined by:

▷ for odd filling factors: the Zeeman gap plus the energy exchange

▷ for even filling factors: the Landau gap minus the Zeeman gap

The result is that the excitation gap for odd or even filling factors is of the same order of magnitude, i.e. high enough so that plateaus for odd as well as even filling factors are visible at 4.2 K.

Confining potential and edge states

Because of the finite size of the sample, one must take into account an additional confining potential. This confining potential is responsible for the emergence of the edge states through which transport occurs. These are the 'electrons beams in condensed matter' that are the object of our study. Let us explain how they appear.

In the semiclassical picture (figure 3.6 (left)), when the confining potential is smooth on the scale of a cyclotron orbit compared to the gap ($e\partial_y U \ll \hbar\omega_c/l_m$), electrons drift along equipotentials with the drift velocity $\mathbf{v_d} = \mathbf{E} \times \mathbf{B}/B^2$ [8]: in the bulk, electrons do not

[8] The tranverse electrical field comes from the confining potential slope: $E = \partial_y U$.

feel the confining potential, they follow circular cyclotron movements, their drift velocity is zero. On the edges, the confining potential is no longer negligible. We must add the electric potential energy to the unperturbed quantized energies, the energy levels are bent upwards at the edges where the electrons acquire a finite drift velocity. When the Fermi energy lies between two energy levels, the only low energy excitations are these drifting states present at the edges (Fig. 3.6 (right)). Since these states follow equipotential lines they define one dimensional conductors called edge states (ESs) [30].

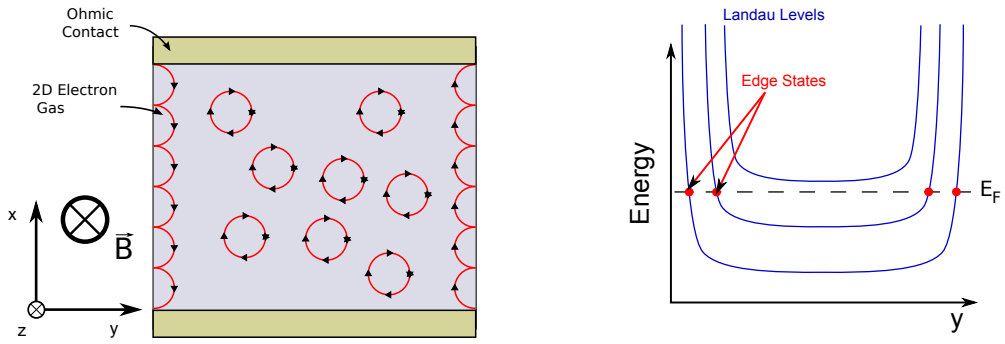

Figure 3.6.: *(left) Semi-classical picture of the ES: in the bulk electrons describe circular cyclotron orbits while they drift along the edges following equipotential lines. (right) LLs as function of the position in the 2DEG. ESs form at the lines (red points on the picture) where the Fermi energy cross the LLs.*

These ES modes are chiral: their direction of propagation is given by the drift velocity so that ESs from opposite edges propagate in opposite directions. Because of the spatial separation between opposite ESs, there is no backscattering, even in the presence of disorder [31]. To be backscattered, an electron must go into the opposite edge.

3.4.3. Transport properties

Now, knowing that transport occurs through ESs, one can amend the classical Hall bar picture of Fig. 3.3 to derive the two points resistance, the Hall resistance and the longitudinal resistance in the quantum case. We represented the Hall bar at $\nu = 1$ on Fig. 3.7 where only one ES is running along the edge. Current is injected at the drain D and goes out at the source S. The other contacts are voltage probes. At integer filling factor ν, transport is insured by ν ESs.

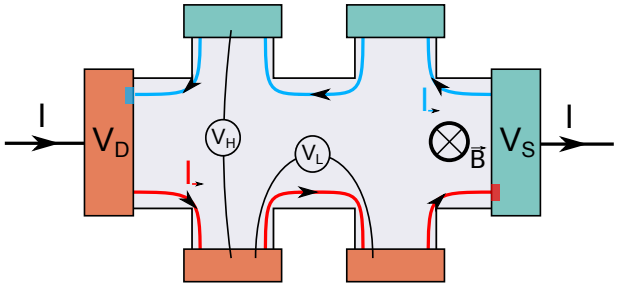

Figure 3.7.: *Hall bar at filling factor $\nu = 1$. Because of chirality, currents flowing on the lower and upper edges ($I_{\rightarrow}$ and $I_{\leftarrow}$) have opposite directions. There is no backscattering because these currents are spatially separated. The electrochemical potential in the ES on the lower(upper) edge is fixed by the voltage bias applied on the drain(source), and is constant in the sample because there is no backscattering during transport. The voltage drop between drain and source – and the dissipation – is localized at the regions where the ES enters a reservoir (red(blue) spot on the drain(source)).*

Longitudinal resistance Because of the absence of backscattering, currents $I_{\rightarrow}$ and $I_{\leftarrow}$ are conserved along the edges. The electrochemical potential imposed by the injecting reservoirs is kept along the propagation, therefore, the longitudinal resistance vanishes. The voltage drop between the drain and the source is localized at the entry points of the ES in the reservoirs [32] as figured on Fig. 3.7.

Two points resistance We will see later that each of these ESs has a two points conductance e^2/h (¶ 3.5.2). At integer filling factor ν, the total two points conductance is therefore equal to the conductance of one ES times the number of ESs, i.e. $G_{2\text{points}} = \nu e^2/h$ and the two points resistance is $R_{2\text{points}} = h/\nu e^2$ [31].

Hall resistance The voltage drop between ESs from opposite edges being the same than the one between the drain and the source, the Hall resistance is equal to the two points resistance: $R_H = h/\nu e^2$.

However, we have still to explain the existence of *plateaus* in the Hall resistance as function of the magnetic field. In the following we show that surprisingly, some disorder (not too strong but some disorder still) is necessary.

Need for some disorder

Here we want to show why some degree of disorder is necessary to explain the Hall resistance plateaus as function of the magnetic field [9]. Suppose there is no disorder. As we said before, the modulation of 2DEG electrical properties (Hall plateaus and Shubnikov-de Haas oscillations) is caused by the periodic passing of the Fermi energy through the energy levels. Quantization of these electrical properties is valid when the Fermi level lies exactly between two levels (see Fig. 3.6 (right)). When an energy level is full, we move straight away to the filling of the next energy level and to the next quantization.

Transition between two quantizations is insured by the filling of the states on the edges, but as soon as $l_m \ll L_y$, their number (L_x/l_m) becomes vanishingly small compared to the number of states in one energy level ($\xi = L_x L_y/(2\pi l_m^2)$). The range of magnetic field for which quantization is valid is extremely narrow compared to the progressive filling of the energy level: there is no plateau in the Hall resistance as function of the magnetic field.

In the following I will consider electrons without spins: the energy levels I will speak of are the LLs, each with degeneracy ξ. In the case of electrons with spins the energy levels are the spin polarized sub-Landau levels, each with the same degeneracy ξ, and the following approach also applies.

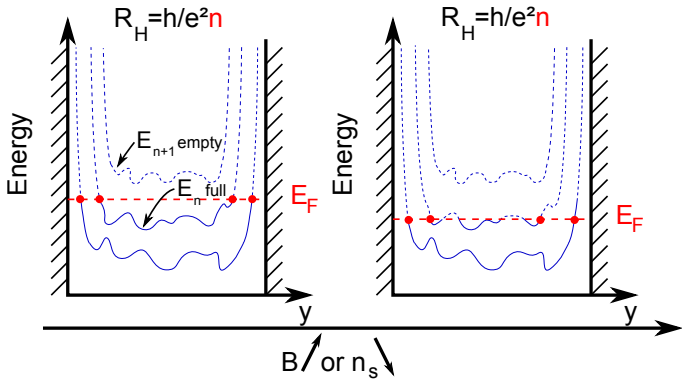

Figure 3.8.: *(left) The n^{th} energy level is full and the $n+1^{th}$ is empty ($\nu = n$ is an integer). The Hall resistance is quantized: $R_H = h/\nu e^2$. (right) As B increases, the Fermi energy decreases relatively to the energy levels. The n^{th} level empties progressively into the regions below the Fermi level. The quantization of R_H holds as long as the number of ESs remains equal to n e.g. on a wider range of B than when there is no disorder.*

[9] The essential reason is that one needs to break the translational invariance in the x-direction in order to observe Hall plateaus. Disorder does that [18, 33]

Percolation, localized states and Hall plateaus Disorder shifts slightly the energy levels in some random regions of the sample. For an appropriate position of the Fermi level, the $(n+1)^{\text{th}}$ level is empty, the n^{th} level being full (then ν is an integer equal to n). Ramping up B for constant electronic density, electrons from regions of the n^{th} energy level which are above the Fermi level start to percolate towards regions of the n^{th} energy level which are below (Fig. 3.8 (right)).

This percolation can be seen as additional localized drifting states in the bulk following the equipotential lines encircling the valleys or hills created by disorder (Fig. 3.9 (b) and (d)). Ramping up B only changes the size of these localized orbits. The localized states do not change the contribution of the n^{th} energy level to the total current and pin the Fermi energy between two levels for a wider range of B, so that there is a Hall resistance plateau as function of the magnetic field (Fig. 3.9 (a)-(b) and (d)-(e)) [29].

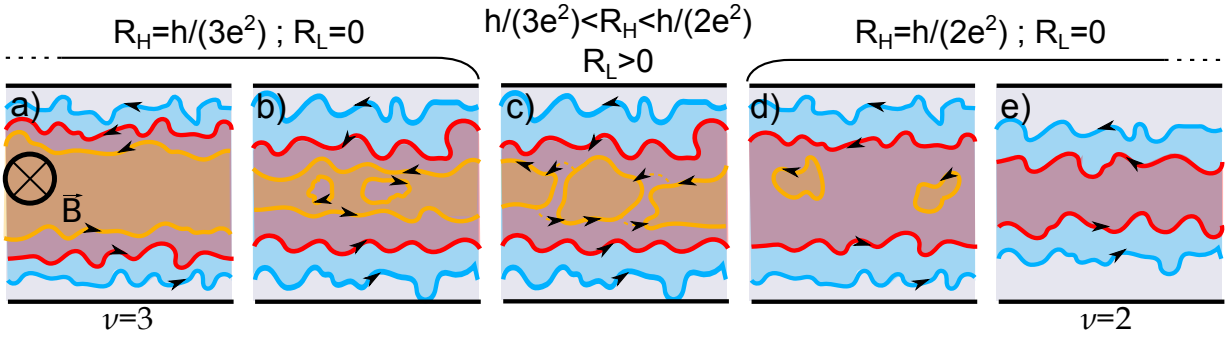

Figure 3.9.: *(a) $\nu = 3$. There are three ESs ($R_H = h/3e^2$) and no backscattering ($R_L = 0$). (b) As B increases, some regions of the 3^{rd} energy level (red regions circled by orange ones), corresponding to localized states (orange clockwise orbits) depopulate. This corresponds to a plateau in R_H. (c) The clockwise orbits increase in size until they connect orange ESs from opposite edges, giving rise to backscattering ($R_L > 0$). Orange ESs still carry some current* via *tunneling (percolation) between orange occupied regions, but R_H is no longer quantized: $h/2e^2 < R_H < h/3e^2$. (d) The 3^{rd} level is emptied further, only localized states remain. There is only two well defined ESs, $R_H = h/2e^2$, $R_L = 0$. (e) Back to picture (a), except that $\nu = 2$.*

Transition between plateaus When B is increased further, opposite current lines from the last energy level (n^{th}) get closer and become more convoluted until they connect one another. Then everything changes: this connection along the y direction suppresses the connection in the x direction, and the contribution of the n^{th} energy level to the current

becomes zero. Actually, on a small range of magnetic field, connection in both directions is possible by tunnel effect. There is then breakdown of the quantization of the Hall resistance - R_H being in between two quantized plateau values - and the longitudinal resitance becomes non zero because of backscattering (Fig. 3.9 (c)).

We have seen how ESs emerge from the quantum Hall effect, in particular we have pointed out the role of disorder: even though it must stay small enough so that quantization of the cyclotron motion holds, disorder is necessary for the Hall plateaus to appear. Additionally, ESs are robust with respect to disorder as long as it is not too strong. This key property makes the ESs one dimensional chiral conductors, ideal to build interferences experiments with 'electron beams'. In the following I detail the general properties of these 1D chiral conductors which, in a first appoach, are considered independent.

3.5. Edge states

Previously we showed how ESs appeared with the confining potential. We showed that they were one dimensional chiral conductors. Let us derive the group velocity of the electrons and the conductance of these 1D channels.

3.5.1. Drift velocity

The energy levels are bent at the edges where they cross the Fermi energy and define the ESs. The confining potential $U(y)$ in these regions can be linearized: $U(y) \approx \partial_y U(y_0) y + U_0$ where $E(y_0) = \partial_y U(y_0)$ is the local transverse electrical field, so that the Hamiltonian becomes $H_k = p_x^2/2{m_e}^* + {m_e}^* \omega_c^2/2 \ (y - k l_m^2)^2 + eE(y_0)y + eU_0$. The oscillator described by this hamiltonian has the equilibrium position $Y_k = k l_m^2 - {m_e}^* E/B^2$ and the energy associated with the ground state becomes: $E_{0,k} = 1/2 \ \hbar\omega_c + eE(y_0)Y_k + eU_0$, so that the eigenstates $\Psi_{0,k}$ group velocity $\mathbf{v_g}$ is equal to the classical drift velocity $\mathbf{v_d}$ associated with the cross configuration $\mathbf{E} \perp \mathbf{B}$ of the electromagnetic field [33]:

$$\mathbf{v_g} = \left(\frac{1}{\hbar} \frac{\partial E_{0,k}}{\partial k}, 0 \right) = \frac{\mathbf{E} \times \mathbf{B}}{B^2} = \mathbf{v_d} \tag{3.8}$$

3.5.2. 1D channel conductance

We derive the conductance of one ES, following [31]. The current flowing through the sample has two chiral contributions coming from the upper edge $I_{\rightarrow}$ (flowing to the source) and from the lower edge $I_{\leftarrow}$ (flowing to the drain) (Fig. 3.7). The total current is: $I = I_{\rightarrow} - I_{\leftarrow} = e\int v_d(\varepsilon)\, n_{1D}(\varepsilon)\, (n_{\rightarrow}(\varepsilon) - n_{\leftarrow}(\varepsilon))\, \mathrm{d}\varepsilon$, where v_d is the drift velocity in the ES, n_{1D} the 1D energy density of states per unit length, and $n_{\rightarrow}(n_{\rightarrow})$ the energy distribution in the D(S) reservoir. D(S) being biased with the voltage $V_D(V_S)$, its energy distribution is the Fermi distribution shifted in energy: $n_{\rightarrow(\leftarrow)}(\varepsilon) = f_0(\varepsilon - eV_{D(S)})$. The drift velocity being $v_d(\varepsilon) = 1/\hbar\,(\partial\varepsilon/\partial k)$, and the 1D energy density of states being $n_{1D}(\varepsilon) = 2\pi\,(\partial\varepsilon/\partial k)^{-1}$, we have $v_d(\varepsilon)\, n_{1D}(\varepsilon) = 1/h$. Then,

$$I = \frac{e}{h}\int\, (f_0(\varepsilon - eV_D) - f_0(\varepsilon - eV_S))\, \mathrm{d}\varepsilon = \frac{e^2}{h}\,(V_D - V_S) \tag{3.9}$$

The two points conductance at $\nu = 1$ is therefore equal to the conductance quantum $G_Q = e^2/h$.

The ES description as an independant ideal 1D chiral conductor does not take into account interactions between electrons which do not challenge the 1D chiral character of the ESs and their 1D conductance: the transport properties described above, like quantization of Hall resistance are still valid in the presence of e-e interactions. However interferences and relaxation experiments challenge this picture.

3.5.3. A challenged picture

ESs can be considered as independent 1D conduction channels [34–36] and handled with the scattering theory. They can be used as electrons beams in interference experiments, taking avantage of the existence of ajustable constrictions (quantum point contacts) which are used as beam splitters (chapter 5). These experiments [1–4, 37–43] probing the coherence of ESs are the focus of this manuscript. They yielded numerous features which cannot yet be explained entirely by any available theory.

Through interference experiments we probe phase breaking by inelastic scattering events [10], but also blurring of the phase by extrinsic dephasing mechanisms (dephasing by the noisy environment). On the contrary, energy relaxation experiments [12–15, 44–46], by studying

[10] Elastic scattering by magnetic impurities also break the electron phase coherence

the evolution of an out-of-equilibrium electron distribution along its propagation, are not sensitive to the blurring of the electron phase by the environment, and specifically probe inelastic scattering of electrons, which are responsible for decoherence, since they are bound to modify the electron initial distribution during propagation. Altimiras *et al.* have developped a specific method to realize the spectroscopy of energy distributions of ESs [14] and found that there was energy relaxation at $\nu = 2$ through energy exchanges between co-propagating ESs [13]. They successfully froze energy relaxation in the outer edge state by localizing the inner edge state in a small closed loop (see § 4.5) [15]. All of this shows that the ideal independent 1D electron beam picture is too simple, as the theory developped by Degiovanni *et al.* [47] suggests, invoking inter-edge interactions treated within the bosonization framework of the Tomonaga-Luttinger theory.

Recently, experiments measuring heat transport at $\nu = 1$ found evidence of heat transport in the direction opposite to the ESs flow [48, 49].

In the following, we amend the simple description of independent edge states by introducing interaction effects in a classical manner (without quantum correlations), the quantum aspect being present only in the 2DEG compressibility [50, 51]. We then discuss briefly the effect of interactions in 1D systems [52].

3.6. Miscellaneous

3.6.1. Edge reconstruction

The one-electron picture doesn't account for the effect of Coulomb interactions which can deeply modify the internal structure of the ES. The repulsive Coulomb interactions and the 2DEG compressibility compete with the attractive confinement potential so that the ES structure depends on which is dominant over the other [50, 51].

In the limit of smooth potential, the confining potential varies slowly on the scale of a cyclotron radius l_m compared to the energy gap between two LLs. This is the semiclassical limit where $\partial_y U \ll \hbar\omega_c/l_m$. Under the influence of e-e interactions, the charge distribution rearranges itself so as to screen the confinement potential. Electrostatic treatment [50] of the system shows that steps appear in the self-consistent potential at the edge of the sample.

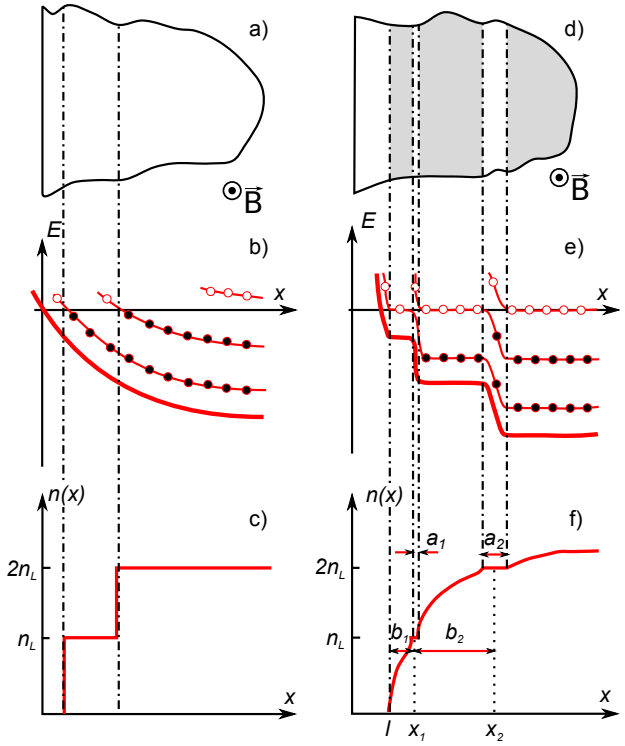

Figure 3.10: *(a)-(c) One electron picture. (a) Top view of the 2DEG plane near the edge. (b) Bending of LLs along the increasing potential energy near the edge. Filled black circles are for filled states, empty circles for empty states. (c) Electron density as function of the distance to the boundary. (d)-(f) Self-consistent electrostatic picture. (d) Top view. Shaded strips represent regions with non integer filling factor (compressible liquid), unshaded strips represent integer filling factor regions (incompressible liquid). (e) Bending of the LLs. Half-filled circles are for partially filled states. (f) Electron density as function of the distance to the middle of the depletion region [50].*

This leads to a series of compressible and incompressible strips represented on Fig. 3.10. Shaded regions in Fig. 3.10 (d) correspond to compressible strips: LLs can be partially filled allowing for zero energy excitations and consequently compressibility, metal-like behaviour. Blank regions correspond to incompressible strips which behave like the former ESs. The electrical potential through incompressible strips is unscreened while it is constant through the metal-like compressible strips [53]. The width of the strips increases as the filling factor increases.

With a depletion length $l = 2000$ Å and the Bohr radius $a_B = h^2\epsilon_0\epsilon_r/\pi e^2 m_e^* \sim 100$ Å ($\epsilon_r = 12.9$ for a GaAs/$Al_{0.3}Ga_{0.7}$As 2DEG), for $\nu = 2$ we find for the OES an incompressible strip of width $a_1 \sim \sqrt{a_B l} = 500$ Å at a distance $x_1 \sim a_1\sqrt{l/a_B} = 3000$ Å from the 2DEG edge (Fig. 3.10 (f)).

The presence of these compressible strips allows for additional modes like collective edge magnetoplasmons [54, 55]. The existence of compressible and incompressible areas has been observed experimentally [53] and the limit of smooth potential corresponds to most experimental situations to our knowledge.

3.6.2. One-dimensional interacting system

How does one describe the low energy excitations of ESs? Indeed we have seen through experimental evidence concerning coherence and energy relaxation that interactions play probably a significant role in these 1D systems. On the other hand, it is known that 1D interacting systems do not behave like Fermi liquids but like Tomonaga-Luttinger liquids (the low energy excitations are in the first case electron quasiparticles and in the latter collective plasmons and spin excitations) [52]. However, while TL liquid behaviour has been experimentally observed in transport and noise experiments in the fractional quantum Hall regime [56–59], there is no experimental proof so far that TL framework is necessary to describe experimental observations in the IQHE regime...

3.7. Conclusion

We introduced the integer quantum Hall effect and in particular showed how 'electron beams' in the form of ESs appeared from the bidimensional electron gas in the presence of a perpendicular magnetic field. We explained the specificities of the ES which make it a good ballistic conductor even in samples not ballistic in zero magnetic field. However, the role of interactions in these systems is an open question. The independent electron picture can be amended to take into account screening of the confinement potential without too much raucuous, but it still is not enough to explain the recent experimental findings on energy relaxation in the ESs at $\nu = 2$ which seems to come from interaction between ESs. Theories which provide fits for these experiments go beyond the mean-field approach and use the TL theory [47]. Interference experiments might be useful to better understand the role of interactions in these systems.

4. Edge state... of the art

Contents

4.1. Introduction

In this chapter I recall the state of the art on edge states. I introduce my work which will answer some of the open questions, and explain how it is pertinent in the context of the present knowledge on edge states.

I recall the first interferences experiments in ballistic systems [60–62] and IQHE interferometers [63,64] as well as their results on the finite temperature coherence length [61,65–71]. I report the conclusion of Roulleau *et al.* [1] on the origin of the zero bias coherence limitation in the electronic Mach-Zehnder interferometer. Then I focus on the finite bias coherence and its peculiar behaviour discovered by Neder *et al.* [4] which suggests interaction effects. I introduce some of the approaches which try to explain this lobe structure. Finally, I try to relate those features to the findings of Altimiras *et al.* [13–15] on energy relaxation in the edge states of the quantum Hall effect at filling factor two.

4.2. Interferences

4.2.1. Fabry-Pérot interferometer

The first interference experiment in the IQHE regime is with a quantum dot (QD) Fabry-Pérot type interferometer (FPI) (see optical equivalent on Fig. 4.2) by Van Wees *et al.* in 1989 [63, 64].

Later, Bird *et al.* [65, 66] studied the temperature dependence of coherence in these systems and found an exponential decrease of the visibility: $\mathcal{V} \propto \exp(-T/T_\varphi)$. This dependence of the visibility with the temperature was found in other FPIs in the ballistic regime like quantum dots [67, 68] and Aharonov-Bohm rings (ABRs) [61, 69–71]. The role of thermal smearing was pointed out in [61], and taking into account multiple interferences, Hansen *et al.* were able to extract the phase coherence length $l_\varphi \propto T^{-1}$ in a ballistic ABR. In [71], Yamauchi *et al.* report Fabry-Pérot interferences in a QD in the IQHE regime at filling factor four. The size of the interferometer was of the order of 1 μm and the interferences disappeared on a temperature scale of the order of 300 mK (see Fig. 4.1).

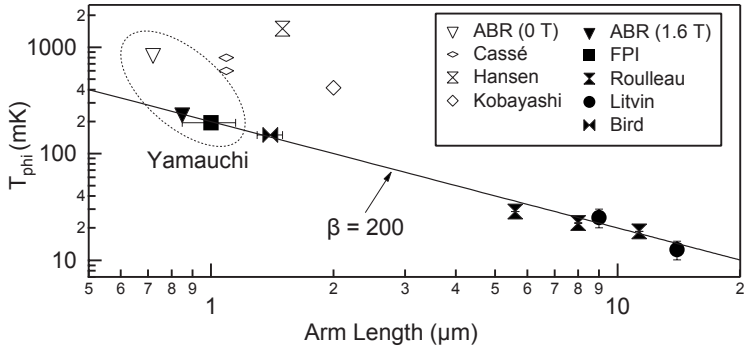

Figure 4.1.: *Temperature decay scale T_φ of the visibility as function of the interferometer arm length (L), scaling as $T_\varphi = \beta/L$ with $\beta = 200$ [71]. Data come from MZIs at $\nu = 2$ (Litvin* et al. *[41], Roulleau* et al. *[2]), a QD at $\nu = 4$, an ABR at 0 T and 1.6 T by Yamauchi* et al. *[71], a ballistic QD by Bird* et al. *[67], ballistic ABRs by Cassé* et al. *[60], Hansen* et al. *[61] and Kobayashi* et al. *[62].*

4.2.2. Mach-Zehnder interferometer

Subsequently, the Weizmann group developped a Mach-Zehnder interferometer (MZI) (I will describe it later) with very high visibility [4, 37, 39]. The MZI is an interesting tool for coherence measurements, because contrary to the Fabry-Pérot interferometer, it is a two-path interferometer (Fig. 4.2) which make it less subject to thermal smearing since the paths can be tuned to be of equal length (¶ 5.4.2).

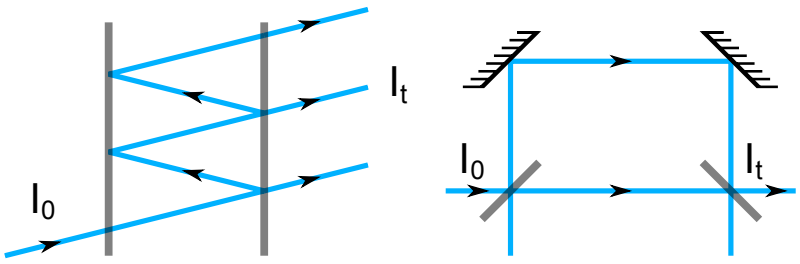

Figure 4.2.: *(left) Fabry-Pérot interferometer. These interferometers are more sensitive to thermal smearing because interferences occur between paths of different lengths* by construction. *(right) Mach-Zehnder interferometer. This is a two-path interferometer: if the two paths have the same 'optic length', there is no thermal smearing (¶ 5.4.2).*

Additionally, there was a proposal for realizing Bell's inequality violation [17] based on two coupled MZIs that rushed several groups into the race to obtain two electrons interferences: a group in Regensburg [41, 42], another in Basel [43] and finally ours in Saclay [1–3, 40].

Finally the Weizmann's group succeeded in doing two-electrons interferences (though they didn't violate Bell's inequalities) [38], however, it brought new interest to QHE ESs.

The decay of the interferences visibility with temperature in the MZI in the IQHE regime at filling factor two was first studied by Roulleau *et al.* in [2] and showed a temperature scale linear with the interferometer size, of the order of 22 mK for an MZI of arm length $L = 11.3$ μm. From these measurements Roulleau *et al.* extracted the coherence length $l_\varphi \propto T^{-1}$ of the order of 20 μm at 20 mK (see § 4.3).

Let me recapitulate the results on finite temperature coherence in the MZI in the IQHE regime.

4.3. Coherence and temperature

4.3.1. Pioneering approach in the ballistic regime

Seelig and Büttiker [72] developped a theory which reproduced the T^{-1} dependence of the coherence length in ballistic rings found in [61, 65, 67, 68]. The mechanism which was invoked are e-e interactions and thermal charge fluctuations within the interfering wire. The interaction was treated in a mean field approach. The relation between the charge and the potential in the wire is mimicked by a geometrical capacitance. The larger is the capacitance, the smaller is the interaction.

4.3.2. First experimental determination

Roulleau *et al.* (Saclay's group) [2] were the first to measure the finite temperature coherence length in a Mach-Zehnder interferometer in the IQHE regime at $\nu = 2$. The procedure which was followed was the same than the one used in [61]: first, one measures the temperature dependence of the visibility and finds an exponential dependence. Then one looks at how the temperature dependence scales with the size of the interferometer. From this, one can extract the coherence length as function of the temperature.

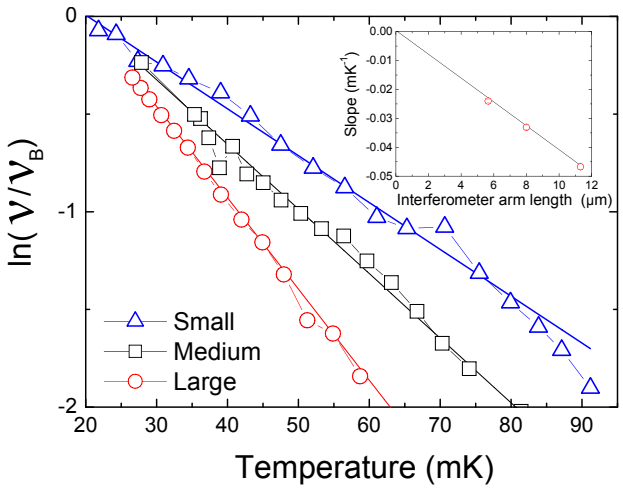

Figure 4.3: *Semi-log plot of the visibility as function of the temperature for three samples of arm lengths $L = 5.6,\ 8,\ 11.3\ \mu m$. The visibility decays exponentially with the temperature with a rate T_φ^{-1} which increases linearly with L (inset) [2].*

Coherence length at finite temperature

When studying the temperature dependence of the interferences visibility, one finds an exponential dependence $\mathcal{V} = \mathcal{V}_0\ \exp(-T/T_\varphi)$ (Fig. 4.3). Doing this for three samples of arm lengths $L \sim 5.6,\ 8$ and $11.3\ \mu m$, one finds $T_\varphi^{-1} \propto L$ (inset of figure 4.3). This proportionality allows to determine a coherence length which varies with the temperature as T^{-1}: $\mathcal{V} = \mathcal{V}_0\ \exp(-2L/l_\varphi)$, where l_φ is the coherence length of the quasiparticles in the interferometer [1].

$$l_\varphi \propto T^{-1} \quad \text{with} \quad l_\varphi = 20\ \mu\text{m} \ @\ 20\ \text{mK} \tag{4.1}$$

Note that I am talking about 'dephasing' and not 'decoherence'. This is because Roulleau *et al.* found in their subsequent work [1] that the origin of the limitation of the coherence length at finite temperature was not intrinsic (like *e-e* interactions within the interfering ES as invoked in [72]) but extrinsic e.g. dephasing by the environment. They were even able to identify this environment.

4.3.3. Theory of dephasing

Without entering too much into detail since I will extensively describe the MZI in chapter 5, let me introduce the system and its environment. The experiments have been conducted at filling factor $\nu = 2$ thus, there are two ESs running on the edge of the 2DEG. The

[1] The factor 2 comes from the fact that both arms of equal length L of the interferometer contribute equally to dephasing.

interferences are observed in the outer edge state (OES) (the one closer to the edge which corresponds to the lower Landau sub-level). The coherence length which has been measured has shown a dependence with the magnetic field (see Fig. 4.5) [1].

What I will show in the following is that the finite coherence length results from charge noise in the environment of the interfering ES. The charge noise blurs the phase acquired by the electrons during their trajectory. This effect depends on the coupling to the environment. At filling factor two, Roulleau *et al.* showed that the inner edge state (IES) was the environment of the interfering OES [1]. I will explain how one characterizes the coupling between the ESs. It is noteworthy that I will also use this method to characterize the coupling when manipulating the ESs with additionnal gates in chapter 7.

Coupling to the environment

Contrary to the simple picture of chapter 3, we find that OES and IES are not independent. The strength of their coupling can be measured: Fig. 4.4 (a) shows a schematic of the MZI with the interfering OES in blue. The IES, represented in red, is capacitively coupled to the OES in the upper arm of the interferometer and can be adressed individually with bias voltage V_2. Usually, one reveals the interferences by sweeping the voltage V_{SG} applied to a side gate electrostatically coupled to the lower arm of the interferometer thus changing the length of the lower arm (oscillations revealed using this method are shown on Fig. 4.4 (b)). One can also use the IES as a gate to reveal the interferences by sweeping V_2 (see the oscillations on Fig. 4.4 (c)). Indeed, as explained in chapter 3, the electrochemical potential in the IES is fixed by the bias applied on the injecting ohmic contact: the IES can be seen as a metallic gate at potential V_2.

The periodicity V_0 of the oscillations revealed by this method is linked to the coupling between the ESs, that we define as the inverse of V_0. V_0 is found to vary with the magnetic field. The origin of this dependence is not clear but one can try to understand why there is a maximum (Fig. 4.5). Using the mean field approach developped by Roulleau *et al.* and reported in appendix A, one shows that V_0 should depend on the geometrical capacitance between the two ESs and the quantum capacitance $C_Q = G_Q\tau$, where τ is the time of flight of an electron through the interferometer and $G_Q = e^2/h$ the quantum conductance [2]: $V_0 \propto C^{-1} + 2C_Q^{-1}$. Increasing the magnetic field should decrease C as the

[2]The ratio between the geometrical and the quantum capacitance is actually $C/C_Q \sim \epsilon_0\epsilon_r R_Q v_d$ which is

distance between ESs increases. It should also decrease the drift velocity e.g. increase τ which means increase the quantum capacitance. As C and C_Q vary in opposite ways with the magnetic field, this can explain the maximum that we are observing.

Of course this approach is too simple and probably does not reflect everything that happens at the microscopic level. Particularly, disorder plays a role as it leads to a trajectory whose length depends on the magnetic field. Incidently so do C, C_Q and V_0. However, as we will see, this dependence of the coupling with the magnetic field perfectly explains the dependence of the coherence length with the magnetic field.

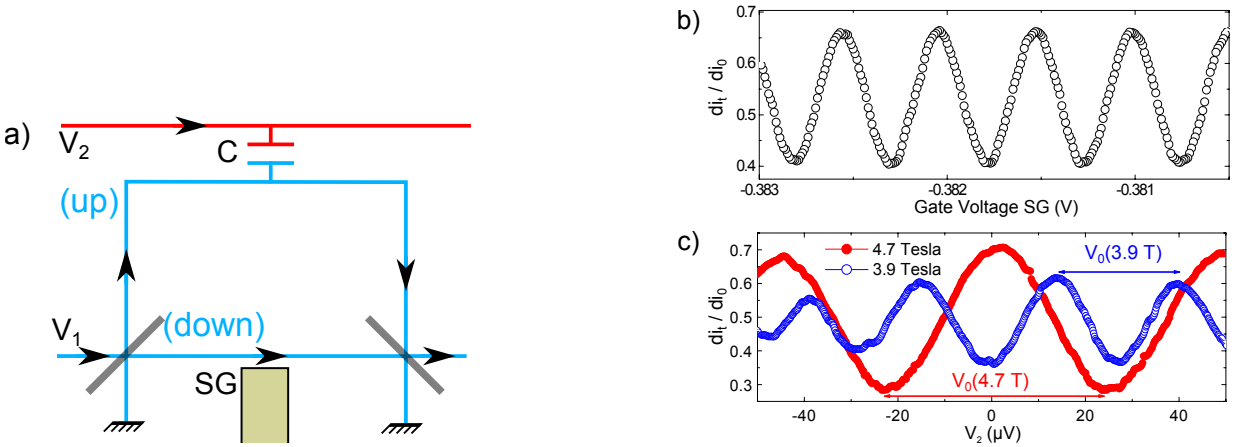

Figure 4.4.: *(a) Schematic of the MZI in the limit $C \ll C_Q$. The interfering OES (blue) is capacitively coupled to the IES (red). Electronic interferences are revealed either by sweeping the gate voltage applied to SG (b) or the voltage bias V_2 (c), using the IES as a gate. The periodicity of the oscillations with respect to V_2, V_0 varies with the magnetic field [1].*

Noise dephasing

Because of the coupling between ESs, charge noise in the IES caused by thermal fluctuations is seen by the electrons travelling in the arms of the MZI and blurs their phase. More precisely, the OES transmitted current averaged over the phase distribution is [3]:

$$\langle I_t \rangle = \frac{e^2 V_1}{h} \left(\mathcal{T}_1\mathcal{T}_2 + \mathcal{R}_1\mathcal{R}_2 + 2\sqrt{\mathcal{R}_1\mathcal{R}_2\mathcal{T}_1\mathcal{T}_2}\ \langle \cos(\varphi) \rangle \right) \tag{4.2}$$

of the order of 10^{-2} to 10^{-1}, for a drift velocity v_d between 10^4 and 10^5 m.s^{-1}. Therefore, $V_0 \propto C^{-1}$.

[3] Eq. (4.2) is derived in chapter 5 in the Landauer-Büttiker formalism. It is the exact analog of the optical case with the incident current $I_0 = G_Q V_1$, where $G_Q = e^2/h$ is the quantum conductance.

where $\mathcal{T}_i$ and $\mathcal{R}_i$ are the transmission and reflection probabilities of the i^{th} beam splitter ($\mathcal{T}_i + \mathcal{R}_i = 1$), V_1 is the voltage bias applied to the interfering OES, and φ is the phase difference accumulated by an electron going through the interferometer. If we assume a gaussian phase averaging [4], $\langle \cos\varphi \rangle = \cos\left(\langle\varphi\rangle\right)\ e^{-\langle \delta\varphi^2 \rangle/2}$ the visibility in the differential transmission of the OES is then:

$$\mathcal{V} = \mathcal{V}_0\ \exp\left(-\frac{\langle \delta\varphi^2 \rangle}{2}\right) \tag{4.3}$$

The upper and lower arms contribute equally to the electron phase fluctuations. The variance of the phase distribution is then $\langle \delta\varphi^2 \rangle = (2\pi)^2 \left(\langle \delta V_U^2 \rangle + \langle \delta V_D^2 \rangle\right)/V_0^2$, where V_U and V_D are the potentials of the upper and lower IES [5]. $\langle \delta V_\alpha^2 \rangle$ ($\alpha = U, D$) is related to the noise power spectrum $S_{\alpha\alpha}$ of V_α through $\langle \delta V_\alpha^2 \rangle = S_{\alpha\alpha}\Delta\nu$, $\Delta\nu$ being an unknown bandwidth on which fluctuations occur, which is inversely proportional to the time of flight through the interferometer [1]. The phase fluctuations become: $\langle \delta\varphi^2 \rangle = (2\pi)^2 \left(S_{UU} + S_{DD}\right)\Delta\nu/V_0^2$.

As one can remark thanks to Eq. (4.3), the variance of the phase distribution is responsible for a decrease in the visibility. At finite temperature, the power noise spectrum is the Johnson-Nyquist noise, proportional to the temperature, and phase noise leads to an exponential decrease of the visibility with the temperature. The temperature dephasing rate is [6]:

$$T_\varphi^{-1} = 2 \times \frac{8\pi^2 k_B R_Q}{V_0^2}\ \Delta\nu \quad \text{with} \quad R_Q = \frac{h}{e^2} \tag{4.4}$$

Check!

To check if this approach is correct, one can generate noise in the environment thanks to an additional QPC $G0$ at the entry of the interferometer (see chapter 5). Setting the transmission of $G0$ so that the interfering OES is fully transmitted, and the IES partially transmitted with the transmission $\mathcal{T}_0$ to the upper arm of the interferometer, when bringing

[4] For a random variable X with normal distribution $\mathcal{N}(\mu, \sigma)$, the random variable $\exp(X)$ has the expectation value $\exp\left(\mu + \sigma^2/2\right)$. Following this, $\langle \exp(\pm iX) \rangle = \exp\left(\pm i\mu - \sigma^2/2\right)$ and then,

$$\langle \cos(X) \rangle = \left(\left\langle e^{iX} \right\rangle + \left\langle e^{-iX} \right\rangle\right)/2i = \cos\left(\langle X \rangle\right) e^{-\sigma^2/2}$$

[5] For the upper arm, $V_U = V_2$ and $\langle \delta V_U^2 \rangle = \langle \delta V_2^2 \rangle$, while for the lower arm $V_D = 0$ (the IES is grounded in the lower arm) but $\langle \delta V_D^2 \rangle \neq 0$ because of thermal noise.

[6] The factor 2 stands for the two equal contriutions of the upper and lower arms to dephasing.

V_2 to a finite value, tunable partition noise is generated in the IES coupled to the upper arm of the interferometer.

The excess noise (compared to the situation when V_2 is zero) has the following power spectrum [73]: $\Delta S_{UU} = 2eR_Q\mathcal{T}_0\,(1-\mathcal{T}_0)\,V_2(\coth\,(eV_2/k_BT) - 2k_BT/eV_2)$. When $eV_2 \gg k_BT$, $\Delta S_{UU} = 2R_Q\mathcal{T}_0\,(1-\mathcal{T}_0)(eV_2 - 2k_BT)$, and the visibility depends exponentially on V_2: $\mathcal{V} = \mathcal{V}_0\; e^{-T/T_\varphi}\; \exp\left(-\mathcal{T}_0(1-\mathcal{T}_0)\;\left(V_2 - 2k_BT/e\right)/V_\varphi\right)$, with

$$V_\varphi^{-1} = \frac{4\pi^2 eR_Q}{V_0^2}\;\Delta\nu \tag{4.5}$$

From Eqs. (4.4) and (4.5), we see that T_φ and V_φ are proportional through:

$$eV_\varphi = 4k_BT_\varphi \tag{4.6}$$

This is the relation that is checked on Fig. 4.5: on the right hand scale both V_φ and $4k_BT_\varphi/e$ are reported as function of the magnetic field, and we see that they fall upon each other without any ajustable parameter!

This confirms our approach which makes the charge noise in the IES responsible for the dephasing in the OES. Moreover, we find that V_φ and T_φ are both proportional to V_0 (and not V_0^2 suggesting that the bandwidth $\Delta\nu$ is also proportional to V_0) with $\left(4k_BT_\varphi/e\right)/V_0 = V_\varphi/V_0 = 8/55 \approx 0.15$, which is to be compared to the main-field result derived by Roulleau *et al.* (appendix A), $V_\varphi/V_0 = 1/\pi^2 \approx 0.10$.

Let me introduce Leviskiviskyi *et al.*'s theory which also derive the proportionality between V_0 and T_φ. We will make a quantative comparison between our theory and their's.

4.3.4. Another approach

Levkiviskyi *et al.* [6] developped a theory involving beating between two collective modes, a fast charge mode with velocity u and a slow spin mode with velocity v, with $u \gg v$. These modes arise because of the coupling between the two ESs and reproduce the multiple side lobe structure of the visibility at finite bias ut it does not reproduce its decay (§ 4.4).

We can derive the coupling from $\partial\varphi/\partial V_2 = (e/\hbar)\,L/2v \equiv 2\pi/V_0$ [6]. It is given by:

$$V_0^{-1} = \left(\frac{e}{\hbar}\right)\;\frac{L}{4\pi v} \tag{4.7}$$

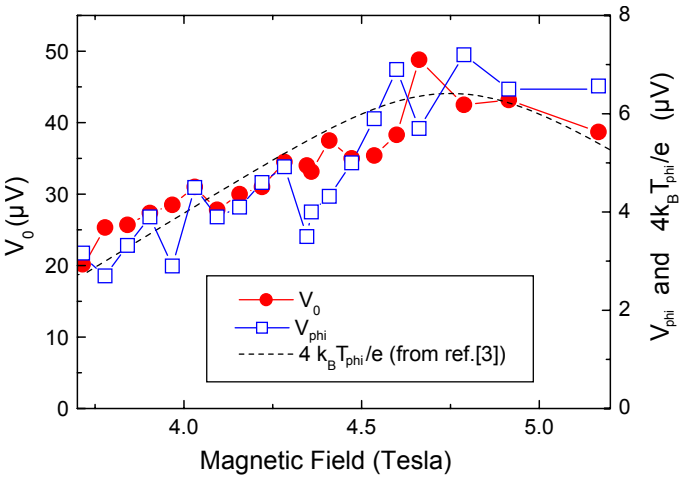

Figure 4.5: *Left scale: V_0 as function of the magnetic field (full red circles). Right scale: V_φ (empty blue squares) and $4k_BT_\varphi/e$ (dashed line) as function of the magnetic field. Fluctuations of V_0 with the magnetic field are proportionnal to the ones of V_φ and $4k_BT_\varphi/e$. V_φ and $4k_BT_\varphi/e$ fall on each other. All these quantities show a maximum at the end of the $\nu = 2$ plateau [1, 3].*

In the $u \gg v$ limit, the authors derive the finite temperature coherence length $l_\varphi = (\hbar/k_B)\, 2v/\pi T$, and finally $l_\varphi = (e/k_B)\, L/\left(2\pi^2 V_0^{-1} T\right)$, which shows that l_φ depends inversely on the temperature and the coupling between ESs. From this one can extract the temperature dephasing rate:

$$T_\varphi^{-1} = \left(\frac{k_B}{e}\right) 4\pi^2 V_0^{-1} \tag{4.8}$$

Then they derive $4k_BT_\varphi/eV_0 = V_\varphi/V_0 = 1/\pi^2 \approx 0.10$, which is to be compared to our experimental result $V_\varphi/V_0 \approx 0.15$. This theory predicts the T^{-1} dependence of the coherence length as well as the propotionality between the temperature dephasing rate T_φ^{-1} and the coupling V_0^{-1} between ESs. Our simple mean field approach, which does not require the bosonization framework, yields also $V_\varphi/V_0 = 1/\pi^2 \approx 0.10$ (appendix A).

Here I have shown that so far experimental results are in very good agreement with the theory developed by Roulleau *et al.* as well as Levkiviskyi *et al.*'s. However, it is yet not clear why one does not observe additional decoherence. For example, in Seelig *et al*'s theory [72], charge noise *in* the interfering ES and the interaction (mimicked by a capacitance) are responsible for the decoherence. In Levkiviskiy *et al.*'s, this is also a decoherence rather than dephasing which is responsible for the visibility decrease.

The last point is that dephasing has been measured and theoretically predicted to be proportional to the coupling V_0^{-1}. Later, I will use this proportionality to analyse the underlying mechanism responsible for the enhancement of the coherence when using additional gates to manipulate the ESs (chapter 7).

In the following section, I will remind the results for the visibility at finite bias and the

conclusions of the available theories, in particular Levkiviskyi's which attempts to find a explanation for this 'unexpected behaviour'.

4.4. Finite bias visibility

When Ji *et al.* [37] first observed a monotonous decrease of the visibility with the bias V_1 and subsequently when Neder *et al.* [4,39] reported oscillations of the visibility, much attention was brought to the subject. Indeed, because of the differential nature of the measurement, it is as if we measured monochromatic interferences. When sweeping the bias voltage, it is as if we sweeped the energy of the electron beam. Hence, for non interacting electrons, we do not expect any variation of the visibility. Here, I briefly report the most striking features of the visibility at finite bias.

4.4.1. 'Unexpected behaviour' at finite bias

First Neder *et al.* [4, 39] from the Weizmann Institute, and then other groups [3, 40, 42, 43], observed a curious behaviour in the visibility of the interferences in the MZ, which cannot be explained in the independent electron picture: the visibility in the differential transmission as function of the voltage bias applied at the injection of the MZI, V_1 exhibits oscillations e.g. multiple extinctions with revivals of the visibility in between. The phase of the interferences is rigid within a 'lobe' of visibility (between two successive extinctions) and undergoes π-jumps at extinctions (Fig. 4.6). The energy scale associated with the oscillations is of the order of $10-20$ μV, and there seems to be some additional dephasing which damps the oscillations: one usually does not observe more than $3-4$ extinctions on each side of the lobe structure. These distinctive features are present both at $\nu = 1$ (only one side lobe, 'single side lobe structure') and $\nu = 2$ (both single and multiple side lobes have been observed) [4]. On Fig. 4.7 for the same sample of arm length $L = 11.3$ μm, both multiple side lobes and single side lobe structures are observed at the same magnetic field but for different configurations of the IES [7]. Here are some features of these lobe structures:

▷ multiple side lobe structures have been found at $\nu = 2$ but not $\nu = 1$

▷ at $\nu = 2$, multiple side lobes are obtained on large samples ($L = 11.3$ μm)

[7] This will be explained further in chapter 7.

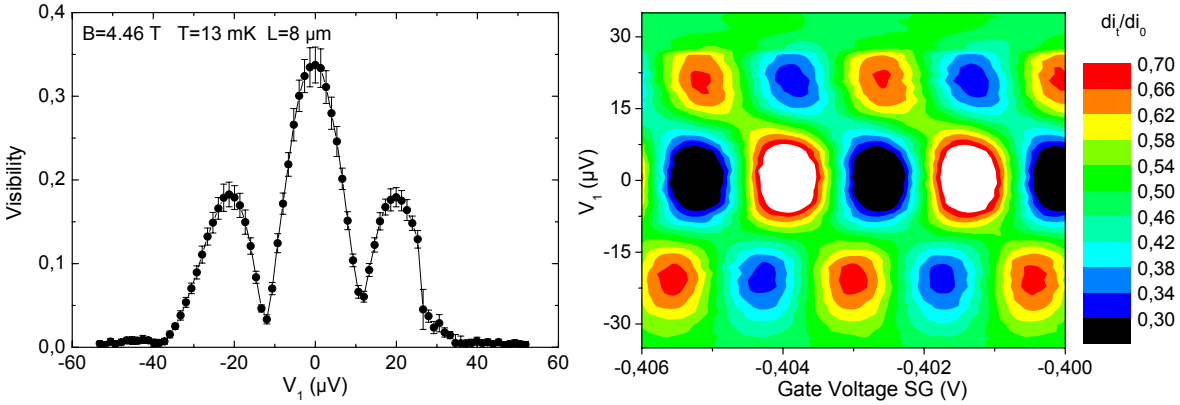

Figure 4.6.: *(left) Visibility as function of the bias voltage V_1 showing oscillations with multiple extinctions, for a sample of arm length $L = 8$ μm, at $B = 4.46$ T and $T = 13$ mK. The oscillations are damped. One can distinguish two lobes on each side of the central lobe. (right) Colorplot of the differential transmission of the interfering OES as function of the side gate voltage V_{SG} along the x-axis, and the bias voltage V_1 on the y-axis. The oscillations of the differential transmission as function of V_{SG} are extinguished at $V_1 \sim \pm 13$, ± 37 μV (periodicity $\Delta V_1 \sim 25$ μV). Within a lobe the phase of the visibility is rigid, and undergoes π-jumps at extinction points.*

▷ to fit multiple/single lobe structures one needs different formulas, suggesting that a single side lobe structure are not only a broad multiple lobe structure, but something different (see ¶ 4.4.4).

Bieri *et al.* reported an enhancement of the visibility [43] which was later explained by P. Roulleau in his PhD thesis [3] (¶ B.1.2). It is noteworthy that this lobe behaviour with the phase rigidity was also observed in Aharonov-Bohm rings in the ballistic regime (at zero magnetic field) [69–71].

Which parameters does this unexpected lobe structure in the visibility depend on? Here I review the features characterizing the lobe structure, to confront them later to the results of the available theories.

4.4.2. Relevant physical parameters

Temperature The lobe structure is not changed by temperature: it is only renormalized by the value of the visibility at zero bias [3, 40].

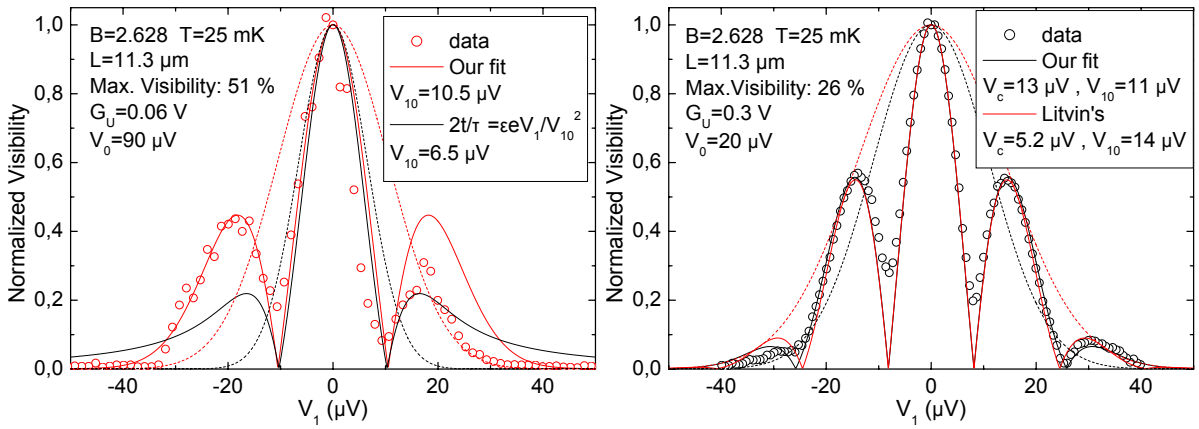

Figure 4.7.: *Lobe structures for the same sample ($L = 11.3\ \mu m$) but different couplings V_0^{-1} of the ESs in the upper arm (chapter 7). (left) Single side lobe. (red solid line) Our fit $V_{10} = 10.5\ \mu V$. (black solid line) The fit from the decoherence hypothesis $\tau_\varphi^{-1} \propto \varepsilon V_1$ does not perform as well ($V_{10} = 6.5\ \mu V$). (dashed lines) Gaussian enveloppes $e^{-V_1^2/2V_{10}^2}$ associated with each fit. (right) Multiple side lobes. 'Our' fit (black solid line) and Litvin's (red solid line) fit the data (open black circles) equally well. V_{10} is about the same for both, but V_c shows a factor* 2.5.

Asymmetry Detuning of the first beam splitter $G1$ from $\mathcal{T}_1 = 0.5$ or modification of the length of one arm does not affect the shape of the lobe structure [3, 4, 39, 40] but only changes the maximum visibility (it does not change the energy scales), following a $\sqrt{\mathcal{T}_1\,(1-\mathcal{T}_1)}$ dependence in agreement with Eq. (4.2).

Magnetic field On the contrary, the magnetic field influence the form of the lobe structure [4, 42]: when increasing the magnetic field along the $\nu = 2$ Hall plateau, Neder *et al.* [4] found that the periodicity increase first from $\sim 10\ \mu$V at the begining of the plateau ($\nu = 2$) to 20 μV at the end. Then it should decrease (but was not measured by Neder *et al.*) since it is again 10 μV at $\nu = 1$. Litvin *et al.* [42] also observed a maximum of the periodicity, however it is reported at $\nu = 1.5$ and interferences are observed only at the end of the $\nu = 2$ plateau, raising questions about the homogeneity of the sample.

Dilution Dilution of the interfering ES also affects the lobe structure as reported in [3, 39, 40]. As dilution tends towards 100 %, the width of the central lobe diverges.

Interferometer size Yamauchi *et al.* [71] found that in ballistic interference experiments (AB-rings and QDs in zero magnetic field) as well as in QHE interference expertiments, the energy scales seem to depend linearly on the interferometer length as seen on Fig. 4.1.

The lobe structure is neither affected by an asymmetry of the interferometer (different arm lengths or detuning of one beam splitter from half transmission of the OES) nor by the temperature (it only renormalizes the maximum visibility), the involved energy scales are proportional to the dimensions of the interferometer and depend on the magnetic field as on the dilution [8]. The distinction between multiple and single side lobe structures points towards the existence of two distinctive energy scales. In the following we are interested in finding suitable functions and in justifying them with a theory.

4.4.3. Gaussian enveloppe and something else

To fit the lobe structure, we use two different functions depending on whether it is a single or a multiple side lobes structure. For the single side lobe structure, we once again assume a gaussian phase averaging (as in ¶ 4.3.3), with an additional assumption on the phase variance dependence on the bias voltage, introducing a corresponding energy scale. For the multiple side lobes structure we add a oscillating factor with a distinct energy scale. These assumptions are justified mainly by the fact that they yield functions which fit our data well. We present another fit function used by Litvin *et al.* for the multiple side lobe structure which also introduce two energy scales.

Single side lobe structure

In the case of a gaussian phase averaging like the one discussed in § 4.3, the coherent part of the current is the sum of the contributions of the whole energy distribution, and if we assume that the mean phase and the phase variance are independent of the energy, the integral becomes: $I_\sim = (2e^2V_1/h)\sqrt{\mathcal{R}_1\mathcal{R}_2\mathcal{T}_1\mathcal{T}_2}\,\cos\left(\langle\varphi\rangle_\varphi\right)\,e^{-\langle\delta\varphi^2\rangle_\varphi/2}$, where $\langle\ \rangle_\varphi$ signals an average over the phase distribution. If we assume that the variance of the phase distribution is $\langle\delta\varphi^2\rangle_\varphi \propto V_1^2$, the interference term in the transmitted current becomes:

$$I_\sim = \frac{2e^2V_1}{h}\,\sqrt{\mathcal{T}_1\mathcal{T}_2\mathcal{R}_1\mathcal{R}_2}\,\cos\left(\langle\varphi\rangle_\varphi\right)\,e^{-V_1^2/2V_{10}^2} \tag{4.9}$$

[8] These aspects will be developped in chapter 6.

with V_{10} a fit parameter. The interference term in the differential conductance is then:

$$G_{\sim} = \frac{\mathrm{d}I_{\sim}}{\mathrm{d}V_1} = \frac{2e^2}{h}\sqrt{\mathcal{T}_1\mathcal{T}_2\mathcal{R}_1\mathcal{R}_2}\ \cos\left(\langle\varphi\rangle_{\varphi}\right)\left(1-\frac{V_1^2}{V_{10}^2}\right)\ e^{-V_1^2/2V_{10}^2} \tag{4.10}$$

And the corresponding visibility,

$$\mathcal{V} = \mathcal{V}_0\left|1-\frac{V_1^2}{V_{10}^2}\right|\ \exp\left(-\frac{V_1^2}{2V_{10}^2}\right) \tag{4.11}$$

fits appropriety single side lobe structures (Fig. 4.7 (left)) and needs quite remarkably, only one fit parameter. This fit derives directly from the gaussian term $e^{-V_1^2/2V_{10}^2}$ in the interfering part of the current (Eq. (4.9)): this term alone is sufficient to explain the single side lobe structure.

The phase of the interferences in the differential conductance is given by $\varphi = \langle\varphi\rangle_{\varphi} + \pi\ \theta(V_1^2/V_{10}^2 - 1)$, where θ is the Heaviside function. As observed in the data, the phase obtained from this fit undergoes π jumps when the term $(V_1^2/V_{10}^2 - 1)$ which modulates the visibility vanishes. The phase rigidity is respected if we consider that $\langle\varphi\rangle_{\varphi}$ does not depend on V_1.

This gaussian envelop has been observed in numerous experiments [4,39,42] and not only in the IQHE regime [70, 71]. it is important to emphasize that to date no theory predicts this envelop. During my PhD thesis I have tried to find what could be the physics involved in such a behaviour (chapter 6).

One notices the particular way Eq. (4.11) is derived: the interfering part of the current is multiplied by a reduction factor. This is not a scattering approach with an energy dependent coherence time of quasiparticle (van der Wiel *et al.* in Ref. [70]). Here, it seems that this reduction factor is due to an external cause. The question is which one? We will see in chapter 6 that this gaussian envelop is not accounted for by a heating effect. Indeed, to justify the V_1^2 dependence of the phase distribution variance, one could say that applying a bias heats the electrons with a temperature proportional to the dissipated power e.g. $\propto V_1^2$. This seems however too simple and we will see that a heat flux alone cannot explain our findings [9].

[9] I will check in ¶ 6.3.4 how energy exchange between ESs can increase the temperature in the neighbouring ES and I will show that it cannot alone explain this behaviour.

Multiple side lobe structure

To fit multiple side lobes structures we add an oscillating factor to Eq. (4.9):

$$I_\sim = \frac{2e^2V_1}{h}\sqrt{\mathcal{T}_1\mathcal{T}_2\mathcal{R}_1\mathcal{R}_2}\,\cos\left(\langle\varphi\rangle_\varphi\right)\,\cos\left(\frac{V_1}{V_c}\right)e^{-V_1^2/2V_{10}^2} \tag{4.12}$$

where V_c is a fit parameter. In addition to a 'not understood' gaussian envelop existing in numerous experiments, there seems to be a 'not fully understood' oscillating term in the visibility which has been so far only observed at $\nu = 2$ [10]. The visibility becomes:

$$\mathcal{V} = \mathcal{V}_0\left|-\frac{V_1}{V_c}\sin\left(\frac{V_1}{V_c}\right)+\cos\left(\frac{V_1}{V_c}\right)\left(1-\frac{V_1^2}{V_{10}^2}\right)\right|\,\exp\left(-\frac{V_1^2}{2V_{10}^2}\right) \tag{4.13}$$

This new fit function allows for visibilities larger than one when $V_c/V_{10} < 2/\pi \approx 0.64$ (§ B.3). However, visibilities in the differential conductance have not the physical signification of visibilities in the transmitted current and are allowed to be larger than one.

According to theses fits, the single side lobe structure arises from a simple gaussian phase averaging with a standard deviation proportional to the bias voltage V_1. The corresponding energy scale is given by the only fit parameter V_{10}. To describe the multiple side lobe structure, we introduce another energy scale, V_c, distinct from V_{10}.

Other derivations

Other groups didn't make this choice: Litvin *et al.* in [42] chose to fit the multiple side lobe structure with a gaussian term modulated by $|\cos(V_1/V_c)|$. The interfering part of the current for the multiple side lobes structure can be written as:

$$I_\sim = \frac{2e}{h}\sqrt{\mathcal{T}_1\mathcal{T}_2\mathcal{R}_1\mathcal{R}_2}\,\int_0^{eV_1}\cos\left(\frac{\varepsilon}{eV_c}\right)\,\cos\left(\langle\varphi\rangle_\varphi\right)\,e^{\langle\delta\varphi^2\rangle_\varphi/2}\,\mathrm{d}\varepsilon \tag{4.14}$$

Then, if we assume a mean phase independent of the energy and the bias, and a phase variance depending only on the energy as $\langle\delta\varphi^2\rangle_\varphi \propto \varepsilon^2$, when deriving the transmitted current with respect to the bias, we obtain the differential conductance, and then we recover Litvin *et al.*'s formula for the visibility in the differential transmission:

$$\mathcal{V} = \mathcal{V}_0\left|\cos\left(\frac{V_1}{V_c}\right)\right|\,\exp\left(-\frac{V_1'^2}{2V_{10}^2}\right) \tag{4.15}$$

[10] We will see in chapter 7 that this oscillating term might originate from the coupling between ESs.

Our choice

Why did we choose the particular fit given by Eq. (4.13) over Litvin's given by Eq. (4.15)? One can argue that for the multiple side lobe structure, both fits perform equally well as can be seen on Fig. 4.7 (right). They both yield two distinctive energy scales, however, depending on the fit choice, they do not have the same value.

Which one is the more adequate? Litvin's is simpler than ours: it consists in a gaussian enveloppe modulated by a cosine term whose zeros correspond to the annulations of the visibility. They are equidistant from each other in terms of bias voltage with the periodicity $2\pi V_c$. In the case of Eq. (4.13), this is not so straightforward. The zeros positions depend both on the gaussian parameter V_{10} and the beating parameter V_c. On Fig. 4.7 (right), it seems that Eq. (4.13) fits the zeros positions better than Eq. (4.15), but this is arguable.

The important point is that our 'model' which yields Eq. (4.13), also yields an equation which fits the signal induced by the IES because of the coupling V_0^{-1} between ESs. Moreover, the fitting parameters obtained for the direct signal (Eq. (4.13)) also work for the induced signal [11]. This strongly favors our approach over Litvin's. Additionally, Eq. (4.13) becomes Eq. (4.11) in the limit $V_{10}/V_c \to 0$, which is not the case if we follow Litvin *et al.* (see appendix B).

The choice of our fit over Litvin's suggests that the dephasing doesn't depend on the energy of the electrons in the distribution, but rather on the mean chemical potential.

We presented the fits that will be used in the future and introduced two energy scales V_c and V_{10}. Eventually, we will be interested in studying the dependence of V_c and V_{10} with the magnetic field, the dilution (chapter 6)... and the coupling V_0^{-1} between the ESs (chapter 7). Indeed, we will find that the coupling is a 'good knob' to tune dephasing by the environment. But for now, we try to justify the V_1^2 dependence of the phase variance which is assumed *ad hoc*, and we present alternative theories that could explain the lobe structure.

4.4.4. Theory

Before the lobe structure was discovered, Seelig *et al.* [72] predicted a monotonic decay of the visibility with the bias voltage caused by intrachannel interactions at $\nu = 1$ treated in

[11] In chapter 7 where we will use the induced signal to compute the coupling between ESs.

a mean-field approach. Then Marquardt *et al.* [74, 75] and Förster *et al.* [76] studied the effect of a coupling to a classical fluctuating field and to a quantum bath [77, 78]. Finally voltage probe dephasing was investigated by Chung *et al.* [79].

In the following, I review some theories starting with the simplest ones which yield fit functions for the single side lobe structure, to show that on two examples at least decoherence does not explain the single side lobe structure. Then I show how a mean-field approach reproduces some features of the multiple side lobe structure although with important discrepancies which are also present in more elaborate theories.

Single side lobe structure - decoherence?

First we focus on the case of the single side lobe structure. We have seen that the model of a gaussian averaging of the phase was able to explain the temperature dependence of the visibility and that it yields an appropriate fit if one assumes a V_1^2 dependence of the phase variance (¶ 4.4.3). This model involves *dephasing*, while we are interested here in the damping of the electron interferences caused by *decoherence* induced by interactions. We attempt two models of an energy and/or bias dependent coherence time τ_φ. The interfering part of the current results from the whole energy distribution [12]:

$$I_\sim(V_1) = \frac{2e}{h}\sqrt{\mathcal{T}_1\mathcal{T}_2\mathcal{R}_1\mathcal{R}_2}\int_0^{eV_1}\cos\left(\varphi\left(\varepsilon, V_1\right)\right)e^{-\tau/\tau_\varphi(\varepsilon,V_1)}\,\mathrm{d}\varepsilon \tag{4.16}$$

where τ is the time of flight of an electron through the interferometer. The integral spans over all energies above the Fermi energy. Lets assume that the phase difference φ doesn't depend on the bias nor on the energy. Then the oscillating term can be taken out of the integral.

We explore two models which yield a gaussian decrease of the visibility as function of the bias: $\tau_\varphi(\varepsilon, V_1)$: $\tau_\varphi^{-1} \propto \varepsilon^2$ and $\tau_\varphi^{-1} \propto \varepsilon V_1$. The latter model is similar to the phenomelogical one proposed by Van der Wiel *et al.* [70] who considered $\tau_\varphi^{-1} \propto \varepsilon$. In our model, V_1 stands for the available phase space for the electron in a mean field approximation [13]. One could then expect the prefactor to be proportional to $\mathcal{T}_1(1-\mathcal{T}_1)$.

[12] Since we are not interested in dephasing, there is no averaging over some phase distribution.

[13] At finite bias, the first QPC set at transmission $\mathcal{T}_1$ creates complementary double step distributions in both arms. Some relaxation is susceptible to happen [13], and the coherence time of the electron could reflect this. Hence the V_1 dependence of τ_φ^{-1}.

First case $\tau_\varphi^{-1} \propto \varepsilon^2$ so that the coherent part of the current reads:

$$I_\sim = \frac{2e}{h}\sqrt{\mathcal{T}_1\mathcal{T}_2\mathcal{R}_1\mathcal{R}_2}\,\cos(\varphi)\int_0^{eV_1} e^{-\varepsilon^2/2\varepsilon_0^2}\,\mathrm{d}\varepsilon \tag{4.17}$$

which yields

$$\mathcal{V} = \mathcal{V}_0\,\exp\left(-\frac{V_1^2}{2V_{10}^2}\right) \tag{4.18}$$

where $V_{10} = \varepsilon_0/e$ is a parameter. We see that the visibility presents no zero, in disagreement with the experimental observations.

Second case $\tau_\varphi^{-1} \propto \varepsilon V_1$ leads to:

$$I_\sim = \frac{2e}{h}\sqrt{\mathcal{T}_1\mathcal{T}_2\mathcal{R}_1\mathcal{R}_2}\,\cos(\varphi)\int_0^{eV_1} e^{-eV_1\varepsilon/2\varepsilon_0^2}\,\mathrm{d}\varepsilon \tag{4.19}$$

and a visibility:

$$\mathcal{V} = 2\mathcal{V}_0\,\left|\left(1+\frac{V_{10}^2}{V_1^2}\right)\,\exp\left(-\frac{V_1^2}{2V_{10}^2}\right) - \frac{V_{10}^2}{V_1^2}\right| \tag{4.20}$$

with $V_{10} = \varepsilon_0/e$. This formula leads to the existence of a zero at finite bias, however, as one can remark on Fig. 4.7 (left), the shape does not agree with the measurements. In addition as I explained previously, such a mechanism would lead to a dependence of V_{10} in $\mathcal{T}_1(1-\mathcal{T}_1)$, which is not observed (chapter 6) [4, 40].

Multiple side lobe structure - mean field approach

I present a mean field model which predicts multiple lobes with only one ES in an asymmetric MZI. This model inspired by Ref. [72], mimicks the interaction between electrons by a capacitance to a fictitious gate. A similar approach was developped by Neder *et al.* [4].

I use the indices U and D for the upper and lower arm of the interferometer. C is a geometrical capacitance mimicking the interaction, with the larger the capacitance, the lower the interaction. V_+ and V_- are the electrochemical potentials applied on the injecting contact and the small inner contact. U denotes the potential seen by the electrons. Following the Buttiker approach in Ref [72], the charges in the arms are:

$$Q_j(\omega) = e^2\nu(\omega)\,(\mathcal{R}_1V_+ + \mathcal{T}_1V_- - U_j) \quad \text{with} \quad Q_j = \frac{U_j}{C} \quad , \quad \nu(\omega) = \frac{i}{h\omega}\left(1-e^{i\omega\tau_j}\right) \tag{4.21}$$

where $j = U, D$, and τ_j is the time of flight through arm j. In the dc limit, this yields:

$$U_U = \frac{\mathcal{R}_1V_+ + \mathcal{T}_1V_-}{1+C/C_{Q_U}} \quad , \quad U_D = \frac{\mathcal{R}_1V_- + \mathcal{T}_1V_+}{1+C/C_{Q_D}} \tag{4.22}$$

where $C_{Q_{U(D)}} = G_Q \tau_{U(D)}$ is the quantum capacitance, and $G_Q = e^2/h$. One can estimate the ratio between the quantum capacitance and the geometrical capacitance $\sim \varepsilon_0 \varepsilon_r R_Q v_d$ which is of the order of 10^{-2} to 10^{-1} for a drift velocity between 10^4 and 10^5 m.s^{-1}. Then the geometrical capacitance is negligible. For a inner ohmic contact set to ground, with $V_- = 0$ and $V_+ = V_1$, one simply gets $U_U = \mathcal{T}_1 V_1$, $U_D = \mathcal{R}_1 V_1$.

As explained in Ref. [4], for an adiabatic process, this variation of the potential leads to a variation of the electron momentum at energy ε above the Fermi energy, $k_j(\varepsilon) = (\varepsilon - eU_j)/\hbar v_d$ giving a variation of the phase $\delta\varphi_j = (\varepsilon - eU_j)\ \tau_j/\hbar$. Finally, the phase difference between the two trajectories is:

$$\Delta\varphi = (\tau_U - \tau_D)\ \frac{\varepsilon}{\hbar} - (\mathcal{T}_1\tau_U - \mathcal{R}_1\tau_D)\ \frac{eV_1}{\hbar} + 2\pi\ \frac{\Phi_B}{\Phi_0} \tag{4.23}$$

where Φ_B is the magnetic flux through the area of the interferometer at the Fermi energy and $\Phi_0 = h/e$ is the quantum of flux.

Case $\mathcal{T}_1$=0.5 Indeed, the maximum visibility is obtained for $\mathcal{T}_1 = \mathcal{T}_2 = 0.5$. If the times of flight through the arms are not identical, $\Delta\tau \equiv \tau_U - \tau_D \neq 0$. This situation leads to oscillation in the visibility. To show this, I will not take into account the Gaussian envelop. In that case the interfering part of the current is:

$$I_\sim \propto \int_0^{eV_1} \cos\left(\left(\varepsilon - \frac{eV_1}{2}\right)\ \frac{\Delta\tau}{\hbar} + 2\pi\ \frac{\Phi_B}{\Phi_0}\right) \mathrm{d}\varepsilon \tag{4.24}$$

yielding the interfering part of the conductance

$$G_\sim \propto \cos\left(\frac{eV_1\Delta\tau}{2\hbar}\right) \cos\left(2\pi\ \frac{\Phi_B}{\Phi_0}\right) \tag{4.25}$$

and hence an oscillation in the visibility with a π shift when the visibility crosses 0 and with a phase rigidity between successive zeros of the visibilty.

Beyond the mean-field approach

Although this model reproduces the periodic oscillations of the visibility, there are discrepancies with the experimental findings.

When the transmission of the first beam splitter is not equal to 0.5, the phase rigidity breaks and the lobes are affected while this is not the case in experiments [3]. This problem is also present in more elaborate theories [5–11, 16, 80, 81] although phase rigidity

seems restored in the strong interaction limit [9, 10]. However, many of these theories are pertubative in tunneling [5,6,11,16,80,81] whereas the experiments are generally conducted at $\mathcal{T}_i = 0.5$. A notable exception is the work of Kovrizhin *et al.* [9, 10] inspired by Neder *et al.* [7] and Youn *et al.* [8] which invokes multiple particles interferences.

Within this mean-field approach, the frequency of the oscillations is proportional to the difference of time of flight between the upper arm and lower arm: there is no lobes in a symmetric interferometer. However, Neder *et al.* [4] have checked by considerably varying the difference of time of flight that this is not the case in experiments. When one treats interactions non perturbatively the beating energy scale no longer depends on $\Delta\tau$ [6–11,16].

Plasmons acquire a phase due to the propagation (t_0 in [6]) and a phase due to interaction ($2\Delta t$ in [6]). Both partially cancel out so that there is a phase rigidity [6–11].

The long-range character of the interaction seems to be of importance according to Refs. [5, 7–11, 80, 81]. Indeed it leads to plasmon dispersion, which could account for multiple lobes structure at $\nu = 1$, through beating of a low energy mode with velocity renormalized by the interactions with a high energy mode with bare drift velocity [80, 81], or multiple particles interferences [7–10]. At $\nu = 2$, Levkiviskyi *et al.* [6] who treat pointlike interactions between ESs, predict no dephasing when $\Delta\tau = 0$. However, when one takes into account the finite range of the interaction, visibility decay is recovered [11].

Although some theories predict a *multiple* side lobes structure at $\nu = 1$ [7–10, 80, 81], so far only *single* side lobe structure has been observed. Schneider *et al.* [11] treated both cases ($\nu = 1$ and $\nu = 2$) with long-range interaction within and betwen ESs in the tunneling limit and found numerically three lobes at $\nu = 1$ and multiple lobes at $\nu = 2$.

To conclude, this simple mean field model helps us understand why the lobe structure is so puzzling. While models including interactions are able to reproduce some features, it appears that there are *always* discrepancies which raise doubt about the real mechanism leading to the lobes.

In the next section, I report another kind of experiment which probe energy relaxation in the edge states. Some interesting findings point out the role of interactions between edge states.

4.5. Relaxation in the edge states

4.5.1. Pioneering work

Is scattering between ESs supressed? Up to which lengthscale? To test scattering between ESs one uses the scheme on Fig. 4.8 first used by Van Wees *et al.* [82], which allows to selectively bias and probe ESs with QPCs [83, 84]. Up to an equilibration length, there is no scattering between adjacent ESs. Then the conductance of the system Fig. 4.8 (left) with one QPC is equal to the conductance of two QPCs in series on Fig. 4.8 (right).

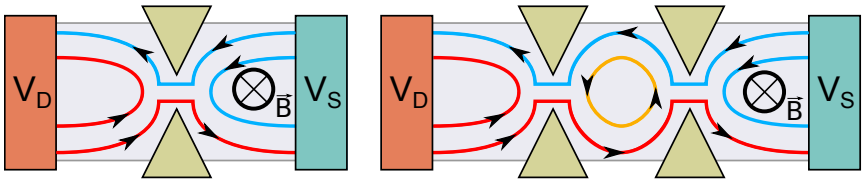

Figure 4.8.: $\nu = 2$. *(left) The QPC totally reflects the IES so that current is carried only by the OES: two points resistance is given by the* $\nu = 1$ *resistance of the QPC. (right) Still, only the OES carries current: two points resistance is equal to the* $\nu = 1$ *resistance.*

This so-called anomalous quantum Hall effect violates the classical law of resistance composition. Because of the absence of scattering between ESs, they keep their potential during propagation. Deviation from this behaviour is a sign of scattering between ESs. One can estimate the equilibration length by testing this law for various propagation lengths.

Inter-edge scattering events are exponentially suppressed when the overlapping between wave functions of electrons from adjacent edges decreases [34, 35], it then depends on the filling factor and on the ES index through the width of the compressible/incompressible strips [50, 84].

The equilibration length at $\nu = 2$ has been measured by Müller *et al.* [36] and was found to be larger than several hundreds of microns for ~ 0.1 K. In the case of $\nu = 2$, suppression of equilibration between ESs is reinforced by spin conservation: an electron tunneling into the adjacent ES requires a nuclear spin-flip. Such an event is rare because of the small hyperfine coupling, hence the large equilibration length.

These experiments show that there is no particle exchange between ESs but what about energy exchange? A recent experiment focus on this aspect.

4.5.2. A recent experiment

Energy relaxation

In the experiment reported in [13, 14], the authors studied in the IQHE regime at $\nu = 2$ the relaxation of an out of equilibrium electron distibution in the OES. To do so, they perfected an energy spectroscopy technique to probe the energy distribution in the OES with a quantum dot (QD). On Fig. 4.9 is an image of the sample by a scanning electronic microscope (SEM).

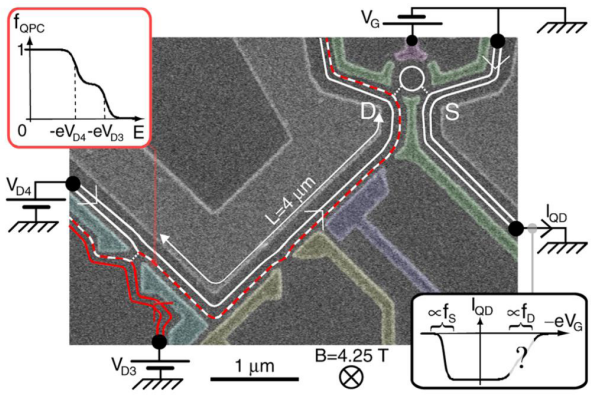

Figure 4.9.: *Sample e-beam micrograph. ESs propagate along lines, dashed lines correspond to out of equilibrium distributions. A double step distribution f_{QPC} is created in the OES outside of the QPC in the lower left corner and propagates on a tunable length L. The resulting distribution f_D is probed by the quantum dot (white circle). Colorized QPCs allow to vary the propagation length. The gates not colorized are grounded.*

Injecting a double step energy distribution in the OES by means of a QPC, they find that the out of equilibrium distribution relaxes into a seemingly hot Fermi distribution which depends on the propagation length along the IES. Data show that relaxation is complete after a $L = 10$ μm propagation. The authors proved the existence of energy exchanges between the OES and the adjacent IES which with some additional energy loss, seems to explain quantitatively the observed energy relaxation in the OES [14].

[14] Kovrizhin *et al.* [85,86] say that the relaxed distriution is actually not a Fermi distribution, and that the procedure used in [13, 14] to quantified energy exchanges with an effective temperature is ambiguous.

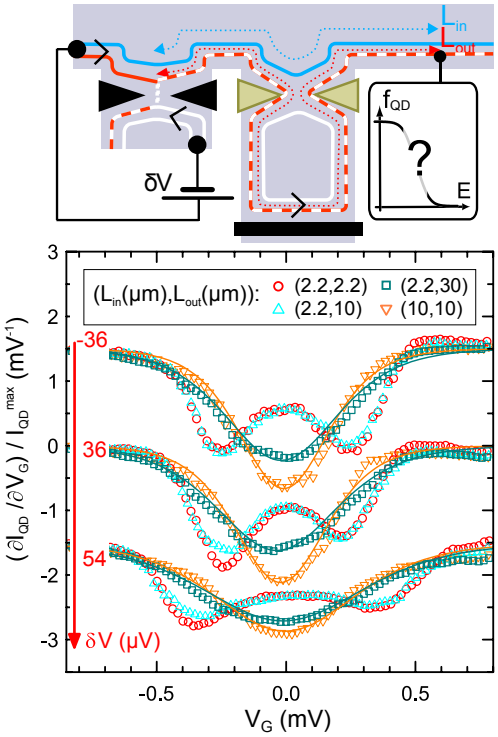

Figure 4.10: *(top) An out of equilibrium distribution propagates in the OES over L_{out} and the IES over L_{in}. L_{out} can be made longer than L_{in} by forcing the OES through a loop. (bottom) Conductance through the QD shows two dips for short distances $(L_{in}, L_{out}) = (2.2, 2.2)$ μm and relaxes in a single broad dip for longer distances $(10, 10)$ μm. Relaxation freezes when the OES goes through a small enough loop (~ 8 μm): $(2.2, 10)$ μm where the adjacent IES is localized [15].*

Freezing energy relaxation

Following these findings, Altimiras *et al.* found a way to 'cure' energy relaxation by localizing the IES into small closed loops of ~ 8 μm length. The results of their experiments are shown on Fig. 4.10 [15].

The explanation for this phenomenon is that when the IES is closed in a ~ 8 μm loop, energy exchanges between the OES and its copropagating IES are frozen because of the energy quantification in the closed IES. The size of the loop determines the level spacing: if the loop is to large there is no freezing of energy relaxation because the level spacing is too small. The gap is $\Delta E_{\text{loop}} = hv_d/L_{\text{loop}}$ where L_{loop} is the loop perimeter and v_d the drift velocity of the electrons. If the drift velocity is taken to be $v_d \sim 5 \times 10^4$ m.s^{-1} [13], the gap is then $\Delta E_{\text{loop}} \sim 26$ μeV $\equiv 300$ mK.

Pertinence in our experiment

Might energy relaxation be present in our sample? Indeed, at finite bias, the first beam splitter creates out of equilibrium distributions in both arms of the MZI. The size of the arms (up to 11.3 μm) allows for relaxation as studied by Altimiras *et al.*. Then, can energy

relaxation (which implies inelastic scattering and phase breaking) account for the observed behaviour at finite bias in the visibility (lobe structure)? And can we freeze it out following the method used in [15]?

4.6. Conclusion

In this chapter, we explained why the Mach-Zehnder interferometer is an appropriate tool to study coherence in the edge states.

We reported the earlier results on the temperature dependence of the coherence at zero bias at $\nu = 2$ [1, 2] and the associated mean-field theory based on a work by Seelig *et al.* [72] which was developped in our group: the coupling of the interfering edge state with its noisy environment which is the adjacent edge state present at $\nu = 2$, is responsible for the limited coherence at finite temperature. An alternative approach by Levkiviskyi *et al.* [6] gives the same quantitative result and also points toward coupling between edge states. We then reported the 'unexpected behaviour' [3, 4, 39–43] observed in the visibility af finite bias and its dependence with the various parameters of the experiment.

We reviewed different formulas to fit the data and presented our choice for a fit. The theories available to explain the lobe structure have multiplied these last years [5–11] but still do not explain the whole range of experimental data. We tried to present these theories in a comprehensive manner that showed their basic ingredients and limits.

Finally we reported a recent experiment by Altimiras *et al.* [13, 14] on energy relaxation in the ESs at $\nu = 2$ which might be present in the MZI and explain the lobe structure. The authors also found a cure against energy relaxation [15].

These elements prompt us in two directions: first, we want to study the finite bias visibility further, trying to relate it to the various theories: Levkiviskyi *et al.* [16] made a prediction on a possible quantum phase transition of the lobe pattern as function of the dilution of the incoming electron beam. We check this prediction. We also try to relate the findings on energy relaxation to the energy scales in our experiment. Second, taking advantage of the conclusions of Altimiras *et al.* [15] on the freezing of energy relaxation, we design a new kind of sample where we try to freeze energy exchanges between the ESs. By the way, we make a quantitative comparison with the theory of Levkiviskyi *et al.* [6].

Before diving into these subjects, let me present the Mach-Zehnder interferometer.

5. The electronic Mach-Zehnder interferometer

Contents

5.1. Introduction

We explain here how to make the condensed matter electrical equivalent of the optical Mach-Zehnder interferometer. First we introduce the consitutive elements of the interferometer and the interferometer itself. Then we present the experimental set-up which allows us to observe one electron interferences in the quantum Hall regime at $\nu = 2$.

5.2. The elements

5.2.1. Electron beams and mirrors

To realize an electronic Mach-Zehnder interferometer, one needs:

i) electron beams which are provided by ESs in the QHE regime as we have seen in § 3.5

ii) mirrors to change the direction of the beams. In the QHE regime the ESs follow naturally the edge of the sample. One can design the paths of the beams just by designing the edges of the sample either with polarized metallic gates or by etching. According to the method used, the confining potential will be different (sharper with the etching method) and so the velocity of the electrons (greater for an etched edge).

iii) beam splitters: one uses quantum point contacts as beam splitters (¶ 5.2.2).

Of course, we study the electronic MZI in the coherent regime [87] where the dimensions of the sample are smaller than or of the order of the coherence length l_φ which was measured to be of the order of 20 μm at 20 mK (chapter 4): we study samples whose arm lengths are $5.6, 8$ and 11.3 μm (Fig. 5.2).

5.2.2. The quantum point contact

A quantum point contact (QPC) [73, 88] is defined by an electrostatic depletion of the 2DEG underneath a gate. The metallic gate is deposited on top of the GaAs/AlGaAs heterostrusture with a ~ 300 nm opening.

On Fig. 5.1 (left) a sketch of the ESs trajectory is represented. Here, the filling factor is two so that there are two ESs: the inner edge state (IES) represented in red and the outer edge state (OES) represented in blue on Fig. 5.1 (left).

On Fig. 5.1 (right) is plotted the differential conductance $\mathrm{d}i_t/\mathrm{d}v_1$ through such a QPC as a function of the voltage V_{gate} applied on its gates. At $V_{gate} = 0.5$ V the 2DEG underneath the gate is not depleted, both ESs are fully transmitted ($\mathrm{d}i_t/\mathrm{d}v_1 = 2e^2/h$). When one decreases the voltage applied on the gate, the counter-propagating ESs from opposite edges are brought closer together and the probability for one incoming electron to be reflected in the outgoing ES on the opposite edge by tunneling effect becomes non zero, the differential conductance decreases. First, only the IES is reflected: the intermediate plateau at $\mathrm{d}i_t/\mathrm{d}v_1 = e^2/h$ as function of V_{gate} indicates that the IES is fully reflected while the OES is still fully transmitted. In that case, it means that when one decreases V_{gate} further, one begins to reflect the OES until reaching pinch-off ($\mathrm{d}i_t/\mathrm{d}v_1 = 0$).

In the future, except when specified, the IES will be fully reflected at the QPCs. The interferences are observed in the OES and one can forget the IES in a first approach.

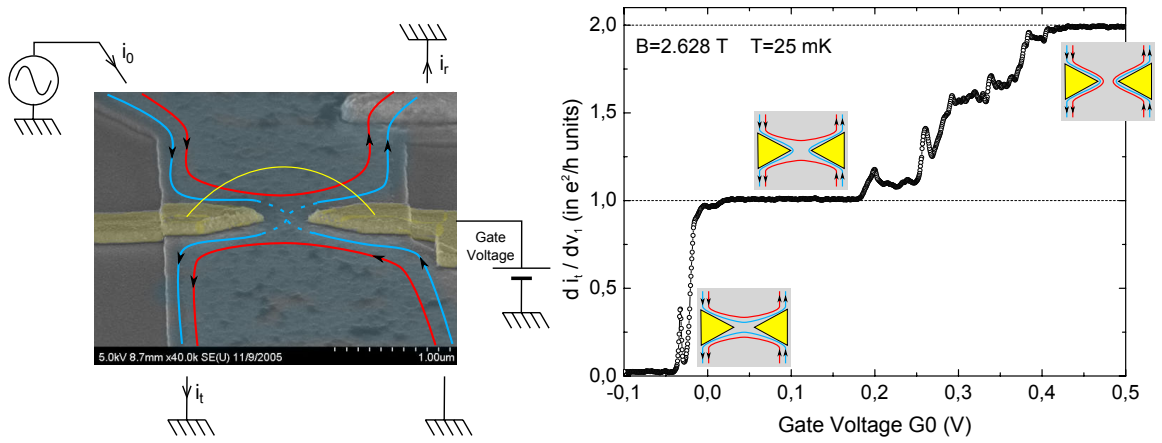

Figure 5.1.: *(left) Scanning electronic microscope (SEM) view of a QPC. In false colors, the 2DEG is blue, the two gates forming the QPC are yellow. The $\nu = 2$ ESs are figured with the IES (in red) being fully reflected and the OES (in blue) being partially transmitted. (right) The differential conductance across the QPC is plotted as a function of the gate voltage in units of the quantum conductance $G_Q = e^2/h$.*

5.2.3. The interferometer

The sample

The electronic Mach-Zehnder interferometer was designed at LPN (Marcoussis) by G. Faini and D. Mailly, on a high mobility 2DEG from A. Cavanna and U. Gennser (density $n_s = 2.0 \times 10^{11}$ cm^{-2}, mobility $\mu_0 = 2.5 \times 10^6$ cm^2.V^{-1}.s^{-1}). We later worked on a 2DEG provided by W. Wegscheider from ETH (Zurich) with density $n_s = 1.1 \times 10^{11}$ cm^{-2} and mobility $\mu_0 = 3 \times 10^6$ cm^2.V^{-1}.s^{-1} (chapter 7).

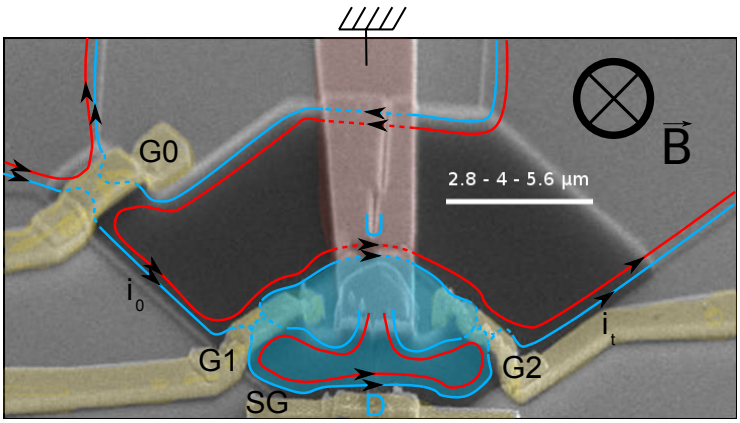

Figure 5.2.: *SEM view of the sample. The small central ohmic contact (pink) is the main difficulty in the fabrication process. At $\nu = 2$, G0 is used to reflect the IES (in red), and to generate shot noise in the IES in the upper arm (¶ 4.3.3). It also allows dilution of the OES (in blue) (§ 6.2 and § 6.3). The OES is split at G1 in two paths U and D, which are recombined at G2. To reveal the interferences in the transmitted current i_t, one has to vary the Aharonov-Bohm phase threading through the surface $\mathcal{S}$ enclosed between the two arms (colorized in blue), by changing either the magnetic field, or $\mathcal{S}$* via *gate SG or the IES in the upper arm.*

Transmission through the MZI

The electronic MZI takes avantage of the electron beams and the beam splitters in the same way than the optic one: within the single particle Landauer-Büttiker formalism, the transmitted amplitude t of an electron in the OES is the sum of the two amplitudes transmitted through paths U and D (Fig. 5.2). With t_i and r_i being the transmission and reflection amplitudes of beam splitter G_i ($|t_i|^2 + |r_i|^2 = 1$), the transmitted amplitude

through the MZI is:

$$t = t_1 \; e^{i\varphi_U} \; t_2 - r_1 \; e^{i\varphi_D} \; r_2 \tag{5.1}$$

where $\varphi_U(\varphi_D)$ is the phase accumulated by the electron traveling in the upper(lower) arm of the interferometer.

The transmission probability at the energy ε above the Fermi energy is [1]:

$$|t|^2 = \mathcal{T}_1\mathcal{T}_2 + \mathcal{R}_1\mathcal{R}_2 + 2\sqrt{\mathcal{T}_1\mathcal{T}_2\mathcal{R}_1\mathcal{R}_2} \; \cos\left(\varphi\left(\varepsilon\right)\right) \tag{5.2}$$

where $|r_i|^2 = \mathcal{R}_i$ and $|t_i|^2 = \mathcal{T}_i$ $(i = 1, 2)$, and where $\varphi\left(\varepsilon\right) = \varphi_U - \varphi_D$ is the Aharonov-Bohm phase [89] corresponding to the area defined by the position of the interfering ES along the upper path U and the lower path D (Fig. 5.2) a small energy ε above the Fermi energy. This phase is linked to the phase at the Fermi energy φ_F through [79]:

$$\varphi\left(\varepsilon\right) = \frac{\varepsilon \Delta L}{\hbar v_d} + \varphi_F \tag{5.3}$$

$\Delta L = L_U - L_D$ being the length difference between the upper path (L_U) and the lower path (L_D), and $v_d = E/B$ the electron drift velocity [2]. The phase at the Fermi energy is $\varphi_F = 2\pi \; \Phi_B/\Phi_0$, where Φ_B is the magnetic flux threading through the area defined by the upper and the lower path at the Fermi energy, $\Phi_0 = h/e$ being the flux quantum.

Revealing interferences

One immediately sees that to reveal the interferences in the transmission of the MZI, there is two possibilities: either sweeping the magnetic field, or changing the area enclosed between the two paths *via* a gate electrostatically coupled to one arm of the interferometer (SG or the IES in the upper arm).

In the following I describe how we measure the interferences in practice e.g. how and why we work at low temperatures and how we make transport measurements.

[1] Indeed, this expression does not include any decoherence/dephasing processes!

[2] Here we assume that it is the same in both arms.

5.3. Experimental set-up

5.3.1. Low temperatures

To see the quantum Hall effect, we need the thermal energy to be small compared to the Landau gap: $k_B T \ll \hbar\omega_c$. At $B \sim 3$ T, this means $T \ll 59$ K which is not difficult to achieve. However since the length coherence scales as T^{-1} and is of the order of 20 μm at 20 mK (chapter 4), the lower the temperature, the better.

We worked with a $^3He/^4He$ dilution refrigerator with a typical base temperature of 20 mK with 12 coaxial cables. Our fridge circulates 30 μmoles/s which corresponds to an approximate cooling power of 30 μW at 120 mK.

A superconductive coil allows us to reach a maximum magnetic field of 12 T at 4.2 K. The experimental space, the mixing chamber and the discrete exchangers are surrounded by a screen thermalized at 170 mK so that 4.2 K black body radiation is suppressed. More importantly, the shield prevents transport of residual ^4He from the 4.2 K surface to the 20 mK surface. The experimental box is thermally anchored to the mixing chamber with a copper rod. Its temperature is measured with a RuO_2 thermometer calibrated between 7 mK and 1 K. The sample is stuck to the sample holder with a PMMA resine. Electrical connections between the sample and the sample holder by golden boundings are done with an ultrasound micro-soldering machine.

At high temperatures electrons are thermalized to the cristal temperature by electron-phonon collisions. For the low temperatures we are working at, these processes are no longer efficient to cool the 2DEG. The 2DEG thermalizes itself *via* the electronic conductivity (Wiedemann-Franz law) to the ohmic contacts which are maintained at low temperature.

To reduce thermal losses, we use homemade coaxial cables made of inox and high resistivity wire. We use specific coaxial cables which strongly attenuate high frequency electromagnetic modes [90]. The attenuation factor is given by $A = \exp(R(f)/Z_c)$, where Z_c is the characteristic impedance of the coaxial cables and $R(f)$ their resistance at frequency f, which increases at high frequency because of the skin effect. The coaxial cable typical capacitance is $C = 20$ pF, the resistance per unit length of the inner conductor – whose diameter is $D = 75$ μm – is given by $R/L = 300\ \Omega.\mathrm{m}^{-1}$. From these values we find an attenuation factor of $A = 2 \times 10^{-3}$ dB.Hz$^{-1/2}$. At 1 GHz, the attenuation of transverse electromagnetic modes is of 6 dB, and increases as the squareroot of the mode frequency.

5.3.2. Transport measurements

Since interferences are seen in the transmission through the interferometer, we are interested in doing transport measurements: we measure differential conductances using standard lock-in techniques [3]. The measurement system is represented on Fig. 5.3.

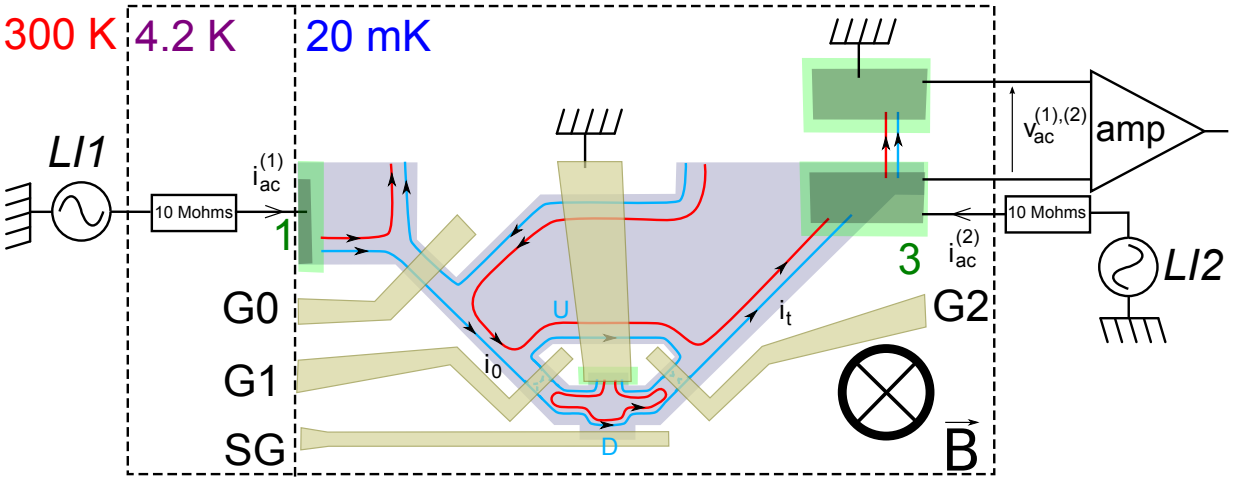

Figure 5.3.: *Schematic of the measurement system. Lock-in LI1 injects current $i_{ac}^{(1)}$ at frequency f_1 at contact n°1 and detects the potential drop $v_{ac}^{(1)}$ at the same frequency at contact n°3. Current polarization for LI1 is realized through a 10 MΩ resistor at 4.2 K to minimize the low frequency cut off due to the coaxial cables. LI2 injects current $i_{ac}^{(2)}$ at f_2 and measures $v_{ac}^{(2)}$ at contact n°3.*

An ac current $i_{\mathrm{ac,in}}$ at $f_0 = 418$ Hz is sent on the sample. The output voltage contains an ac component $v_{\mathrm{ac,out}}$ synchronized with the excitation and a noisy component. This output signal is amplified by a low noise amplifier [4], and demodulated with the reference signal at f_0 [5]: the measured signal is the response of the system excited at the frequency f_0, around the energy eV_i above the Fermi energy, where V_i is the dc bias applied in addition to the tiny excitation. Finally we extract the differential conductance $G(eV_i) = i_{\mathrm{ac,in}}/v_{\mathrm{ac,out}}$.

The ac excitation must be low enough: its amplitude fixes the energy range on which we probe the system. To observe temperature dependent properties, it is necessary that $ev_{\mathrm{ac,in}} \ll k_B T$. In our experiment, the lowest electronic temperature was ~ 20 mK, which imposes $v_{\mathrm{ac,in}} \ll 2\ \mu$V. On the other hand, to have the best sensitivity we must choose

[3] We use the lock-in amplifier model 5210, EGG Princeton Applied Research.
[4] We use the low noise preamplifier model LI75A, NF electronic instruments.
[5] The lock-in amplifier realizes an average of the output signal during a time constant τ_{av}, and strongly reduces the bandwidth defined by $\sim 1/\tau_{\mathrm{av}}$ and hence the noise.

$v_{\mathrm{ac,in}}$ close to this limit. Typically we injected an ac current of 0.1 nA, which gives at $\nu = 2$, for a 12.9 kΩ input resistance [6], $v_{\mathrm{ac,in}} \sim 1.3\ \mu$V.

One must avoid multiples of 50 Hz. In some experiments realized on the MZI, we used two lock-ins with excitations frequencies $f_1 = 418$ Hz and $f_2 = 619$ Hz. To protect the experiment from microwave pollution, the fridge is inside a copper box that prevents the environmental electromagnetic noise from reaching the sample.

To get rid of the resistance of the wires and of the ohmic contacts (resistance of the wires about 200 Ω at 300 K plus ohmic contacts resistance and 2DEG resistance at zero magnetic field about 100 Ω), we should do four points measurements. However, because of the geometry of the sample, we limit ourselves to two points and three points measurements. We must then figure what we are really measuring.

Two points resistance

To adjust the magnetic field at a value corresponding to a specific integer filling factor in each arm of the interferometer, we proceed as follows. One injects current $i_{\mathrm{ac}}^{(2)}$ at ohmic contact n°3 and leave all the QPCs open. ${v_{\mathrm{ac}}}^{(2)}$ measured at contact n°3 by lock-in $LI2$ yields [7]:

$$R_{\mathrm{2points}} = \frac{{v_{\mathrm{ac}}}^{(2)}}{{i_{\mathrm{ac}}}^{(2)}} = R_L + R_H + \text{offset (wires+contacts)} \tag{5.4}$$

On a Hall plateau, the longitudinal resistance vanishes, leaving only the quantized Hall resistance and the offset due to wires and ohmic contacts (which can be substracted). When sweeping the magnetic field, we observe quantized plateaus of Hall resistance (Fig. 5.4). From this measurement we can tune the magnetic field to obtain the desired filling factor.

[6] Ohmic contacts are grounded before and after the QPCs so that the two points resistance seen at the injection is the Hall resistance: $v_{\mathrm{ac,in}} = R_H i_{\mathrm{ac,in}}$.

[7] I will abusively call Hall resistance the two points resistance. This resistance has the same quantification properties as the Hall resistance, if one neglects the contacts and wire resistance (see § 3.4.3).

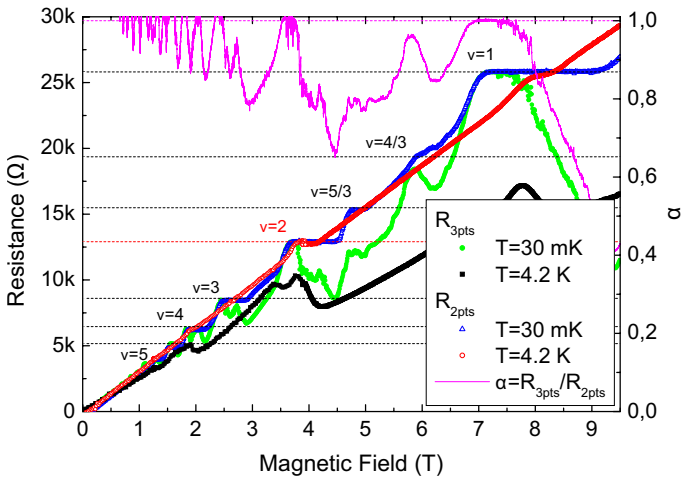

Figure 5.4: *Plateaus in $R_{2points}$ shrink and $R_{3points}$ lowers as the temperature rises because of variable range phonon-assisted hopping between localized states [18] inducing backscattering. At 30 mK for $\nu = 1$, backscattering is absent at the beginning of the plateau ($\alpha = 1$) and appears as the magnetic field is increased ($\alpha < 1$). Wires and contacts resistances ($\sim$ 600 Ω) have been substracted from $R_{2points}$.*

Three points resistance

Three points resistance measurements are done by injecting a current $i_{\mathrm{ac}}^{(1)}$ at ohmic contact n°1 and measuring the corresponding potential drop ${v_{\mathrm{ac}}}^{(1)}$ at contact n°3 with lock-in $LI1$:

$$R_{3\mathrm{points}} = \frac{{v_{\mathrm{ac}}}^{(1)}}{{i_{\mathrm{ac}}}^{(1)}} = \alpha R_H \tag{5.5}$$

where α is 1 if all the QPCs are open and if there is no backscattering. $R_{3\mathrm{points}}$ and α are plotted on Fig. 5.4 as function of the magnetic field.

5.3.3. Characterizing the sample

Backscattering

As one can remark on Fig. 5.4, the transmission α reaches one when R_H is on a plateau: as explained in the chapter devoted to the Hall effect (chapter 3), the transport is ballistic and there is no backscattering. However α is not 1 on all the Hall plateau. This is most probably due to the mesoscopic aspect of the sample. While one is measuring R_H on a region where the mesa is large, $R_{3\mathrm{points}}$ probes the transmission trough narrow regions. These regions have a width comparable to the screening length on the edge [50]. Thus the density does not reach the bulk value, which corresponds to the one probed in the two points measurement.

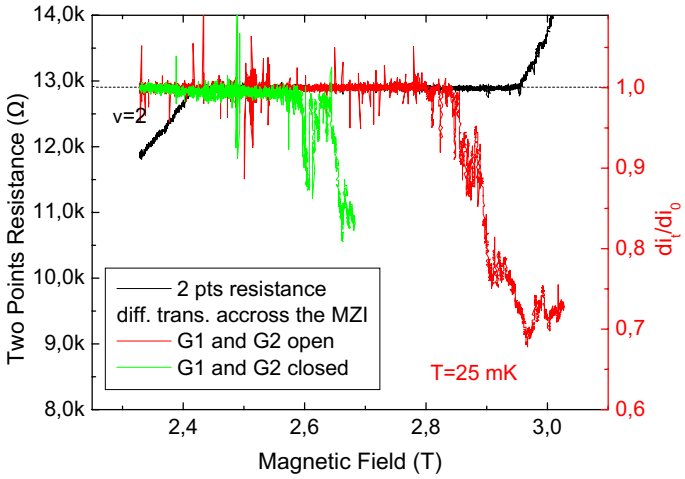

Figure 5.5: *Two points resistance (black) and differential transmission through the lower (red) and upper arm of the MZI (green) as function of the magnetic field at $T \sim 25$ mK. The transmission through the upper arm decreases at a lower magnetic field than through the upper arm, hinting of a smaller density in the upper than in the lower arm.*

Asymmetry

On Fig. 5.5 backscattering is not the same in the upper and lower arm of the interferometer. It seems that the density in the lower arm is smaller than the density in the bulk but larger than the density in the upper arm. Indeed the variation is not so large. If one estimate it from the plateaus ends, the relative variation is of the order of 8 %.

The origin of the density mismatch between the upper and lower arm is not clear. It could be due either to the presence of the small ohmic contact, or to the additional gates that are present in this particular sample and that we will use later in chapter 7. Nevertheless, it is legitimate to think that such a small density mismatch in both arms cannot lead to a strong velocity drift mismatch.

Characterizing the QPCs

Three points resistance is useful to characterize QPCs. For example, lets examine $G0$: we let $G1$ and $G2$ open and sweep the gate voltage applied to $G0$. Lock-in $LI1$ measures a voltage drop proportional to the transmitted current i_t: ${v_{ac}}^{(1)} = i_t \times R_H$. In most situations, the IES is fully reflected at all QPCs, we then define the transmission of the OES through $G0$ by: $\mathcal{T}_0 = 2i_t/{i_{ac}}^{(1)}$ [8]. If there are impurities, the differential conductance $\mathrm{d}i_t/\mathrm{d}v_1$ as function of the gate voltage V_{G_U} shows resonances. This is an impediment when one wants to study the dependence of the interferences on the transmission of one QPC. Our new samples (from W. Wegscheider) QPC's characteristics are much smoother that the ones of our previous samples (Fig. 5.6), indicating that they have a better mobility.

[8] $\mathcal{T}_0 = 1(0)$ when the OES is fully transmitted(reflected), the IES being totally reflected.

This data also tells us what voltage we must apply to have a transmission of the OES at QPC $G1$ and $G2$ about $\mathcal{T}_{1,2} \sim 0.5$ (the maximum of visibility should be achieved for $\mathcal{T}_1 = \mathcal{T}_2 = 0.5$).

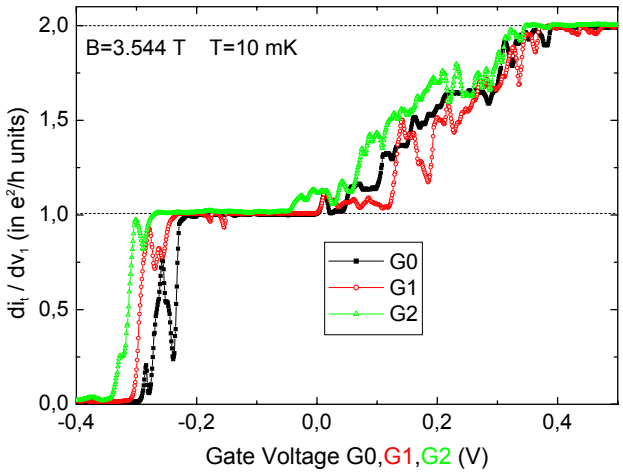

Figure 5.6.: *Characteristics of QPCs $G0$ (black curve), $G1$ (red curve) and $G2$ (green curve).*

We proceed in the following way:

1st step We measure the differential conductance between contacts n°1 and n°3, with $G1$ and $G2$ open while we sweep the gate voltage applied on $G0$ (black curve on figure 5.6).

2nd step $G0$ is set so that the IES is fully reflected and the OES fully transmitted ($\mathcal{T}_0 = 1$), on the first plateau of the black curve at $V_{G0} = -0.1$ V and we successively measure the differential conductance of $G1(G2)$ as function of $V_{G1}(V_{G2})$ with $G2(G1)$ open.

5.4. Tuning the interferometer

5.4.1. Electron interferences

Once we have obtained the characteristics of gates $G0$, $G1$ and $G2$, we fully reflect the IES at $G0$, and tune $G1$ and $G2$ to the voltages for which we measured a transmission one half of the OES. We note $\mathcal{T}_1$ and $\mathcal{T}_2$ the transmissions of the OES by QPCs $G1$ and $G2$. The process described above is not enough to achieve the best tuning of the interferometer. It results from the fact that QPCs are very sensitive to the gate voltage when working around

half transmissions of the OES. Cross talk between QPCs is responsible for the detuning. To fine-tune $G1$ and $G2$ we proceed in the following manner: we know that if $\mathcal{T}_1 = 0.5$, the differential transmission of the OES averaged over the oscillations caused by interferences (the mean transmission) is independant of $\mathcal{T}_2$ since $\langle \mathrm{d}i_t/\mathrm{d}i_0 \rangle_{\mathrm{osc}} = [1 - \mathcal{T}_2 + 2(\mathcal{T}_2 - 0.5)\mathcal{T}_1]$, then if $\mathcal{T}_2 > 0.5 (\mathcal{T}_2 < 0.5)$, the mean transmission $\langle \mathrm{d}i_t/\mathrm{d}i_0 \rangle_{\mathrm{osc}}$ increases(decreases) with $\mathcal{T}_1$ and so with V_{G1}. On the contrary, if $\mathcal{T}_2 = 0.5$ it is constant. On the curves of figure 5.7 (left), we ajust $\mathcal{T}_2$ so that when we change V_{G1}, the mean transmitted current remains constant. The green curve for a given V_{G2} is decreasing with V_{G1}, so $\mathcal{T}_1 < 0.5$. We then increase slightly V_{G2}: the transmitted current is constant, because then we have $\mathcal{T}_1 = \mathcal{T}_2 = 0.5$. On figure 5.7 (left), for fixed gate voltages of $G2$, the voltage applied to $G1$ is slowly sweeped, to see if there are electronic interferences. Indeed, oscillations of the transmitted signal hint at electronic interferences, with maximum amplitude when $G2$ is tuned exactly to $\mathcal{T}_2 = 0.5$.

The interferences revealed with the side gate and shown on Fig. 5.7 (right) have a 34 % visibility at 12 mK. This is for a low density sample which was meant for the study of coherence in the fractional quantum Hall regime [9] with arm length $L = 11.3$ μm. The visibility of the interferences in the differential transmission is given by:

$$\mathcal{V} = \frac{\mathrm{Max} - \mathrm{Min}}{\mathrm{Max} + \mathrm{Min}} \tag{5.6}$$

where Max and Min are the maximum and minimum values of the differential transmission as a function of Φ_{AB}.

The MZI samples are designed so that the upper and lower arms have the same length, however in some samples, we observe a small dependence of the phase of the interferences with the bias voltage which hints at a small asymmetry which would lead to *thermal smearing*. Here we explain what thermal smearing is and how this trivial effect can cause temperature dependence of the visibility. This effect must be systematically checked so as not to confuse it with other interesting effects like decoherence or environment dephasing.

[9] During my thesis, I tried several times to observe quantum interferences in the FQHE regime at $\nu = 1/3$. We never succeed and, to our knowledge, the Weizmann group which tried this experiment also failed. It is as though a phase shift accompanying trapping or detrapping of quasi-particle in the MZI blurred the phase of interferences (exchange between A. Stern and P. Roche)

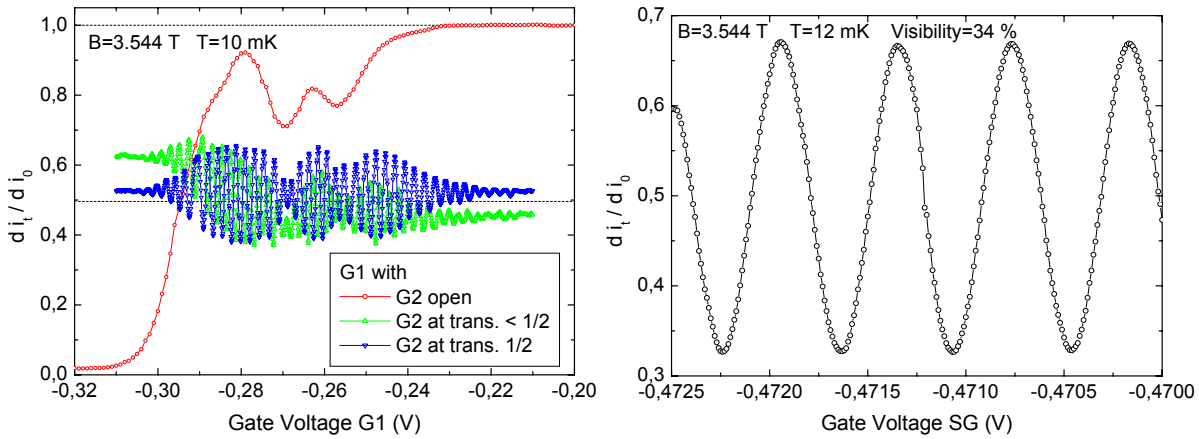

Figure 5.7.: *(left) The IES is reflected at all QPCs. (red curve) With* $\mathcal{T}_2 = 1$*, the transmission through the MZI goes from* 1 *to* 0 *when* $G1$ *is closed. (green curve)* $\mathcal{T}_2 < 0.5$*,* $\langle \mathrm{d}i_t/\mathrm{d}i_0 \rangle_{osc}$ *decreases as* $\mathcal{T}_1$ *increases. Interferences are seen in the oscillations of* $\mathrm{d}i_t/\mathrm{d}i_0$ *around its mean value. (blue curve)* $\langle \mathrm{d}i_t/\mathrm{d}i_0 \rangle_{osc}$ *is constant, meaning that* $\mathcal{T}_2 = 0.5$*. The oscillations of* $\mathrm{d}i_t/\mathrm{d}i_0$ *have a maximum amplitude directly reflecting the amplitude of the interferences revealed with the side gate. (right) Electronic interferences with a* 34 *% visibility, revealed when sweeping the side gate voltage.*

5.4.2. Thermal smearing

Non interacting model

Chung *et al.* [79] have studied the effect of a bias voltage V_1 on the visibility, treating the non interacting case. Their theory explains the impact of a finite temperature on the visibility in the case where there is a length difference ΔL between the two arms.

First let us derive how the phase should vary with the energy when there is a length difference. Lets consider s which measures directly the path length, i.e. $(x(s), y(s))$ (coordinates of the electron), and the local coordinate $s_\perp$, perpendicular to the equipotential line. In these coordinates, an ES which follows the equipotential line a small energy ε away from E_F acquires an additional phase $\delta\varphi = \int \Delta s_\perp / l_m^2 \, \mathrm{d}s$, where $l_m^2 = \hbar/eB$ and $e\,(\mathrm{d}U/\mathrm{d}s_\perp)\,\Delta s_\perp = \varepsilon$. Moreover, we know that the potential gradient $\mathrm{d}U/\mathrm{d}s_\perp$ is related to the local electric field by $F(s) = -\mathrm{d}U/\mathrm{d}s_\perp$. From this relation we can define the drift velocity of the guiding center of the cyclotron orbit at point s of the edge state $v_d(s) = F(s)/B$. Thus a small increase in energy leads to a phase increment $\delta\varphi = (e/\hbar v_d) \int F(s)\, \Delta s_\perp \, \mathrm{d}s$,

which gives finally $\delta\varphi = \varepsilon\Delta L/\hbar v_d$, where I have introduced ΔL, the length difference between the upper and down arm of the MZI. The spectral current density a small energy ε away from the Fermi energy is then:

$$j(\varepsilon) = \frac{e}{h}\ (f(\varepsilon) - f_0(\varepsilon)) \left(\mathcal{T}_1\mathcal{T}_2 + \mathcal{R}_1\mathcal{R}_2 + 2\sqrt{\mathcal{T}_1\mathcal{T}_2\mathcal{R}_1\mathcal{R}_2}\ \cos\left(\frac{\varepsilon}{E_c} + \varphi_F\right)\right) \tag{5.7}$$

with φ_F the Ahoronov Bohm (AB) phase through the area defined by the position of the ES at the Fermi energy, $f_0(\varepsilon) = (1 + \exp(\varepsilon/k_BT))^{-1}$ the Fermi distribution function of the grounded terminal, $f(\varepsilon) = f_0(\varepsilon - eV_1)$ the distribution function of the terminal injecting the current and $E_c = \hbar v_d/\Delta L$. The current is given by $I = \int j(\varepsilon)\ \mathrm{d}\varepsilon$.

Experimentally, we measure the differential conductance, which within this theory is related to the temperature T and the bias voltage V_1 in the following way:

$$G(eV_1) = \frac{e^2}{h}\ \left(\mathcal{T}_1\mathcal{T}_2 + \mathcal{R}_1\mathcal{R}_2 + 2\sqrt{\mathcal{T}_1\mathcal{T}_2\mathcal{R}_1\mathcal{R}_2}\ \frac{\pi k_BT/E_c}{\sinh(\pi k_BT/E_c)}\ \cos\left(\frac{eV_1}{E_C} + \varphi_F\right)\right) \tag{5.8}$$

Visibility In the non interacting approach, the visibility does not depend on the voltage. However this model gives a temperature dependence via the sinh, which leads to an exponential dependence of the visibility with the temperature (also called thermal smearing) when $k_BT \gtrsim E_c$. Lets give an idea of why the finite temperature scrambles the phase: the phase increment $\delta\varphi = \varepsilon\Delta L/\hbar v_d$ when there is a length difference $\Delta L = L_U - L_D$ between two arms of the MZI, v_d being the drift velocity. Since we work at finite temperature, the energy is averaged over a typical energy range of k_BT, which leads to an average of the phase of the order of $k_BT \times \Delta L/\hbar v_d$. To be more precise, Eq. (5.8) leads to a visibility:

$$\mathcal{V} = \mathcal{V}_0\ \frac{T/T_T}{\sinh(T/T_T)} \tag{5.9}$$

where we have introduced $k_BT_T = \hbar v_d/\pi\Delta L$ and $\mathcal{V}_0$ the visibility at zero temperature. This formula gives a quasi exponential dependence of the visibility with the temperature when $T \gtrsim T_T$.

Phase rigidity breaking Additionally, through Eq. (5.8), we see that in this model the phase of the interferences is not rigid when $\Delta L \neq 0$. The asymmetry of the MZI induces an energy dependence of the phase and is also responsible for thermal smearing T_T^{-1}:

$$\left(\frac{\partial\varphi}{\partial\varepsilon}\right) = \frac{\Delta L}{\hbar v_d} \quad \text{and} \quad T_T^{-1} = \frac{\pi k_B\Delta L}{\hbar v_d} \tag{5.10}$$

As already said, our MZI samples are specifically designed to have an upper and lower arm with equal length so as to minimize thermal smearing. This is not possible in FPI samples where interferences occurs *by construction* between paths of different lengths (see Fig. 4.2). This is the reason why FPI are more sensitive to thermal smearing than MZI [61].

Discussion

Can thermal smearing account for the exponential decay of the visibility with the temperature which was reported in chapter 4? Roulleau *et al.* carefully checked the effect of thermal smearing and found that it could not explain their experimental observations [2]. Indeed if it were, the corresponding temperature scale would be $T_T = 14$ mK for the large sample ($L = 11.3$ μm). This temperature scale would lead to a bias dependence of the phase $\partial\varphi/\partial V_1 \approx 0.26$ rad.μV^{-1} which makes $\approx 1.3\pi$ over 16 μV, while the data show a rigid phase over this scale.

In the sample that we study in chapter 7 however, we observe a slight dependence of the interferences phase with the bias. From this dependence we extract the value $T_T = 60 \pm 20$ mK whereas the temperature dependence scale is measured to be $T_\varphi = 9 \pm 0.4$ mK, for a temperature ranging from 20 to 50 mK and a large sample $L = 11.3$ μm: this time we are not even in the limit were the sinh of the thermal smearing can be approximated by a decaying exponential, and the temperature scales are not of the same order.

6. Visibility at finite energy

Contents

6.1. Introduction

We are now interested in the energy dependence of the electronic Mach-Zehnder interferences. To do that, we simply apply a dc voltage V_1 on the ohmic contact where the interfering electrons are injected (contact n°1) as represented on the schematic Fig. 6.1.

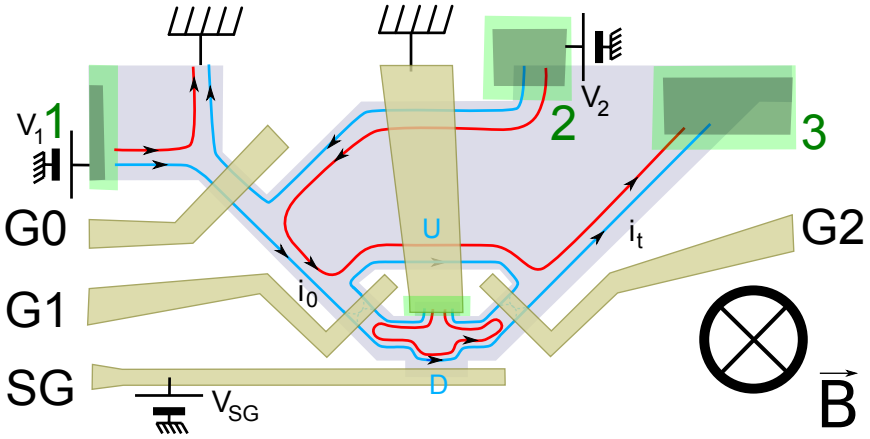

Figure 6.1.: *Schematic of the Mach-Zehnder interferometer at $\nu = 2$. The injecting QPC, G0 is set as to fully reflect the IES. The interfering electrons are injected at contact n°1 with the energy $E_F + eV_1$, where V_1 is the dc voltage applied to contact n°1. Interferences are revealed by sweeping the gate voltage V_{SG} applied to the side gate SG or by using the IES in the upper arm like a gate polarized with the dc voltage V_2 applied to contact n°2. The latter method gives access to the coupling between the IES and the OES in the upper arm (¶ 4.3.3).*

We apply voltages up to 50 μV. We do a differential measurement with a standard lock-in technique: we modulate the current of incoming electrons which have the energy eV_1 above the Fermi energy at equilibrium, with a frequency f_1, and look at the transmitted current modulated at the same frequency. In a sense we do monochromatic interferences: although we inject electrons with energy from E_F up to $E_F + eV_1$, we only look at electrons with energy $E_F + eV_1$.

If we were to do this with laser photons, we would obtain a flat visibility. With electrons in a condensed matter system, this is different. Indeed, electrons are charged and interact with their environment much more than photons (bulk, other electrons, external potential fluctuations....). However, until now the independent electrons picture was enough to describe the general transport properties of the IQHE regime: up to the gap energy ($\hbar\omega_c \sim$ 50 meV for $B \sim 3$ T), the visibility was not expected to depend of the bias voltage.

This is not what is observed experimentally: as we detailed in chapter 4, the visibility as function of the bias voltage decays and oscillates showing phase rigidity between extinctions with π phase jumps between two subsequent 'lobes'. Once this lobe behaviour and its associated energy scales were discovered, soon arised the question of their dependence on the various physical parameters of the experiment.

Several groups [4, 42] did a systematic study of the lobe pattern as function of the magnetic field around $\nu = 2$ and found that the lobes shape depends strongly on the magnetic field (Fig. 6.2): Neder *et al.* [4] found that at $\nu = 2$, the multiple side lobes structure broadens into a single one as the magnetic field increases, suggesting that both energy scales, the one describing the gaussian behaviour, V_{10}, and the one associated with the multiple side lobes, V_c, are affected by the magnetic field.

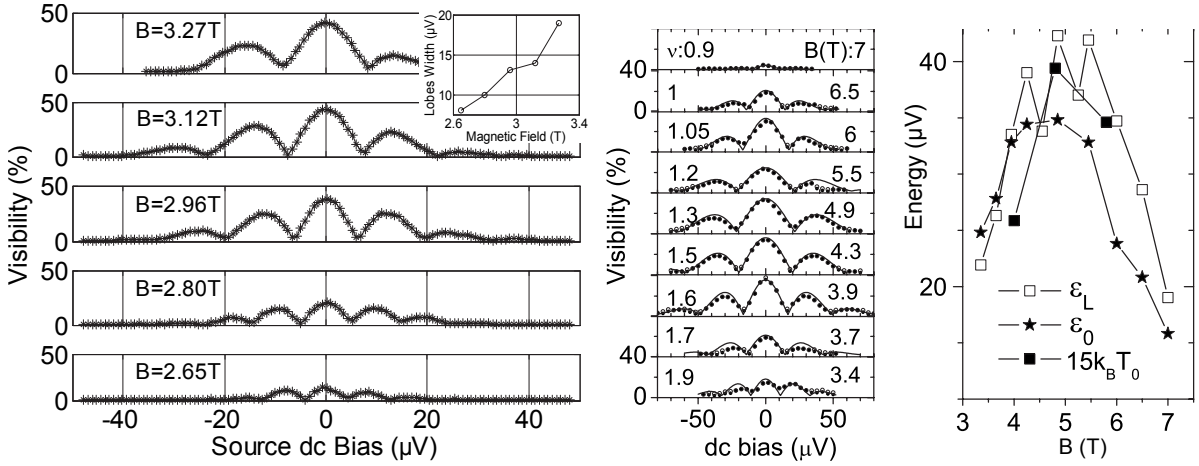

Figure 6.2.: *Lobe pattern as function of the magnetic field measured by two different groups: (left) Weizmann's Institute [4]: the multiple side lobes structure is present at the lowest magnetic field. Its energy scale and the maximum visibility increase as the magnetic field increases. Then the multiple side lobe structure turns into a single side lobe structure. (middle) Regensburg's University [42]. At low magnetic field, a multiple side lobe structure is found which broadens as the magnetic field increases and seems to morph into a single side lobe structure. The strange thing is that the maximum visibility is achieved at $\nu = 1.5$ and that the interferences become visible at the end of the $\nu = 2$ plateau. The determination of the filling factor might be wronged by some asymmetry between the electronic density of the MZI arms. (right) Regensburg's group [42]. Energy scales describing the beating of the visibility (ϵ_L) and the gaussian dependence (ϵ_0) of the lobe pattern as function of the magnetic field. The energy scale of the temperature dependence ($k_B T_0$) is also reported. All energy scales evolve proportionnally to each other.*

Litvin *et al.* [42] also found a strong dependence of the lobes on the magnetic field, but strangely enough they found a maximum visibility at $\nu = 1.5$. Heterogeneities in the 2DEG might explain this result. Additionally, both energy scales describing the gaussian behaviour and the beating evolve along the same trend as function of the magnetic field.

We did not make an extended study of the lobe dependence on the magnetic field, however our few points seem to agree with the results of the Weizmann's: multiple side lobes are obtained at the beginning of the $\nu = 2$ plateau, and single side lobes at the end.

It seems then that the magnetic field influence both energy scales V_{10} and V_c. Do they proceed from the same physical origin? When one changes the magnetic field, one changes at the same time the electronic interactions, the electron trajectory because of disorder, the distance between ESs (hence the coupling between them)... It is difficult to point out one cause in particular. Later (chapter 7), we will present some results showing that we can act on the multiple side lobe structure whitout affecting the gaussian dependence.

For now, we will focus on yet another physical parameter which has an influence over the shape of the visibility as function of the bias voltage: the dilution strength $\mathcal{T}_0$.

6.2. Influence of the dilution $\mathcal{T}_0$

6.2.1. Main effects

Another parameter which influences strongly the shape of the lobe pattern is the transmission $\mathcal{T}_0$ of the OES through the injecting QPC, $G0$.

We represented on Fig. 6.3 two lobe structures for two different values of $\mathcal{T}_0$: the black curve corresponds to $\mathcal{T}_0 \sim 1$, whereas the red curve corresponds to $\mathcal{T}_0 \sim 0.1$. The first zero in the visiblity as function of V_1 seems to go from ~ 7 μV for $\mathcal{T}_0 \sim 1$ to ~ 25 μV for $\mathcal{T}_0 \sim 0.1$. Additionally, we have a multiple side lobes structure for $\mathcal{T}_0 \sim 1$ which seems to transform into a single side lobe structure when $\mathcal{T}_0 \sim 0.1$. The gaussian behaviour seems to be affected by the dilution. We see the effect on the gaussian behaviour in the broadening of the central lobe which is mainly parametrized by V_{10} (the dependence of the fit with V_c/V_{10} is studied in appendix B).

What is the precise form of this dependence? What about its physical origin? A possible origin is the energy redistribution of the electrons as they propagate: electrons inside the

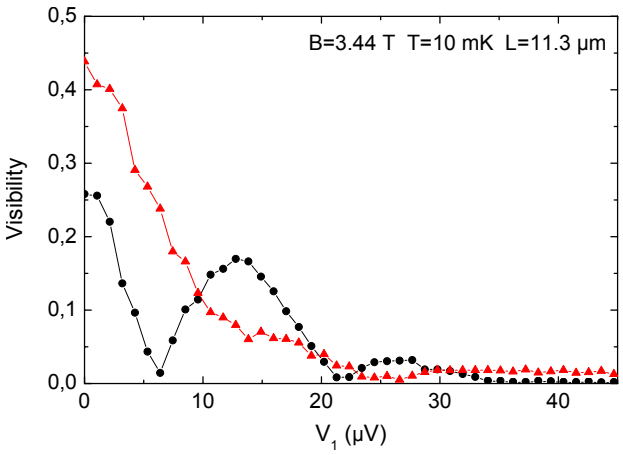

Figure 6.3: *Visibility as function of the bias voltage V_1 for two different dilutions of the incoming current in the OES. $\mathcal{T}_0 \sim 1$ (black curve), $\mathcal{T}_0 \sim 0.1$ (red curve). The multiple side lobes structure seems to transform into a single side lobe structure and the shape of the visibility as function of V_1 is strongly affected by $\mathcal{T}_0$: the width of the central lobe goes from $\sim 7\ \mu V$ when $\mathcal{T}_0 \sim 1$ to $\sim 25\ \mu V$ for $\mathcal{T}_0 \sim 0.1$.*

MZI are in an out-of-equilibrium energy distribution at finite bias V_1 thanks to $G1$ and to $G0$. Is it possible that they redistribute to reach equilibrium, thus affecting the visibility? This redistribution (and the shape of the visibility versus the energy) should depend on the available phase space, and in particular on the shape of the out of equilibrium distribution which is set by V_1, V_2, $\mathcal{T}_1$ and $\mathcal{T}_0$. This is the reason why, in section 6.3, we will fix $\mathcal{T}_0$ and study the dependence of the visibility on V_1, and in particular the evolution of the width of the central lobe as function of $\mathcal{T}_0$, as well as on V_2 (which was set to 0 until now).

In the next section, we study the multiple side lobe structure as function of $\mathcal{T}_0$ which has been predicted to undergo a quantum transition to a single side lobe structure induced by partition noise in the OES at $\mathcal{T}_0 = 0.5$ [16].

6.2.2. A quantum phase transition?

The model and a prediction

A model developped by Levkiviskyi *et al.* [6] works out at $\nu = 2$. It explains the oscillations in the visibility as function of the voltage bias and the phase rigidity (Fig. 6.4) by the beating of two modes arising from the coupling of two copropagating edge states. These two collective modes are a symmetric fast charge mode and a antisymmetric slow dipolar mode. The authors also reproduce the T^{-1} dependence of the coherence length (¶ 4.3.4).

However, the decay of the envelop is not reproduced, the model is derived in the weak tunneling $\mathcal{T}_1 \to 1$ and weak backscattering $\mathcal{T}_1 \to 0$ limits while the experiments are done at $\mathcal{T}_1 = 0.5$. Moreover, it does not explain the results for $\nu = 1$.

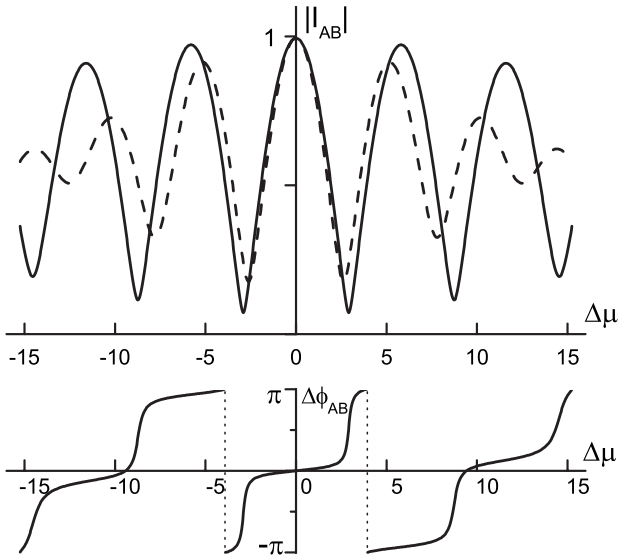

Figure 6.4: *Visibility and phase shift as function of the bias computed by Levkiviskyi* et al *[6]. The multiple extinctions are reproduced along with the phase rigidity between them. The π phase jumps are recovered. However, the decay of the oscillations with the bias voltage is non existent unless $\Delta L \neq 0$.*

Nevertheless, using this model, the authors predicted a quantum phase transition from a multiple to a single side lobe structure induced by non gaussian noise partition noise generated by $G0$ [16] (Fig. 6.5 (left)). They predict a continuous increase of the dephasing as $\mathcal{T}_0$ decreases from 1 to 0.5 with a rigidity of the zeros position with respect to the voltage bias. At $\mathcal{T}_0 = 0.5$, the multiple side lobe structure transforms into a single side lobe structure, and for $\mathcal{T}_0 < 0.5$, the single zero evolves as $(\mathcal{T}_0\,(1-\mathcal{T}_0))^{-1}$.

Results

For $V_2 = 0$, we measured the visibility as function of V_1 for different values of $\mathcal{T}_0$ ranging from 0 to 1. We didn't impose the value of $\mathcal{T}_0$ but rather the gate voltage V_{G0}, and we plotted the data as function of the transmission $\mathcal{T}_0$ at zero bias because $\mathcal{T}_0$ varies with the bias. The dependence of $\mathcal{T}_0$ with V_1 might be responsible for smearing the final picture (Fig. 6.5 (right)). The figure we obtain resembles the prediction of Levkiviskyi [16] (Fig. 6.5 (left)).

However, the occurence of the transition at precisely $\mathcal{T}_0 = 0.5$ as well as the dependence of the lobe size as function of $\mathcal{T}_0$ requires a more quantitative treatment. Moreover, the lobe structures are not symmetric with respect to V_1: there is two additional lobes on the positive side whereas there is only one side lobe on the negative side (not represented on Fig. 6.5 (right)).

For all these reasons we chose to look at the position of zeros of the visibility with respect

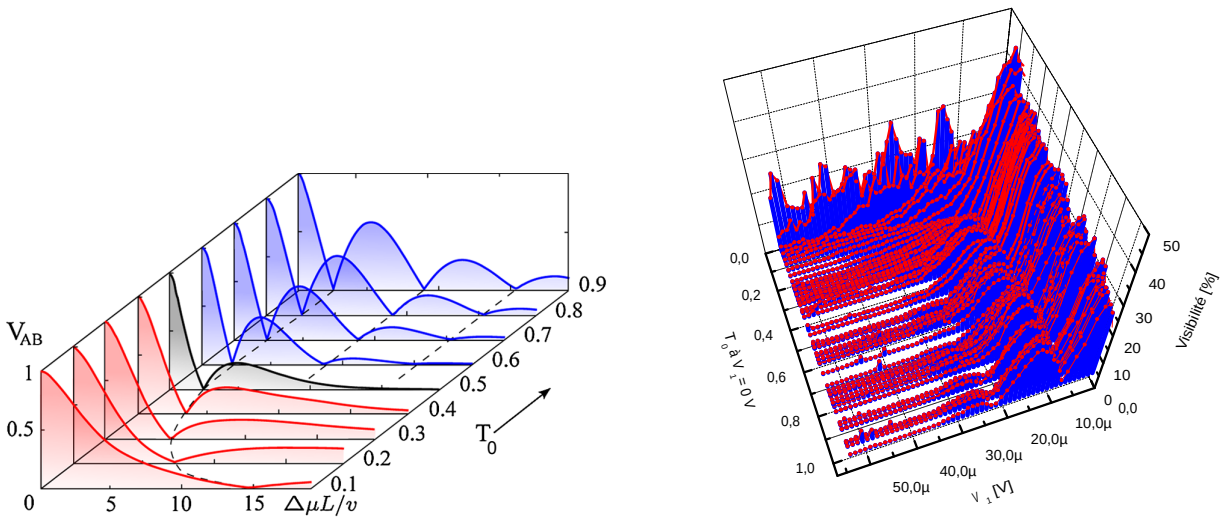

Figure 6.5.: *(left) Prediction on a quantum phase transition induced by non gaussian noise at* $\mathcal{T}_0 = 0.5$ *from a multiple side lobe structure to a single side lobe structure [16]. (right) 3D plot of the visibility as function of the bias voltage* V_1 *for various values of the transmission* $\mathcal{T}_0$ *at zero bias. The final picture resembles the prediction of Lekvkiviskyi* et al. .

to the bias voltage V_1, as function of the transmission $\mathcal{T}_0$. This raised an important question concerning the value of the transmission one must consider. Indeed, since it appears that the transmission $\mathcal{T}_0$ depends on the bias voltage V_1 [1], must we plot the zeros of the visibility as function of the zero bias visibility or as function of the finite bias transmission (or even an intermediate value)? To be fair, we plotted both on Fig. 6.6.

Starting from $\mathcal{T}_0 = 1$ and decreasing $\mathcal{T}_0$, we get a multiple side lobes structure whose zeros have a seemingly fixed position with respect to the bias voltage V_1 as long as $\mathcal{T}_0 \geq 0.5$ if we consider the data as function of the finite bias transmission $\mathcal{T}_0$. The second and third zeros seem to vanish for smaller values of $\mathcal{T}_0$. An alternative interpretation could be that we didn't 'make the measurement': because of the dependence of $\mathcal{T}_0$ with the bias voltage, we didn't reach values of $\mathcal{T}_0$ below 0.5 for bias voltages around $20 - 40$ μV where second and third zeros are found.

However, below a given value of $\mathcal{T}_0 \leq 0.5$, the multiple side lobe structure gives birth to a single side lobe structure whose central lobe increases in width as $\mathcal{T}_0 \to 0$. The size of the central lobe actually diverges in a way compatible with Levkiviskyi's prediction (a $[\mathcal{T}_0(1-\mathcal{T}_0)]^{-1}$ behaviour) as well as a $\mathcal{T}_0^{-1/2}$ dependence, as can be seen on Fig. 6.6.

[1] I discuss the non-linearities of $\mathcal{T}_0$ as function of the energy later in ¶ 6.3.3.

Levkiviskyi *et al*'s prediction is interesting as it gives the underlying mechanism for the visibility decrease which was not considered in the first paper of Levkiviskyi [6]. Partition noise from $G0$ in the OES seems responsible for the visibility decay in [16]. However this decay is not gaussian, and does not explain the gaussian decay observed when $G0$ transmits the OES perfectly or when there is only one edge state ($\nu = 1$).

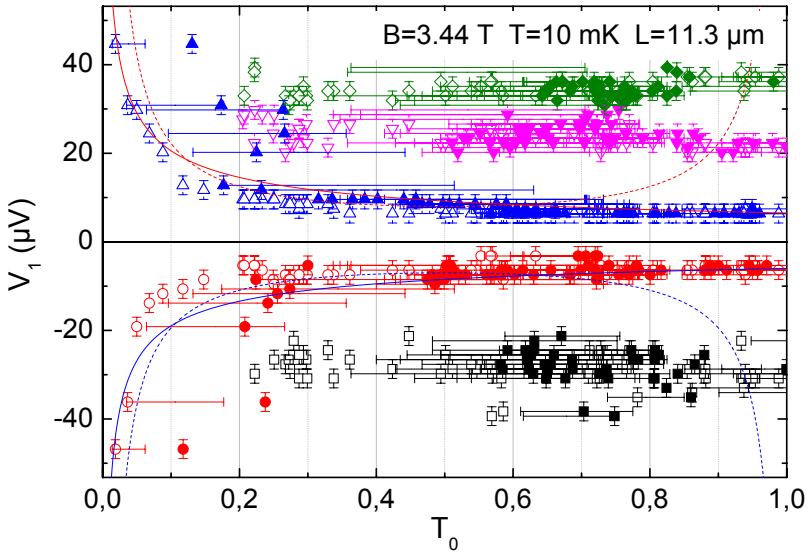

Figure 6.6.: *Zeros positions with respect to the bias voltage V_1 both as function of the transmission $\mathcal{T}_0$ at zero bias (open symbols) and at the bias voltage V_1 (full symbols). The error bar with respect to $\mathcal{T}_0$ is due to its dependence with the bias voltage V_1 and is centered on its mean value. As function of the transmission at finite bias (full symbols), second and third zeros are visible for $\mathcal{T}_0 \geq 0.5$ and the position of the zeros seems fixed. Their non-observation for $\mathcal{T}_0 < 0.5$ might also be explained by the fact that we didn't reach these transmissions at finite bias. For smaller values of $\mathcal{T}_0$, if one considers that the zero bias conductance is the good parameter, the size of the central lobe increases as $[\mathcal{T}_0(1-\mathcal{T}_0)]^{-1}$ below $\mathcal{T}_0 = 0.5$ (dashed lines). It is also compatible with a $\mathcal{T}_0^{-1/2}$ dependence (solid lines).*

Comparison with Levkiviskyi's prediction

We find that if we consider the transmission at finite bias voltage, the results are quantitatively compatible whith the prediction of Levkiviskyi *et al.* on the following points: first, the rigidity of the zeros visibility, from $\mathcal{T}_0 = 1$ down to $\mathcal{T}_0 \sim 0.5$. Second, at $\mathcal{T}_0 = 0.5$, the multiple side lobes disappear to give rise to a single side lobe structure. Finally, for $\mathcal{T}_0 \leq 0.5$ the width of the central lobe increases as $[\mathcal{T}_0(1-\mathcal{T}_0)]^{-1}$.

6.2.3. Gaussian enveloppe

Injecting an out of equilibrium distribution

When diluting the incoming current from the OES by pinching $G0$ to partial transmission $\mathcal{T}_0 < 1$, we create a two-step out of equilibrium energy distribution in the OES, at the output of the QPC $G0$ as represented on Fig. 6.7. The two-step distribution results from the mixing by $G0$ of the electrons of the OES coming from ohmic contacts n°1 and n°2. Its shape is parametrized by the bias voltage applied on ohmic contact n°1, V_1, the bias voltage applied on ohmic contact n°2, V_2, and the transmission of QPC $G0$, $\mathcal{T}_0$.

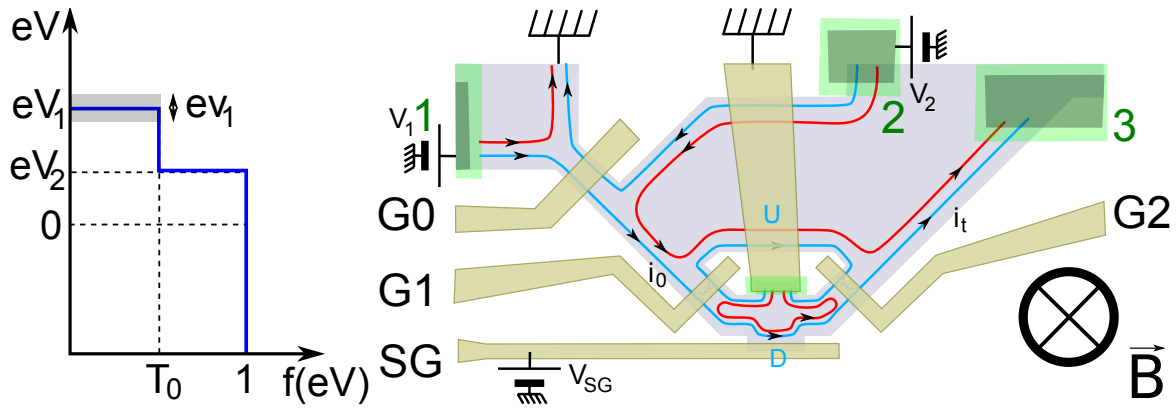

Figure 6.7.: *(left) Energy distribution in the injected OES (blue) at $G0$ output. The energy distribution for the OES is an out of equilibrium double step distribution created by QPC $G0$ set to transmission $\mathcal{T}_0 < 1$ for the OES. V_1 is the bias voltage applied on contact n°1 and V_2 is the bias voltage applied on contact n°2. (right) Schematic of the Mach-Zehnder interferometer.*

In the previous section, V_2 was set to zero and we were looking at shape of the visibility as function of V_1 (we saw multiple side lobes and single side lobe structures) for various values of $\mathcal{T}_0$. Here we will be interested in the gaussian shape of the visibility (e.g. the first zero of the visibility) as function of $\mathcal{T}_0$. It is also possible to study the shape of the visibility with respect to V_2 (with V_1 set to zero), that we have also found to be gaussian. In the next section (§ 6.3) we will see what happens when *both* V_1 and V_2 have finite values.

To what end do we study the dependence of the visibility with the shape of the injected energy distribution? Works from another group (LPN's group at Marcousis) showed that in the QHE regime at $\nu = 2$, when put out of equilibrium, the OES relaxes by exchanging energy with the adjacent IES on a typical lengthscale of 10 μm. This energy relaxation

was considered as a possible explanation to the peculiar dephasing in the Mach-Zehnder interferometer. Hence came the idea of injecting electrons in an out of equilibrium energy distribution in the MZI and see if there was any effect on the visibility.

Next we study the visibility as function of V_1 with $V_2 = 0$, and as function of V_2 while $V_1 = 0$. It is important to remark that we inject an out of equilibrium distribution and measure the visibility for quasi particles close to the $E_F + eV_1$. A visibility dependence on $V_1(V_2)$ *cannot* be obtained when considering non interacting quasiparticles: such an observation would be a direct manifestation of interaction effects in the IQHE regime.

As function of V_1

For now V_2 is set to zero, and we study the visibility as function of V_1 for different values of $\mathcal{T}_0$ from 0 to 1. The visibility shows a single side lobe pattern. The gaussian parameter V_{10} is then extracted as function of $\mathcal{T}_0$.

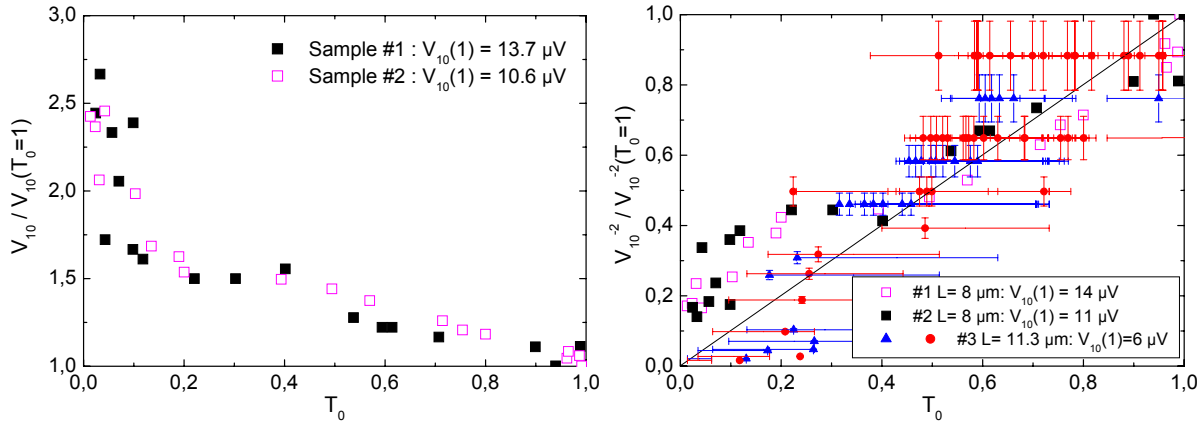

Figure 6.8.: *(left) V_{10} renormalized by its value at $\mathcal{T}_0 = 1$ as function of $\mathcal{T}_0$ [40], follows the same variations for two samples. (right) Same data plotted as $1/V_{10}^2$ as function of $\mathcal{T}_0$: $1/V_{10}^2$ seems proportional to $\mathcal{T}_0$. Data from the 'dilution experiment' (¶ 6.2.2) (blue and red points) show the same behaviour, with large error bars with respect to $1/V_{10}^2$, widening as V_{10} decreases, and also large error bars with respect to $\mathcal{T}_0$ because of its dependence with the bias.*

The measurement has actually already been done by my predecessor P. Roulleau on two samples with the same size (arm length of $L = 8$ μm) at the same magnetic field of 5.2 T, the results were reported in [40] and are reproduced on Fig. 6.8 (left). At the time, the dependence of V_{10} with $\mathcal{T}_0$ was not clear. We could only say that V_{10} is decreasing when $\mathcal{T}_0$

increases and diverges when $\mathcal{T}_0 \to 0$. We now plot the same data in a different way: $1/V_{10}^2$ is represented on Fig. 6.8 (right) as function of $\mathcal{T}_0$. We see clearly that $1/V_{10}^2$ dependence on $\mathcal{T}_0$ can be considered linear:

$$\left(\frac{V_{10}(1)}{V_{10}(\mathcal{T}_0)}\right)^2 = \mathcal{T}_0 \tag{6.1}$$

This yields $V_{10}(1) \approx 14$ μV and $V_{10}(1) \approx 11$ μV. We also reported on Fig. 6.8 (right) the above results ($L = 11.3$ μm, $B = 3.44$ T) for the negative and the positive first zeros, for the multiple side lobe structure. Albeit large error bars with respect to the y-axis widening when $1/V_{10}^2$ increases, and also with respect to the x-axis because of the bias dependence of $\mathcal{T}_0$, the data follow the same law. The typical energy scales are now 6 and 6.5 μV. We see that the gaussian parameter $V_{10}\,(\mathcal{T}_0 = 1)$ increases when L decreases in agreement with Yamauchi *et al.* [71].

As function of V_2

Now V_1 is set to zero, and we study the visibility as function of V_2 for different values of $\mathcal{T}_0$. The logarithm of the visibility shows a parabolic dependence in V_2 with a coefficient which depends on $\mathcal{T}_0$ (see Fig. 6.9 (left)). The parabolic curves are a direct manifestation of the gaussian shape of the visibility with respect to V_2. Coefficients $1/(2V_{20}^2)$ [2] are reported on Fig. 6.9 (right). Their dependence on $\mathcal{T}_0$ seems also linear,

$$\left(\frac{V_{20}(\mathcal{T}_0 \to 0)}{V_{20}(\mathcal{T}_0)}\right)^2 = 1 - \mathcal{T}_0 \tag{6.2}$$

except for $\mathcal{T}_0 = 0$. Indeed when we extrapolate the $1 - \mathcal{T}_0$ dependence to $\mathcal{T}_0 = 0$, we should get the greatest $1/V_{20}^2$, however we find that $1/V_{20}^2 \to 0$ when $\mathcal{T}_0 \to 0$.

We tested two samples of different sizes. Sample #1 had an arm length of $L = 11.3$ μm and was tested at 4.29 T. Sample #2 had an arm length of $L = 8$ μm, had a lower electron density and the magnetic field was 3.74 T. The crossover between the $1 - \mathcal{T}_0$ dependence and the point at $\mathcal{T}_0 = 0$ occurs for different values of $\mathcal{T}_0$ on the two samples we tested ($\mathcal{T}_0 \sim 0.1$ for sample #1 and $\mathcal{T}_0 \sim 0.3$ for sample #2). The two different samples yielded $V_{20}(\mathcal{T}_0 \to 0) \approx 9$ μV for sample #1, and $V_{20}(\mathcal{T}_0 \to 0) \approx 12$ μV for sample #2. As for V_{10}, we see that the gaussian parameter $V_{20}\,(\mathcal{T}_0 \to 0)$ increases when L decreases in agreement

[2] Coefficients $1/(2V_{20}^2)$ are extracted directly from the fits, this is why the error bars with respect to the y-axis are smaller than on Fig. 6.8 (right).

with Yamauchi *et al.* [71]. Additionally, the values found for $V_{20}\,(\mathcal{T}_0 \to 0)$ are of the same order as the ones found for $V_{10}\,(\mathcal{T}_0 = 1)$.

Here, once more the result is surprising. Thinking about energy relaxation inside the wire, this would lead to a reduction of the visibility as function of $\mathcal{T}_0(1-\mathcal{T}_0)$. At least this is something we would obtain in case of a kernel of interaction independent of the energy. Surprisingly, our findings seems to indicate that the decoherence is proportional to $1-\mathcal{T}_0$ while in the previous one (injecting through V_1) it was proportional to $\mathcal{T}_0$.

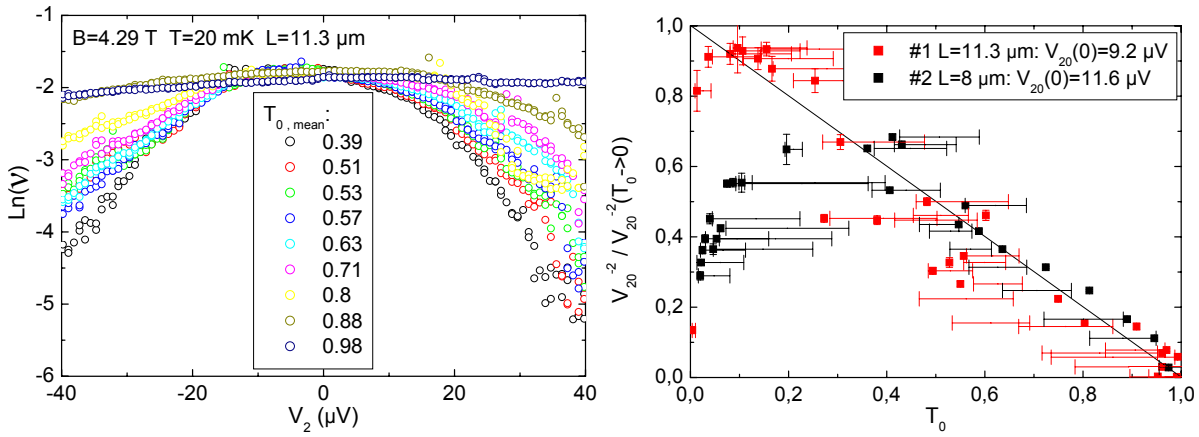

Figure 6.9.: *(left) Logarithm of the visibility is parabolic in the bias voltage V_2 showing the gaussian shape of the visibility. As $\mathcal{T}_0$ increases, the curvature of the parabola decreases until the curve is almost flat. (right) The parabola coefficient $1/V_{20}^2$ renormalized by its extrapolated value when $\mathcal{T}_0 \to 0$ as function of $\mathcal{T}_0$ at zero bias ($V_2 = 0$), for two different samples. The error bars relative to $\mathcal{T}_0$ (coming from the dependence of $\mathcal{T}_0$ with V_2) are centered on the mean value of $\mathcal{T}_0$ which differs from the value of $\mathcal{T}_0$ at zero bias. Red points: $V_{20}(\mathcal{T}_0 \to 0) \sim 9\ \mu V$. Black points: $V_{20}(\mathcal{T}_0 \to 0) \sim 12\ \mu V$. For $\mathcal{T}_0$ above a certain value which depends on the sample, there is a linear dependence of $1/V_{20}^2$ with $\mathcal{T}_0$.*

6.2.4. Questions

On V_{20} dependence on $\mathcal{T}_0$, how do we explain the deviation from the $1-\mathcal{T}_0$ behaviour at $\mathcal{T}_0 = 0$? Why does the crossover occurs at different $\mathcal{T}_0$ for the two samples? Since $V_{10}(\mathcal{T}_0 = 1)$ and $V_{20}(\mathcal{T}_0 \to 0)$ are of the same order, if we assume that they are equal and

putting aside the $\mathcal{T}_0 = 0$ point, the transmitted current can be written as:

$$I \propto (\mathcal{T}_0 V_1 + (1-\mathcal{T}_0)\, V_2) \left\{1 + \ \exp\left[-\left(\mathcal{T}_0 {V_1}^2 + (1-\mathcal{T}_0)\, {V_2}^2\right)/V_0^2\right] \ \cos\left(\langle\Phi\rangle\right)\right\} \qquad (6.3)$$

There is then only two free parameters in the fit: V_0 and $\mathcal{T}_0$ at zero bias and $\mathcal{T}_0$ in the first term which depends on $|V_1 - V_2|$ (this will be discussed later).

Dephasing coming from V_1 and V_2 is gaussian and their contributions seems proportional to the amount of current coming from each and transmitted by G_0, as if the mecanism which provokes this gaussian dephasing were occuring *before* G_0.

In the previous experiment, I have shown that measuring interferences at energy eV_1 while keeping $V_2 = 0$ and measuring interferences at zero energy while applying $V_2 \neq 0$ leads to a visibility decrease as a function of V_1 and V_2. In the two cases cited above, the out of equilibrium distribution in one arm of the interferometer is a single step function. Now if V_1 and V_2 are not equal to zero, nor to the same values, one obtains a double step function. Once more, if the energy relaxation in the wires is responsible for the finite bias visibility decrease, it should be sensitive to the distribution in the wire. This is what we will study in the next section.

6.3. Two-step distribution

6.3.1. Two faces of the same coin

The lobe eraser

We then inject this two-step energy distribution created at $G0$, with $\mathcal{T}_0 \sim 0.5$ into the interferometer. We find a strange behaviour (Fig. 6.10 (left)): when $V_2 = 0$, the visibility as function of V_1 show the usual single side lobe structure. When $V_2 = \pm 20\ \mu$V, one side lobe is 'erased', the positive one for $V_2 < 0$, the negative one for $V_2 > 0$. Finally the conductance seems to follow the same symmetry as the visibility (Fig. 6.10 (right)): is it enough to explain this 'lobe eraser' [3] behaviour?

To have a more complete picture, in the following section we measure the visibility as function of V_1 for more values of V_2.

[3] This behaviour was reported in P. Roulleau PhD thesis manuscript [3].

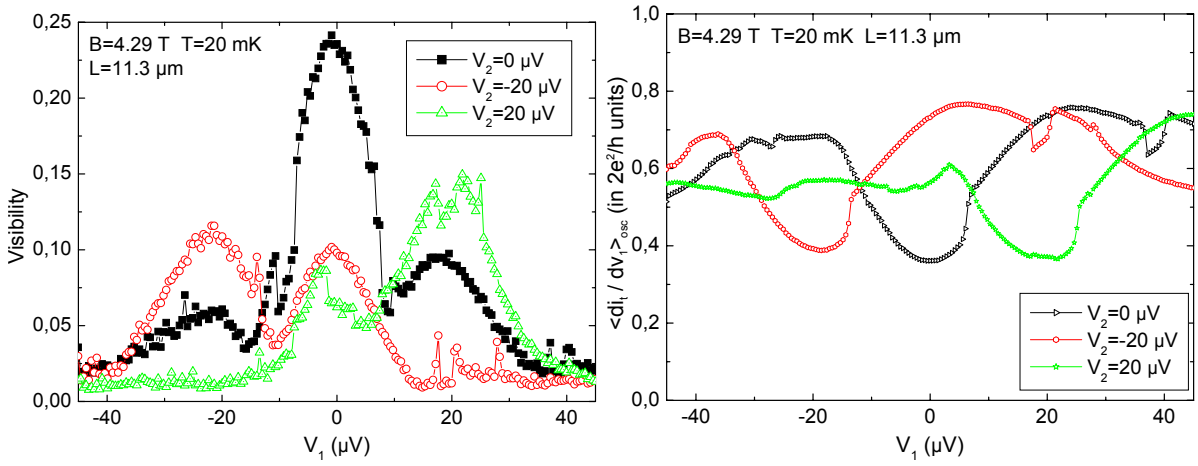

Figure 6.10.: *(left) Visibility as function of the bias voltage V_1 for $\mathcal{T}_0 \sim 0.5$, $V_2 = -20$ μV (red circles), $V_2 = 0$ V (full black squares), and $V_2 = 20$ V (green triangles). For $V_2 = 0$ V, the structure is symmetric, while for $V_2 = -20$ μV ($V_2 = 20$ μV) the side lobe for $V_1 > 0$ ($V_1 < 0$) is 'erased'. (right) The conductance varies with V_1 and has the same symmetry as the lobes.*

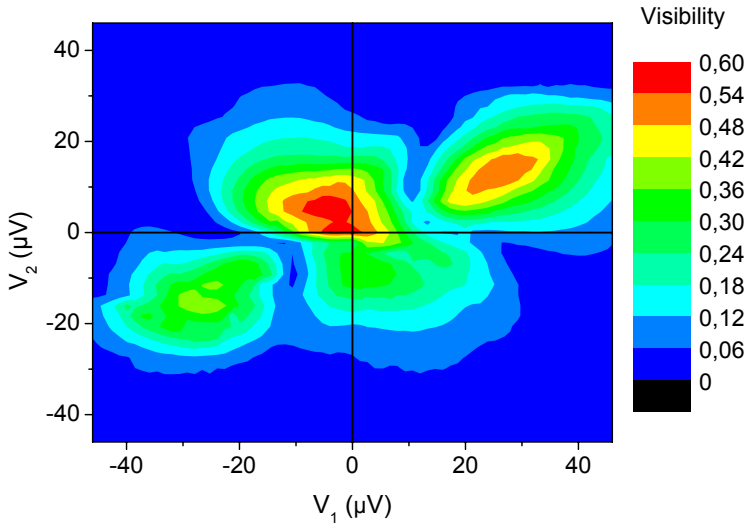

Figure 6.11.: *Visibility as function of the bias voltages V_1 and V_2 for $\mathcal{T}_0 = 0.2$ at zero bias.*

The butterfly

For each value of V_2 from -40 μV to 40 μV, we measured the visibility as function of V_1 for $\mathcal{T}_0 = 0.2$ at zero bias. The results are plotted on Fig. 6.11. We then see how it is possible to go from a situation where the negative side lobe is 'erased' to the opposite situation where the positive side lobe disappears. The whole picture of the visibility as function of V_1 and V_2 in a 2D colorplot has a tilted butterfly shape: for $|V_2|$ above a certain value, one of the wings of the butterfly is no longer visible. The tilt angle being $\sim +30°$, the positive(negative) wing disappears when a negative(positive) bias voltage V_2 is applied.

6.3.2. Reproducing the results

Visibility

We try to reproduce these results assuming a gaussian dependence of the interfering part of the current with respect to V_1 and V_2. The transmitted current is then:

$$I \propto (\mathcal{T}_0 V_1 + (1-\mathcal{T}_0)\, V_2) \left\{1 + \ \cos(\langle\Phi\rangle)\ \exp\left[-\left({V_1}^2/2{V_{10}}^2 + {V_2}^2/2{V_{20}}^2\right)\right]\right\} \tag{6.4}$$

and the differential conductance:

$$\frac{\mathrm{d}I}{\mathrm{d}V_1} \propto \mathcal{T}_0 \left\{1 + \left(1 - \frac{V_1}{V_{10}^2}\left(V_1 + (1/\mathcal{T}_0 - 1)\, V_2\right)\right)\ \cos(\langle\Phi\rangle)\ e^{-\left({V_1}^2/2{V_{10}}^2 + {V_2}^2/2{V_{20}}^2\right)}\right\} \tag{6.5}$$

Hence, the visibility of the interferences in the differential conductance:

$$\mathcal{V} = \mathcal{V}_0 \left|1 - \frac{V_1}{V_{10}^2}\left(V_1 + \left(\frac{1}{\mathcal{T}_0} - 1\right) V_2\right)\right| \ \exp\left[-\left(\frac{{V_1}^2}{2{V_{10}}^2} + \frac{{V_2}^2}{2{V_{20}}^2}\right)\right] \tag{6.6}$$

This is the formula used to reproduce the results on Fig. 6.12 (c). To obtain the asymmetry observed in the data of Fig. 6.12 (a), one must introduce an offset in the gaussian dependence of Eq. (6.4), with respect to V_1 and V_2 (the asymmetry is stronger for V_1). This has been done on Fig. 6.12 (e). According to Eq. (6.6), the gaussian shape of the visibility is modulated by the factor $|1 - 2\,(V_1 - V_{1\mathrm{off}})\,(V_1 - (1/\mathcal{T}_0 - 1)V_2)\,/V_{10}^2|$ which sets the zeros in the visibility (appendix B).

Main features

We have measured the visibility of the interferences as function of V_1 and V_2 for two different values of $\mathcal{T}_0$: $\mathcal{T}_0 = 0.2$ (Fig. 6.12 (a)), and $\mathcal{T}_0 = 0.95$ (Fig. 6.12 (b)) (values at

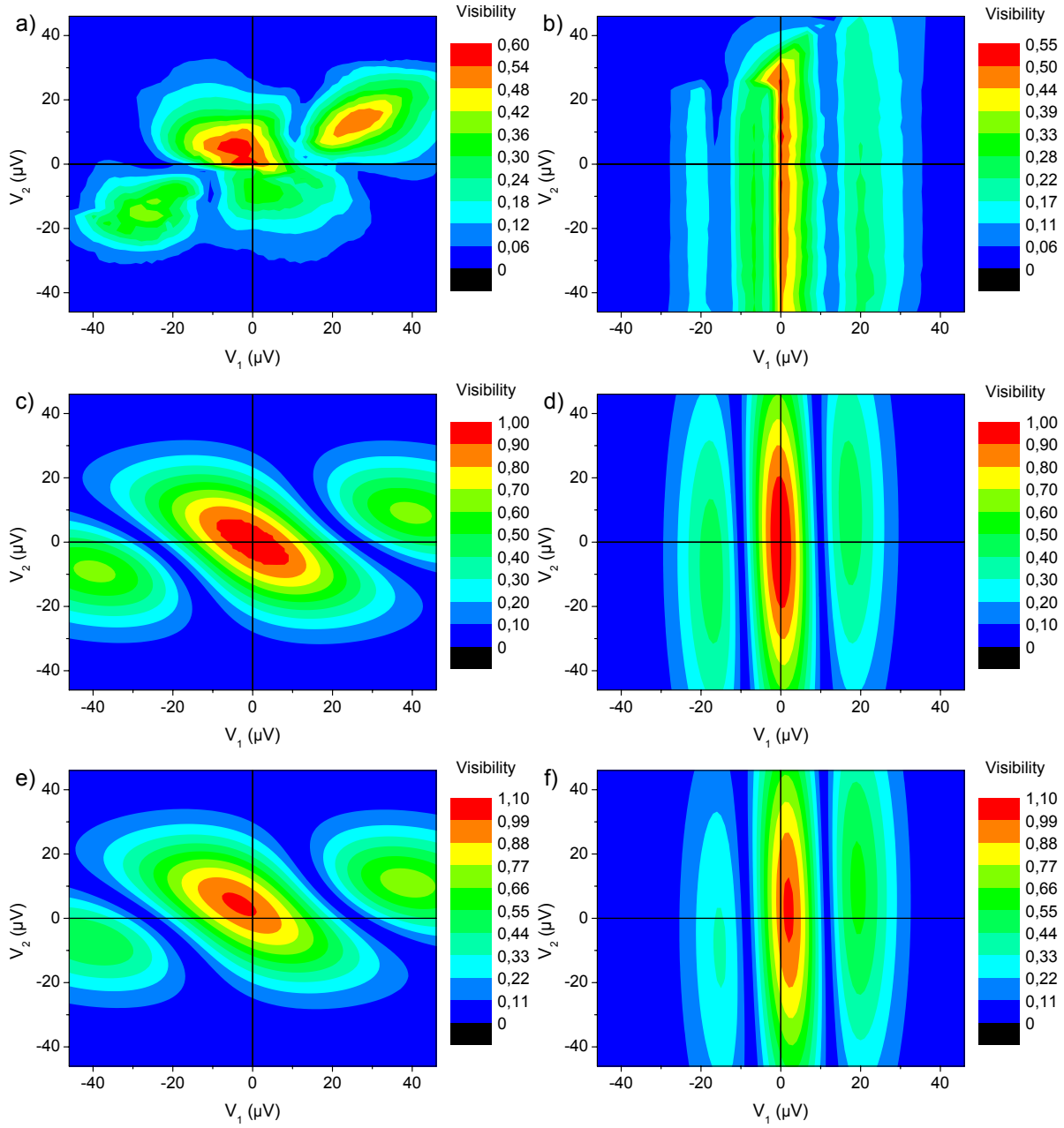

Figure 6.12.: *Colorplots of the visibility as function of the bias voltage V_1 applied on contact $n°1$ along the x-axis, and the bias voltage V_2 applied on contact $n°2$ on the y-axis, with G0 set to transmission $\mathcal{T}_0 \sim 0.2$ at zero bias (a), and to transmission $\mathcal{T}_0 \sim 1$ (b). Visibility obtained with the formula (6.6) with fit parameters $\mathcal{T}_0 = 0.3$ (c) and $\mathcal{T}_0 = 1$ (d) (in the fit $\mathcal{T}_0$ is considered independent of the bias). Ajusting the fit with an offset on V_1 and V_2 with $\mathcal{T}_0 = 0.3$ (e) and $\mathcal{T}_0 = 1$ (f).*

zero bias). We see that the zeros of the visibility follow a curve in the $V_1 - V_2$ plane which qualitatively resemble the hyperbola described on Fig. B.9 and its evolution as function of $\mathcal{T}_0$, as far as one can tell on only two points: for $\mathcal{T}_0 = 0.2$, the opening angle of the hyperbola is close to 90°, and for $\mathcal{T}_0 = 0.95$, it is almost flat ($2\varphi \sim 180°$). The data are qualitatively reproduced using the fit discussed above (Figs. 6.12 (c) and 6.12 (d)), and even better when one takes into account an small offset on both V_1 and V_2 (Figs. 6.12 (e) and 6.12 (f)). The parameters used to reproduce the results are the following:

▷ For $\mathcal{T}_0 = 0.2$ (value at zero bias), the data are plotted on Fig. 6.12 (a). Actually, as we will see later, $\mathcal{T}_0$ depends strongly on $|V_1 - V_2|$ and varies between 0.2 and 0.5. Thus, for the following fits where $\mathcal{T}_0$ is considered as independent of the bias, we used an intermediate value for the transmission ($\mathcal{T}_0 = 0.3$).

- Fig. 6.12 (c): $V_{10} = 26\ \mu\text{V}$, $V_{20} = 13\ \mu\text{V}$, $V_{1\text{off}} = V_{2\text{off}} = 0$,
- Fig. 6.12 (e): $V_{10} = 26\ \mu\text{V}$, $V_{20} = 13\ \mu\text{V}$, $V_{1\text{off}} = 0$, $V_{2\text{off}} = 2.5\ \mu\text{V}$,

▷ For $\mathcal{T}_0 = 0.95$, the data are plotted on Fig. 6.12 (b). Here $\mathcal{T}_0$ does not depend so strongly on $|V_1 - V_2|$: we used the value $\mathcal{T}_0 = 0.95$ in the following fits which is the zero bias value.

- Fig. 6.12 (d): $V_{10} = 10\ \mu\text{V}$, $V_{20} = 45\ \mu\text{V}$, $V_{1\text{off}} = V_{2\text{off}} = 0$,
- Fig. 6.12 (f): $V_{10} = 10\ \mu\text{V}$, $V_{20} = 45\ \mu\text{V}$, $V_{1\text{off}} = 3\ \mu\text{V}$, $V_{2\text{off}} = 1.5\ \mu\text{V}$.

The reasons for the offsets in V_1 and V_2 might be thermoelectric effects caused by the temperature gradient between the sample at 20 mK and the measurement circuit at 300 K.

Gaussian parameters [4] V_{10} and V_{20} depend on $\mathcal{T}_0$. This has been studied in a previous section (see ¶ 6.2.3). The fit given by Eq. (6.6) reproduces qualitatively the data: it explains the 'lobe eraser' behaviour as detailed in the following. It can be refined by taking into account the dependence of $\mathcal{T}_0$ with V_1 and V_2.

Next we explain how the 'lobe eraser' behaviour can be reproduced by this simple fit which is nothing more than a consequence of the gaussian shape visibility.

[4] For $\mathcal{T}_0 \sim 0.3$, we took the same paramaters as the ones used to reproduce the data when taking into account the dependence of $\mathcal{T}_0$ with V_1 and V_2 (see below 'refining').

The 'lobe eraser'

At the beginning of this section, we reported a 'lobe eraser' behaviour (Fig. 6.10): starting from a simple side lobe structure with $\mathcal{T}_0 \sim 0.5$ and $V_2 = 0$, we 'erase' the positive(negative) side lobe by applying a negative(positive) voltage bias $V_2 = -20\ \mu\text{V}(V_2 = 20\ \mu\text{V})$. We are now able to qualitatively reproduce these results with the fit described above. We can conclude that according to this empirical model, the lobe eraser behaviour can be explained by the mixing of the distributions at G_0 and of the gaussian dependence with respect to V_1.

Until then, we didn't consider $\mathcal{T}_0$ dependence on the energy. Does $\mathcal{T}_0$ actually depends on V_1 and V_2? How does it affect the butterfly pattern?

Refining

Now we look at the transmission $\mathcal{T}_0$ as function of V_1 and V_2. To do that, we extract the mean value of the differential conductance by averaging it over a side gate voltage sweep so that the interferences oscillations cancel out. The transmission $\mathcal{T}_0$ is then obtained by normalizing the result by the differential conductance through the interferometer when $\mathcal{T}_0 = 1$. We plotted the transmission $\mathcal{T}_0$ thus obtained as function of V_1 and V_2 on Fig. 6.13 (left). We find that $\mathcal{T}_0$ depends strongly on $|V_1 - V_2|$, rising from $\mathcal{T}_0 \approx 0.2$ when $|V_1 - V_2| \approx 0$ to $\mathcal{T}_0 \approx 0.5$ when $|V_1 - V_2| \approx 15\ \mu\text{V}$.

The results prompt the following remark: $\mathcal{T}_0$ appears in the term that modulates the visibility and which determines the zeros (see Eq. (B.24)). If $\mathcal{T}_0$ depends strongly on $V_1 - V_2$, this should, among other things, deform the hyperbola describing the zeros position that we studied in appendix B. We then compute the visibility obtained when taking into account the dependence of $\mathcal{T}_0$ with V_1 and V_2 reported on Fig. 6.13 (left), and try to fit the data with parameters V_{10}, $V_{1\text{off}}$, V_{20}, $V_{2\text{off}}$. We expect this should refine the fit. The result is represented on Fig. 6.13 (right), it resembles the data a little more, as expected: we introduced a dependence in $|V_1 - V_2|$ in the visibility *via* $\mathcal{T}_0$ that is visible in the data (the figure for the experimental data is a little more streched along the $V_1 = V_2$ axis than the figure obtained when taking $\mathcal{T}_0$ constant).

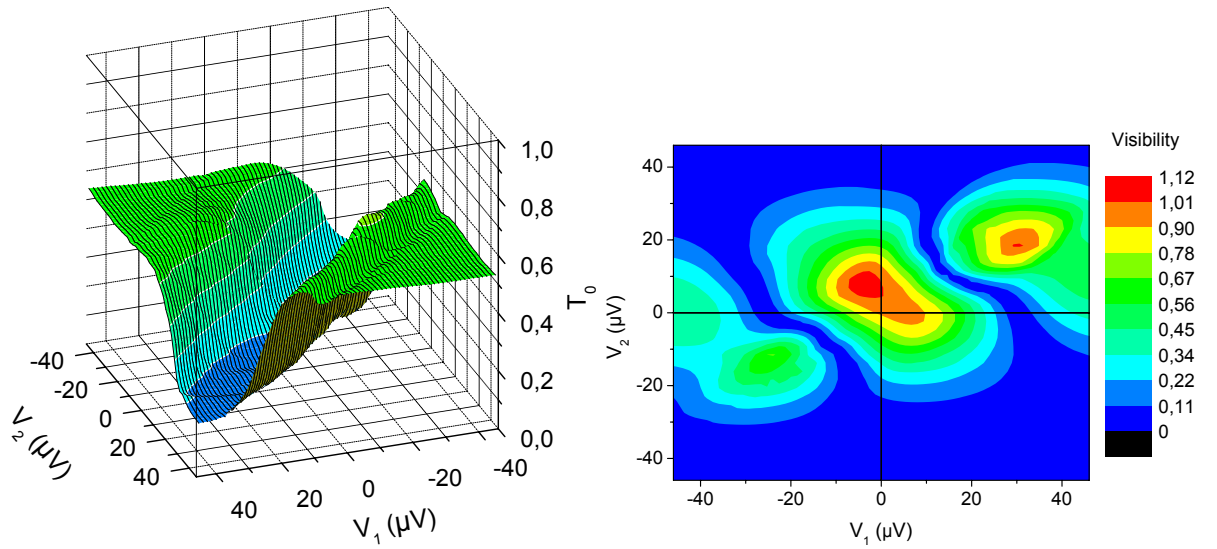

Figure 6.13.: *(left) Colorplot of the transmission $\mathcal{T}_0$ as function of V_1 and V_2. We clearly see that $\mathcal{T}_0$ depends on $|V_1 - V_2|$. (right) Colorplot as function of V_1 and V_2 of the visibility obtained with Eq. (6.6) with offsets on V_i and the dependence of $\mathcal{T}_0$ measured on the left figure. Fit parameters are $V_{10} = 27\ \mu V$, $V_{20} = 13\ \mu V$, $V_{1off} = 1\ \mu V$, $V_{2off} = 2\ \mu V$. The shape of the 'butterfly' is closer to the one measured on Fig. 6.12 (a).*

6.3.3. Non linearities of the transmission

We observed a strong dependence of $\mathcal{T}_0$ on $|V_1 - V_2|$. This is quite unexpected. Indeed, a simple self-biasing hypothesis leads rather to a dependence of $\mathcal{T}_0$ on the mean potential on the ES at the QPC e.g. $V_1 + V_2$. A toy model which takes into account the effect of the coupling between IES and OES explain the $|V_1 - V_2|$ dependence of $\mathcal{T}_0$. However, it does not explain the intriguing saturation of $\mathcal{T}_0$ for $|V_1 - V_2| \gtrsim 20\ \mu$V.

Self-biasing

Self-biasing easily explains a dependence of a QPC transmission on the bias voltage V_1. Indeed, the transmission of one QPC is set by the landscape of the electrical potential resulting from the voltage V_g applied to the gate *and* by the electrochemical potential of the incoming electrons which is determined by the bias voltage V_1: when applying the voltage V_g to the gate, one charges the gate with the charge $-Q_1$. This charge is screened by a charge of opposite sign Q_1 appearing in the 2DEG as a depletion charge, thus raising the internal potential U_1 seen by an electron traveling in the ES. U_1 also screens the excess

charge injected in the ES because of the voltage bias V_1 applied to the injecting ohmic contact (see appendix A) [72], it is then fixed by two equations: $Q_1 = \nu(\omega)(V_1 - U_1) = C(U_1 - V_g)$ where $\nu(\omega) = ie^2(1 - e^{i\omega\tau})/h$ with τ the electron time of flight, and C is the capacitance between the gate and the ES. Then we have:

$$U_1 = \frac{CV_g + \nu(\omega)V_1}{C + \nu(\omega)} \tag{6.7}$$

The potential barrier which determines the QPC transmission is set by the internal potential U_1 which is shown to depend both on V_g and V_1. This is explained on Fig. 6.14 (left).

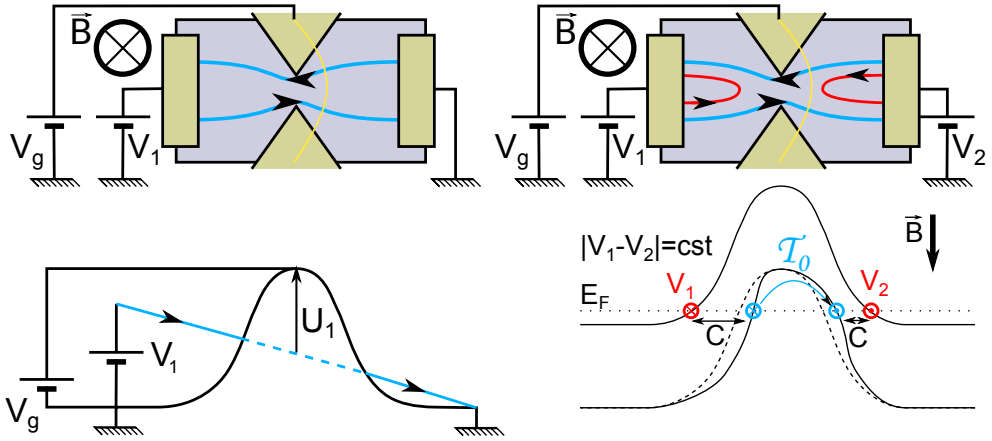

Figure 6.14.: *(left) A QPC is polarized with gate voltage V_g with a single ES biased with voltage V_1. The transmission is controlled by the height of the potential barrier with respect to the ES chemical potential (eV_1), and* not *with respect to the ground. For a fixed value of the gate voltage V_g, the transmission of the QPC depends on V_1. This is the so-called self biasing. (right) First two energy levels with the potential barrier created by G0: the IES (red) is fully reflected, the OES (blue) transmitted with transmission $\mathcal{T}_0$. The IES potential is V_1 on the left side and V_2 on the right side. Because of the capacitance between ESs, sweeping V_1 and V_2 with $|V_1 - V_2|$ constant does not change $\mathcal{T}_0$ since it keeps the height and width of the barrier unchanged.*

In the case of QPC G0 at half transmission which generates a double step distribution, *both* incoming currents are biased with bias voltages V_1 and V_2. The 'mean bias' is then $(V_1 + V_2)/2$ (Fig. 6.15). The self-biasing hypothesis leads to a $V_1 + V_2$ dependence of the transmission $\mathcal{T}_0$.

This is not what is observed on Fig. 6.13 (left). Here is a toy model which explains the observed dependence of the transmission $\mathcal{T}_0$ on V_1 and V_2.

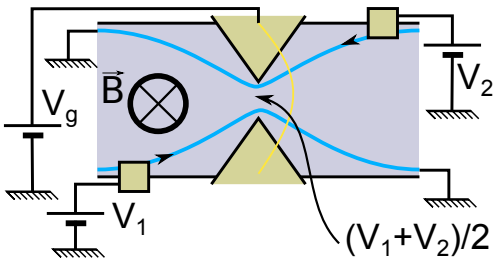

Figure 6.15: *For a QPC set at transmission* 0.5 *for an incoming ES, the 'mean bias' when the two incoming currents are biased with voltages* V_1 *and* V_2 *is* $(V_1 + V_2)/2$.

A toy model

$\mathcal{T}_0$ depends on $|V_1 - V_2|$: on Fig. 6.13 (left), the mean differential transmission of the oscillations shows lines of equal transmission running parallel to $V_1 = V_2$ and symmetric with respect to this line. We try to explain this dependence with the toy model schematized on Fig. 6.14 (right) which takes into account the electrostatic effect of the IES.

Let us look at what happen on a $|V_1 - V_2| = \text{cst}$ line when QPC $G0$ fully reflects the IES (red on the schematic) and partially transmits the OES (blue) with transmission $\mathcal{T}_0$. The internal potential on the IES is set by V_1 on the left side of the QPC barrier and V_2 on the right side. Because of the capacitance between the IES and the OES, if one decreases V_1 and increases V_2 by the same amount so that $|V_1 - V_2|$ remains constant, the energy levels will be deformed as represented on the schematic Fig. 6.14 (right): the potential barrier for the OES will be deformed but will keep the same width an height in a first approximation so that the tunneling rate (and the transmission $\mathcal{T}_0$) will stay unchanged.

We have seen the ubiquity of the gaussian shape of the visibiliy, with respect to V_1 as well as to V_2: it is sufficient to fit everything we observed as long as there is only one single side lobe. We are able to reproduce the 'butterfly' and the intriguing 'lobe eraser' behaviour which is now no longer mysterious. This gaussian shape visibility which seems at the root of our experimental observations hasn't been explained yet. The linear dependence of the coefficients $1/V_{10}^2$ and $1/V_{20}^2$ with $\mathcal{T}_0$ also remains unexplained.

Not long ago, the LPN's group found elements on the energy relaxation in the $\nu = 2$ quantum Hall regime [12–15]. In the following, we are interested in comparing our results. The LPN's group proved the existence of energy relaxation in the OES by energy exchange with the co-propagating IES [13]. We present their results and try to see if they could explain the ubiquituous gaussian shape of the visibility that we observe.

6.3.4. Energy relaxation?

Dependence of the effective temperature with the bias

Le Sueur *et al.* report in [13] the evolution of $T_{\rm exc}$, an effective temperature which measures the energy of the particule-holes pairs in the out of equilibrium distribution in the OES after a propagation over the length L, with the voltage difference δV_d applied across the QPC which creates the out of equilibrium distribution in the OES. The data show that when L is close to zero ($L = 0.8$ μm), $T_{\rm exc}$ is close to its predicted value just outside of the QPC, linear in δV_d, $T_{\rm qpc} = \left(\sqrt{3}e/2\pi k_B\right)\ |\delta V_d|$. As L increases, the OES distribution looses energy, exchanging it with the 'cool' Fermi distribution in the adjacent IES and maybe with other degrees of freedom.

We introduce $T_{\rm loss}(L) \equiv T_{\rm qpc} - T_{\rm exc}(L)$ which measures the amount of energy associated with the electron-holes pairs that has been lost to the environment or exchanged with the IES during propagation. After a propagation over $L \geq 10$ μm, the distribution in the OES no longer evolves, it has reached a steady state. Let us look then at the dependence of $T_{\rm loss}(L = 30\ \mu{\rm m})$ with δV_d.

Assuming that all the energy that has been lost by the OES distribution is exchanged with the IES, we want to see if an effective temperature quadratic in δV_d in the IES could explain the gaussian dependence of the interfering current in the MZI. It looks like $T_{\rm loss}(L = 30\ \mu{\rm m})$ has two contributions, one linear with δV_d, the other quadratic (Fig. 6.16): for the linear contribution, we find:

$$T_{\rm loss}^{(1)} == \alpha_1\,|\delta V_d| \quad \text{with} \quad \alpha_1 = 0.94\ {\rm mK}.\mu{\rm V}^{-1} \tag{6.8}$$

Then there is a quadratic contribution:

$$T_{\rm loss}^{(2)} = \alpha_2\,\delta V_d^2 \quad \text{with} \quad \alpha_2 = 0.0075\ {\rm mK}.\mu{\rm V}^{-2} \tag{6.9}$$

Impact on the visibility

Can the quadratic part of the effective temperature $T_{\rm loss}^{(2)}$ explain the single lobe structure of the visibility? Let us take a look at the energy scales.

$$\exp\left(-\frac{T_{\rm loss}(L = 30\ \mu{\rm m})}{T_\varphi(L = 11.3\ \mu{\rm m})}\right) = \exp\left(-\frac{\delta V_d^2}{2V_{10}^2}\right) \tag{6.10}$$

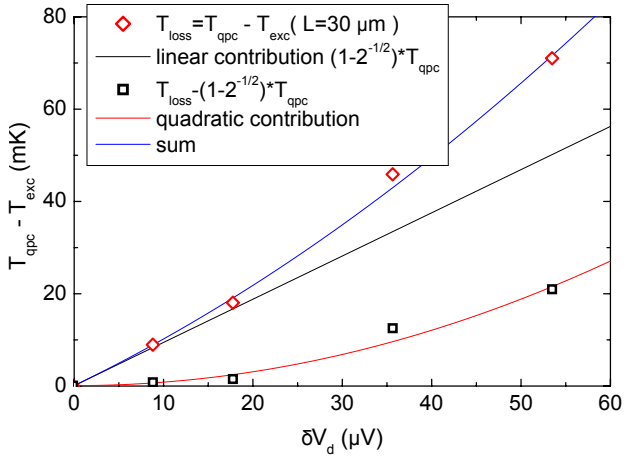

Figure 6.16: *Energy lost by the OES during its $L = 30$ μm propagation along the IES, expressed in terms of the effective temperature T_{loss}, as function of the voltage difference δV_d between the two steps of the out-of-equilibrium energy distribution generated in the OES. T_{loss} dependence with δV_d is shown to have a linear and a quadratic contribution [13].*

We consider temperature dephasing for a large sample ($L = 11.3$ μm) so that energy relaxation is complete. In this case Roulleau *et al.* measured [2] $T_\varphi = 22$ mK, then

$$V_{10} = \sqrt{\frac{T_\varphi}{2\alpha_2}} = 38\ \mu\text{V} \tag{6.11}$$

This is about 3 to 4 times more than the values obtained in ¶ 6.2.3. It seems at first glance that effective heating of the IES by energy relaxation of the OES does not explain quantitatively the observed lobe structure in our experiment.

Pertinence of the comparison

We tried to estimate the energy scale of the gaussian behaviour which would come from phase fluctuations caused by an effective temperature in the IES quadratic with the voltage bias. In order to do so, we studied how in Altimiras *et al.* experiment the energy lost by the OES depends on δV_d^2. The numerical coefficient α_2 we obtain is then injected in the exponential dependence of the visibility with the temperature which was obtained for our 'big' samples ($L = 11.3$ μm). From this we extracted a value for the gaussian parameter V_{10} which is three times larger that the usual value. How can one explain the discrepancy? An important point is that we do not know whether both experiments were conducted in the same regimes, in particular we do not know if we could have observed interferences at the magnetic field at which they have been working.

Additionally, we followed Altimiras *et al.* by assuming that the steady-state distributions in the ESs were fully characterized by $T_{\rm exc}$, implying that they are Fermi distributions. This assumption is not correct according to Kovrizhin *et al.* [85, 86], therefore, characterizing

the charge fluctuations in the IES with an effective temperature is quantitatively wrong. This might explain why our approach doesn't yield the right energy scales.

6.3.5. 'Something' happening before injection in the MZI?

Inspired by the results of Altimiras *et al.* [15] who brought back a double-step distribution to equilibrium through a floating ohmic contact used as a voltage probe, we try to see if a floating ohmic contact at the injection has any influence on the visibility at finite bias. This attempt is also justified by our findings on the dependences of V_{10} and V_{20} on $\mathcal{T}_0$ which suggest that the mechanism which causes the gaussian enveloppe happens before $G0$.

To do so we return the magnetic field to change the direction of the ESs as schematized on Fig. 6.17 (left). Then we can either inject the electrons directly into the interferometer through contact n°3, or through contact n°5 so that the electrons go through floating ohmic contact n°3 before entering the interferometer. However, because of the design of the sample, there is no QPC to indepedently bias the two ESs upon entering the MZI as in the other configuration (**B** in the opposite direction). Boths ESs are fed with the same bias, then as already reported by Bieri *et al.* [43] and explained by Roulleau [3], we do not obtain a lobe structure with well marked extinctions (see Fig. 6.17 (right)). We fit the data on Fig. 6.17 (right) using the fit for a single side lobe structure [5]:

$$\mathcal{V} = \mathcal{V}_0 \sqrt{\left[\left(1 - \frac{V_1^2}{V_{10}^2}\right)\right]^2 + 4\pi^2 \frac{V_1^2}{V_0^2}} \exp\left(-\frac{V_1^2}{2V_{10}^2}\right)$$

We find the gaussian parameter $V_{10} = 7.3$ μV and the coupling parameter $V_0 = 45$ μV. The sample has an arm length $L = 11.3$ μm. We see that the structure doesn't change on choosing a 'direct' or 'indirect' injection of the electrons.
We also checked the existence of a counter propagating heat flow – which was measured at $\nu = 1$ by Granger *et al.* in [48] – by applying a DC voltage at contact n°3, with the magnetic field in the usual orientation (ESs circulating from contact n°1 to n°3). No change was detected in the visibility when sweeping this DC voltage.

The conclusion one must draw is that either there is one effect which is not affected by the floating ohmic contact or there is simply no effect taking place before $G0$.

[5] We recall the fit derivation in ¶ B.1.2.

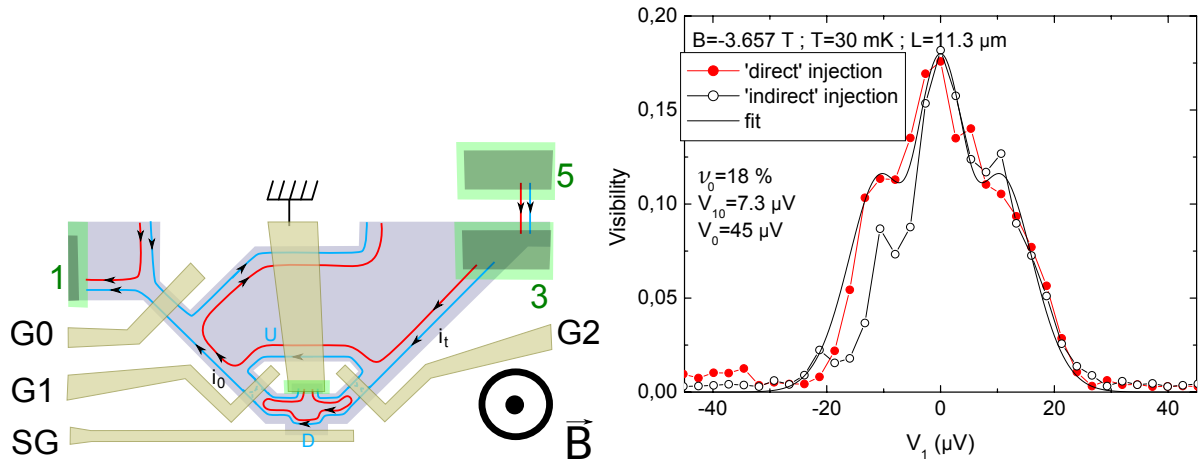

Figure 6.17.: *(left) The magnetic field has been flipped: injection occurs at contact n°3 ('direct' injection) or n°5 ('indirect' injection) and the transmitted current is collected at contact n°1. G0 fully reflects the outgoing IES. Because there is no QPC to separate IES and OES upon entering the MZI, both ESs are biased with the same bias voltage V_1. (right) Visibility as function of the bias voltage. Red dots: 'direct' injection. Black open dots: 'indirect' injection. ESs are biased at contact n°5 then supposedly thermalized at contact n°3 before entering the interferometer. Red thick line: fit with parameters $V_{10} = 7.3\ \mu V$ and $V_0 = 45\ \mu V$.*

6.4. Conclusion

In this chapter we adressed several questions pertaining the lobe structure. We checked the prediction of Levkiviskyi *et al.* on the existence of a quantum phase transition from multiple to single side lobes prompted by partition noise on $G0$. Our data seem to agree with Levkiviskyi *et al.*'s theory suggesting that multiple side lobes arise from the beating of two collective modes because of the coupling between ESs. However, it does not explain the gaussian enveloppe which is enough to derive the single side lobe structure, the 'lobe eraser' behaviour and the 'butterfly' pattern. Recent experiments showing the existence of energy relaxation by energy exchange between ESs motivated us to study further the gaussian envelop. We injected an out of equilibrium distribution and observed how the visibility depended on the form of the distribution. The extracted gaussian energy scale dependence with $\mathcal{T}_0$ is unexpectedly linear. We then try to relate quantitatively the results of Altimiras *et al.* on energy relaxation to our data. Effective heating of the IES by energy relaxation of the OES does not explain the measured gaussian energy scale. To date there is no theory explaining the gaussian envelop and the impact of dilution.

7. Engineering coherence at filling factor 2

Contents

7.1. Motivations

From our previous work (chapter 4) we have identified one source of decoherence: the accumulated phase of the electrons travelling in the arms of the interferometer is blurred by potential fluctuations coming from the charge noise of the environment. In the specific case of the IQHE regime at filling factor two, the environment of one ES is the other. Thus, the thermal charge noise in one ES blurs the phase in the other.

The lobe structure in the interferences visibility as function of the bias voltage is a robust pattern that is found at $\nu = 2$ as well as $\nu = 1$ although no multiple side lobes have been found at $\nu = 1$ (§ 4.4). Many theories try to explain this behaviour (¶ 4.4.4). One in particular [6] reproduces the multiple side lobes behaviour at $\nu = 2$ with plasmonic excitations arising from Coulomb interaction between ESs. In this model, the lobes width is inversely proportional to the coupling strength between ESs. Other theories [8–10] predict multiple side lobes at $\nu = 1$ invoking multiple particles interferences caused by intra-channel e-e interactions.

According to the work of the LPN group, it seems that at $\nu = 2$, when out of equilibrium, an ES relaxes by exchanging energy with the adjacent ES. The LPN group also provided a cure to energy relaxation of out of equilibrium electrons: one can freeze energy relaxation in one ES by confining the adjacent one in a closed loop of diameter ≤ 10 μm, inducing energy quantization, and thus preventing energy transfer to the adjacent ES as long as the available energy remains lower than the opened gap.

From all this evidence, it seems that coupling to the adjacent ES is responsible for dephasing by potential fluctuations caused by the thermal charge noise, energy relaxation at finite bias in the arms of the interferometer and the beating of two collective modes which gives rise to multiple side lobes structure.

With our new design, we want to adress the following questions: is energy relaxation at finite bias in the arms of the interferometer responsible for the single side lobe pattern in the interferences visibility as function of the bias voltage? Can we freeze it as did the LPN group? This will surely change the coupling to the noisy environment (the adjacent ES), how will it impact decoherence in our system at zero bias like temperature dependence? Once we suppress the coupling to the noisy environment, what about intrinsic Coulomb interactions within the ES? Will we be able to see their effects more clearly? How will it change the lobe pattern? By decoupling the ESs at $\nu = 2$ will we find a multiple or

a simple lobe structure like at $\nu = 1$? Will the energy scales change as predicted by [6]? Are these aspects – coupling to the noisy adjacent ES, energy relaxation and beating of two modes – compatible and how? In any case, we hope to increase the coherence of the quasiparticles in the interferometer.

I will begin by presenting the new sample with its additionnal gates which allow the confinment of the IES. Then I will show how we control the coupling between the interfering ES and its neighbour. I will present the impact of the decreasing coupling on the zero bias visibility and the temperature dependence and finally on the lobe structure. Inspired by the LPN group's findings, we implemented additional gates in the design of the sample to localize the IES into small loop to try to freeze the IES excitations by the opening of a gap. The focus of this chapter will be to report this attempt and its consequences.

7.2. Sample

7.2.1. General description

We work around $T = 25$ mK, at magnetic fields $B \sim 3$ T in the middle of the $\nu = 2$ plateau (Fig. 7.1 (left)). The sample was made by D. Mailly, H. LeSueur who did the preparatory tests for the fabrication of the ohmic contacts, G. Faini and U. Gennser at LPN (Marcoussis) on a 2DEG provided by W. Wegscheider from ETH (Zurich).

The surface $\mathcal{S}$ enclosed by the two interfering arms of the Mach-Zehnder was measured by revealing the electronic interferences with the magnetic field. Indeed, the amount of magnetic field ΔB needed to vary the phase of the interferences by 2π is related to $\mathcal{S}$ through $\Phi_0 = h/e = \Delta B \mathcal{S}$. We measured $\mathcal{S} = 40.0 \pm 0.1$ μm^2 (Fig. 7.1 (right)). The lithographic length of the arms $L = 11.3$ μm is consistent with the measured area: if we consider the surface $\mathcal{S}$ to be a circle, the length of the arms of the interferometer is half of the circle's perimeter which is: $\sqrt{\pi \mathcal{S}} = 11.2$ μm.

The new design features additional gates G_U and G_D which act respectively on the upper and on the lower arm of the interferometer (Fig. 7.2). We define the transmission of the IES through $G_U(G_D)$ as $\mathcal{T}_U(\mathcal{T}_D)$. When we lower $\mathcal{T}_U(\mathcal{T}_D)$ towards 0, the trajectory of the IES (red) is progressively deformed into small loops which are finally disconnected from one another and from the ohmic contact n°2(n°4) at localization of the IES, (fig. 7.2 (right)).

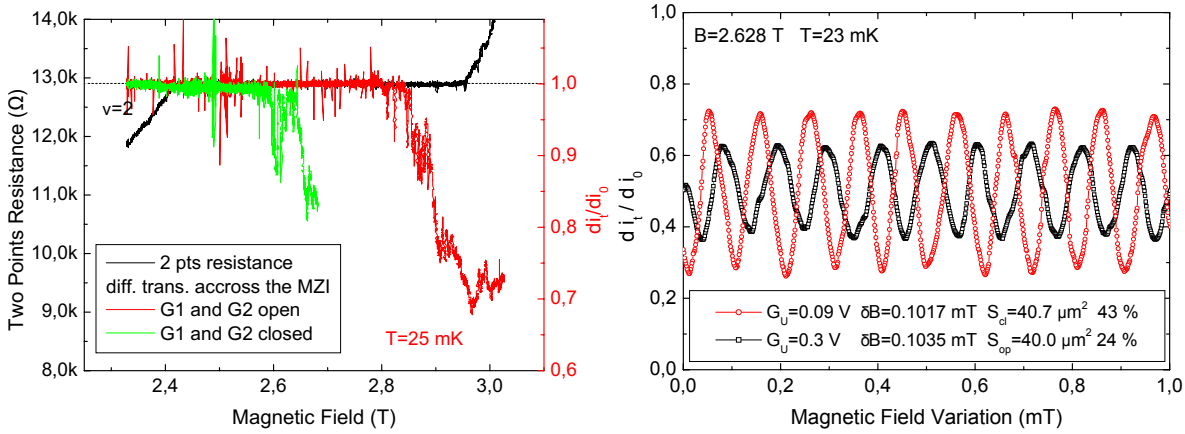

Figure 7.1.: *(left) Two points resistance (black) and differential transmission through the upper (green) and lower arm (red) as function of the magnetic field ,around $\nu = 2$. Electronic density is smaller in the upper arm. (right) Differential transmission of the OES as function of the magnetic field variation, for G_U open (black), and G_U pinched with the IES localized (red). The surface between the two arms is estimated from the oscillations periodicity: $\mathcal{S} = 40.0 \pm 0.1\ \mu m^2$ when G_U is open, $\mathcal{S} = 40.7 \pm 0.1\ \mu m^2$ when G_U is at $\mathcal{T}_U \sim 0$. $\mathcal{S}$ increases by $\Delta S = 0.7 \pm 0.2\ \mu m^2$ as G_U is closed. A more precise estimation of ΔS is done in ¶ 7.3.3.*

We thus hope to diminish the coupling between the interfering channel (blue) in the arms of the interferometer and the noisy environment. We also hope that when the IES is localized, we will freeze charge fluctuations in the IES which are though to be the main cause of dephasing in our system, and see some manifestation in the temperature dependence. Finally, we want to test the theory of charge relaxation occuring in the interfering ES. Will we be able to freeze charge relaxation at localization of the IES and see some incidence in the visibility at finite bias?

For now we must characterize the new gates G_U and G_D, to see how they modify the Mach-Zehnder interferometer.

7.2.2. Additional gates

Asymmetry

The gate G_U depletes the 2DEG underneath in the upper arm as compared to the 2DEG in the lower arm: the effect of G_U is clear on Fig. 7.1 (left) where the resistance plateau

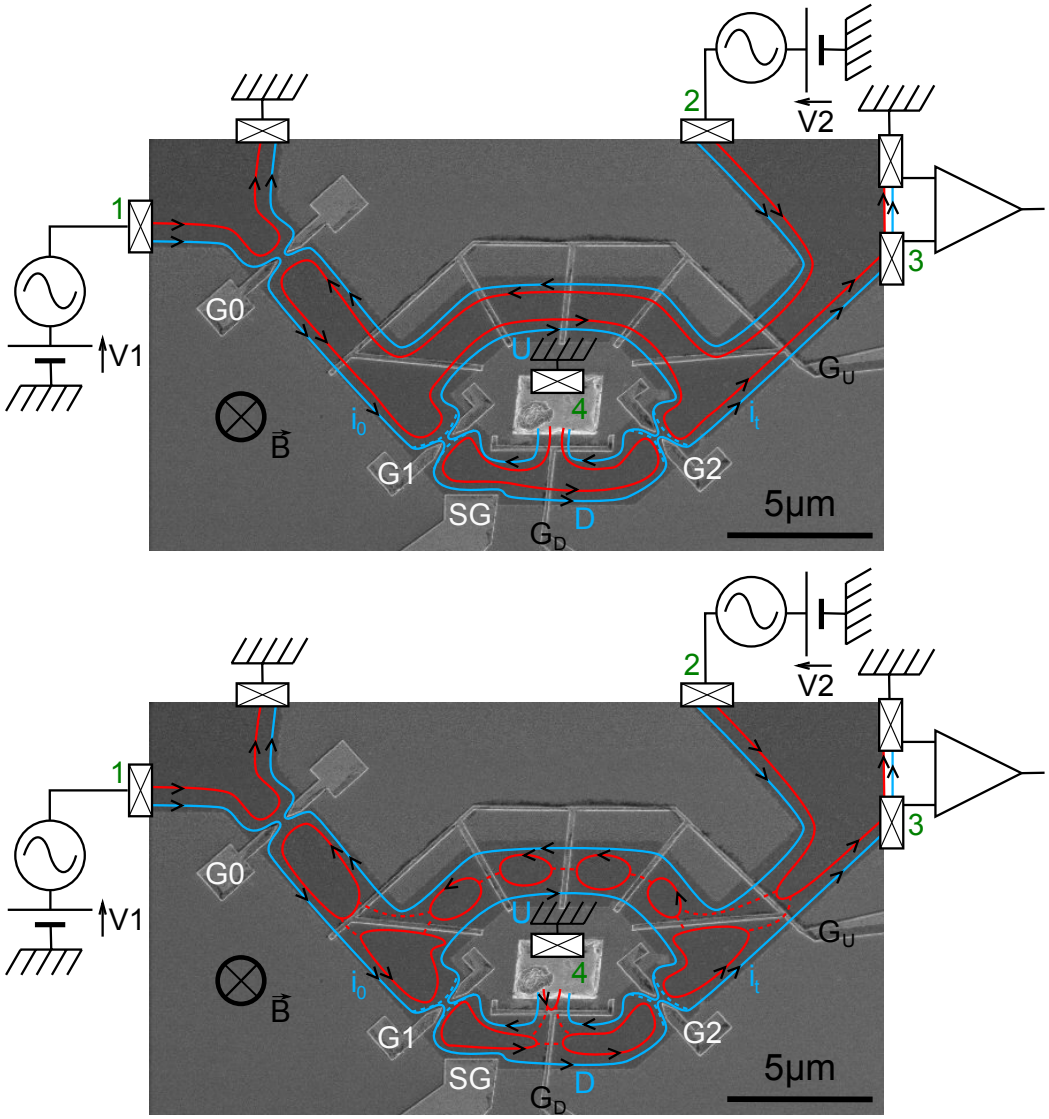

Figure 7.2.: *SEM view of the sample. Current is injected at contact n°1. Contact n°2 biases the IES in the upper arm and is used to measure the coupling V_0^{-1} and in the 'which path' experiment. The transmitted current is measured at contact n°3, thanks to the voltage-current convertor provided by the quantum Hall state, and contact n°4 grounds the backscattered current in the lower arm. (top) G_U and G_D are open. The OES (blue) in the arms of the interferometer is coupled to the IES (red). (bottom) G_U and G_D are at transmission $\mathcal{T}_{U,D} < 1$ for the IES deformed into small orbits which will close when the transmission $\mathcal{T}_{U,D}$ will reach 0. Then if charge fluctuations in the closed red dots are indeed frozen by the opening of a gap in the IES excitations, the only charge fluctuations in the environment are in the opposite OES which is coupled to the interfering one through the IES dots with a lower coupling.*

through the upper arm of the interferometer is shifted to a lower magnetic field than the one corresponding to transmission through the lower arm. The electronic density in the upper arm is therefore smaller by $8 \pm 2\%$. This is deduced from the ratio between the upper limit of the resistance plateaus with respect to the magnetic field: $B_U = 2.60 \pm 0.03$ T for the upper arm , and $B_D = 2.82 \pm 0.03$ T for the lower arm.

Using these curves, we optimized the value of the field so that despite the asymmetry, backscattering was minimum: we chose a field for which the three points resistance through both arms was at its plateau value. Additional backscattering due to G_U is visible in the characteristics of G_U (Fig. 7.3 (left)): the transition between plateaus happens on a broader range of gate voltage when the current goes in the upper arm (red curve) than when it flows through the lower arm (black curve), probably because of the respective shapes of G_U and G_D (see explaination below).

We also wanted to obtain interferences with the best contrast possible. This was achieved by setting the magnetic field to $B = 2.628$ T, which corresponds to the maximum value for which there is no backscattering in the upper arm according to Fig. 7.1 (left).

In the case of a symmetric MZI, experience tells us that maximum coherence length is obtained at the end of the $\nu = 2$ plateau, where coupling between ESs is minimum [1, 3]. Here because of the asymmetry, time of flight through each arm is in general different (the electronic densities being different), leading to thermal smearing. In our situation, coherence is influenced by the coupling of the OES to the environment *and* the symmetry of the MZI, which are both affected by the magnetic field.

Characteristics of the additional gates

Here I will characterize the new gates (see Fig. 7.3). We proceed in the same manner as for the other gates: the injecting QPC G_0 is fully open ($V_{G0} = 0.5$ V), we inject current at the ohmic contact n°1 and measure what is transmitted through the interferometer at contact n°3 (Fig. 7.2).

'Upper' Gate On Fig. 7.3 (left) the characteristics of G_U are reported, with G_D open ($V_{G_D} = 0.3$ V). The differental transmission is measured as function of V_{G_U} in various configurations to check whether electrons are well transmitted in all parts of the MZI.

We find that even when the magnetic field is such that transmission is equally good in the upper and lower arms when G_U and G_D are open, backscattering by G_U occurs at

higher polarization in the upper arm (when $G1$ and $G2$ are closed, $V_{G1} = V_{G2} = -0.2$ V) than in the lower arm (when $G1$ and $G2$ are open, $V_{G1} = V_{G2} = 0.5$ V). The fact that conductance starts to decrease at a higher gate voltage in the upper arm than in the lower arm reflects once more that density in the upper arm is smaller than in the upper arm: when reaching the conductance plateau, the 2DEG below the gates is at filling factor one. As the lower arm needs more depletion than the upper one, density is larger in the lower arm than in the upper arm as already observed when varying the magnetic field.

There is also additional backscattering in the upper arm because of the fan shape of G_U (Fig. 7.2): the total transmission of G_U is roughly the product of the transmissions of each 'finger' (if we do not count multiple reflexions), and since each of them probably does not transmit exactly the same amount of current at the same gate voltage, the transition between plateaus which corresponds to the IES reflection occurs on a broader range in the upper arm than in the lower arm.

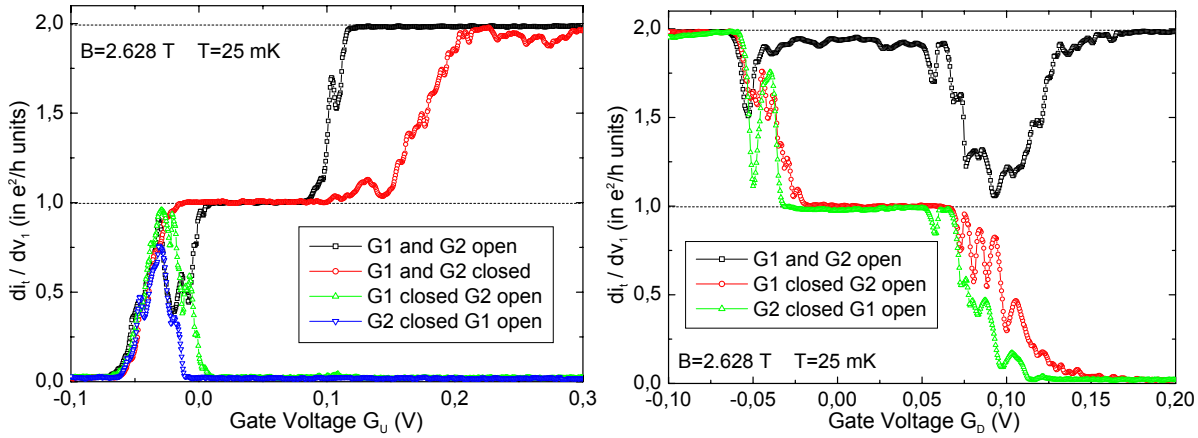

Figure 7.3.: *(left) G_U. (black) $G1$ and $G2$ open, current flows through the lower arm. (red) $G1$ and $G2$ closed, current flows through the upper arm. Backscattering occurs earlier in the upper arm than in the lower arm when closing G_U,because of the smaller density. (right) G_D. (black) $G1$ and $G2$ open, transmission is 1 except between plateaus when some of the current is lost at contact n°4. (red) $G1$ closed and $G2$ open, current is reflected into the upper arm by $G1$, we measure the part reflected by G_D. (green) $G1$ open and $G2$ closed, we measure the current reflected by G_D in the upper arm and then by $G2$ towards contact n°3.*

'Lower' gate We characterize G_D. G_U is fully open ($V_{G_U} = 0.3$ V). When $G1$ and $G2$ are open, one would think that all the injected current at contact n°1 would be recovered

at ohmic contact n°3 whatever the transmission of G_D: the current not transmitted by G_D towards contact n°3 would be reflected in the upper arm and finally reflected by G_D towards contact n°3. This is not the case (Fig. 7.3 (right)) because of the shape of G_D which is a 'three way' gate: one way towards contact n°1, one towards contact n°3, and another towards contact n°4 (Fig. 7.2 (bottom)). Between plateaus of transmission, a fraction of the current is lost at contact n°4 to ground. Therefore, transmission through the lower arm of the MZI is constant equal to one, except between G_D transmission plateaus (black squares on Fig. 7.3 (right)).

To observe G_D transmission plateaus when sweeping V_{G_D}, one needs to either close $G1$ and open $G2$ (red circles) – we then detect the current reflected by G_D after having been reflected by $G1$ in the upper arm – or do the reverse (green triangles) – we then measure the current reflected by G_D in the upper arm.

A simple model for the lower gate

We are able to reproduce the two dips observed in the characteristic of G_D for $G1$ and $G2$ open (black curve on Fig. 7.3 (right)), with a simple model for G_D. The model is drawn as a schematic on Fig. 7.4 (left), and the resulting characteristic is plotted on Fig. 7.4 (right).

Let us consider that G_D is a three way gate with input at potential V_{in}, output at potential V_{out}, ground and fictitious floating ohmic contact M at potential V_M. Incoming current can either be transmitted towards output contact, transmitted to ground, or reflected towards contact M. Current from contact M can be transmitted to ground, or reflected towards output. For the sake of simplicity, transmission and reflexion probabilities are set equal whatever the input and the output, and we consider only one ES: $\mathcal{T}$ and $\mathcal{R}$ are the reflexion and transmission probabilities of the ES.

Applying Landauer-Büttiker relations to the output contact and to contact M, one obtains the following set of equations:

$$V_{\text{out}} = \mathcal{R}^2 V_M + \mathcal{T} V_{in} \tag{7.1}$$

$$V_M = \mathcal{R}^2 V_{\text{in}} + \mathcal{R}\mathcal{T}\mathcal{R} V_M + \mathcal{T}^2 V_M \tag{7.2}$$

By eliminating V_M, one can extract the differential transmission through the lower gate G_D (for one ES):

$$\frac{\mathrm{d}i_t}{\mathrm{d}i_0} = \frac{V_{\text{out}}}{V_{\text{in}}} = 1 - \frac{2\mathcal{R}\mathcal{T}}{\mathcal{R}^2 + 2\mathcal{T}} \tag{7.3}$$

then one injects a fit for $\mathcal{T}$ as function of $x = V_{G_U}$ in Eq. (7.3):

$$\mathcal{T}(x) = \frac{1}{1 + e^{-(x-x_0)/\delta x}} \tag{7.4}$$

where δx is the width of the transition between plateaus and x_0 its position. The fit parameters are:

- for the reflection of the IES: $x_0 = 0.097$ V and $\delta x = 0.01$ V
- for the reflection of the OES: $x_0 = -0.04$ V and $\delta x = 0.005$ V

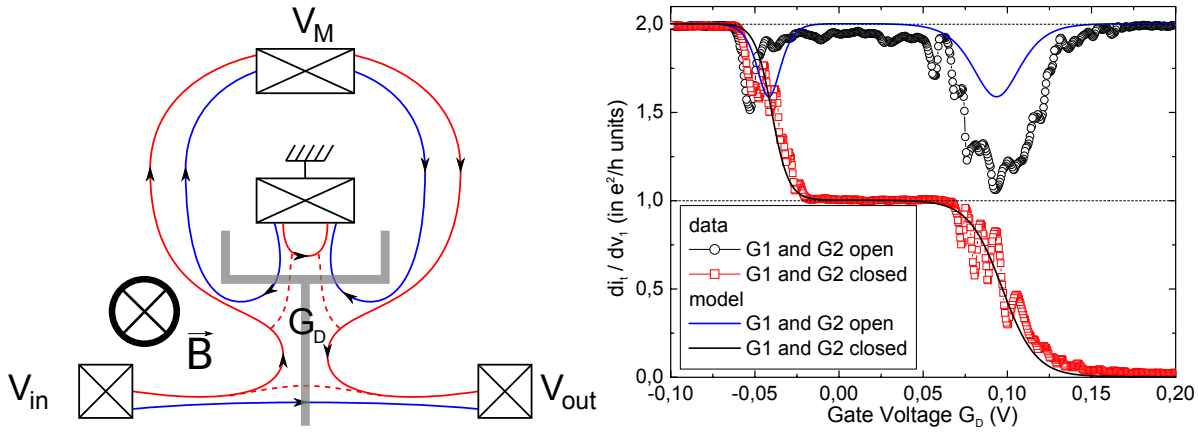

Figure 7.4.: *(left) Schematic of the model for G_D. G_D is a three way gate with input V_{in}, output V_{out}, ground and fictitious floating ohmic contact M at potential V_M. The input current can be transmitted towards the output contact, to ground, or reflected towards contact M. Current from contact M can be transmitted to ground, or reflected towards the output contact. (right) The experimental characteristics of G_D for $G1$ closed and $G2$ open (red squares) and open (black circles) are well reproduced by the model (solid lines), in particular the two dips when $G1$ and $G2$ are open (blue curve), although the dip at $V_{G_D} \approx 0.1$ V is twice larger in the data maybe because of interferences in the IES.*

We obtain a 20 % reduction of the differential transmission at both dips (Fig. 7.4 (right)), whereas experimentally we have a reduction of 50 % for the dip corresponding to the reflexion of the IES and 20 % for the dip corresponding to the reflexion of the OES (see Fig. 7.3 (right)). The 50 % dip might be caused by interference effects for the IES between the direct path from V_{in} to V_{out} and the one going through contact M (Fig. 7.4 (left)).

From now on we will focus on the effect of G_U, G_D will stay open.

7.3. Behaviour at zero bias

7.3.1. Visibility and coupling

The effect of G_U on the visibility of the interferences is spectacular as one can see on Fig. 7.5: it goes from ~ 20 % when G_U is open to ~ 50 % when the IES is localized.

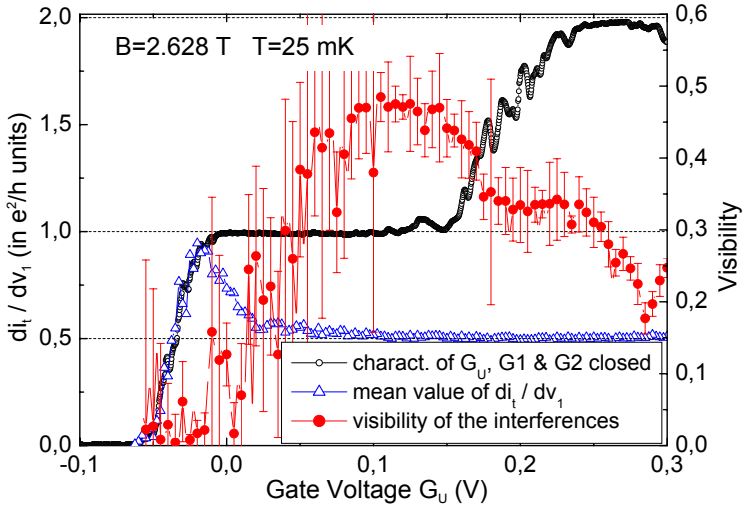

Figure 7.5.: *The visibility increases from* 20 % *at full transmission of the IES ($V_{G_U} \approx 0.3$ V) to almost* 50 % *when the IES is completely localized ($V_{G_U} \approx 0.1$ V). Localization of the IES has no dramatic effect on the visibility which saturates well into the transmission plateau. When G_U is pinched further, the interference signal is no longer a pure cosine leading to widening of the error bars. Departure of the mean conductance from* 0.5 *(in e^2/h units) is a sign of detuning of QPCs G*1 *and G*2 *from half transmission of the OES, thus decreasing the visibility.*

Going from $\mathcal{T}_U = 1$ to $\mathcal{T}_U = 0$

At first G_U is open ($V_{G_U} = 0.3$ V) and the Mach-Zehnder is in the configuration represented on Fig. 7.2 (top). We obtain a visibility of ~ 20 % (Fig. 7.1 (right)). For intermediate transmissions, the Mach-Zehnder is in the configuration of Fig. 7.2 (bottom) where the upper IES is deformed in small loops. The visibility increases up to 50 %.

Beyond localization of the IES, it seems that the interference signal is no longer a pure cosine, but that some additional signal is super-imposed to the former one with another periodicity, as the data presented on Fig. 7.6 (right) suggest. This probably originates from phase jumps because of electron tunneling between the closed IES dots.

We are able to continuously go from one situation to the other while measuring the coupling parameter V_0, even when the IES is disconnected from contact n°2 (see below). The detuning of the interferometer (cross-talk between G_U and $G1/G2$) is slight so that we don't need to ajust V_{G1} and V_{G2} when we increment V_{G_U}. This is known by the value of the mean conductance through the MZI which stays at 0.5 (in e^2/h units) until $V_{G_U} \approx 0.1$ V (open blue triangles on Fig. 7.5). A departure from this value is a sign of detuning of both QPCs $G1$ *and* $G2$ (this happens for $V_{G_U} < 0.1$ V as can be seen on the blue curve on Fig. 7.5).

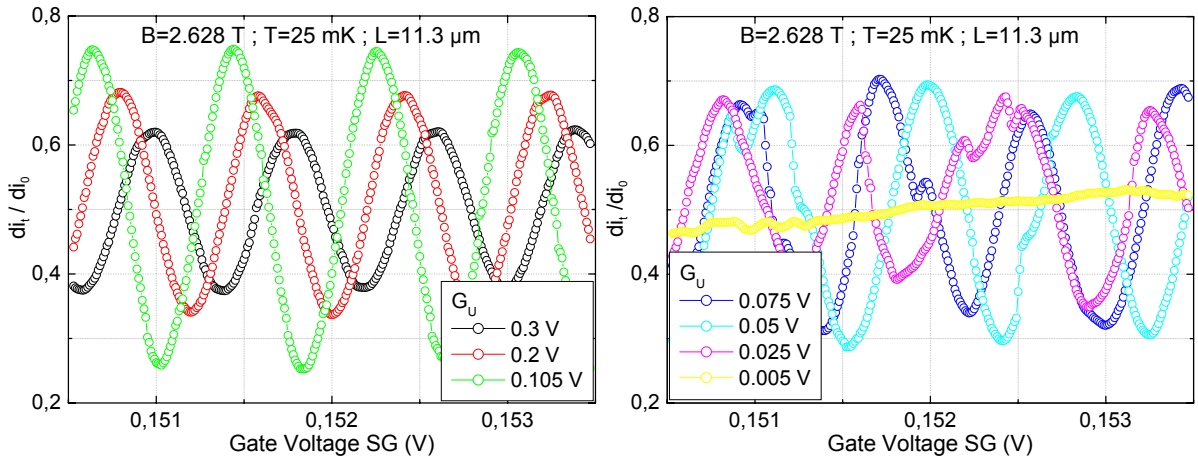

Figure 7.6.: *Interferences revealed with the side gate SG, (left) for $V_{G_U} \in [0.105; 0.3]$ V, before localization of the IES, (right) and after, for $V_{G_U} \in [0; 0.075]$ V, where the interference signal is no longer a pure cosine because of stochastic charging of the closed IES dots.*

Measuring the coupling

We use the same method than before (chapter 4) to measure the coupling parameter V_0 between ESs in the upper arm.

As long as the IES is connected to contact n°2, its potential is defined by contact n°2, and we can use it as a gate to reveal the interferences, although it becomes less coupled to the upper arm of the interferometer as it is deformed. This is done by sweeping the voltage applied to contact n°2, namely V_2. When closing G_U, we manage to reveal interferences down to $V_{G_U} = 0.08$ V, only, we need to sweep V_2 on a larger domain because the period of the interferences V_0, increases from 25 μV to 80 μV (Figs. 7.7 (a) and 7.7 (b)) as the coupling between the IES and the upper arm of the MZI is decreasing.

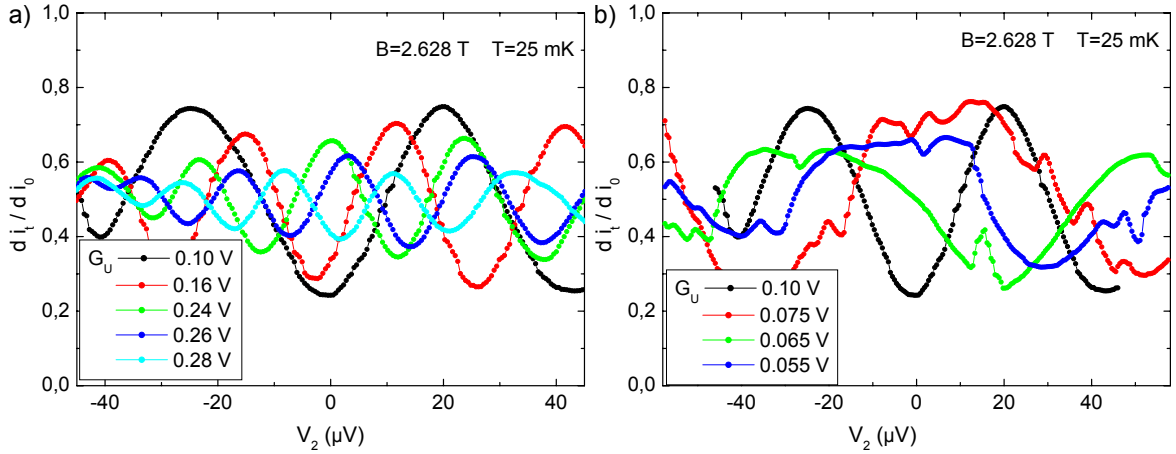

Figure 7.7.: *Interferences revealed with the upper IES used as a gate, (a) before localization of the IES ($V_{G_U} \in [0.1; 0.055]$ V), (b) and across ($V_{G_U} \in [0.1; 0.28]$ V). As G_U is closing, the amplitude and period V_0 of the oscillations increase, then the amplitude saturates while the periodicity V_0 doubles. At localization, a stochastic phase shift appears, uncorrelated with the side gate voltage, probably from stochastic charging of the IES dots when their energy levels are aligned with the Fermi energy. These phase shifts hinder the determination of V_0.*

At some point, this method is no longer suitable to measure V_0 which becomes too large. Additionally, when the IES is localized in small closed dots, stochastic phase shifts appear in the interference signal, probably caused by electron tunneling from contact n°2 towards the IES dots, when their energy levels are aligned with the Fermi energy. These phase shifts deform the interferences and impede the direct determination of V_0. We then extract V_0 from the interference signal induced by the IES in the upper arm (see Fig. 7.8 and appendix B).

Finally, V_0 increases sharply at $V_{G_U} = 0.08$ V to reach a plateau at 120 μV (Fig. 7.9 (b)), this is a sign that we have reached localization of the IES for the IES and that it is disconnected from contact n°2. We still manage to reveal the interferences, *via* the counterpropagating OES injected at contact n°2 – along the top edge of the sample, in blue on Fig. 7.2 (bottom) – in the same manner than previously the IES is used to reveal the interferences through its capacitive coupling to the upper arm of the interferometer. It is indeed coupled to the upper arm of the interferometer through the closed loops of the IES.

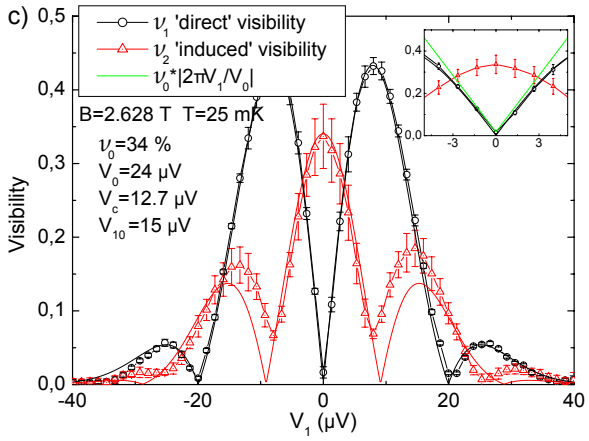

Figure 7.8: *Fitting the visibility of the induced signal by the adjacent IES in the upper arm as function of the voltage bias V_1 also yields an estimation of V_0 (appendix B).*

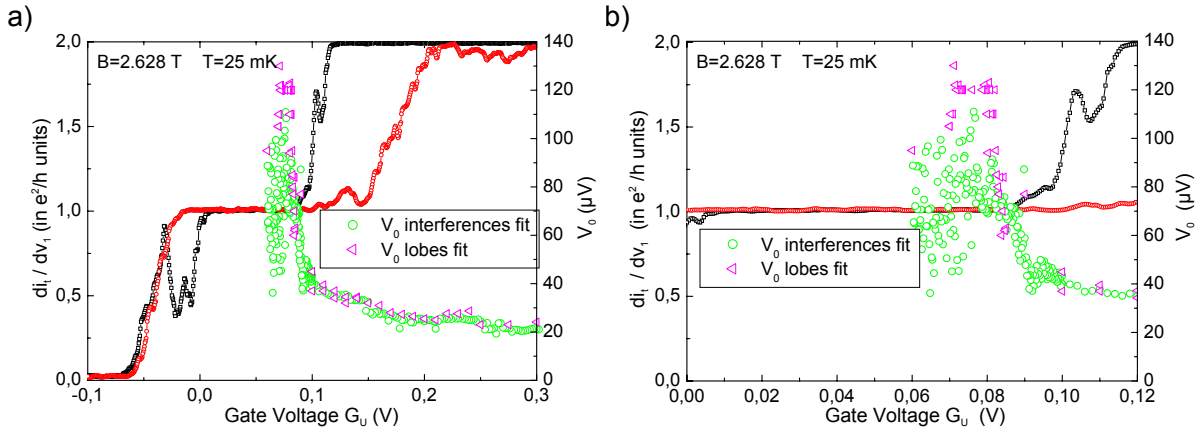

Figure 7.9.: *On all graphs G_U transmission through the upper (red curve) and the lower arm (black curve) are figured on the left scale. On the right scale, as function of V_{G_U}: (a) V_0 rises slowly from 25 μV to 60 μV as $\mathcal{T}_U$ decreases from 1 to 0.5 because of the deformation of the IES. It increases sharply at $\mathcal{T}_U = 0.5$ when the IES is disconnected from contact n°2. (b) Zoom. At localization of the IES, V_0 rises sharply and then stabilizes to 120 μV.*

7.3.2. Correlation between coupling and visibility

As long as the IES is connected to contact n°2 ($V_{G_U} \geq 0.08$ V), the visibility and the coupling are correlated: the visibility increases with V_0 (Figs. 7.9 (a) and 7.10 (a)).

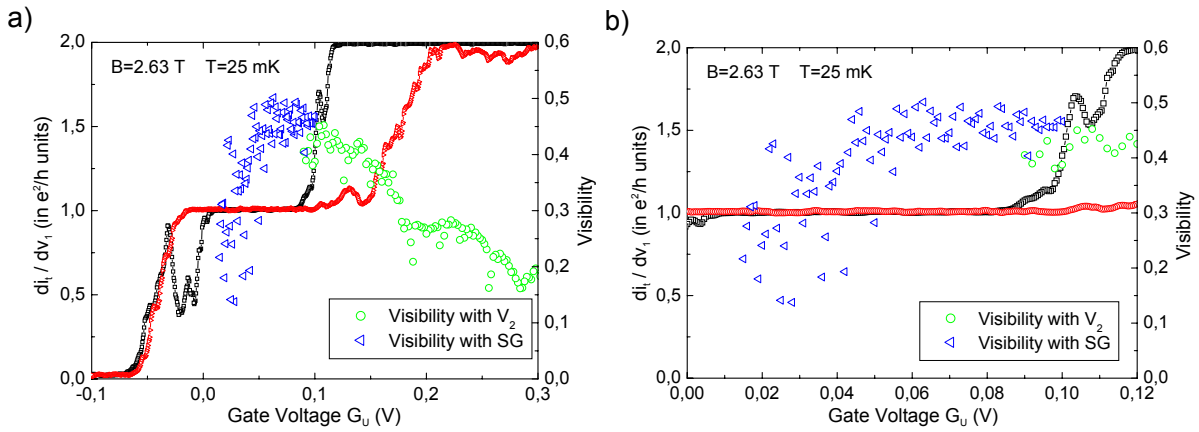

Figure 7.10.: *On all graphs G_U transmission through the upper (red curve) and the lower arm (black curve) are figured on the left scale. On the right scale, as function of V_{G_U}: (a) The visibility increases with V_0 until localization of the IES where it saturates. (b) Zoom. The visibility remains constant far into the $\mathcal{T}_U = 0.5$ plateau. It finally decreases because of detuning as we have checked by seeing the departure of the mean transmission from the optimum value when tuned (Fig. 7.5 (top)).*

This is compatible with our earlier results which make the coupling between the interfering arms of the MZI and the noisy IES responsible for the limitation of the coherence length at zero bias and finite temperature. Indeed the strength of the coupling between the upper arm and the IES connected to contact n°2 is directly V_0^{-1}, which we are able to measure and control. We find that when we decrease this coupling, the visibility increases, meaning that coherence is strengthened!

However, at $V_{G_U} = 0.08$ V, as we reach $\mathcal{T}_U = 0$ and as the IES is localized in small closed loops disconnected from contact n°2, there is a sharp increase of V_0, while at the same time the visibility saturates at 50 %. Then V_0 stabilizes. The saturation of the visibility lasts until $V_{G_U} = 0.05$ V (middle of the plateau) where the detuning of the interferometer becomes significant and reduces the visibility (this is seen through the mean value of the differential transmission of the OES which departs from 0.5 on Fig. 7.5).

7.3.3. A relevant effect?

A question we are entitled to ask is whether this enhancement of visibility is not simply caused by the fine-tuning of the interferometer's symmetry between the upper and lower arm when changing G_U polarization. Assuming that the drift velocity is the same in both arms and remains constant, if the lengths of the arms of the interferometer differ, the two components of the wave packet entering the interferometer do not overlap exactly in the outgoing signal, reducing the visibility of the interferences. This is the so-called *thermal smearing* already explained in ¶ 5.4.2

Thermal smearing

At finite temperature T, a difference of length $\Delta L_\varphi = L_u - L_d$ between the arms of the interferometer gives rise to an averaged phase difference of order $k_B T \times \Delta L/\hbar v_d$ (see ¶ 5.4.2) [79]. In a non interacting model, the visibility is then given by:

$$\mathcal{V} = \mathcal{V}_0 \, \frac{T/T_T}{\sinh\left(T/T_T\right)} \quad \text{with} \quad T_T = \frac{\hbar v_D}{\pi k_B \Delta L} \tag{7.5}$$

The asymmetry of the interferometer is responsible for a decay of the visibility with the temperature, which becomes exponential when $T \gtrsim T_T$. This decay is easily understood: the phase difference at energy ε away from the Fermi energy is $\varphi(\varepsilon) = \varepsilon \Delta L/\hbar v_d + \varphi_F$, where $\varphi_F = 2\pi\Phi_B/\Phi_0$ is the phase at the Fermi energy. If $\Delta L \neq 0$, the phase difference depends on the energy of the electrons, and then at finite temperature the broadening of the Fermi distribution blurs the interferences.

It is possible that by changing V_{G_U}, L_U and the drift velocity in the upper arm are affected, 'improving the symmetry' of the interferometer. A change in the surface enclosed by both arms was indeed measured on Fig. 7.1 (right) upon changing V_{G_U}. If thermal smearing were responsible for the temperature dependence of the interference visibility, an improvement of the symmetry of the MZI arms would decrease the thermal decay rate T_T^{-1}, and the sample being at a finite temperature, the visibility would increase.

Impact of the upper gate on the arm length

To answer this criticism, we can first adress the following questions: is L_U shortened or lengthened under the action of G_U? by how much? and the follow-up question: how does it affect the accumulated phase along the upper arm?

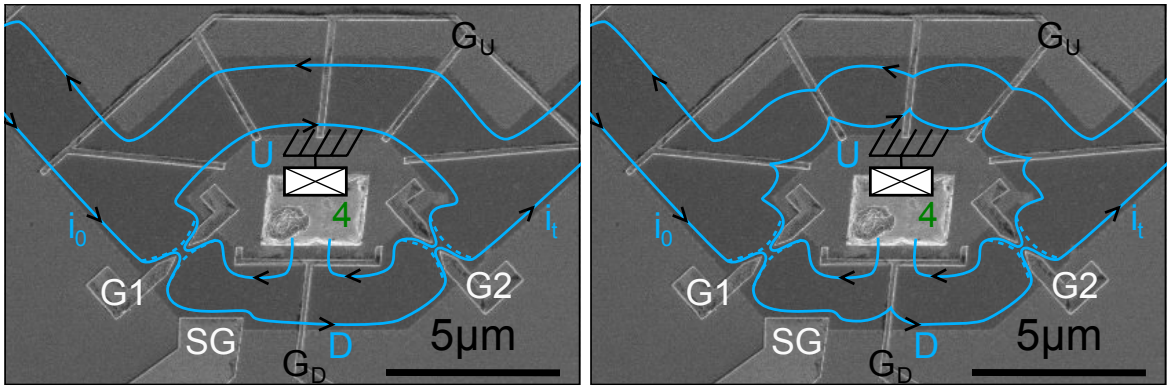

Figure 7.11.: *Schematic of the OES path with G_U and G_D open (left), and with G_U and G_D pinched (right): the OES is deformed so that the lengths of the upper and lower arm of the interferometer are increased. The IES is not figured.*

The answer to the first question comes from the data shown on Fig. 7.1 (right) where we see that the periodicity of the interferences with respect to the magnetic field decreases as V_{G_U} decreases, showing that the surface enclosed by the two arms of the interferometer $\mathcal{S}$ increases as G_U is closing. We easily see, by drawing a simple schematic that this is achieved by lengthening the upper arm (see Fig. 7.11).

Then when V_{G_U} goes from 0.3 V to 0.1 V, L_U increases by $\Delta L_U \geq 0$. To make an estimation of ΔL_U we slowly sweep V_{G_U} from 0.3 V to 0.1 V and count the fringes we see in between (Fig. 7.12). We count 257 fringes. Unfortunately we did not sweep V_{G_U} until 0.08 V where we believe that localization of the IES occurs. However we can extrapolate the curve of Fig. 7.12 (right) with a 2^{nd} degree polynom. We find that it would take around 62 extra fringes to reach 0.08 V, which makes $N \approx 319$.

This means that between $V_{G_U} = 0.3$ V and $V_{G_U} = 0.08$ V (localization of the IES), the magnetic flux enclosed by the arms of the interferometer has varied by $\Delta\Phi_B = N\Phi_0$, and the surface enclosed by the arms has varied by $\Delta\mathcal{S} = \Delta\Phi_B/B = N\Phi_0/B$. For $B = 2.628$ T and $N = 319$, we find $\Delta\mathcal{S} = 0.503 \pm (0.002 \times \delta N)$ μm^2, where δN is the error on the number of fringes. This estimation is compatible with, but more precise than the one from the interferences as function of the magnetic field which gives $\Delta S = 0.7 \pm 0.2$ μm^2.

If we consider that the surface $\mathcal{S}$ is a disk of perimeter $L_U + L_D$ ($\mathcal{S} = 40.0 \pm 0.1$ μm^2 from § 7.2) and that the deformation on the upper arm is uniform, then the corresponding

variation of L_U under the action of G_U is:

$$\Delta L_U = \sqrt{\frac{\pi}{\mathcal{S}}}\,\Delta\mathcal{S} = 141.0 \pm (0.5 \times \delta N)\ \text{nm} \tag{7.6}$$

where we considered $\Delta\mathcal{S} = 0.503 \pm (0.002 \times \delta N)\ \mu$m, obtained with $N = 319$.

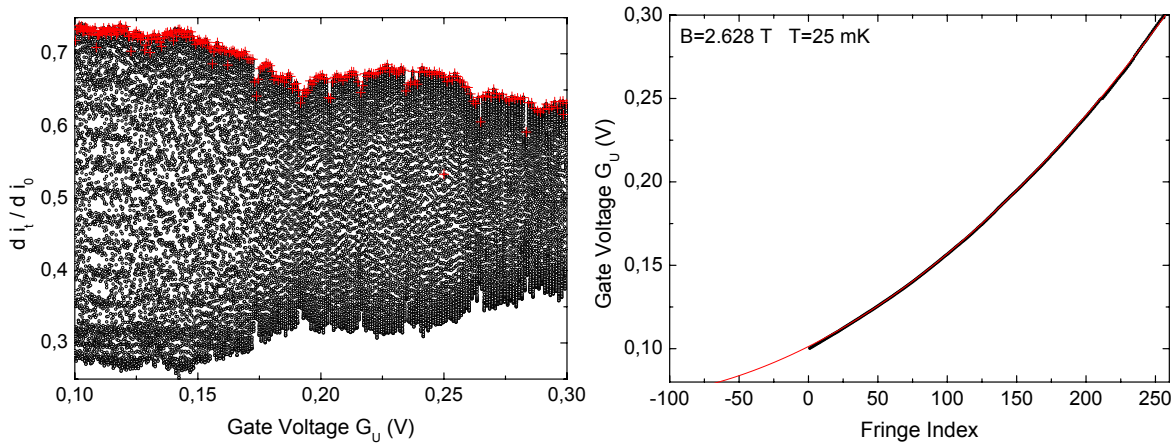

Figure 7.12.: *(left) Interferences in the differential transmission of the OES, revealed with G_U. As G_U is closing, the path of the OES which constitutes the upper arm is deformed and its length changes. The amplitude increases as the IES transmission decreases. Red crosses mark the positions of the fringes. (right) For V_{G_U} from 0.3 V to 0.1 V, we manage to reveal $N = 257$ fringes. The fringe index, hence the variation of the accumulated phase on the upper arm, is not linear with the gate voltage: it accelerates when getting closer to localization of the IES.*

Impact of the upper gate on the drift velocity

To answer the question 'what is the impact of G_U on the accumulated phase on the upper arm?' we must know how G_U affects the drift velocity.

The accumulated phase on the upper(lower) arm is $\varphi_U = \varepsilon L_U/\hbar v_{d,U}(\varphi_D = \varepsilon L_D/\hbar v_{d,D})$, with $v_{d,U}(v_{d,D})$ the drift velocity in the upper(lower) arm. The difference of phase accumulated in each arm is given by:

$$\varphi = \varphi_U - \varphi_D = \frac{\varepsilon}{\hbar}\left(\frac{L_U}{v_{d,U}} - \frac{L_D}{v_{d,D}}\right) \tag{7.7}$$

If the drift velocity is the same in both arms and remains constant equal to v_d under the action of G_U then $\varphi = \varepsilon\Delta L/\hbar v_d$, where $\Delta L = L_U - L_D$.

The length difference between the two arms is relevant provided that v_d is constant. However, this is probably not the case here since we modify strongly the electrical potential landscape when we change the transmission of G_U. Then we cannot say how φ_U evolves with V_{G_U} whitout knowing how $v_{d,U}$ is affected.

By looking at the sketch Fig. 7.13 with the equipotential lines, we see that when G_U is closing, the bottom of the potential is raised at the places where G_U fingers are. The electron following an equipotential line, its path along the upper arm is lengthened as we already remarked, but the slope of the potential along the equipotential is also weakened. Thus the drift velocity at these places is decreased. In short: as G_U is closed, the path of the electron in the upper arm is deformed, e.g. lengthened at the places where the fingers constituting G_U are found and where the bottom of the electrical potential is raised. At the same time the electron slows down at these places. We see then that the effect of G_U when pinched, both on L_U and $v_{d,U}$ is to increase the accumultated phase on the upper arm, φ_U.

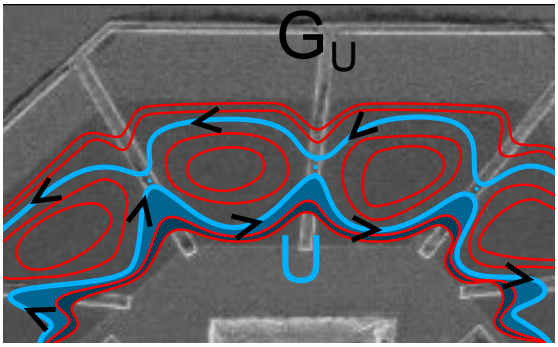

Figure 7.13.: *Schematic of the potential landscape in the upper arm. As the red solid lines (isopotential lines) spacing increases, the landscape becomes flatter and the drift velocity decreases. The OES path just before G_U pinch-off is figured by the turquoise solid line. The area in dark(lighter) blue corresponds to the surface increase $\Delta\mathcal{S}$ when pinching G_U a little(a lot). $\Delta\mathcal{S}$ increases as one gets closer to pinch-off.*

A contradictor can then argue that the enhancement of visibility we observe is caused by this increase of φ_U. It would mean that when G_U is open $\varphi_U < \varphi_D$, and that we reduce the phase difference $|\varphi| = |\varphi_U - \varphi_D|$ when pinching G_U. It is noteworthy that the visibility is not affected on the plateau corresponding on a perfectly transmitted OES and a fully reflected IES, suggesting that the coherence increase is not a tuning effect.

Non linearity of the phase variation with V_{G_U} To explain the observed non linearity of the variation of the phase accumulated on the upper arm with the gate voltage V_{G_U} on Fig. 7.12 (right) [1], one can argue than when getting closer to the localization of the IES value ($V_{G_U} = 0.08$ V), the potential landscape at the points delimitating the future dots becomes flatter so that the displacement of the OES path becomes more sensitive to a change in V_{G_U} (Fig. 7.13). Hence the observed acceleration of the fringe index variation with V_{G_U} on Fig. 7.12 (right).

Effect of the lower gate

We see that pinching G_D deforms the lower arm of the intererometer as well (Fig. 7.11). The same reasoning than before tells us that the effect on both L_D and $v_{d,D}$ is to increase the accumulated phase φ_D along the lower arm. As for G_U we can evaluate how many fringes we pass between two values of V_{G_D}. This is what has been done on Fig. 7.14.

We find $N = 90$ fringes between $V_{G_D} = 0.23$ V and $V_{G_D} = 0.1$ V: G_D is smaller than G_U and does not deform the lower arm as much as G_U deforms the upper arm.

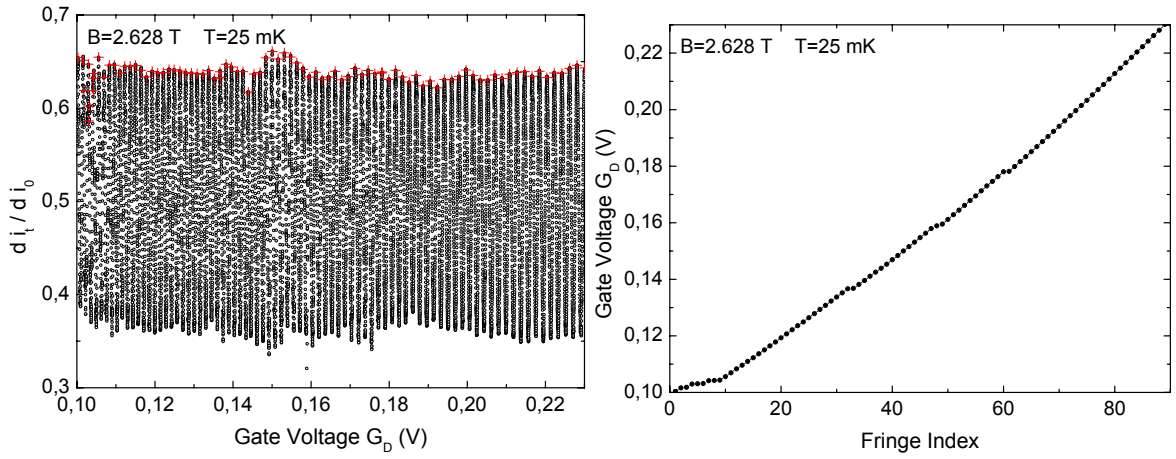

Figure 7.14.: *(left) Interferences in the OES differential transmission, revealed with G_D. As G_D is closing, the path of the ES forming the upper arm is deformed and its length changes. Red crosses mark the positions of the fringes. (right) For V_{G_D} from 0.23 V to 0.1 V, we manage to reveal $N = 90$ fringes.*

We can be more specific: the deformation of the surface $\mathcal{S}$ comes mostly from the deformation of the trajectory below the fingers. There are five fingers on G_U and only one on

[1] This non linearity is present for G_D with a lower amplitude (see Fig. 7.14 (right)).

G_D. Then when sweeping G_D from $V_{G_D} = 0.23$ V to 0.1 V, we expect to see a number of fringes of the order of $200/5 = 40$, since 200 corresponds more or less to the number of fringes for V_{G_U} varying from 0.23 V to 0.1 V. Instead, we see 90 fringes, e.g. twice more fringes than expected! Does it means that some finger is not working properly in the upper arm, hence explaining why we do not have a freezing of the charge fluctuations (§ 7.4)? We previously estimated that the density in the lower arm was larger than the one in the upper by ≈ 8 %. This would make G_U more 'efficient' than G_D in depleting the 2DEG below so as to 'see more fringes' when sweeping V_{G_U} than when sweeping V_{G_D} by the same amount. However the density mismatch is small.

We are interested in the effect G_D has on the visibility of the interferences: starting from a situation where both G_U and G_D are open, pinching G_U will increase φ_U and the interferences visibility. If this is a tuning effect of the MZI then it means that we started from a situation where $\varphi_U < \varphi_D$. Pinching G_D will increase φ_D. Then it should also increase the interferometer asymmetry further and decrease the interferences visibility. On our first try, this is what is observed (red points on Fig. 7.15 (right)).

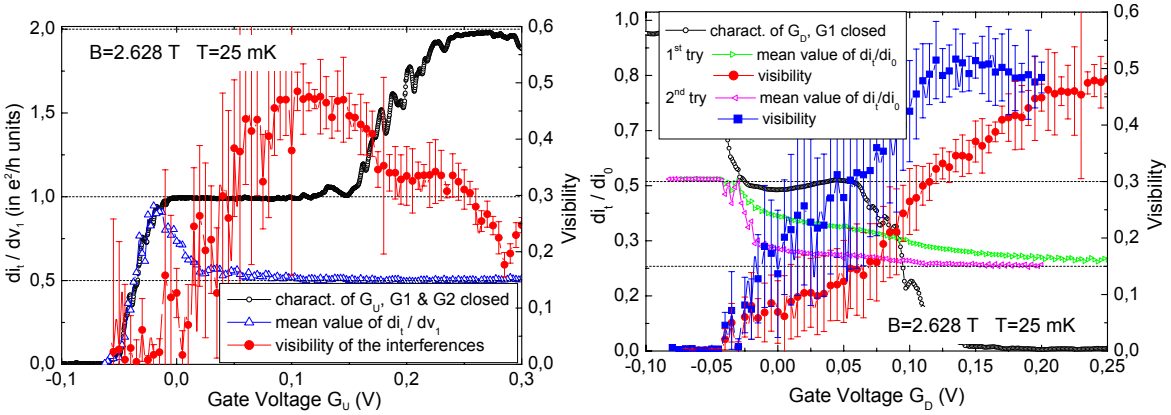

Figure 7.15.: *(left) Left scale: (black circles) G_U characteristic through the upper arm. Right scale: (red full circles) interferences visibility. As the IES transmission decreases, visibility doubles, is stable on the first half of the* $\mathrm{d}i_t/\mathrm{d}i_0 = 0.5$ *plateau, then decreases as detuning becomes significant as seen in the departure of* $\langle \mathrm{d}i_t/\mathrm{d}i_0 \rangle_{osc}$ *from* 0.25 *(blue open triangles). (right) Left scale: (black circles) G_D characteristic, G1 closed. Right scale: interferences visibility. (red full circles) MZI tuned for G_U open, with $V_{G_U} = 0.1$ V. The visibility decreases steadily as G_D is closing. (blue full squares) MZI is tuned for $V_{G_U} = 0.1$ V, the visibility increases slightly before decreasing. MZI detuning is seen through (green triangles) 1^{st} try, and (magneta triangles) 2^{nd} try. Detuning far stronger in the 1^{st} try might explain the absence of a visibility maximum.*

However, when we look at the mean value of the differential transmission as function of V_{G_D}, we see that it departs from its standard value for a well tuned interferometer with respect to $\mathcal{T}_1 = \mathcal{T}_2 = 0.5$: cross-talk between G_D and $G1/G2$ is not negligible, so that we have to ajust V_{G1} and V_{G2} to get a relevant result. This has been done on our second try. Eventually we see a small maximum of the visibility around $V_{G_D} = 0.12\ V$ (blue squares on Fig. 7.15 (right)). G_D doesn't seem to have an effect as strong as G_U, the reason for this is not known. Anyway, increasing φ_D doesn't decrease the interferometer visibility.

This invalidates the critic mentioned before: we have shown that the enhancement of visibility we observe when pinching G_U is *not* due to a tuning of the symmetry of the interferometer. It seems that the reason for this is that we decouple the interfering OES in the upper arm from the IES.

With G_U we are able to control and in particular, weaken the coupling between the noisy ES coming from the ohmic contact n°2, and the visibility seems to be correlated to V_0 (it increases) as long as $V_{G_U} \geq 0.08$ V.

One puzzling fact remains concerning the data presented on Fig. 7.9 (b) and Fig. 7.10 (b): when $V_{G_U} \leq 0.08$ V, the coupling sharply decreases while the visibility saturates. We have no difficutly in understanding the sharp increase of V_0 at localization of the IES, but then if dephasing results from the coupling of the OES in the upper arm to the opposite counter-propagating OES through the dots formed by the IES, the visibility should increase accordingly, which is not the case.

7.4. A puzzling transition

7.4.1. Expectations

As we have already pointed out, there is a capacitive coupling between the IES and the arms of the interferometer. We are able to measure the static coupling V_0^{-1} between the IES and the OES in the upper arm of the interferometer. Because of this coupling, potential fluctuations in the IES are directly reflected on the phase of the electrons travelling in the arms of the interferometer, affecting the visibility. The conclusion of our group's previous work [1, 3] is that excitations of the IES (thermal charge fluctuations) are responsible for the temperature dependence of the visibility and its limited coherence length.

When closing G_U , as long as the IES is connected to contact n°2 in the upper arm, the static coupling V_0^{-1} between ESs decreases continuously probably because of the deformation of the IES path. Thermal charge fluctuations on the IES should have a decreasing impact on the loss of coherence on the upper arm of the interferometer and the visibility should increases as the coupling decreases in a correlated manner.

A measurement of the temperature dependence of the visibility would yield an exponential decay with a temperature rate T_φ^{-1} decreasing proportionally to the coupling V_0^{-1}. This variation of the coherence length with the coupling parameter V_0^{-1} (controlled by G_U) would confirm the observation of such a behavior when varying the magnetic field [1]. This measurement is done in ¶ 7.5.1.

7.4.2. Localization of the IES

At localization, the IES in the upper arm is formed of small closed loops which are no longer connected to ohmic contact n°2. In principle, these closed loops open a gap in the excitations at the dot. This gap in the excitations prevents any charge fluctuations inside the dot, as long as the available energy is negligible compared to the gap's value.

One important question is then the real value of this gap. Also, do the small dots close at the same time or close at all? Does a 'zero mode' for the dots (displacement of the mass center) exist, leading to charge fluctuations in the environment of the IES? ...

Evolution of the coupling

Let us explain the sudden increase of V_0 at localization of the IES. We compare the situations just before and after localization of the IES ($V_{G_U} \approx 0.08$ V): when decreasing V_{G_U}, V_0 jumps from 60 μV to 120 μV. This can be explained if we consider that one can modelize this by a transition from the situation of Fig. 7.16 (left) when $V_{G_U} > 0.08$ V to the situation of Fig. 7.16 (right) when $V_{G_U} < 0.08$ V.

Just before localization, the potential of the IES adjacent to the upper arm is still defined by contact n°2 to which it is connected. After localization however, the adjacent IES is diconnected from contact n°2 and becomes floating. The counter-propagating OES is still connected to contact n°2 which defines its electrical potential. Now its the OES which couples the potential fluctuations of contact n°2 to the upper arm. The coupling occurs through the closed loops formed by the floating IES.

If we follow the model developped by Roulleau *et al.* and reported in appendix A, in the low frequency limit, the coupling between the OES and the adjacent IES is given by $V_0 \propto 2C_Q^{-1} + C^{-1}$, and as already said in our mean field approach in ¶ 4.4.4, the geometrical capacitance is negligible compared to the quantum capacitance ($C \ll C_Q$), so that $V_0 \propto C^{-1}$ as represented on Fig. 7.16. It is then straightfoward to see that the coupling V_0^{-1} should be divided by 2 when going from the situation before localization of the IES to the situation after. This is roughly what is observed.

However, this is for zero mode excitation of the ES. What about finite wave vectors? Indeed, if the IES is actually confined into small closed loops, there should be a radical change in the spectrum of the excitations of the IES in the upper arm occuring when we reach localization of the IES.

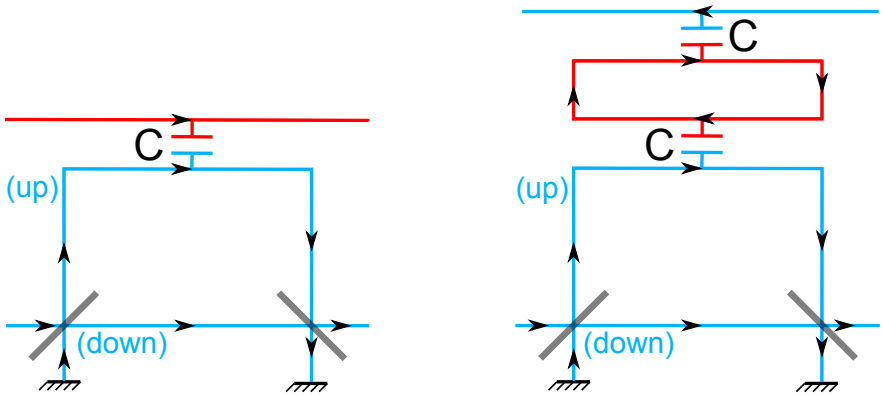

Figure 7.16.: *Schematic of the MZI in the low frequency limit and in the case $C \ll C_Q$. (left) Schematic of the ESs before IES localization. The OES in the upper arm (blue) is coupled to the noisy IES (red) through capacitance C. (right) After localization, the OES is coupled to the counterpropagating OES through the IES loop with two capacitances C in series.*

Opening a gap in the excitations of the IES?

When the new gates G_U and G_D are at localization, the IES in the upper and lower arm is disconnected from contacts n°2 and n°4 and confined into dots. Because of the confinement, the dots energies become quantized. The size of the gap in the IES excitation spectrum is $\Delta E_{\text{loop}} = hv_D/L_{\text{loop}}$. If we estimate the drift velocity about $v_D \sim 5 \times 10^4$ m.s^{-1}, and the loop perimeter $L_{loop} \sim 8$ μm, we find a separation in energy between levels $\Delta E_{\text{loop}} \sim 26$ μeV which corresponds to a temperature of ~ 300 mK.

However, the value of the drift velocity can vary greatly and is not known with a great accuracy [13]. We do not know the size of the dots either: G_U and G_D might not perform in accordance with the schematic of Fig. 7.2 (bottom) and form larger dots (L_{loop} up to 30 μm), thus dividing the gap value by up to ~ 4. In the future, we want to implement independent gates to better control the formation of dots and the opening of the gap.

As seen in ¶ 4.3.3, thermal charge fluctuations in the counter-propagating OES couple to the upper arm through the closed dots of the IES. We have just determined that the coupling is divided by ~ 2 compared to the situation just before localization of the IES. If the gap estimation is correct, charge fluctuations in the IES for energies below ~ 26 μeV ($T \lesssim 300$ mK) should be frozen because of the opening of a gap in the spectrum of the IES excitations as the IES is localized in small closed loops. This should translate into a radical improvement of the coherence. However the visibility saturates as the coupling is divided by ~ 2 at localization of the IES.

According to the works of the LPN group, energy relaxation in the OES which occurs through energy exchange with the IES is also frozen as the IES is localized in small closed loops. If energy relaxation plays a role in the lobe pattern of the visibility, we should see a change at localization of the IES like a sharp increase of the central lobe width. As we will see later, this is not observed either.

An possible explanation is that the IES is not confined into loops of length L_{loop} small enough for the gap opening to be significant. We actually cannot know the loops size. Another reason could be that $v_{d,U}$ is smaller than expected. In both instances, if the gap is not large enough, there is no freezing of the excitations of the IES, consequently charge fluctuations in the IES still occur and contribute to dephasing of the electrons in the upper arm of the interferometer through capacitive coupling V_0^{-1} (the one measured just before localization of the IES) however disminished. This could explain why the visibility saturates while the coupling to contact n°2 is divided by ~ 2.

In this experiment we have measured the evolution of the visibility and the coupling with the gate voltage applied to the 'magic gate' G_U at the base temperature. While we do observe a clear correlation between $\mathcal{V}$ and V_0^{-1}, we have to show that the temperature dependence itself is modified by G_U to check that coherence is indeed strengthened. These temperature measurements are reported in the following section. Next we will try to understand what type of mechanism account for our observations.

7.5. Temperature dependence

7.5.1. Temperature measurements

The visibility decays exponentially with the temperature (chapter 4). How does the temperature decay rate, ${T_\varphi}^{-1}$, changes with G_U? For temperatures from 23 to 50 mK and for V_{G_U} from 0.4 V to 0.09 V, we reveal the interferences and measure V_0 (Fig. 7.17 (left)), as explained in ¶ 7.3.1. We then plot the visibility as function of the temperature for various values of V_{G_U} in a semi-log plot. We obtain an array of straight curves (Fig. 7.17 (right)).

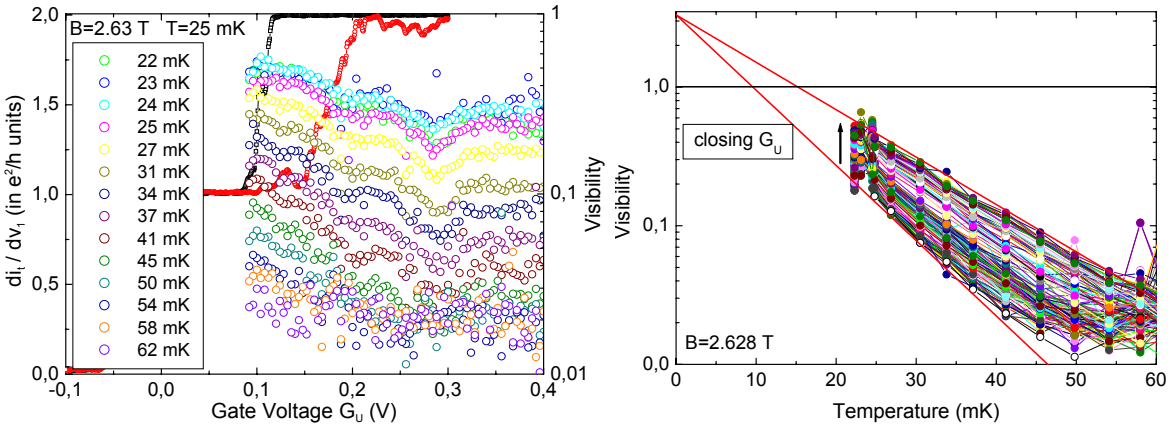

Figure 7.17.: *(left) Left scale: G_U characteristics. Right scale: semi-log plot of visibility as function of the gate voltage V_{G_U}, for different temperatures $T \in [22\ ;\ 62]$ mK. (right) Same data as function of the temperature for $V_{G_U} \in [0.09\ ;\ 0.4]$ V, showing the exponential decay of the visibility. The decay rate T_φ^{-1} decreases as the IES transmission $\mathcal{T}_U$ goes from 1 to 0.*

Their slope, ${T_\varphi}^{-1}$, decreases as G_U is closing e.g. the visibility depends less on the temperature as the coupling lessens. Solid red lines on Fig. 7.17 (right) are guides to the eye and give a visibility larger than one at zero temperature: there is probably a cross-over, that we cannot observe since it occurs at temperatures lower than the base temperature (23 mK), between two regimes [42]. For temperatures above the visibility decays exponentiallly with the temperature, and for temperatures below, it saturates. Red lines converge on the y-axis, suggesting that both T_φ^{-1} and the cross-over temperature change with V_{G_U}.

Thermal dephasing has two contributions: one induced on both arms of the interferometer by thermal noise and another which is due to the asymmetry of the interferometer. We are now interested in the latter one.

7.5.2. Estimation of thermal smearing

The temperature rate T_T^{-1} of the thermal smearing is given by (¶ 5.4.2):

$$T_T^{-1} = \frac{\pi k_B \Delta L}{\hbar v_d} = \pi k_B \left(\frac{\partial \varphi}{\partial \varepsilon}\right)_{(\varepsilon=0)} \tag{7.8}$$

To obtain T_T^{-1} we just have to measure the phase variation with the bias around zero bias, since $(\partial\varphi/\partial\varepsilon) = (\partial\varphi/\partial\,(eV_1))$. A good point is that we don't need to know the precise value of the drift velocity or the assymetry ΔL of the MZI.

For a given value of V_{G_U}, the differential conductance is plotted in a colorplot, as function of the bias voltage V_1 applied on the injecting ohmic contact (contact n°1) and of the side gate voltage which reveals the interferences (Fig. 7.18). The bending of the central lobe gives the energy dependence of the phase of the oscillations. We measure T_T^{-1} for different values of V_{G_U} ranging from 0.3 to 0.09 V and find that it decreases slightly and that its mean value is (Fig. 7.21):

$$\left\langle T_T^{-1} \right\rangle \approx 16 \pm 5 \text{ K}^{-1} \tag{7.9}$$

Then $T_T \approx 60$ mK, we are not in the limit $T \gtrsim T_T$ where the thermal smearing contribution to the temperature decay of the visibility is exponential. Therefore T_T^{-1} cannot be simply added to the non-trivial contribution. A precise estimation of the thermal smearing effective (additive) contribution yields 5 K^{-1}.

On Fig. 7.21 we reported the evolution of the non corrected temperature decay rate T_φ^{-1} (ref filled squares), the thermal smearing temperature rate T_T^{-1}, along with the corrected temperature decay rate T_φ^{-1} (blue solid line), as function of the gate voltage V_{G_U}: the correction is slight, thermal smearing does not contribute much to the temperature decay rate. This is compatible with the conclusion of ¶ 7.3.3 which stated that an improvement of the symmetry of the MZI arms could not explain the spectacular improvement of the zero bias visibility when pinching G_U.

Before analyzing the other contributions to the temperature decay of the visiility, we explore further the thermal smearing to draw some interesting information: we make a rough estimation of the drift velocity using two different methods and then conclude on the gap estimation.

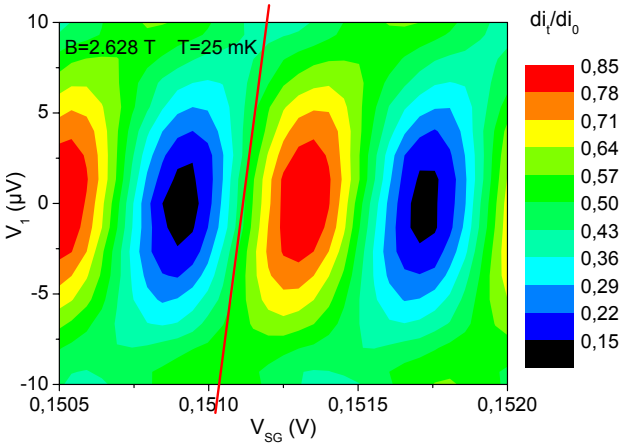

Figure 7.18: *Colorplot of the differential transmission as a function of V_{SG} along the x-axis and V_1 along the y-axis. Only the central lobe is shown. For each of these plots for a given value of V_{G_U}, the parameter T_T^{-1} is extracted from the central lobe bending.*

Rough estimation of the drift velocity

From the decrease of the thermal smearing Thermal smearing is not constant when pinching G_U as can be seen on Fig. 7.19: though T_T^{-1} fluctuates a lot, one sees that it globally decreases when G_U closes. This decrease is evaluated to be

$$\delta T_T^{-1} = 7 \pm 5 \text{ K}^{-1} \tag{7.10}$$

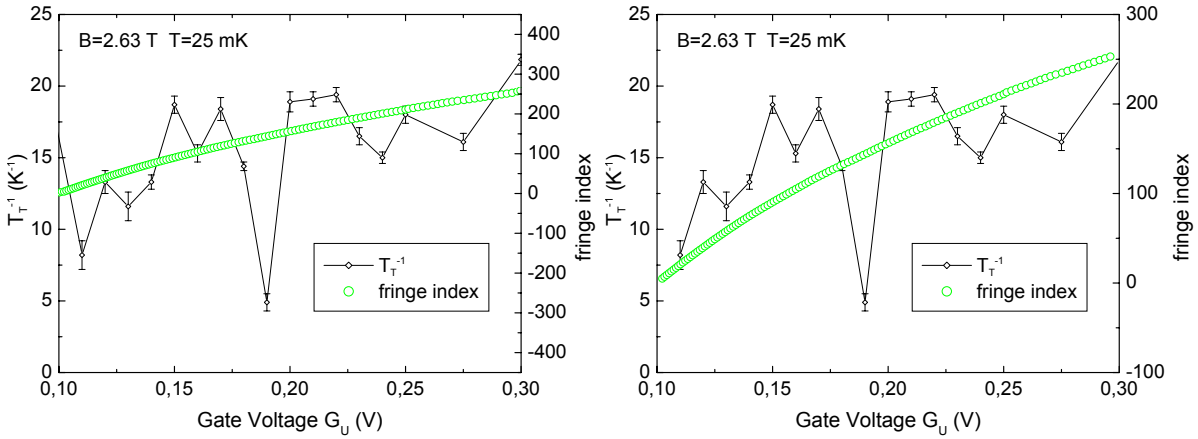

Figure 7.19.: *T_T^{-1} (left scale, black line) and fringe index (right scale, green circles) as function of V_{G_U}. A mapping yields for v_d: (left)* 1 *and (right)* 0.4×10^4 *m.s^{-1} (extreme case)*

Knowing the variation of the length difference ($\delta(\Delta L) = 143$ nm from ¶ 7.3.3), we can make an estimation of the drift velocity v_d, assuming it remains the same in both arms when V_{G_U} changes. Indeed, $v_d = (\pi k_B/\hbar)\ \delta(\Delta L)/\delta T_T^{-1}$, which yields

$$0.5 \times 10^4 \text{ m.s}^{-1} \lesssim v_d \lesssim 3 \times 10^4 \text{ m.s}^{-1} \tag{7.11}$$

This estimation of the drift velocity is 2 to 10 times smaller than the one used in Ref. [15] ($v_d \sim 5 \times 10^4$ m.s^{-1}). The uncertainty on this estimation of v_d is great because of the uncertainty on δT_T^{-1} which is also important.

From the estimation of the asymmetry ΔL On Fig. 7.19 (left) we see the correlation between δT_T^{-1} and $\delta(\Delta L)$ as G_U is closing. This reinforces the idea that the asymmetry of the interferometer is responsible for the energy dependence of the interferences phase. It also provides us with an estimation of this asymmetry: if T_T^{-1} is indeed proportional to the asymmetry of the interferometer, it would take $N = 800$ fringes to annul T_T^{-1} from $V_{G_U} = 0.3$ V, which corresponds to

$$\Delta L = \sqrt{\frac{\pi}{\mathcal{S}}}\,\frac{\Phi_0}{B} \times N = 354 \text{ nm} \quad \text{and} \quad v_d = 1 \times 10^4 \text{ m}.s^{-1} \tag{7.12}$$

with $T_T^{-1} = 16$ K^{-1}. The 'extreme' mapping of Fig. 7.19 (right) provide us with a lower bound for ΔL and v_d: we estimate $N_{\min} = 350$, then

$$(\Delta L)_{\min} = 154 \text{ nm} \quad \text{and} \quad (v_d)_{\min} = 0.4 \times 10^4 \text{ m.s}^{-1} \tag{7.13}$$

Both estimations are compatible with Eq. (7.11) suggesting that the decrease of thermal smearing is indeed caused by an improvement of the symmetry between the MZI arms.

However, a large uncertainty comes from the subjectivity of the fitting procedure, and from the relation linking the area and the trajectory length. The relation obtained by assimilating the paths to half circles is approximate: the real trajectory is affected by disorder and the upper gate probably deforms the ES as represented on Fig. 7.11 (right).

This leads to an approximate value of ΔL, more precisely to an underestimated value of ΔL and as a consequence, to an underestimated value of the drift velocity.

However approximate, both these approaches lead to a value of the drift velocity smaller than expected, affecting the gap estimation.

Consequence on the gap estimation

It is then possible that we overestimate the actual value of the drift velocity and hence overestimate the value of the gap which opens in the IES excitation spectrum at localization of the IES.

For a dot of size $L_{\text{loop}} \sim 8$ μm, and for a drift velocity:

$$0.4 \times 10^4 \text{ m.s}^{-1} \lesssim v_d \lesssim 3 \times 10^4 \text{ m.s}^{-1} \tag{7.14}$$

the gap $E_{\text{loop}} = hv_d/L_{\text{loop}}$ is estimated to be between:

$$2\ \mu\text{V} \equiv 24 \text{ mK} \lesssim E_{\text{loop}} \lesssim 16\ \mu\text{eV} \equiv 180 \text{ mK} \tag{7.15}$$

We cannot really draw any conclusion at this point on whether we do open a gap large enough in the IES low energy excitations to freeze them

7.5.3. Analysis of the temperature dependence

Here I show how the theory developed by Roulleau *et al.* explains our results. Lets assume that the temperature dephasing rate can be decomposed as follows:

$$T_\varphi^{-1} = \underbrace{T_{\varphi,U}^{-1} + T_{\varphi,D}^{-1}}_{T_{\varphi,\text{corr}}^{-1}} + T_{T,\text{eff}}^{-1} \tag{7.16}$$

$T_{\varphi,U}^{-1}$ being the contribution of the upper arm, $T_{\varphi,D}^{-1}$ the one of the lower arm, and $T_{T,\text{eff}}^{-1}$ the thermal smearing term whose estimation is done in the previous section [2]. We see on Fig. 7.21 that the variations of the non-trivial temperature decay rate $T_{\varphi,\text{corr}}^{-1}$ and of the coupling V_0^{-1} are remarkably similar, strongly suggesting a microscopic connection between these two quantities. Decomposing $T_{\varphi,\text{corr}}^{-1}$ into the temperature decay rate $T_{\varphi,U}^{-1}$ caused by dephasing in the upper arm, and $T_{\varphi,D}^{-1}$ caused by dephasing in the lower arm, we assume that $T_{\varphi,U}^{-1}$ is proportional to V_0^{-1}, in agreement with our previous work [1,3]. Indeed, when pinching G_U, we probably only affect the upper arm of the MZI.

Our goal is to estimate $T_{\varphi,U}^{-1}$ and $T_{\varphi,D}^{-1}$, and possibly reduce $T_{\varphi,U}^{-1}$ by reducing the coupling V_0^{-1} of the upper arm to the noisy IES.

Upper arm contribution

As already said, we assume that $T_{\varphi,\text{corr}}^{-1} = T_{\varphi,D}^{-1} + T_{\varphi,U}^{-1}$, with $T_{\varphi,U}^{-1} = \alpha V_0^{-1}$. We set the proportionality coefficient α so as to reproduce the observed variations of $T_{\varphi,\text{corr}}^{-1}$. The

[2] The thermal smearing temperature rate T_T^{-1} is not additive, the thermal smearing contribution is an effective one and has been estimated in section 7.5.2: $T_{T,\text{eff}}^{-1} \approx 5 \text{ K}^{-1}$

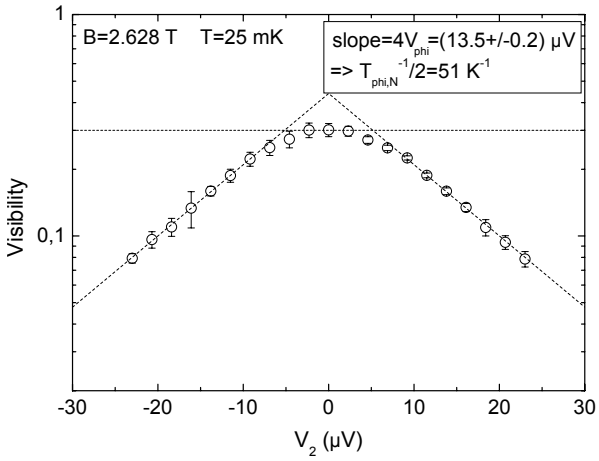

Figure 7.20: *Partition noise experiment. G_U is open ($V_{G_U} = 0.3$ V). Semi-logarithmic plot of the visibility as function of the bias voltage V_2 for G_0 at transmission ~ 0.5 for the IES (the OES being fully transmitted). The visibility decays exponentially with $|V_2|$ because of the additional partition noise with a rate $(4V_\varphi)^{-1}$ ($4V_\varphi = 13.5\ \mu$V). In terms of thermal dephasing for the upper arm: $T_{\varphi,U}^{-1} = T_{\varphi,N}^{-1}/2 = 51\ K^{-1}$.*

coefficient $\alpha = 1.5 \times 10^{-3}$ V.K^{-1} fixes the ratio between right and left scales on Fig. 7.21. We then obtain the variations of $T_{\varphi,U}^{-1}$ represented by open black circles on Fig. 7.21.

Independently, we estimate $T_{\varphi,U}^{-1}$ when G_U is open, by doing a partition noise experiment: as described in chapter 4, we wash out the interferences by adding partition noise in the adjacent IES with the help of the injecting QPC, G_0, brought to transmission 0.5 for the IES (the OES being fully transmitted) and contact n°2, put at finite bias voltage V_2.

The data are plotted on Fig. 7.20. The exponential decay of the visibility with $|V_2|$ yields the decay rate $(4V_\varphi)^{-1}$ which is linked to $T_{\varphi,U}$ by $T_{\varphi,U}^{-1} = 2k_B/e \times V_\varphi^{-1}$. We measure $4V_\varphi = 13.5 \pm 0.2\ \mu$V, which yields

$$T_{\varphi,U}^{-1} = 51 \pm 3\ \text{K}^{-1} \tag{7.17}$$

represented by the solid black square on Fig. 7.21, in remarkable agreement with the estimation based on the variations of V_0^{-1} (open black circles).

When pinching G_U from $V_{G_U} = 0.3$ V to 0.1 V, the coupling V_0^{-1} is divided by 2 going from 42×10^3 V^{-1} to 21×10^3 V^{-1}. Then dephasing in the upper arm $T_{\varphi,U}^{-1}$ is reduced proportionally. As explained in ¶ 7.4.1, the decrease of the coupling described here before localization of the IES is mostly caused by the continuous deformation of the ESs paths along the upper arm.

Lower arm contribution

The contribution of the lower arm $T_{\varphi,D}^{-1}$ to dephasing is the difference between $T_{\varphi,\text{corr}}^{-1}$ and $T_{\varphi,U}^{-1}$. As expected it is found to be mostly constant on Fig. 7.21, largely unaffected by G_U.

Its mean value is:

$$T_{\varphi,D}^{-1} = 52 \pm 7 \text{ K}^{-1} \tag{7.18}$$

We find then that both arms contibute equally to dephasing when G_U is open.

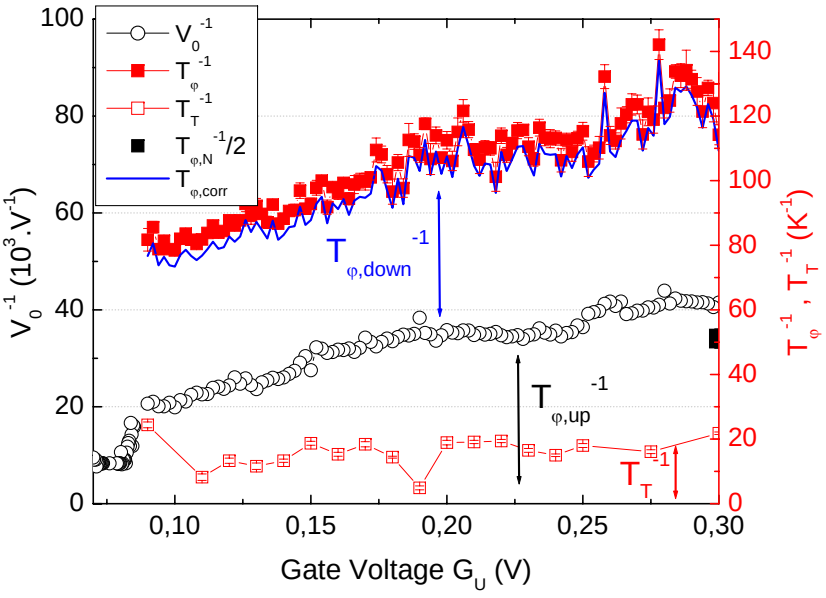

Figure 7.21.: *Left scale: (black open circles) coupling V_0^{-1} as function of the gate voltage V_{G_U}. V_0^{-1} is extracted from: the interferences revealed with the adjacent IES for $V_{G_U} \geq 0.09$ V, the signal induced by the adjacent IES for $V_{G_U} < 0.09$ V. Right scale: (red filled squares) decay rate T_φ^{-1} extracted from the data of Fig. 7.17 (right) as function of the gate voltage V_{G_U}, (red open squares) thermal smearing contribution T_T^{-1}, (solid blue line) non-trivial temperature decay rate $T_{\varphi,corr}^{-1}$ obtained by substracting the effective thermal smearing contribution from T_φ^{-1}, (black filled square) estimation of $T_{\varphi,U}^{-1}$ from the partition noise experiment. Left and right scales are chosen so that V_0^{-1} variations reproduce the ones of T_φ^{-1}.*

As one can remark, the improvement of the coherence is rather well explained by a variation of the coupling between ESs. However, the absence of an improvement of the visibility at pinch off remains puzzling. Our results seems to indicate that charge fluctuations continue to exist in the small loop. We don't know why, and so far, possible overestimation of the drift velocity and/or larger loops due to unconnected gates (problem in the fabrication process) may explain this result.

7.6. Visibility at finite bias

Energy exchange is shown to be frozen when opening a gap in the IES low energy excitations (§ 4.5) [15]. If energy exchanges are responsible for the finite bias visibility decrease, our set-up should strongly modify the robustness of the interferences with regard to the bias. More precisely, will we observe multiple or single side lobe structures? Will there be a change in the energy scales? How will they depend on V_0^{-1}?

We are interested in the effect of G_U on the lobe structure. We measured, for various values of V_{G_U} from 0.3 V to 0.06 V the visibility of the interferences as function of the voltage bias V_1 (Fig. 7.22).

7.6.1. Multiple or simple side lobe structure?

As before, we see an increase of the visibility at zero bias. We also observe a multiple side lobes structure when G_U is open, with a second side lobe small in visibility (Fig. 7.22 (left)). The side lobes are more easily seen in the visibility of the interferences induced by the IES (Fig. 7.22 (right)), because of an amplification effect: the visibility of the interferences induced by the IES is proportional to V_1. The consequence is that when there is no second side lobe visible in the 'direct' visibility, we can still see it in the 'indirect' visibility. We note $\mathcal{V}_1$ the 'direct' visibility and $\mathcal{V}_2$ the 'indirect' visibility. For a multiple side lobes structure, there are given by the following expressions (see appendix B):

$$\mathcal{V}_1 = \mathcal{V}_0 \left| -\frac{V_1}{V_c} \sin\left(\frac{V_1}{V_c}\right) + \left(1 - \frac{V_1^2}{V_{10}^2}\right) \cos\left(\frac{V_1}{V_c}\right) \right| \exp\left(-\frac{V_1^2}{2V_{10}^2}\right) \tag{7.19}$$

$$\mathcal{V}_2 = \mathcal{V}_0 \left| 2\pi \frac{V_1}{V_0} \cos\left(\frac{V_1}{V_c}\right) \right| \exp\left(-\frac{V_1^2}{2V_{10}^2}\right) \tag{7.20}$$

The presence in the 'indirect' visibility $\mathcal{V}_2$ of a zero at a finite value of V_1 followed by a revival of the visibility is a sign of a second side lobe. According to the Eq. (7.20), the position of this zero is $\pi/2 \times V_c$. Around $V_1 \approx 0$, Eq. (7.20) becomes $\mathcal{V}_2 \approx \mathcal{V}_0 \, |2\pi V_1/V_0|$. We use this expression to fit $\mathcal{V}_2$ near $V_1 \approx 0$ to extract the value of the coupling V_0^{-1}. We already showed the data obtained using this method on Fig. 7.21.

7.6.2. Transition and lobe width

Eventually, as G_U closes, the second side lobe is no longer visible. There might be a transition from a multiple side lobes structure to a single side lobe structure occuring as

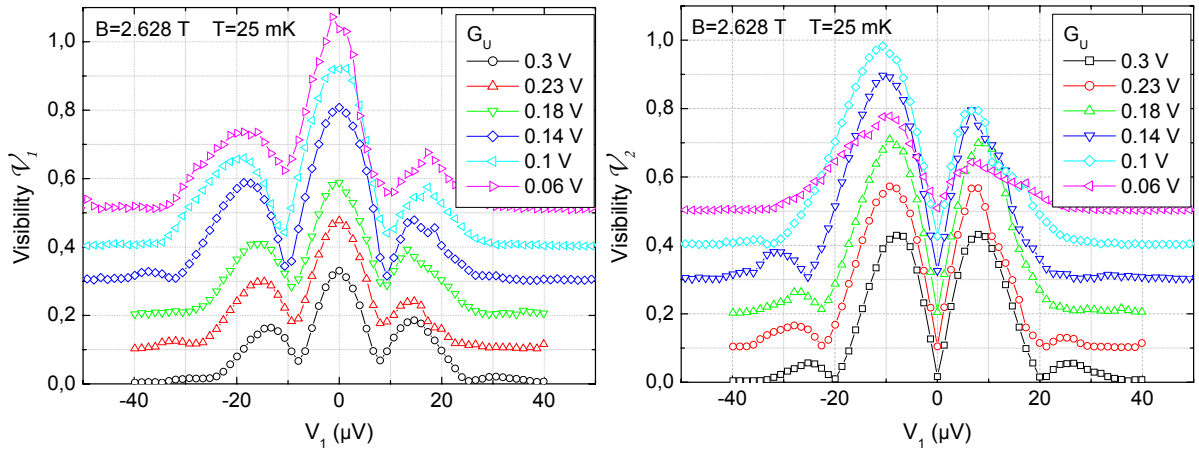

Figure 7.22.: *Smart plot of the visibility as function of the bias voltage V_1. (left) 'Direct' visibility $\mathcal{V}_1$. The visibility at zero bias $\mathcal{V}_0$ increases, the side lobes broden and the second side lobe decreases in size as G_U closes. (right) 'Indirect' visibility $\mathcal{V}_2$. At $V_{G_U} = 0.1$ V, a zero at $-\pi/2 \times V_c$ indicates a multiple side lobes structure, whereas there is no sign of a second side lobe in $\mathcal{V}_1$. For $V_{G_U} \in [0.1\ ;\ 0.3]$ V, the increase of $\mathcal{V}_0$ compensates the decrease of the coupling V_0^{-1} so that $\mathcal{V}_2$ is stable. For $V_{G_U} \in [0.06\ ;\ 0.1]$ V a sharp decrease of V_0^{-1} while $\mathcal{V}_0$ saturates diminishes $\mathcal{V}_2$.*

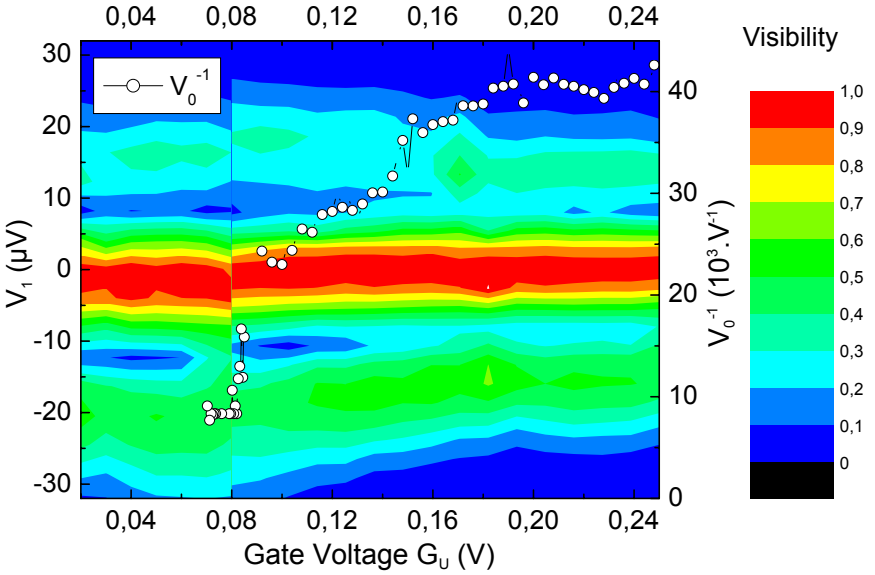

Figure 7.23.: *Left scale: colorplot of the normalized visibility as function of the gate voltage V_{G_U} on the x-axis, and the bias voltage V_1 on the y-axis. Right scale: V_0^{-1} as function of V_{G_U}.*

G_U is closing and the IES is being localized, but this is not clear because second side lobes are not very high in visibility. On Fig. 7.22, we remark that the width of the structure in terms of bias voltage V_1 seems to increase as G_U is closing.

To investigate this point further, we normalize the visibility of each lobe structure to its visibility at zero bias, and plot it in a two dimensional colorplot, as function of the gate voltage V_{G_U} on the x-axis, and as function of the bias voltage V_1 on the y-axis (Fig. 7.23). We see that the width of the central lobe remains constant whatever the value of V_{G_U}, and that indeed the width of the side lobes increases as V_{G_U} decreases. It increases from 20 μV to 30 μV until localization of the IES after which it remains constant.

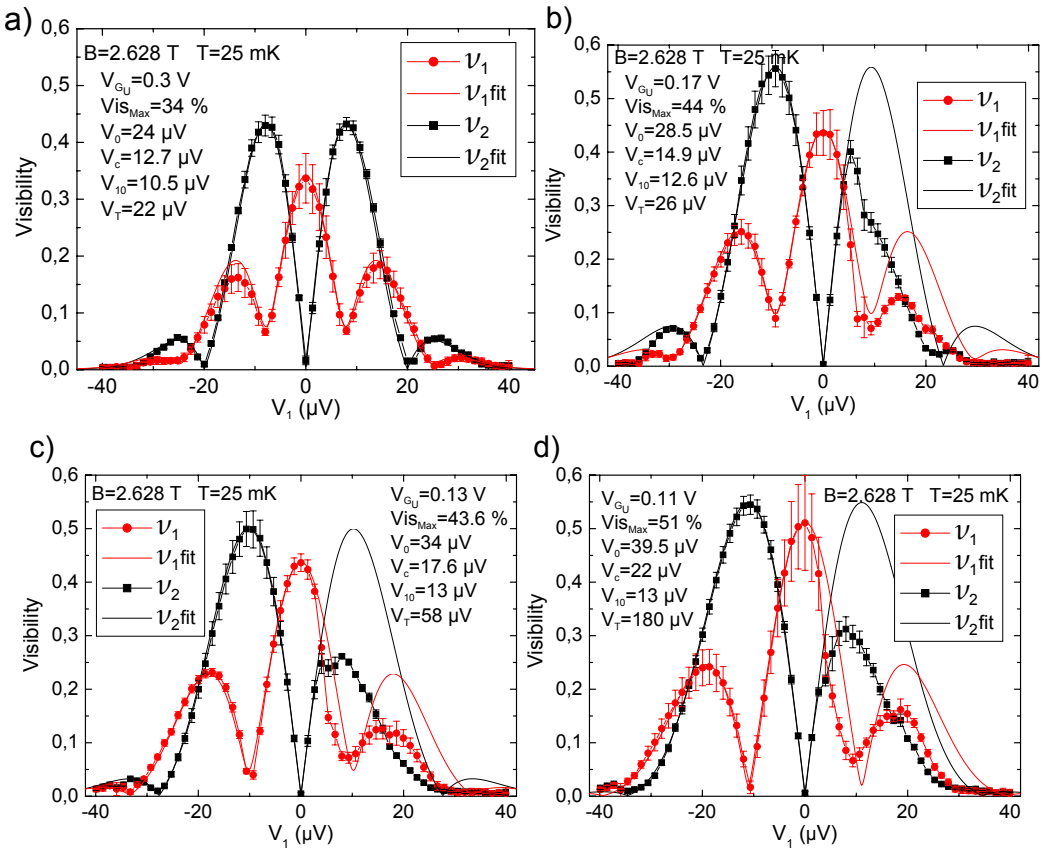

Figure 7.24.: *Evolution of the lobe structure as G_U is pinched. The parameters V_c and V_{10} are extracted by fitting both the 'direct' visibility $\mathcal{V}_1$ (red points) and the 'indirect' visibility $\mathcal{V}_2$ (black points). The fits are figured in solid lines. (a) $V_{G_U} = 0.3$ V. (b) $V_{G_U} = 0.17$ V. (c) $V_{G_U} = 0.13$ V. (d) $V_{G_U} = 0.11$ V. To better fit the data we also take into account the effect of thermal smearing through the parameter V_T (appendix B).*

We can be more precise by using the expressions for $\mathcal{V}_1$ and $\mathcal{V}_2$ (Eq. (7.19) and Eq. (7.20)): for each value of V_{G_U} we extract from the 'indirect' visibility $\mathcal{V}_2$ as function of the bias voltage V_1, the value of the zeros corresponding to $\pm\pi/2 \times V_c$. We extract V_0 using the method described earlier, knowing the visibility at zero bias $\mathcal{V}_0$ from $\mathcal{V}_1$. The values of the gaussian parameter V_{10} and of the coupling parameter V_0 are refined by ajusting the fits for both $\mathcal{V}_1$ and $\mathcal{V}_2$ (Fig. 7.24). We then plot V_c and V_{10} as function of V_0 (Fig. 7.25). We find that V_c is proportional to V_0 until localization of the IES after which it is independent of V_0, while V_{10} increases much less: the ratio V_c/V_{10} goes from 1.1 to 1.7 as V_0 increases from 23 μV to 40 μV.

It seems that the beating parameter V_c is much more strongly affected by the coupling between ESs that the gaussian parameter V_{10}. This isn't the case when one changes the magnetic field: although the coupling V_0^{-1} is affected through the magnetic field [1], it was found that V_c and V_{10} evolve proportionally to each other when sweeping the magnetic field [42]. Additionally, this confirm the existence of two distinct energy scales which proceed from different mechanisms.

7.6.3. Link with other theories/experiments

LPN's experiments on energy relaxation

It seems that in our sample the electron drift velocity is five times smaller that in the sample of the LPN group ($v_d \sim 1 \times 10^4$ m.s^{-1} instead of $v_d \sim 5 \times 10^4$ m.s^{-1}). For dots of approximately the same size, we might have a gap opening in the IES excitations five times smaller than the one they obtain. This and/or the fact that the dots might be not small enough, might explain why we observe a saturation of the visibility at localization of the IES (instead of the expected sharp increase caused by the freezing charge fluctuations in the IES) and that we do not observe anything noteworthy on the lobe structure of the visibility as function of the bias voltage at localization of the IES.

With this sample, we are not able to validate or invalidate the idea that energy relaxation in the OES because of coupling to the IES is responsible for the lobe structure in the visibility. In future experiments, one should design a sample where one is able to *measure* how large is the gap opening at localization of the IES.

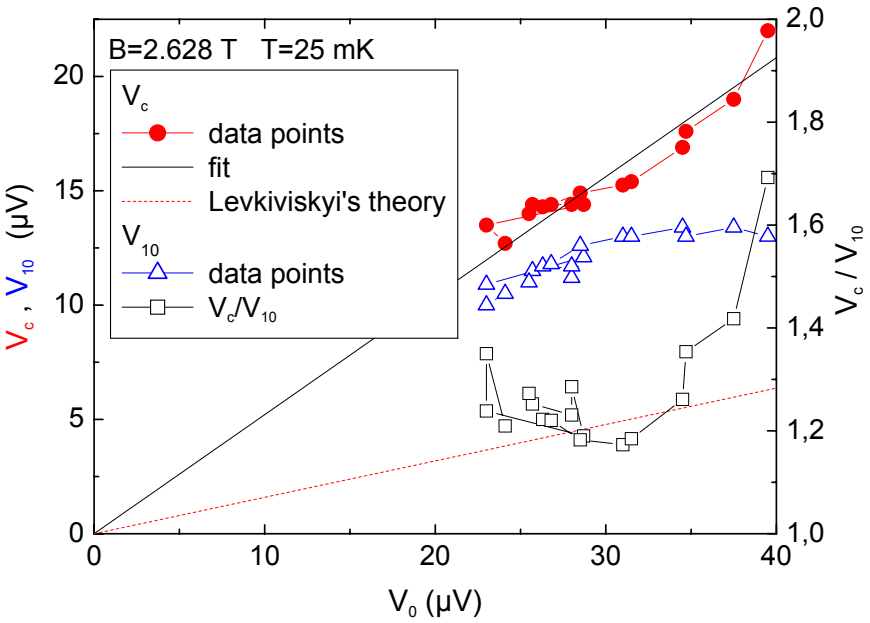

Figure 7.25.: *Left scale: V_c and V_{10} as function of V_0. Right scale: V_c/V_{10} as function of V_0. As G_U is closing, the central lobe width mainly parametrized by V_{10} hardly increases, while the 1^{st} side lobe width measured by V_c increases linearly with V_0 until localization of the IES ($V_{G_U} = 0.08$ V) after which it remains constant.*

Theory of plasmons beating

The results we obtain are compatible with the model developped by Levkiviskyi *et al.* [6].

- ▷ The multiple side lobe structure changes into a single side lobe structure as the coupling between ESs decreases, suggesting that the multiple side lobe structure is linked to the presence of *two* ESs.

- ▷ As the coupling decreases, the energy scale V_c which characterizes the multiple side lobe structure increases. V_c is linear in V_0 as predicted by Levliviskyi *et al.* [6].

More quantitatively, in this theory, if we consider $v \gg u$, where u is the group velocity of the fast charge mode, and v is the group velocity of the slow dipolar mode, the visibility's oscillations with the energy are given by the slow mode:

$$\left|\cos\left(\frac{1}{\hbar}\,\frac{\varepsilon L}{2v}\right)\right| = \left|\cos\left(\frac{\varepsilon}{eV_c}\right)\right| \tag{7.21}$$

Then,

$$\frac{V_c}{V_0} = \frac{1}{2\pi} \quad \text{with} \quad V_0 = \left(\frac{\hbar}{e}\right)\frac{4\pi v}{L} \tag{7.22}$$

On Fig. 7.25 (right) the data and the prediction are reported. We find a discrepancy between the proportionality coefficient yielded by the prediction ($V_c/V_0 \approx 0.16$) and the one obtained by fitting the data ($V_c/V_0 \approx 0.54$). They are however, of the same order. The prediction is made by assuming that the coupling of *both* arms of the MZI to the IES is modified while the data are obtained by tuning only the coupling of *one arm* (the upper one) to the IES. One would then expect naively that the increase of V_c with V_0 would be twice less in the data that in the prediction. We observe the inverse!

From the expression for the coupling (Eq. (7.22)) , one can extract the slow dipolar mode velocity v: $v = (e/\hbar)\ LV_0/4\pi$ and estimate its value.

$$\text{For} \quad 25\ \mu\text{V} \leq V_0 \leq 45\ \mu\text{V} \quad , \quad 3.4 \times 10^4\ \text{m.s}^{-1} \leq v \leq 6.1 \times 10^4 \text{m.s}^{-1} \tag{7.23}$$

This estimation of the slow dipolar mode velocity is to be compared to the results from the *time of flight* experiments [91, 92] which give an estimation of the group velocity as function of the interaction strength. For the 'ungated sample' Kumada *et al.* find that at filling factor $\nu = 2$, $v_g \sim 2 \times 10^6$ m.s^{-1}. This group velocity corresponds to the fast charge mode velocity u which is supposed to be large compared to v.

7.7. Conclusion

In this chapter, we showed how we weakened the coupling between the upper arm of the interferometer and the IES in a controlled manner. The effect of this 'decoupling' on the visibility at zero bias and its temperature decay was studied: we were able to identify the different contributions to the temperature dephasing and in particular we showed that coherence enhancement was caused by the upper arm contribution which deccreases when one decouples the upper arm from the noisy IES These findings confirm Roulleau *et al.* approach of dephasing in the MZI at zero bias. Next we focused on the effect of the decoupling on the visibility at finite bias. We found that the beating parameter V_c is proportional to the coupling parameter V_0 as predicted by Levkiviskyi *et al.* while the gaussian parameter V_{10} stays unchanged. This favors the idea that the lobe structure has two aspects: the multiple lobes which seem to come from the beating of two collective modes arising from the coupling between ESs, and 'something else' not yet explained, which causes the decaying 'gaussian' enveloppe and the single side lobe structure.

8. Conclusion and perspectives

8.1. Engineering coherence

We were able to enhance coherence by a factor two in our sytem by tuning the coupling between the system (the outer edge state) and its environment (the inner edge state). In the near future, we would like to make sure that we freeze charge fluctuations in the environment and see the effect of the system coherence. Another idea is to tune the coupling between edge states through the Zeeman gap by tilting the sample with respect to the magnetic field orientation.

However, when we put the system out of equilibrium, coherence decay seems almost unaffected by the coupling between edge states. This is still not understood.

8.2. Understanding decoherence/dephasing

At $\nu = 2$, where the environment of the system is identified as the other edge state, we have now a better understanding of the physics involved in dephasing. The interactions between edge states are responsible for the coupling between the system and its noisy environment, thus decreasing its coherence.

Because of this coupling between edge states, energy exchanges between electronic distributions occurs during their propagation in the edge states. It is not clear yet how this affects the visibility of our sytem out of equilibrium. To investigate this, we would like to see how injecting electrons at a definite energy above the Fermi sea by means of an energy filter at the interferometer entry, modifies the visibility. Indeed, until now whole energy distributions were injected into the MZI.

Theories at $\nu = 2$ are now giving some physical idea of the mechanism involved for the observed multiple oscillations of the visibility with the voltage bias: collective plasmonic modes with different veolcities arise because of the inter channel interaction, and their

beating seems responsible for the multiple side lobes structure. However, this does not explain the remaining dependence of the visibility with the bias voltage (single side lobe structure) at $\nu = 2$ when both edge states are well decoupled, or at $\nu = 1$. The role of intrachannel interactions has still to be experimentally investigated.

8.3. Long term

There is still much work to be done in order to improve the robustness of coherence in the interger quantum Hall effect. To find the means of improving the coherence, we must investigate further the reasons for its limitation.

Hoping that in the future we succeed in increasing enough the system coherence, we would like to couple two Mach-Zehnder interferometers to do two-particles interferences and verify the violation of Bell inequalities.

A. Finite frequency coupling

A.1. Phase fluctuations induced by the noisy IES

We first consider the coupling between ESs. Fluctuations of the charge in the IES couple to the charge in the neighbouring arm of the MZI and influence electron transport in this arm. This interaction effect is taken into account by introducing a time dependent potential $V_1(x,t)$ into the Hamiltonian [72]:

$$H = -\frac{\hbar^2}{2m_e{}^*}\frac{\partial^2}{\partial x^2} + \varepsilon_1 + V_1(x,t)$$

for the upper arm. Here ε_1 is the sub-band energy due to the lateral confining potential of the arm and $m_e{}^*$ is the effective mass of the electron. We make the assumption that the fluctuating potential factorizes in a space and time-dependent part, writing $V_1(x,t) = h_1(x)eU_1(t)$. We will suppose for the following, that $h_1(x)$ is constant all along the length of the interferometer L. To solve the Schrödinger equation with the Hamiltonian above we make the ansatz:

$$\Psi_\varepsilon(x,t) = \exp\left(-\frac{i\varepsilon t}{\hbar} + ik_1(\varepsilon)x + i\varphi(x,t)\right)$$

where $k_1(\varepsilon) = \sqrt{2m_e{}^*(\varepsilon-\varepsilon_1)}/\hbar$ and $\varphi(x,t)$ is the phase accumulated due to fluctuations. We introduce

$$U_1(t) = \int \frac{\mathrm{d}\omega}{2\pi}\, U_1(\omega)e^{i\omega t} \quad \text{and} \quad \varphi(x,t) = \int \frac{\mathrm{d}\omega}{2\pi}\, \varphi(x,\omega)e^{i\omega t}$$

Since $h_1(x)$ is constant all along the length of the interferometer L, one obtains by WKB approximation:

$$\varphi(L,\tau) = \int_0^\tau \frac{eU_1(t)}{\hbar}\,\mathrm{d}t \tag{A.1}$$

where $\tau = L/v_d$ is the time of flight through the MZI and L stands for the length of one arm of the interferometer. This last relation allows to relate the phase noise $S_\varphi(\omega)$ to the

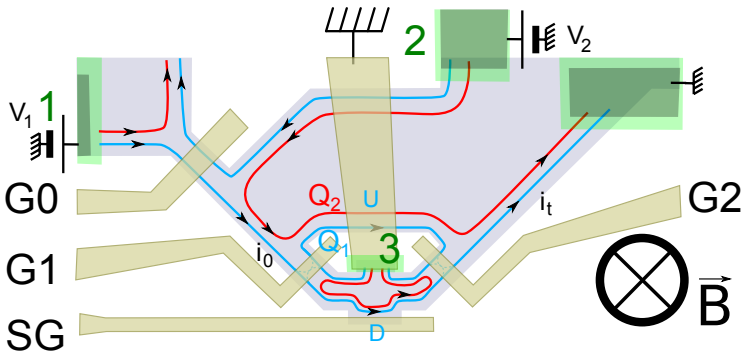

Figure A.1: *Schematic representation of the charge injectivity: we have to consider three sources. We are interested in the charge $Q_1(Q_2)$ in the outer(inner) ES.*

potential noise $S_{U_1U_1}(\omega)$:

$$S_\varphi(\omega) = \frac{4e^2}{\hbar^2}\, S_{U_1U_1}(\omega)\, \frac{\sin^2(\omega\tau/2)}{\omega^2} \tag{A.2}$$

A.2. Admittance matrix

In this part we propose the calculation of the admittance matrix $G_{12}(\omega) = \mathrm{d}I_1(\omega)/\mathrm{d}V_2(\omega)$. We concentrate on the limit $\hbar\omega \ll k_BT \ll E_F$. First we consider the charge density injected into the upper arm of the MZI due to a modulation of the voltage at contacts n°1, 2 and 3 (contact n°3 being the inner ohmic contact connected to the ground on Fig. A.1). The charge distribution in the sample can be expressed through the Fermi-field

$$\hat{\Psi}(\mathbf{r},t) = \sum_\alpha \int \frac{\mathrm{d}\varepsilon}{\sqrt{h v_{\alpha,\varepsilon}}}\, e^{-i\varepsilon t/\hbar}\psi_\alpha(\mathbf{r},\varepsilon)\hat{a}_\alpha(\varepsilon)$$

which annihilates an electron at point $\mathbf{r}$ and time t. $\hat{a}_\alpha(\varepsilon)$ is an operator which creates an electron coming from contact n°α, in a state of energy ε, and $\psi_\alpha(\mathbf{r},\varepsilon)$ is a scattering state describing carriers with energy ε incident from contact n°α, with phase velocity $v_{\alpha,\varepsilon}$. The charge density in the ring at point $\mathbf{r}$ and time t is $\hat{\rho}(\mathbf{r},t) = e\hat{\Psi}^\dagger(\mathbf{r},t)\hat{\Psi}(\mathbf{r},t)$. Fourier transforming with regard to time and quantum averaging we get $\rho(\mathbf{r},\omega) = \langle\hat{\rho}(\mathbf{r},\omega)\rangle$, where

$$\rho(\mathbf{r},\omega) = e\sum_{\beta,\gamma}\int \frac{\mathrm{d}\varepsilon}{\sqrt{v_{\beta,\varepsilon}v_{\gamma,\varepsilon+\hbar\omega}}}\, \psi^*_\beta(\mathbf{r},\varepsilon)\psi_\gamma(\mathbf{r},\varepsilon+\hbar\omega)\left\langle \hat{a}^\dagger_\beta(\varepsilon)\hat{a}_\gamma(\varepsilon+\hbar\omega)\right\rangle$$

The average charge may be split into an equilibrium part $\rho^{(0)}(\mathbf{r},\omega)$ and a contribution due to the external voltage at contact n°α, $\delta\rho_\alpha(\mathbf{r},\omega)$: $\rho(\mathbf{r},\omega) = \rho^{(0)}(\mathbf{r},\omega) + \delta\rho_\alpha(\mathbf{r},\omega)$. When calculating the quantum average of the charge density operator the effect of the external voltage $V_\alpha(t)$ is taken into account through the modified distribution function for charge

carriers coming in from reservoir α. The distribution for contact n°α to linear order in the applied voltage is:

$$\left\langle \hat{a}_\alpha^\dagger(\varepsilon)\hat{a}_\alpha(\varepsilon+\hbar\omega)\right\rangle = \delta(\hbar\omega)f_\alpha(\varepsilon) + \frac{e}{h}V_\alpha(\omega)F(\varepsilon,\omega)$$

where $V_\alpha(\omega)$ is the Fourier component to frequency ω of the voltage $V_\alpha(t)$ and $F(\varepsilon,\omega)$ is defined through $F(\varepsilon,\omega) = \left(f_\alpha(\varepsilon) - f_\alpha(\varepsilon+\hbar\omega)\right)/\hbar\omega$. When $\mathcal{T}_0 = 1$ and $\mathcal{T}_1 = 0.5$, the scattering states $\psi_\alpha(\mathbf{r},\varepsilon)$ in the arms of the interferometer for a constant internal potential are of the form

$$\psi_1(\mathbf{r},\varepsilon) = \psi_3(\mathbf{r},\varepsilon) = \frac{\chi(\mathbf{r}_\perp)}{\sqrt{2}}\ \exp\left(ik_\varepsilon x + i\Phi_{U,1}(x)\right)$$
$$\text{and}\quad \psi_2(\mathbf{r},\varepsilon) = \chi(\mathbf{r}_\perp)\ \exp\left(ik_\varepsilon x + i\Phi_{U,2}(x)\right)$$

where $\Phi_{U,i}$ is the magnetic phase acquired going through upper arm to point x and $\chi(\mathbf{r}_\perp)$ is the transverse part of the function. We then obtain for the fluctuating part of the charge

$$\begin{aligned}
\delta\rho_1(x,\omega) &= \frac{e^2}{2h}\int \frac{\mathrm{d}\varepsilon}{\sqrt{v_{1,\varepsilon}v_{1,\varepsilon+\hbar\omega}}}\, e^{i\omega x/v_\varepsilon}V_1(\varepsilon)F(\varepsilon,\omega)\\
\delta\rho_2(x,\omega) &= \frac{e^2}{h}\int \frac{\mathrm{d}\varepsilon}{\sqrt{v_{2,\varepsilon}v_{2,\varepsilon+\hbar\omega}}}\, e^{i\omega x/v_\varepsilon}V_2(\varepsilon)F(\varepsilon,\omega)\\
\delta\rho_3(x,\omega) &= \frac{e^2}{2h}\int \frac{\mathrm{d}\varepsilon}{\sqrt{v_{3,\varepsilon}v_{3,\varepsilon+\hbar\omega}}}\, e^{i\omega x/v_\varepsilon}V_3(\varepsilon)F(\varepsilon,\omega)
\end{aligned}$$

To find the charge $Q_\alpha^e(\omega)$ induced by the Fourier component of the potential $V_\alpha(\omega)$ into upper arm of the MZI we integrate over the length of the arm, L_U: $Q_\alpha^e(\omega) = \int_0^{L_U} \mathrm{d}x\ \delta\rho_\alpha(x,\omega)$. Performing the integration we get:

$$\begin{aligned}
Q_1^e(\omega) &= \frac{e^2}{2h}\int \mathrm{d}\varepsilon\ F(\varepsilon,\omega)\ \frac{i}{\omega}\ \left(1-e^{i\omega\tau}\right)V_1(\omega)\\
Q_2^e(\omega) &= \frac{e^2}{h}\int \mathrm{d}\varepsilon\ F(\varepsilon,\omega)\ \frac{i}{\omega}\ \left(1-e^{i\omega\tau}\right)V_2(\omega)\\
Q_3^e(\omega) &= \frac{e^2}{2h}\int \mathrm{d}\varepsilon\ F(\varepsilon,\omega)\ \frac{i}{\omega}\ \left(1-e^{i\omega\tau}\right)V_3(\omega)
\end{aligned}$$

In the limit $\hbar\omega/k_BT \ll 1$, we have $\int \mathrm{d}\varepsilon\ F(\varepsilon,\omega) \sim 1$. We can rewrite the charge as $Q_\alpha^e(\omega) = e^2\nu_\alpha(\omega)V_\alpha(\omega)$ where we have introduced the injectivity $\nu_\alpha(\omega)$ defined as

$$\begin{aligned}
\nu_1(\omega) &= \frac{i}{\omega}\,\frac{1}{2h}\left(1-e^{i\omega\tau}\right)\\
\nu_2(\omega) &= \frac{i}{\omega}\,\frac{1}{h}\left(1-e^{i\omega\tau}\right)\\
\nu_3(\omega) &= \frac{i}{\omega}\,\frac{1}{2h}\left(1-e^{i\omega\tau}\right)
\end{aligned}$$

In the dephasing type experiments $V_1(\omega) = V_3(\omega) = 0$ while $V_2(\omega)$ is varying. One finally obtains:

$$Q_1^e(\omega) = Q_3^e(\omega) = 0 \quad \text{and} \quad Q_2^e(\omega) = e^2\nu_2(\omega)V_2(\omega)$$

Now if interactions are taken into account, the excess injected charge will induce a shift in the effective internal potential, which in turn gives rise to a screening charge. This screening charge is proportional to the internal potential $eU_\alpha(\omega)$ and to the total charge density available for screening. Thus $Q_1^s(\omega) = -e^2U_1(\omega)\,(\nu_1 + \nu_3)$ and $Q_2^s(\omega) = -e^2U_2(\omega)\nu_2$. One finally obtains for the total charge in regions 1 and 2:

$$Q_1^{\text{tot}}(\omega) = \nu(\omega)\,(-U_1(\omega)) \quad \text{and} \quad Q_2^{\text{tot}}(\omega) = \nu(\omega)\,(V_2(\omega) - U_2(\omega))$$

with $\nu(\omega) = iG_Q\,(1 - e^{i\omega\tau})\,/\omega$ and $G_Q = e^2/h$. Moreover, $Q_1^{\text{tot}}(\omega)$ and $Q_2^{\text{tot}}(\omega)$ are opposite and related to the potential difference via the relation:

$$Q_1^{\text{tot}}(\omega) = -Q_2^{\text{tot}}(\omega) = C\,(U_1(\omega) - U_2(\omega))$$

which gives three relations for $Q_{U,2}^{\text{tot}}(\omega)$:

$$\begin{aligned} Q_2^{\text{tot}}(\omega) &= C\,(U_2(\omega) - U_1(\omega)) \\ Q_2^{\text{tot}}(\omega) &= \nu(\omega)\,(V_2(\omega) - U_2(\omega)) \\ Q_2^{\text{tot}}(\omega) &= \nu(\omega)U_1(\omega) \end{aligned}$$

From these relations we can extract $Q_2^{\text{tot}}(\omega)$ as function of $V_2(\omega)$: $Q_2^{\text{tot}}(\omega) = -V_2(\omega)/\,(2\nu(\omega)^{-1} + C^{-1})$. The current in the arm 1 is given by $I_1(\omega) = i\omega Q_{U,2}^{\text{tot}}(\omega)$. We finally obtain:

$$G_{12}(\omega) = \frac{\mathrm{d}I_1(\omega)}{\mathrm{d}V_2(\omega)} = \frac{-i\omega}{2\nu(\omega)^{-1} + C^{-1}} \tag{A.3}$$

A.3. Noisy inner edge state

To characterize the coupling at finite frequency, one has to know how the fluctuations of the electro-chemical potential V_2 are related to the fluctuations of the internal potential U_1 seen by the electrons in the MZI. What happens is the following: changing V_2, affects the charge of the IES. This in turn leads to a variation of the potential U_1 which is partially screened. We are describing here the dynamic of the screening [93–96]. The notations that I will use, as well as the resulting electrical circuit are represented in Fig. A.2 (a). The

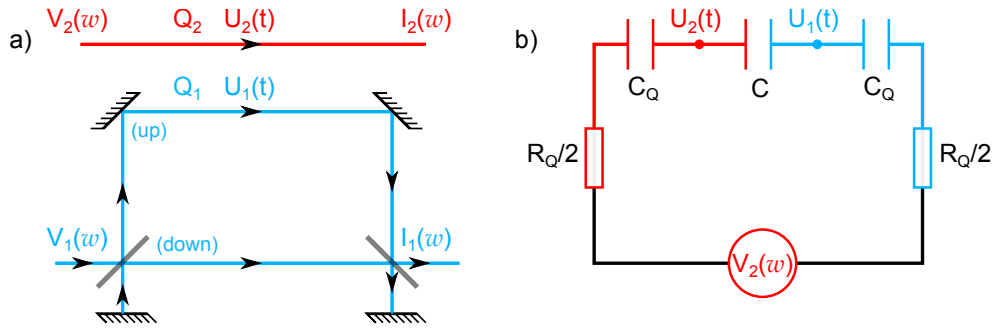

Figure A.2.: *(a) Schematic representation coupled* via *a geometrical capacitance C. (b) Low frequency equivalent circuit with V_1 set to ground. The two relaxation resistances $R_Q/2$ in series with the coupling capacitance C acount for the non ideality of the two 'gates' (the ESs) forming the capacitor C. The quantum capacitances C_Q account for the 1D density of states in the ESs.*

admittance $G_{12}(\omega) = \mathrm{d}I_1(\omega)/\mathrm{d}V_2(\omega)$ is calculated in detail in section A.2. We just give here the final result:

$$G_{12}(\omega) = \frac{\mathrm{d}I_1(\omega)}{\mathrm{d}V_2(\omega)} = \frac{-i\omega}{2\nu(\omega)^{-1} + C^{-1}} = \left(\frac{1}{i\nu(\omega)\omega} + \frac{1}{iC\omega} + \frac{1}{i\nu(\omega)\omega}\right)^{-1}$$

with $V_2(\omega)$ the electro-chemical potential applied on S2 , $I_1(\omega)$ the current along the OES, $\nu(\omega) = iG_Q\left(1 - e^{i\omega\tau}\right)/\omega$, $G_Q = e^2/h$ and C the capacitance between the IES and OES. In the low frequency limit, this expression becomes:

$$G_{12}(\omega)^{-1} \approx \frac{i}{\omega C_Q} + \frac{R_Q}{2} + \frac{i}{\omega C} + \frac{i}{\omega C_Q} + \frac{R_Q}{2}$$

with $C_Q = G_Q\tau$. We deduce from the expression the schematic representation of the coupling between the IES and OES Fig. A.2 (b). The OES is composed of a quantum capacitance C_Q with a relaxation resistance $R_Q/2$ in series because of the non ideality of the lateral gate (IES). We are interested in the fluctuations of the potential $U_1(\omega)$ as a function of $V_2(\omega)$:

$$U_1(\omega) = \nu(\omega)^{-1}\, Q^{\mathrm{tot}}_{U,2}(\omega) = \frac{-\nu(\omega)^{-1}}{2\nu(\omega)^{-1} + C^{-1}}\, V_2(\omega)$$

with $Q^{\mathrm{tot}}_{U,2}(\omega)$ the total charge fluctuation in the region 2. In the low frequency limit: $U_1(\omega) \approx -{C_Q}^{-1}\left(2{C_Q}^{-1} + C^{-1}\right)^{-1} V_2(\omega)$. Then from Eq. (A.1) and from the definition[1] of V_0, we get:

$$V_0 \approx -e\left(2C_Q^{-1} + C^{-1}\right) \tag{A.4}$$

[1] $2\pi/V_0 \equiv \partial\varphi/\partial V_2$

Finally for the fluctuations of $U_1(\omega)$, $S_{U_1U_1}(\omega) = |\nu(\omega)^{-1}/\left(2\nu(\omega)^{-1} + C^{-1}\right)|^2 S_{22}(\omega)$ which can be written: $|\omega\nu(\omega)|^2 S_{U_1U_1}(\omega) = |G_{12}(\omega)|^2 S_{22}(\omega)$. We now consider the case of white partition noise $S_{22} = 2eR_QV_2\mathcal{T}_0\left(1-\mathcal{T}_0\right)$. Using Eq. (A.2) and $\langle\delta\varphi^2\rangle = \int_0^\infty S_\varphi(\omega)\,\mathrm{d}\omega/2\pi$, one finds[2] for ${V_\varphi}^{-1}$:

$$V_\varphi^{-1} = \frac{e}{\hbar}\int_0^\infty \mathcal{I}(\omega)\,\mathrm{d}\omega, \quad \text{with} \quad \mathcal{I}(\omega) = \left(\omega^2 + \left(\omega\tan\left(\omega\tau/2\right)^{-1} + G_Q/C\right)^2\right)^{-1}$$

In the low frequency limit $\mathcal{I}(\omega) \approx \left(\omega^2 + \left(eV_0/h\right)^2\right)^{-1}$, which leads to:

$$V_0 = \pi^2 V_\varphi \tag{A.5}$$

This is a result of importance which tells that in principle the ratio between V_0 and V_φ should be universal. It means that without screening of the interaction, whatever be the coupling and the quantum capacitance, the ratio between V_0 and V_φ should be π. This is not what we have observed in our experiment (we measure $V_0/V_\varphi = \pi^2/1.4$). Indeed, the approach that we have developed is very simple and we have to think now on the simplifications which are abrupt. The experimental data show that V_φ is larger than expected which means that there is less dephasing. A natural way is to include something in the model which reduces the bandwidth on which fluctuations play a role. This can be easily done by inserting screening effects which are modelled by two capacitances C_0 which mimic the capacitive coupling of the wires to the ground and will short cut the high frequency fluctuations. Indeed, this screening can also be viewed as modelling the interaction in the wire itself: the larger C_0 is, the fewer interactions there are.

[2] ${V_\varphi}^{-1} \equiv 2\left\langle\delta\varphi^2\right\rangle/\mathcal{T}_0\left(1-\mathcal{T}_0\right)V_2$

B. Fitting the lobe structure

B.1. Our approach

In this section, we consider the coupling between the IES and the OES, which in a mean field approximation can be simply viewed as a capacitive coupling. The scheme one uses to feed the ESs with different bias is represented in Fig. B.1. The IES is figured in red and the outer interfering ES in blue. The coupling between the IES and the OES was first demonstrated by Neder *et al.* [97]: the IES was used as a 'which path' detector in the two-path MZI. Here we propose an approach based on a mean field approximation which catches most of the features of the lobe structure when the two ESs are fed with the same bias. Of course a mean field approximation alone does not lead to a lobe structure. However assuming that it exists, I will show that the coupling between ESs modifies their shape.

B.1.1. Edge states independently biased

QPC $G0$ is tuned so as to fully reflect the IES and fully transmit the OES: IES and OES are fed with different bias. Then, the interferences emitted by contact n°1 and its capacitively induced signal by the IES emitted at contact n°2 are measured: the main signal is obtained by sweeping the gate voltage V_{SG}, while the induced signal is seen when sweeping the bias

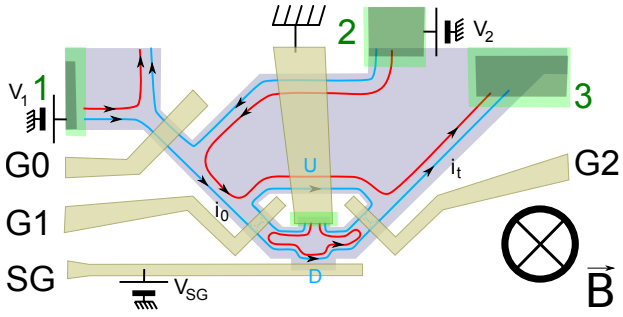

Figure B.1: *Schematic of the MZI with the IES (red) and the OES (blue) fed with distinct bias V_1 and V_2 respectively.*

voltage applied to the IES, V_2. Indeed, when deriving the visibility of the interferences in ¶ 4.4.3, the influence of the charge in the IES on the phase of the electrons in the OES was not considered . However, when a dc bias voltage V_2 is applied at contact n°2, electrons in the IES modify the potential seen by the electrons in the OES, hence their phase. In this picture, the IES can be viewed as a lateral gate and used to reveal the interferences as well (Fig. B.2).

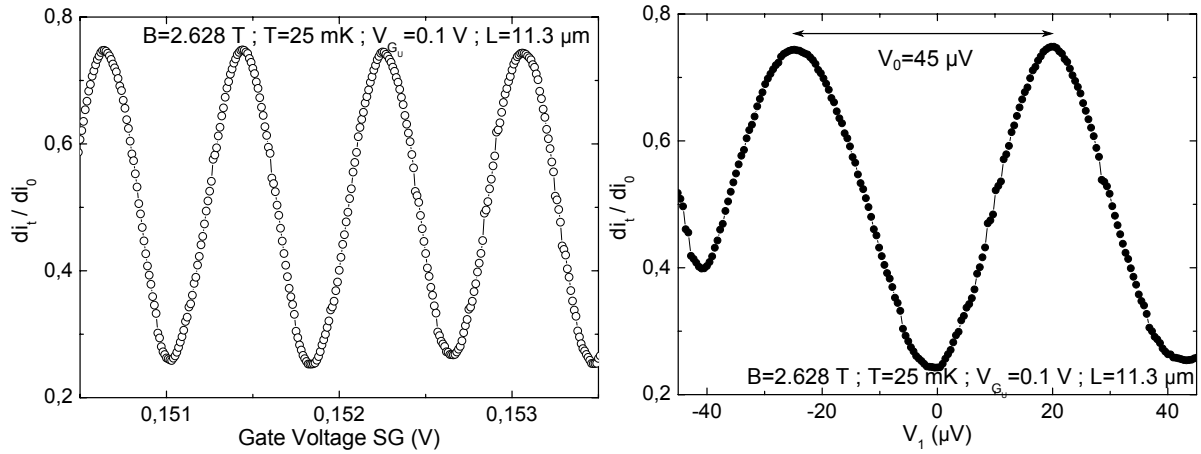

Figure B.2.: *Interferences revealed with SG (left), with the IES used as a gate (right). V_0 is defined as the periodicity of the oscillations with respect to V_2. For this particular sample of arm length $L = 11.3\ \mu m$, $V_0 = 45\ \mu V$ is large because of the upper gate G_U which decouples the IES and the OES (chapter 7).*

Parameter V_0 defined as the periodicity of the oscillations with respect to V_2, characterizes the coupling between the ESs. It changes the oscillations phase in Eq. (4.9) along:

$$I_{\sim} = \frac{2e^2 V_1}{h}\ \sqrt{\mathcal{T}_1\mathcal{T}_2\mathcal{R}_1\mathcal{R}_2}\ e^{-V_1^2/2V_{10}^2}\ \cos\left(\varphi - 2\pi\ \frac{V_2}{V_0}\right) \tag{B.1}$$

where $V_1(V_2)$ is the bias voltage applied on contact n°1(2). One immediately remarks that when the two ESs are fed with the same bias, $\mathrm{d}I_{\sim}/\mathrm{d}V_1$ contains a term resulting from the capacitive coupling. This case is obtained when $G0$ transmit both ESs completely. Let first assume that $V_2 \neq V_1$, in practice obtained when $G0$ only transmit the OES. Deriving Eq. (B.1) with respect to V_1 and to V_2, one obtains:

$$\begin{aligned}
\frac{\mathrm{d}I_{\sim}}{\mathrm{d}V_1} &\propto \left(1 - \frac{V_1^2}{V_{10}^2}\right)\ e^{-V_1^2/2V_{10}^2}\ \cos\left(\varphi - 2\pi\ \frac{V_2}{V_0}\right) \\
\frac{\mathrm{d}I_{\sim}}{\mathrm{d}V_2} &\propto 2\pi\ \frac{V_1}{V_0}\ e^{-V_1^2/2V_{10}^2}\ \sin\left(\varphi - 2\pi\ \frac{V_2}{V_0}\right)
\end{aligned}$$

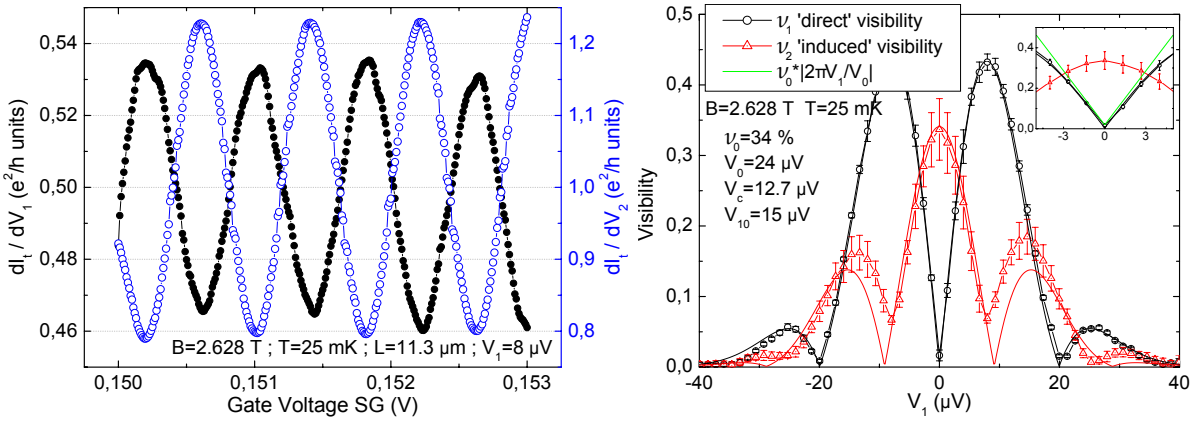

Figure B.3.: *(left) differential conductance as function of V_{SG} for $V_1 = 8\ \mu V$. left scale: $\mathrm{d}I_t/\mathrm{d}V_1$ (full black circles). right scale: $\mathrm{d}I_t/\mathrm{d}V_2$ (open blue circles). Both signals are in quadrature. (right) 'direct' visibility $\mathcal{V}_1$ (black open circles) and 'induced' visibility $\mathcal{V}_2$ (full red circles) as function of V_1. Solid lines are fits (B.6) and (B.7) yielding: $V_{10} = 15\ \mu V$, $V_c = 12.7\ \mu V$, $V_0 = 24\ \mu V$ and $\mathcal{V}_0 = 34$ %, for $L = 11.3\ \mu V$, with $V_{G_U} = 0.1$ V (chapter 7).*

which yields for the visibilities of the single side lobe structure:

$$\mathcal{V}_{1,s} = \mathcal{V}_0 \left|1 - \frac{V_1^2}{V_{10}^2}\right| \exp\left(-\frac{V_1^2}{2V_{10}^2}\right) \tag{B.2}$$

$$\mathcal{V}_{2,s} = \mathcal{V}_0 \left|2\pi \frac{V_1}{V_0}\right| \exp\left(-\frac{V_1^2}{2V_{10}^2}\right) \tag{B.3}$$

For multiple lobe structures, Eq. (4.12) becomes:

$$I_\sim = \frac{2e^2 V_1}{h} \sqrt{\mathcal{T}_1\mathcal{T}_2\mathcal{R}_1\mathcal{R}_2}\, e^{-V_1^2/2V_{10}^2} \cos\left(\frac{V_1}{V_c}\right) \cos\left(\varphi - 2\pi \frac{V_2}{V_0}\right)$$

which finally gives:

$$\frac{\mathrm{d}I_\sim}{\mathrm{d}V_1} \propto \left(-\frac{V_1}{V_c} \sin\left(\frac{V_1}{V_c}\right) + \cos\left(\frac{V_1}{V_c}\right)\left(1 - \frac{V_1^2}{V_{10}^2}\right)\right) e^{-V_1^2/2V_{10}^2} \cos\left(\varphi - 2\pi \frac{V_2}{V_0}\right) \tag{B.4}$$

$$\frac{\mathrm{d}I_\sim}{\mathrm{d}V_2} \propto 2\pi \frac{V_1}{V_0} \cos\left(\frac{V_1}{V_c}\right) e^{-V_1^2/2V_{10}^2} \sin\left(\varphi - 2\pi \frac{V_2}{V_0}\right) \tag{B.5}$$

From these equations, one derives the visibility of the interferences:

$$\mathcal{V}_{1,m} = \mathcal{V}_0 \left|-\frac{V_1}{V_c} \sin\left(\frac{V_1}{V_c}\right) + \cos\left(\frac{V_1}{V_c}\right)\left(1 - \frac{V_1^2}{V_{10}^2}\right)\right| \exp\left(-\frac{V_1^2}{2V_{10}^2}\right) \tag{B.6}$$

$$\mathcal{V}_{2,m} = \mathcal{V}_0 \left|2\pi \frac{V_1}{V_0} \cos\left(\frac{V_1}{V_c}\right)\right| \exp\left(-\frac{V_1^2}{2V_{10}^2}\right) \tag{B.7}$$

where $\mathcal{V}_0$ is the visibility at zero bias. On Fig. B.3 (left) are reported, in full black circles $\mathrm{d}I_\sim/\mathrm{d}V_1$ for the OES, and in blue open circles $\mathrm{d}I_\sim/\mathrm{d}V_2$ induced by the IES with $V_1 = 8\ \mu$V. Both signals are in quadrature, in agreement with Eqs. (B.4) and (B.5). On Fig. B.3 (right) $\mathcal{V}_1$ and $\mathcal{V}_2$ are plotted for the same sample. The dots are the data while the solid lines are fit to the data using Eqs. (B.6) and (B.7). The very good agreement validates our approach. From these one extracts the fit parameters V_c, V_0 and V_{10}.

Effect of thermal smearing

In the case where there is an asymmetry between the arms of the MZI, we do not obtain full extinctions in the lobe structure. It is noteworthy that it does not affect the 'indirect' visibility $\mathcal{V}_2$. This is because the phase of the interferences depends on the energy. One can derive functions that take thermal smearing into account to better fit the visibility $\mathcal{V}_1$. For multiple lobe structures, the interference term of the transmitted current is:

$$I_\sim = \frac{2e^2V_1}{h}\sqrt{\mathcal{T}_1\mathcal{T}_2\mathcal{R}_1\mathcal{R}_2}\,\frac{\pi k_BT/eV_T}{\sinh\left(\pi k_BT/eV_T\right)}\,e^{-V_1^2/2V_{10}^2}\,\cos\left(\frac{V_1}{V_c}\right)\,\cos\left(\varphi_F+\frac{V_1}{V_T}-2\pi\,\frac{V_2}{V_0}\right)$$

where $V_T = \hbar v_d/e\Delta L$ characterizes the thermal smearing. Then the interfering parts of the differential conductances are given by:

$$\begin{aligned}\frac{\mathrm{d}I_\sim}{\mathrm{d}V_1} \;\propto\; &\left[\left(-\frac{V_1}{V_c}\,\sin\left(\frac{V_1}{V_c}\right)+\cos\left(\frac{V_1}{V_c}\right)\left(1-\frac{V_1^2}{V_{10}^2}\right)\right)\,\cos\left(\varphi_F+\frac{V_1}{V_T}-2\pi\,\frac{V_2}{V_0}\right)\right. &\text{(B.8)}\\ &\left.+\,\frac{V_1}{V_T}\,\cos\left(\frac{V_1}{V_c}\right)\,\sin\left(\varphi_F+\frac{V_1}{V_T}-2\pi\,\frac{V_2}{V_0}\right)\right]\,e^{-V_1^2/2V_{10}^2} &\text{(B.9)}\\ \frac{\mathrm{d}I_\sim}{\mathrm{d}V_2} \;\propto\; &2\pi\,\frac{V_1}{V_0}\,\cos\left(\frac{V_1}{V_c}\right)\,e^{-V_1^2/2V_{10}^2}\,\sin\left(\varphi_F+\frac{V_1}{V_T}-2\pi\,\frac{V_2}{V_0}\right) &\text{(B.10)}\end{aligned}$$

From these equations, one derives the visibility of the interferences:

$$\begin{aligned}\mathcal{V}_{1,m} \;=\; \mathcal{V}_0\;&\left[\left(-\frac{V_1}{V_c}\,\sin\left(\frac{V_1}{V_c}\right)+\cos\left(\frac{V_1}{V_c}\right)\left(1-\frac{V_1^2}{V_{10}^2}\right)\right)^2 &\text{(B.11)}\\ &\left.+\left(\frac{V_1}{V_T}\,\cos\left(\frac{V_1}{V_c}\right)\right)^2\right]^{1/2}\,\exp\left(-\frac{V_1^2}{2V_{10}^2}\right) &\text{(B.12)}\\ \mathcal{V}_{2,m} \;=\; \mathcal{V}_0\;&\left|2\pi\,\frac{V_1}{V_0}\,\cos\left(\frac{V_1}{V_c}\right)\right|\,\exp\left(-\frac{V_1^2}{2V_{10}^2}\right) &\text{(B.13)}\end{aligned}$$

Now that we have observed and characterized the coupling between the IES and the OES, we are going to treat the case when $G0$ transmit both ESs. The physics remaining the same, we can guess that the measured current will be the sum of the two terms given by Eqs. (B.4) and (B.5).

B.1.2. Edge states biased together

When $G0$ only transmit the OES, the lobes are well defined with complete extinctions and the phase is rigid within a lobe with a π-jump when the visibility goes to zero as illustrated on Fig. B.4 (left). The situation is different when both ESs are transmitted. The IES and the OES are fed with the same bias, one reproduces the very first experiment of Ji *et al.* [37] and Bieri *et al.* [43]: lobes almost disappear and the phase is not rigid anymore (Fig. B.4 (right)).

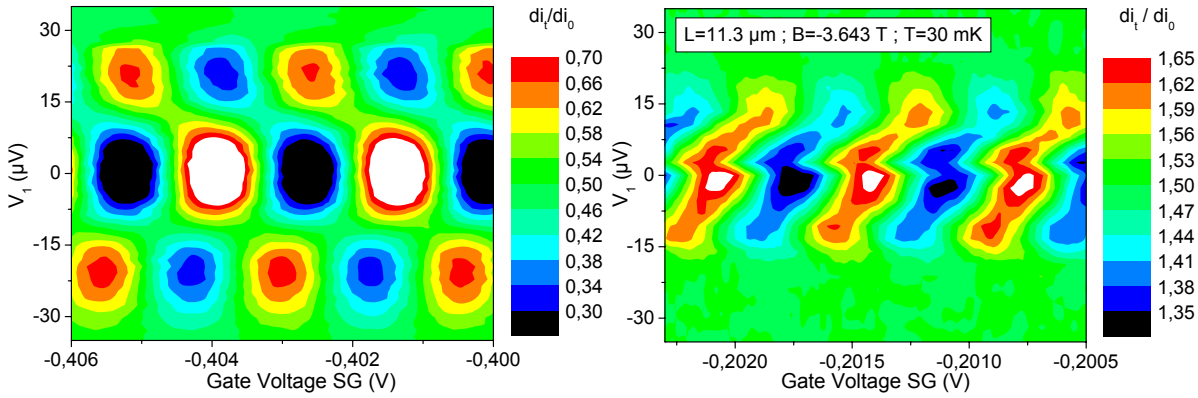

Figure B.4.: *(left) IES and OES are independently biased: the differential transmission as function of the bias voltage V_1 shows lobes with well marked extinctions. Within a lobe the phase of the oscillations as function of the side gate voltage V_{SG} is rigid and undergoes π-jumps at extinction points. (right) IES and OES are biased by the same ohmic contact: we no longer see well defined lobes and the phase is no longer rigid (the data are from a different sample).*

Bieri *et al.* [43] have shown that an unexpected enhancement of the visibility could be obtained for a transmission of $\mathcal{T}_1$ close to 1. Roulleau *et al.* [3] showed that this result could be explained with the coupling between ESs. To derive the visibility, one has to take into account the induced signal from the IES which is in quadrature with the main signal, so that the total conductance is given by:

$$\frac{\mathrm{d}I_\sim}{\mathrm{d}V_1} \propto \sqrt{\left[\left(1-\frac{V_1^2}{V_{10}^2}\right)\,\cos\left(\frac{V_1}{V_c}\right)-\frac{V_1}{V_c}\,\sin\left(\frac{V_1}{V_c}\right)\right]^2+\left[2\pi\,\frac{V_1}{V_0}\,\cos\left(\frac{V_1}{V_c}\right)\right]^2}\,e^{-V_1^2/2V_{10}^2}\,\cos\left(\theta\right) \tag{B.14}$$

with the phase:

$$\theta=\varphi-2\pi\,\frac{V_1}{V_0}-\arctan\left(\frac{2\pi\,V_1/V_0\times\cos(V_1/V_c)}{(1-V_1^2/V_{10}^2)\,\cos(V_1/V_c)-V_1/V_c\,\sin(V_1/V_c)}\right) \tag{B.15}$$

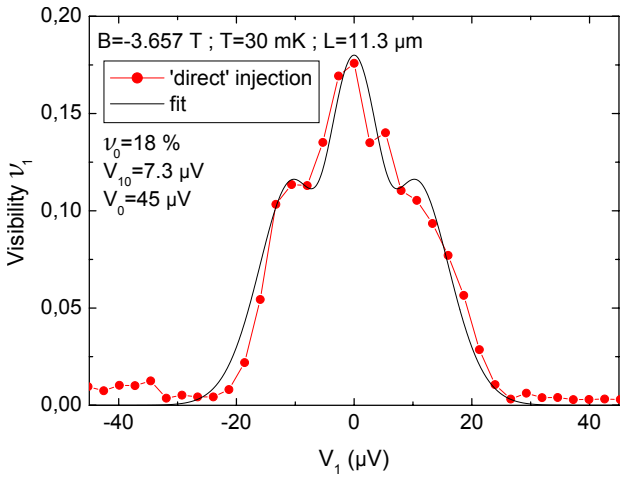

Figure B.5: *Both ESs are fed with the same bias voltage V_1. The visibility as function of V_1 shows no lobe structure with well marked extinctions (red dots), but can be fitted by Eq. (B.17) with parameters $V_{10} = 7.3\ \mu V$ and $V_0 = 45\ \mu V$, for a sample of arm length $L = 11.3\ \mu m$.*

Then the visibility is:

$$\mathcal{V}_{1,m} = \mathcal{V}_0 \sqrt{\left[\left(1 - \frac{V_1^2}{V_{10}^2}\right) \cos\left(\frac{V_1}{V_c}\right) - \frac{V_1}{V_c} \sin\left(\frac{V_1}{V_c}\right)\right]^2 + \left[2\pi \frac{V_1}{V_0} \cos\left(\frac{V_1}{V_c}\right)\right]^2} \exp\left(-\frac{V_1^2}{2V_{10}^2}\right) \tag{B.16}$$

which, for a single side lobe structure becomes:

$$\mathcal{V}_{1,s} = \mathcal{V}_0 \sqrt{\left[\left(1 - \frac{V_1^2}{V_{10}^2}\right)\right]^2 + 4\pi^2 \frac{V_1^2}{V_0^2}} \exp\left(-\frac{V_1^2}{2V_{10}^2}\right) \tag{B.17}$$

We see indeed, through Eq. (B.15) that the phase is no longer rigid and that the fit given by Eq. (B.17) reproduces the data (Fig. B.5).

B.2. Litvin's approach

B.2.1. Visibilities

Following Litvin's approach, voltage bias V_2 on the IES shifts the averaged phase $\langle\varphi\rangle_\varphi$ because of charging effects:

$$I_\sim = \frac{2e}{h} \sqrt{\mathcal{T}_1\mathcal{T}_2\mathcal{R}_1\mathcal{R}_2} \int_0^{eV_1} \cos\left(\frac{\varepsilon}{eV_c}\right) \cos\left(\langle\varphi\rangle_\varphi - 2\pi \frac{V_2}{V_0}\right) e^{-\varepsilon^2/2\varepsilon_0^2}\, \mathrm{d}\varepsilon \tag{B.18}$$

which yield the interfering parts of the differential conductances:

$$\frac{\mathrm{d}I_\sim}{\mathrm{d}V_1} \propto \cos\left(\frac{V_1}{V_c}\right) \cos\left(\langle\varphi\rangle_\varphi - 2\pi \frac{V_2}{V_0}\right) e^{-V_1^2/2V_{10}^2} \tag{B.19}$$

$$\frac{\mathrm{d}I_\sim}{\mathrm{d}V_2} \propto -\frac{2\pi}{eV_0} \sin\left(\langle\varphi\rangle_\varphi - 2\pi \frac{V_2}{V_0}\right) \int_0^{eV_1} \cos\left(\frac{\varepsilon}{eV_c}\right) e^{-\varepsilon^2/2\varepsilon_0^2}\, \mathrm{d}\varepsilon \tag{B.20}$$

with $V_{10} = \varepsilon_0/e$. Then the visibilities for the multiple side lobes structure are given by:

$$\mathcal{V}_{1,m} = \mathcal{V}_0 \left|\cos\left(\frac{V_1}{V_c}\right)\right| \exp\left(-\frac{V_1^2}{2V_{10}^2}\right) \tag{B.21}$$

$$\mathcal{V}_{2,m} = \mathcal{V}_0 \frac{2\pi}{eV_0} \left|\int_0^{eV_1} \cos\left(\frac{\varepsilon}{eV_c}\right) \exp\left(-\frac{\varepsilon^2}{2\varepsilon_0^2}\right) \mathrm{d}\varepsilon\right| \tag{B.22}$$

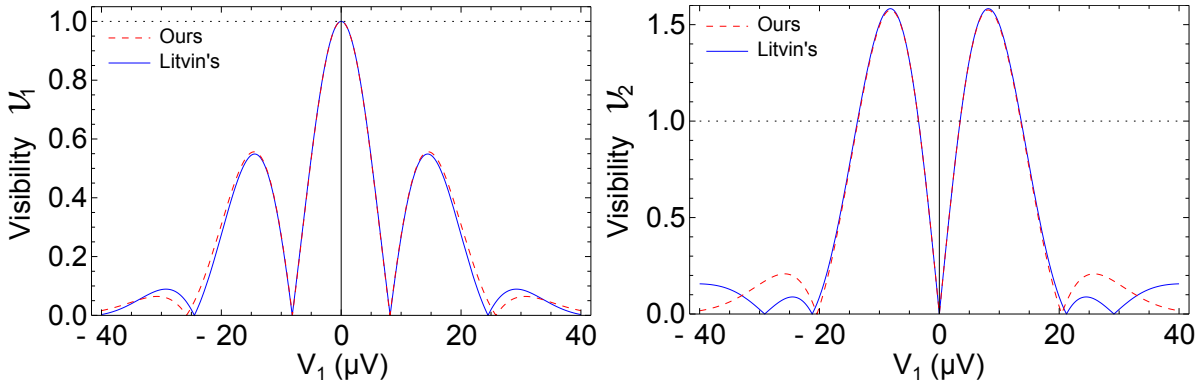

Figure B.6.: *(left) $\mathcal{V}_1$ as function of V_1 given by Eqs. (B.6) (red dashed line) and (B.21) (solid blue line). (right) $\mathcal{V}_2$ as function of V_1 given by Eq. (B.7) (red dashed line) and Eq. (B.22) (solid blue line) for $V_0 = 20\ \mu V$. The fit parameters are for 'ours' (red dashed line): $V_c = 13\ \mu V$, $V_{10} = 11\ \mu V$, and for 'Litvin's' (solid blue line): $V_c = 5.2\ \mu V$, $V_{10} = 14\ \mu V$.*

B.2.2. Comparison with our approach

We found in ¶ 4.4.1 that Eqs. (B.6) and (B.21) for the 'direct' visibility $\mathcal{V}_1$, given by respectively Litvin's and our approaches, both fit the data equally well. On Fig. B.6 (left), we represented Litvin's and our fit with the parameters: $V_c = 13\ \mu$V and $V_{10} = 11\ \mu$V for ours, $V_c = 5.2\ \mu$V and $V_{10} = 14\ \mu$V for Litvin's. For the 'indirect' visibility $\mathcal{V}_2$, Eqs. (B.7) and (B.22) diverge from each other beyond the first zero at finite bias. On Fig. B.6 (right), the fits are represented with the coupling parameter $V_0 = 20\ \mu$V.

In practice, our fit for the 'indirect' visibility $\mathcal{V}_2$ works well, in particular beyond the first finite zero $\pm\pi/2\ V_c$. We can then conclude that Litvin's fit is not appropriate, which invalidates his approach. It seems then that the 'gaussian averaging' result rather from a mean-field mechanism independent on the energy of the electron as suggestes by our approach with the variance of the phase distribution quadratic with the voltage bias: $\langle\delta\varphi^2\rangle_\varphi \propto V_1^2$.

B.3. Fits analysis

B.3.1. Fit functions

Here I recall the functions used to fit the visibility as funtion of the bias voltage respectively for the single and for the multiple side lobes structures:

$$\begin{aligned}\mathcal{V}_{1,s} &= \mathcal{V}_0 \left|1 - \frac{V_1^2}{V_{10}^2}\right| \exp\left(-\frac{V_1^2}{2V_{10}^2}\right) \\ \mathcal{V}_{1,m} &= \mathcal{V}_0 \left|-\frac{V_1}{V_c}\sin\left(\frac{V_1}{V_c}\right) + \cos\left(\frac{V_1}{V_c}\right)\left(1 - \frac{V_1^2}{V_{10}^2}\right)\right| \exp\left(-\frac{V_1^2}{2V_{10}^2}\right)\end{aligned}$$

B.3.2. Zeros

It is not always possible to fit the data with these functions: the lobe structure is not always symmetric because of resonances in the QPCs, the interferometer can be detuned when the bias voltage is sweeped (cross-talk), the transmissions (for example $\mathcal{T}_0$) can depend on the bias, etc... In these situations, one will rather look at the zeros of the visibility, and how they depend on the parameters of the system like the magnetic field, the dilution or the coupling between ES. Next step is seeing how the fit parameters depend on these physical parameters, and maybe finding an explanation for their origin. The choice of the fit function becomes then important, since it determines how the zeros depend on the fit parameters: if we choose Eq. (4.15) to fit the multiple side lobe structure, it is very simple, the zeros are just the zeros of $|\cos(V_1/V_c)|$. In our case, it is not so straightforward, the zeros depend on both V_{10} and V_c. We must evaluate how exactly the zeros of the visibility depend on these parameters. The zeros position is given by the equation:

$$-\frac{V_1}{V_c}\sin\left(\frac{V_1}{V_c}\right) + \cos\left(\frac{V_1}{V_c}\right)\left(1 - \frac{V_1^2}{V_{10}^2}\right) = 0$$

which can be written as:

$$-\frac{V_1}{V_c}\sin\left(\frac{V_1}{V_c}\right) + \cos\left(\frac{V_1}{V_c}\right)\left(1 - \frac{V_c^2}{V_{10}^2}\,\frac{V_1^2}{V_c^2}\right) = 0$$

$$\frac{V_c}{V_{10}} = \sqrt{\frac{1 - (V_1/V_c)\tan(V_1/V_c)}{(V_1/V_c)^2}} \tag{B.23}$$

This is what has been plotted in solid red lines on Fig. B.7 and determines the position of the zeros of the multiple side lobes structure. What is then the influence of V_c and V_{10} on the position of these zeros? First, let us examine two limits:

- ▷ when $V_{10}/V_c \to 0$, the multiple side lobes fit merges with the one of the single side lobe: the first zeros are given by $V_1 = \pm V_{10}$, the other zeros are not visible because of the gaussian envelope, this is already the case for $V_c/V_{10} = 2$, as seen on Fig. B.7,
- ▷ when $V_c/V_{10} \to 0$, the zeros are in principle given by $\tan(V_1/V_c) = V_c/V_1$, however, we never reach this limit: in practice we observe multiple side lobes which correspond to $V_c/V_{10} \geq 1$.

Now let us see what happens in the domain of V_c/V_{10} usually accessible, that is to say for V_c/V_{10} between 1 and 2. For a given V_c, we see that the width of the central lobe increases by 50 % when going from $V_c/V_{10} = 2$ to $V_c/V_{10} = 1$, whereas the first side lobe increases by 23 %.

How do these energy scales depend on the other parameters of the experiment like, the magnetic field? In the following, we study how these zeros vary with V_1 and V_2 as function of the parameters $\mathcal{T}_0$ and V_{10}.

B.3.3. Dependence on the dilution

The zeros are determined by the following equation:

$$(V_1 - V_{1\text{off}})\,(V_1 + (1/\mathcal{T}_0 - 1)V_2) = V_{10}^2 \tag{B.24}$$

This is a conic section in the $x - y$ plane of equation:

$$(x - x_0)(x + \alpha y) = \beta \tag{B.25}$$

$$x^2 + \alpha x y - x_0 x - \alpha x_0 y - \beta = 0 \tag{B.26}$$

with $x = V_1$, $y = V_2$, $x_0 = V_{1\text{off}}$, $\alpha = 1/\mathcal{T}_0 - 1$ and $\beta = V_{10}^2$. We do the usual transformations to make this equation more explicit: we rotate the coordinate system by an angle θ so that the term in xy vanishes in the new sytem (new coordinates x' and y', see Fig. B.9). This is achieved with:

$$\theta = -\frac{1}{2}\arctan(\alpha) = -\frac{1}{2}\arctan(1/\mathcal{T}_0 - 1) \tag{B.27}$$

and correlatively:

$$\alpha = -\tan(2\theta) \tag{B.28}$$

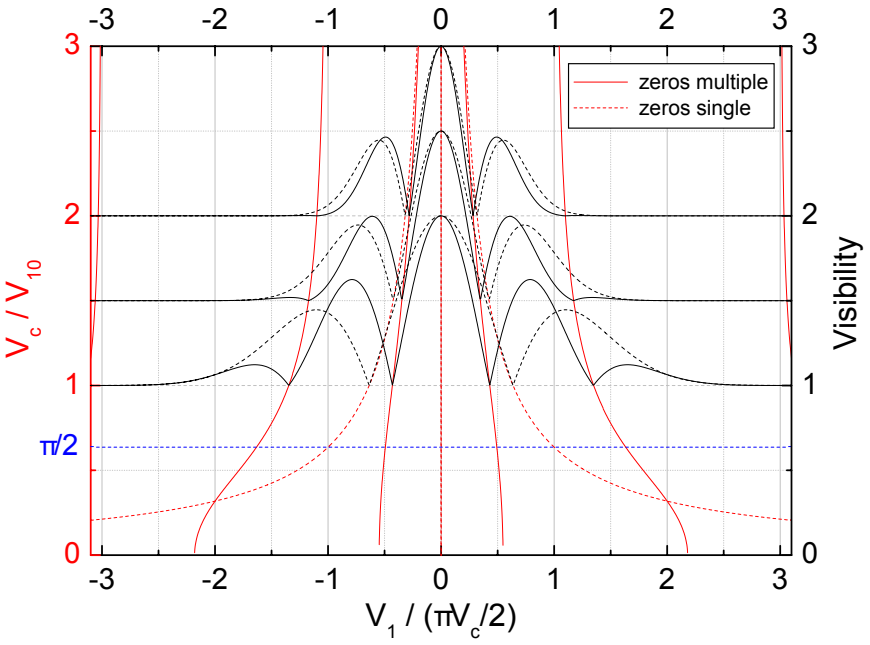

Figure B.7.: *Zeros positions as function of* $V_1/(\pi V_c/2)$ *(x-axis) and* V_c/V_{10} *(left y-axis), for the multiple (solid red lines), and the single side lobe structure (dashed red lines). Fit functions are in black. The baselines cross the left axis at their* V_c/V_{10} *values. The first zero for the multiple side lobes structure merges with the zero of the single side lobe structure in the limit* $V_{10}/V_c \to 0$*. For large values of* V_c/V_{10} *(*~ 2*), the multiple side lobes fit much resembles the one of the single side lobe. Multiple lobes become visible for* $V_c/V_{10} \leq 1.5$*. When the blue dashed line is crossed (for* $V_c/V_{10} < \pi/2$*), side lobes reach visibilities larger than* 1*. In practice, only multiple side lobes for* $V_c/V_{10} \geq 1$ *are observed.*

After a few trigonometry tricks, we obtain the equation of an hyperbola:

$$\left(\frac{x' - x_{\text{off}}}{a}\right)^2 - \left(\frac{y' - y_{\text{off}}}{b}\right)^2 = 1 \tag{B.29}$$

with:

$$\begin{cases} x_{\text{off}} = \dfrac{V_{1\text{off}}}{2\cos(\theta)}, & y_{\text{off}} = \dfrac{V_{1\text{off}}}{2\sin(\theta)} \\ a = V_{10}\dfrac{\sqrt{\cos(2\theta)}}{|\cos(\theta)|}, & b = V_{10}\dfrac{\sqrt{\cos(2\theta)}}{|\sin(\theta)|} \end{cases} \tag{B.30}$$

In the rotated coordinate system, the asymptots of the hyperbola make an angle $\pm\varphi$ with the x' absciss axis:

$$\varphi = \arctan\left(\frac{1}{|\tan(\theta)|}\right) \tag{B.31}$$

▷ The asymptots only depend on $\mathcal{T}_0$ (opening between branchs and rotation angle)

▷ The apex a depends on V_{10} and $\mathcal{T}_0$. It gives the central lobe width.

Analysis as function of $\mathcal{T}_0$

If we study more precisely the evolution of the hyperbola as function of $\mathcal{T}_0$ according to this empirical fit, we see that as $\mathcal{T}_0$ goes from 0 to 1:

▷ one of the hyperbola's asymptots stays vertical and the other has an angle 2φ with the first one, which increases from 90° to 180° (see figures B.8(a) and B.9).

▷ the evolution of the apex a of the hyperbola is the result of two contributions:

- the angular dependence $\sqrt{\cos(2\theta)}/|\cos(\theta)|$, which is represented by the black curve on Fig. B.8(b) and goes to zero as $\mathcal{T}_0 \to 0$,
- $V_{10} \propto 1/\sqrt{\mathcal{T}_0}$ whose divergence as $\mathcal{T}_0 \to 0$ (measured in ¶ 6.2.2) compensates the evolution of the angular dependence so that a remains finite at $\mathcal{T}_0 = 0$. It is represented by the green curve on Fig. B.8(b). $\pm V_{10}$ are the values of V_1 for which the visibility is zero for $V_2 = 0$, it diverges at $\mathcal{T}_0 = 0$ because the asymptots of the hyperbola are the axis of the coordinate system $x - y$.

The resulting evolution of a is represented by the red curve on Fig. B.8 (right).

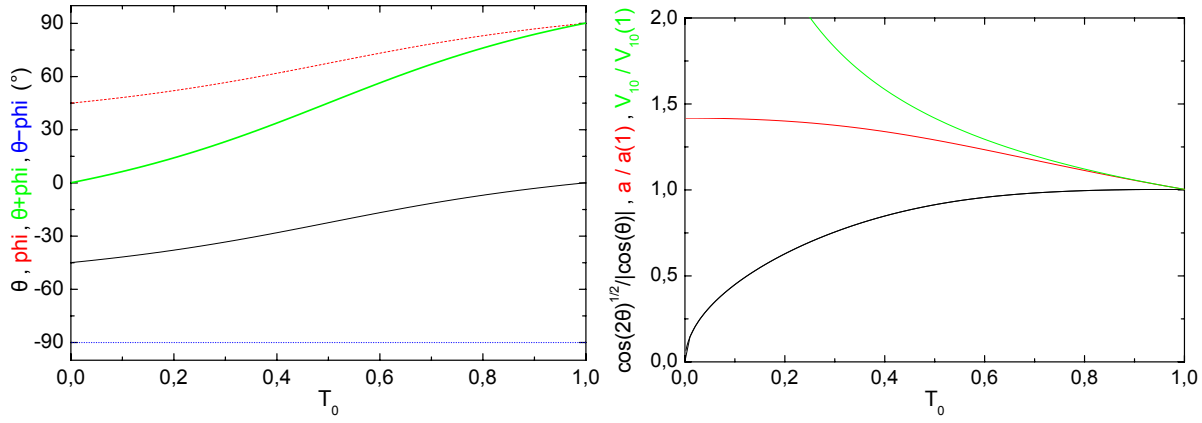

Figure B.8.: *(left) Evolution of angles θ (rotation angle of the new coordinate system $x' - y'$ with respect to $x - y$), φ (angle of one of the asymptots with respect to (Ox')), $\theta + \varphi$ and $\theta - \varphi$ as function of $\mathcal{T}_0$. $\theta + \varphi$ and $\theta - \varphi$ are the angles between the asymptots and (Ox'). As $\mathcal{T}_0$ increases from 0 to 1, one asymptot remains vertical while the other rotates from a 90° angle with respect to the other to a 180° angle. This is schematized on Fig. B.9. (right) The hyperbola's apex a depends on $\mathcal{T}_0$ through both the angle θ as seen on the left side graph, and V_{10} as we will see later ($V_{10}^{-2} \propto \mathcal{T}_0$). In arbitrary units we represented: in black the angular dependence of a, in green the dependence of V_{10} on $\mathcal{T}_0$, and in red a as function of $\mathcal{T}_0$. $2a$ measures the smallest distance between the two branches of the hyperbola (see the first drawing on Fig. B.9), whereas V_{10} measures the width of the central lobe when $V_2 = 0$. The angular dependence compensates the divergence of V_{10} for $\mathcal{T}_0 \sim 0$ so that a remains finite. a decreases monotically from $\sqrt{2}$ to 1.*

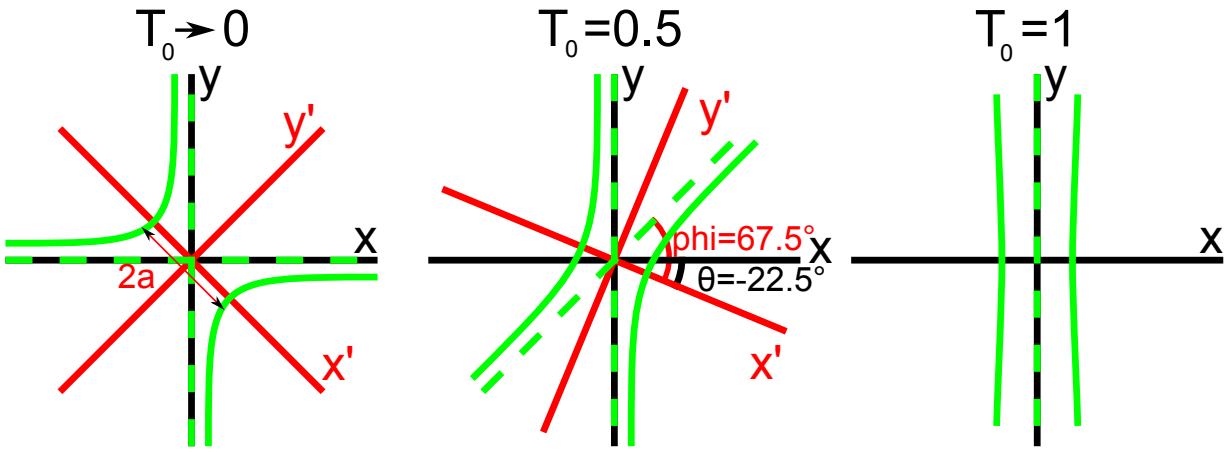

Figure B.9.: *On this figure, we schematized the evolution of the hyperbola representing the zeros of the visibility in the $V_1 - V_2$ plane for different values of $\mathcal{T}_0$. The original coordinate system $x - y$ is in black. The new sytem of coordinates $x' - y'$ is in red and has been rotated by the angle θ compared to the old one. The asymptots have an angle $\pm\varphi$ with respect to (Ox') and are represented in by green dashed lines. The hyperbola is a green solid line. (left) $\mathcal{T}_0 \to 0$: the new coordinate system is rotated by an angle $\theta = -\pi/4$. The asymptots are the axes of the old system. (center) $\mathcal{T}_0 = 0.5$: the new coordinate system is rotated by an angle $\theta = -\pi/8$. The hyperbola's opening angle is $2\varphi = 3\pi/4$. (right) $\mathcal{T}_0 = 1$: the new coordinate system is identical to the previous one, the hyperbola is reduced to two verticals at $x = \pm a$.*

Bibliography

[1] P. Roulleau, F. Portier, P. Roche, A. Cavanna, G. Faini, U. Gennser, and D. Mailly. Noise Dephasing in Edge States of the Integer Quantum Hall Regime. *Physical Review Letters*, 101(18):186803–4, October 2008.

[2] Preden Roulleau, F. Portier, P. Roche, A. Cavanna, G. Faini, U. Gennser, and D. Mailly. Direct Measurement of the Coherence Length of Edge States in the Integer Quantum Hall Regime. *Physical Review Letters*, 100(12):126802, 2008.

[3] Preden Roulleau. Etude de la cohérence quantique dans le régime d'effet Hall quantique entier, November 2008.

[4] I. Neder, M. Heiblum, Y. Levinson, D. Mahalu, and V. Umansky. Unexpected Behavior in a Two-Path Electron Interferometer. *Physical Review Letters*, 96(1):016804–4, January 2006.

[5] J. T. Chalker, Yuval Gefen, and M. Y. Veillette. Decoherence and interactions in an electronic Mach-Zehnder interferometer. *Physical Review B (Condensed Matter and Materials Physics)*, 76(8):085320–11, 2007.

[6] Ivan P. Levkivskyi and Eugene V. Sukhorukov. Dephasing in the electronic Mach-Zehnder interferometer at filling factor $\nu = 2$. *Physical Review B*, 78(4):045322, July 2008.

[7] I. Neder and E. Ginossar. Behavior of Electronic Interferometers in the Nonlinear Regime. *Physical Review Letters*, 100(19):196806–4, May 2008.

[8] Seok-Chan Youn, Hyun-Woo Lee, and H. S. Sim. Nonequilibrium Dephasing in an Electronic Mach-Zehnder Interferometer. *Physical Review Letters*, 100(19):196807–4, May 2008.

[9] D. L. Kovrizhin and J. T. Chalker. Exactly solved model for an electronic Mach-Zehnder interferometer. *Physical Review B*, 80(16):161306, October 2009.

[10] D. L. Kovrizhin and J. T. Chalker. Multiparticle interference in electronic Mach-Zehnder interferometers. *Physical Review B*, 81(15):155318, April 2010.

[11] Martin Schneider, Dmitry Bagrets, and Alexander Mirlin. Theory of the nonequilibrium electronic Mach-Zehnder interferometer. *Physical Review B*, 84(7):075401, August 2011.

[12] Carles Altimiras. *Inelastic mechanisms in mesocopic circuits realized in two dimensional electron gases*. PhD thesis, October 2010.

[13] H. Le Sueur, C. Altimiras, U. Gennser, A. Cavanna, D. Mailly, and F. Pierre. Energy Relaxation in the Integer Quantum Hall Regime. *Physical Review Letters*, 105(5):056803, July 2010.

[14] C. Altimiras, H. le Sueur, U. Gennser, A. Cavanna, D. Mailly, and F. Pierre. Nonequilibrium edge-channel spectroscopy in the integer quantum Hall regime. *Nature Physics*, 6(1):34–39, October 2009.

[15] C. Altimiras, H. Le Sueur, U. Gennser, A. Cavanna, D. Mailly, and F. Pierre. Tuning Energy Relaxation along Quantum Hall Channels. *Physical Review Letters*, 105(22):226804, November 2010.

[16] Ivan P. Levkivskyi and Eugene V. Sukhorukov. Noise-Induced Phase Transition in the Electronic Mach-Zehnder Interferometer. *Physical Review Letters*, 103(3):036801, July 2009.

[17] P. Samuelsson, E. V. Sukhorukov, and M. Büttiker. Two-Particle Aharonov-Bohm Effect and Entanglement in the Electronic Hanbury Brown–Twiss Setup. *Physical Review Letters*, 92(2):026805, January 2004.

[18] Richard E. Prange and Steven M. Girvin. *The Quantum Hall effect*. Springer-Verlag, 1990.

[19] D. Stein, Klitzing, and G. Weimann. Electron Spin Resonance on GaAs-$Al_xGa_{1-x}As$ Heterostructures. *Physical Review Letters*, 51:130–133, July 1983.

[20] M. Dobers, Klitzing, and G. Weimann. Electron-spin resonance in the two-dimensional electron gas of GaAs-$Al_xGa_{1-x}As$ heterostructures. *Physical Review B*, 38:5453–5456, September 1988.

[21] S. Melinte, N. Freytag, M. Horvatić, C. Berthier, L. P. Lévy, V. Bayot, and M. Shayegan. Spin polarization of two-dimensional electrons in GaAs quantum wells around Landau level filling $\nu = 1$ from NMR measurements of gallium nuclei. *Physical Review B*, 64(8):085327, August 2001.

[22] Klitzing, G. Dorda, and M. Pepper. New Method for High-Accuracy Determination of the Fine-Structure Constant Based on Quantized Hall Resistance. *Physical Review Letters*, 45(6):494–497, August 1980.

[23] V. Narayanamurti. Artificially Structured Thin-Film Materials and Interfaces. *Science*, 235(4792):1023–1028, February 1987.

[24] Loren Pfeiffer, K. W. West, H. L. Stormer, and K. W. Baldwin. Electron mobilities exceeding 10^7 $cm^2.V^{-1}.s^{-1}$ in modulation-doped GaAs. *Applied Physics Letters*, 55(18):1888–1890, 1989.

[25] J. H. English, A. C. Gossard, H. L. Störmer, and K. W. Baldwin. GaAs structures with electron mobility of 5×10^6 $cm^2.V^{-1}.s^{-1}$. *Applied Physics Letters*, 50(25):1826–1828, 1987.

[26] Horst L. Störmer. 'Nobel Lecture'. Nobelprize.org. 4 May 2011, December 1998.

[27] Neil W. Ashcroft and Mermin. *Solid state physics*. Brooks/Cole, 1st edition, January 1976.

[28] L. D. Landau and L. M. Lifshitz. *Course of Theoretical Physics, Volume III: Quantum Mechanics (Non-Relativistic Theory)*. Butterworth-Heinemann, 3 edition, January 1981.

[29] B. I. Halperin. Quantized Hall conductance, current-carrying edge states, and the existence of extended states in a two-dimensional disordered potential. *Physical Review B*, 25(4):2185–2190, February 1982.

[30] R. B. Laughlin. Quantized Hall conductivity in two dimensions. *Physical Review B*, 23(10):5632–5633, May 1981.

[31] M. Büttiker. Absence of backscattering in the quantum Hall effect in multiprobe conductors. *Physical Review B*, 38(14):9375–9389, November 1988.

[32] U. Klaß, W. Dietsche, K. von Klitzing, and K. Ploog. Imaging of the dissipation in quantum-Hall-effect experiments. *Zeitschrift für Physik B Condensed Matter*, 82(3):351–354, October 1991.

[33] John D. Jackson. *Classical Electrodynamics Third Edition*. Wiley, 3 edition, August 1998.

[34] Thierry Martin and Shechao Feng. Suppression of inter-edge-state equilibration due to multiple scattering with impurities. *Physical Review B*, 44:9084–9087, October 1991.

[35] Thierry Martin and Shechao Feng. Suppression of scattering in electron transport in mesoscopic quantum Hall systems. *Physical Review Letters*, 64:1971–1974, April 1990.

[36] G. Müller, D. Weiss, A. Khaetskii, K. von Klitzing, S. Koch, H. Nickel, W. Schlapp, and R. Lösch. Equilibration length of electrons in spin-polarized edge channels. *Physical Review B*, 45(7):3932–3935, February 1992.

[37] Yang Ji, Yunchul Chung, D. Sprinzak, M. Heiblum, D. Mahalu, and Hadas Shtrikman. An electronic Mach-Zehnder interferometer. *Nature*, 422(6930):415–418, March 2003.

[38] I. Neder, N. Ofek, Y. Chung, M. Heiblum, D. Mahalu, and V. Umansky. Interference between two indistinguishable electrons from independent sources. *Nature*, 448(7151):333–337, 2007.

[39] I. Neder, M. Heiblum, Y. Levinson, D. Mahalu, and V. Umansky. Coherence and Phase in an Electronic Mach-Zehnder Interferometer: An Unexpected Behavior of Interfering Electrons. July 2005.

[40] Preden Roulleau, F. Portier, D. C. Glattli, P. Roche, A. Cavanna, G. Faini, U. Gennser, and D. Mailly. Finite bias visibility of the electronic Mach-Zehnder interferometer. *Physical Review B (Condensed Matter and Materials Physics)*, 76(16):161309–4, October 2007.

[41] L. V. Litvin, H. P. Tranitz, W. Wegscheider, and C. Strunk. Decoherence and single electron charging in an electronic Mach-Zehnder interferometer. *Physical Review B*, 75:033315, January 2007.

[42] L. V. Litvin, A. Helzel, H. P. Tranitz, W. Wegscheider, and C. Strunk. Edge-channel interference controlled by Landau level filling. *Physical Review B (Condensed Matter and Materials Physics)*, 78(7):075303–4, 2008.

[43] E. Bieri, M. Weiss, O. Göktas, M. Hauser, C. Schönenberger, and S. Oberholzer. Finite-bias visibility dependence in an electronic Mach-Zehnder interferometer. *Physical Review B*, 79(24):245324, June 2009.

[44] H. Pothier, S. Guéron, Norman O. Birge, D. Esteve, and M. H. Devoret. Energy Distribution Function of Quasiparticles in Mesoscopic Wires. *Phys. Rev. Lett.*, 79:3490–3493, 1997.

[45] H. Pothier, S. Guéron, Norman O. Birge, D. Esteve, and M. H. Devoret. Energy Distribution Function of Quasiparticles in Mesoscopic Wires. *Physical Review Letters*, 79:3490–3493, November 1997.

[46] F. Pierre, A. B. Gougam, A. Anthore, H. Pothier, D. Esteve, and Norman O. Birge. Dephasing of electrons in mesoscopic metal wires. *Physical Review B*, 68:085413, August 2003.

[47] P. Degiovanni, Ch, G. Fève, C. Altimiras, H. Le Sueur, and F. Pierre. Plasmon scattering approach to energy exchange and high-frequency noise in $\nu = 2$ quantum Hall edge channels. *Physical Review B*, 81(12):121302, March 2010.

[48] G. Granger, J. P. Eisenstein, and J. L. Reno. Observation of Chiral Heat Transport in the Quantum Hall Regime. *Physical Review Letters*, 102(8):086803, February 2009.

[49] H. A. Fertig. A view from the edge. *Physics*, 2, February 2009.

[50] D. B. Chklovskii, B. I. Shklovskii, and L. I. Glazman. Electrostatics of edge channels. *Physical Review B*, 46(7):4026–4034, August 1992.

[51] C. Chamon and X. G. Wen. Sharp and smooth boundaries of quantum Hall liquids. *Physical Review B*, 49(12):8227–8241, March 1994.

[52] Thierry Giamarchi. *Quantum Physics in One Dimension*. The International Series of Monographs on Physics. Oxford University Press, February 2004.

[53] A. Yacoby. Electrical imaging of the quantum Hall state. *Solid State Communications*, 111(1):1–13, June 1999.

[54] D. C. Glattli, E. Y. Andrei, G. Deville, J. Poitrenaud, and F. I. B. Williams. Dynamical Hall Effect in a Two-Dimensional Classical Plasma. *Physical Review Letters*, 54:1710–1713, April 1985.

[55] I. Aleiner and L. I. Glazman. Novel edge excitations of two-dimensional electron liquid in a magnetic field. *Physical Review Letters*, 72(18):2935–2938, May 1994.

[56] L. Saminadayar, D. C. Glattli, Y. Jin, and B. Etienne. Observation of the $e/3$ Fractionally Charged Laughlin Quasiparticle. *Physical Review Letters*, 79:2526–2529, September 1997.

[57] B. Trauzettel, P. Roche, D. C. Glattli, and H. Saleur. Effect of interactions on the noise of chiral Luttinger liquid systems. *Physical Review B*, 70:233301, December 2004.

[58] M. Heiblum. *Measuring the fractional charge and its evolution*, volume 40 of *Advances in Solid State Physics*, chapter 2, pages 21–34. Springer Berlin Heidelberg, Berlin, Heidelberg, 2000.

[59] M. Heiblum. *Fractional Charge Determination via Quantum Shot Noise Measurements*, chapter 7, page 115. World Scientific, August 2010.

[60] M. Cassé, Z. D. Kvon, G. M. Gusev, E. B. Olshanetskii, L. V. Litvin, A. V. Plotnikov, D. K. Maude, and J. C. Portal. Temperature dependence of the Aharonov-Bohm oscillations and the energy spectrum in a single-mode ballistic ring. *Physical Review B*, 62:2624–2629, July 2000.

[61] A. E. Hansen, A. Kristensen, S. Pedersen, C. B. Sørensen, and P. E. Lindelof. Mesoscopic decoherence in Aharonov-Bohm rings. *Physical Review B*, 64(4):045327, July 2001.

[62] Kensuke Kobayashi, Hisashi Aikawa, Shingo Katsumoto, and Yasuhiro Iye. Probe-Configuration-Dependent Decoherence in an Aharonov-Bohm Ring. *Journal of the Physics Society Japan*, 71(9):2094–2097, September 2002.

[63] B. J. van Wees, L. P. Kouwenhoven, C. J. P. M. Harmans, J. G. Williamson, C. E. Timmering, M. E. I. Broekaart, C. T. Foxon, and J. J. Harris. Observation of zero-dimensional states in a one-dimensional electron interferometer. *Physical Review Letters*, 62:2523–2526, May 1989.

[64] B. W. Alphenaar, A. A. M. Staring, H. van Houten, M. A. A. Mabesoone, O. J. A. Buyk, and C. T. Foxon. Influence of adiabatically transmitted edge channels on single-electron tunneling through a quantum dot. *Physical Review B*, 46:7236–7239, September 1992.

[65] J. P. Bird, K. Ishibashi, M. Stopa, Y. Aoyagi, and T. Sugano. Coulomb blockade of the Aharonov-Bohm effect in GaAs/$Al_xGa_{(1-x)}$As quantum dots. *Physical Review B*, 50:14983–14990, November 1994.

[66] Jonathan P. Bird, Koji Ishibashi, Yoshinobu Aoyagi, and Takuo Sugano. Observation of Aharonov-Bohm Oscillations in the Magnetoresistance of a GaAs/AlGaAs Quantum Dot. *Japanese Journal of Applied Physics*, 33(Part 1, No. 5A):2509–2510, May 1994.

[67] J. P. Bird, K. Ishibashi, Y. Aoyagi, T. Sugano, and Y. Ochiai. Spectral characteristics of conductance fluctuations in ballistic quantum dots. *Physical Review B*, 50:18678–18681, December 1994.

[68] J. P. Bird, K. Ishibashi, D. K. Ferry, Y. Ochiai, Y. Aoyagi, and T. Sugano. Phase breaking in ballistic quantum dots: Transition from two- to zero-dimensional behavior. *Physical Review B*, 51:18037–18040, June 1995.

[69] A. Yacoby, R. Schuster, and M. Heiblum. Phase rigidity and $h/2e$ oscillations in a single-ring Aharonov-Bohm experiment. *Physical Review B*, 53:9583–9586, April 1996.

[70] W. G. van der Wiel, Yu, S. De Franceschi, T. Fujisawa, J. M. Elzerman, E. W. G. M. Huizeling, S. Tarucha, and L. P. Kouwenhoven. Electromagnetic Aharonov-Bohm effect in a two-dimensional electron gas ring. *Physical Review B*, 67:033307, January 2003.

[71] Y. Yamauchi, M. Hashisaka, S. Nakamura, K. Chida, S. Kasai, T. Ono, R. Leturcq, K. Ensslin, D. C. Driscoll, A. C. Gossard, and K. Kobayashi. Universality of bias- and temperature-induced dephasing in ballistic electronic interferometers. *Physical Review B*, 79:161306, April 2009.

[72] Georg Seelig and Markus Büttiker. Charge-fluctuation-induced dephasing in a gated mesoscopic interferometer. *Physical Review B*, 64(24):245313, December 2001.

[73] Ya Blanter and M. Büttiker. Shot noise in mesoscopic conductors. *Physics Reports*, 336(1-2):1–166, September 2000.

[74] Florian Marquardt and C. Bruder. Influence of Dephasing on Shot Noise in an Electronic Mach-Zehnder Interferometer. *Physical Review Letters*, 92(5):056805, February 2004.

[75] Florian Marquardt and C. Bruder. Effects of dephasing on shot noise in an electronic Mach-Zehnder interferometer. *Physical Review B*, 70(12):125305, September 2004.

[76] Heidi Förster, Sebastian Pilgram, and Markus Büttiker. Decoherence and full counting statistics in a Mach-Zehnder interferometer. *Physical Review B*, 72(7):075301, August 2005.

[77] F. Marquardt. Fermionic Mach-Zehnder interferometer subject to a quantum bath. *EPL (Europhysics Letters)*, 72:788–794, December 2005.

[78] Florian Marquardt. Equations of motion approach to decoherence and current noise in ballistic interferometers coupled to a quantum bath. *Physical Review B*, 74(12):125319, September 2006.

[79] V. S. W. Chung, P. Samuelsson, and M. Büttiker. Visibility of current and shot noise in electrical Mach-Zehnder and Hanbury Brown Twiss interferometers. *Physical Review B*, 72(12):125320, September 2005.

[80] Clemens Neuenhahn and Florian Marquardt. Dephasing by electron-electron interactions in a ballistic Mach-Zehnder interferometer. *New Journal of Physics*, 10(11):115018, November 2008.

[81] Clemens Neuenhahn and Florian Marquardt. Universal Dephasing in a Chiral 1D Interacting Fermion System. *Physical Review Letters*, 102(4):046806, January 2009.

[82] B. J. van Wees, E. M. M. Willems, C. J. P. M. Harmans, C. W. J. Beenakker, H. van Houten, J. G. Williamson, C. T. Foxon, and J. J. Harris. Anomalous integer quantum Hall effect in the ballistic regime with quantum point contacts. *Physical Review Letters*, 62:1181–1184, March 1989.

[83] S. Komiyama, H. Hirai, S. Sasa, and S. Hiyamizu. Violation of the integral quantum Hall effect: Influence of backscattering and the role of voltage contacts. *Physical Review B*, 40:12566–12569, December 1989.

[84] B. Alphenaar, P. McEuen, R. Wheeler, and R. Sacks. Selective equilibration among the current-carrying states in the quantum Hall regime. *Physical Review Letters*, 64(6):677–680, February 1990.

[85] D. Kovrizhin and J. T. Chalker. Equilibration of integer quantum Hall edge states. *Physical Review B*, 84(8), August 2011.

[86] D. L. Kovrizhin and J. T. Chalker. Relaxation in driven integer quantum Hall edge states. November 2011.

[87] Supriyo Datta. *Electronic Transport in Mesoscopic Systems (Cambridge Studies in Semiconductor Physics and Microelectronic Engineering)*. Cambridge University Press, May 1997.

[88] B. J. van Wees, H. van Houten, C. W. J. Beenakker, J. G. Williamson, L. P. Kouwenhoven, D. van der Marel, and C. T. Foxon. Quantized conductance of point contacts in a two-dimensional electron gas. *Physical Review Letters*, 60(9):848–850, February 1988.

[89] Y. Aharonov and D. Bohm. Significance of Electromagnetic Potentials in the Quantum Theory. *Physical Review Online Archive (Prola)*, 115(3):485–491, August 1959.

[90] D. C. Glattli, P. Jacques, A. Kumar, P. Pari, and L. Saminadayar. A noise detection scheme with 10 mK noise temperature resolution for semiconductor single electron tunneling devices. *Journal of Applied Physics*, 81(11):7350–7356, 1997.

[91] R. Ashoori, H. Stormer, L. Pfeiffer, K. Baldwin, and K. West. Edge magnetoplasmons in the time domain. *Physical Review B*, 45(7):3894–3897, February 1992.

[92] N. Kumada, H. Kamata, and T. Fujisawa. Edge magnetoplasmon transport in gated and ungated quantum Hall systems. *Physical Review B*, 84:045314, July 2011.

[93] M. Büttiker, A. Prêtre, and H. Thomas. Dynamic conductance and the scattering matrix of small conductors. *Physical Review Letters*, 70(26):4114, 1993.

[94] A. Prêtre, H. Thomas, and M. Büttiker. Dynamic admittance of mesoscopic conductors: Discrete-potential model. *Physical Review B*, 54(11):8130, 1996.

[95] J. Gabelli, G. Feve, J. M. Berroir, B. Placais, A. Cavanna, B. Etienne, Y. Jin, and D. C. Glattli. Violation of Kirchhoff's Laws for a Coherent RC Circuit. *Science*, 313(5786):499–502, 2006.

[96] G. Feve, A. Mahe, J. M. Berroir, T. Kontos, B. Placais, D. C. Glattli, A. Cavanna, B. Etienne, and Y. Jin. An On-Demand Coherent Single-Electron Source. *Science*, 316(5828):1169–1172, May 2007.

[97] I. Neder, M. Heiblum, D. Mahalu, and V. Umansky. Entanglement, Dephasing, and Phase Recovery via Cross-Correlation Measurements of Electrons. *Physical Review Letters*, 98(3):036803, January 2007.